Development of small-scale fluidised bed bioreactor for 3D cell culture

Joana Mendonça da Silva

Submitted for the degree of Doctor of Philosophy

UCL Department of Medical Physics and Biomedical Engineering

University College London

2019

Declaration

I, Joana Mendonça da Silva confirm that the work presented in this thesis is my own. Where information has been derived from other sources, I confirm that this has been indicated in the thesis.

Acknowledgments

Firstly, I would like to thank my supervisors Prof Clare Selden, Prof Barry Fuller and Dr Tarit Mukhopadhyay for the opportunity of working in such a stimulating project and in a field that I'm passionate about. I would also like to thank the Liver Group Charity and the Institute of Healthcare Engineering for funding this project.

This work would not have been properly concluded without the collaboration with Dr Gui Teoh. Thank you for the help, support, exchange of ideas and laughter. It was great to work with you!

To Korsa Khan a special thank you for all the incomparable help, time and friendship at any situation, scientific or not. Also, to Jeries Abu-Hanna for the patience and time to teach and help me at such a crucial time of both our projects, thank you!

I would like to thank Márcia Baptista for all the mathematical and biostatistical support throughout all these years.

To all the Liver Group members for the day to day technical and scientific exchange but also for the fun times in and out of the lab. A special thank you to Eloy, without whom this project would not have been possible. Thank you for always being there! To Mo for all the help and time at this final stage. To Natasha for the guidance, long working hours and friendship. To Anna for the friendship in and out of the lab. And to Jordi, without whom these years would have not been the same. Thank for the time, support, discussions, fun and laughter, even long-distance, and I can't wait to see what the future holds for us. JoJos!

Finally, I want to thank my parents and sister for always believing and encouraging me, giving me the greatest opportunities in life and making me see the bright side whenever times get a bit harder. This journey would not have been possible without you! Thank you!

Abstract

Three-dimensional cell culture has gained significant importance by producing physiologically relevant *in vitro* models with complex cell-cell and cell-matrix interactions. However, current constructs lack vasculature, efficient mass transport and tend to reproduce static or short-term conditions.

The work presented aimed to design a benchtop fluidised bed bioreactor (sFBB) for hydrogel encapsulated cells to generate perfusion for homogenous diffusion of nutrients and, host substantial biomass for long-term evolution of tissue-like structures and "per cell" performance analysis.

The sFBB induced consistent fluidisation of hydrogel spheres while maintaining their shape and integrity. Moreover, this system expanded into a multiple parallel units' setup with equivalent performances enabling simultaneous comparisons.

Long term culture of alginate encapsulated hepatoblastoma cells under dynamic environment led to proliferation of highly viable cell spheroids with a 2-fold increase in cellular density over static (27.3 vs 13.4 million cells/mL beads). Upregulation of hepatic phenotype markers (transcription factor C/EBP-α and drug-metabolism CYP3A4) was observed from an early stage in dynamic culture. This environment also affected ERK1/2 signalling pathway, progressively reducing its activation while increasing it in static conditions.

Furthermore, culture of primary human mesenchymal stem cells was evaluated. Cell proliferation was not observed but continuous perfusion sustained their viability and undifferentiated phenotype, enabling differentiation into chondrogenic and adipogenic lineages after de-encapsulation.

These biological readouts validated the sFBB as a robust dynamic platform and the prototype design was optimised using computer-aided design and computational fluid dynamics, followed by experimental tests.

This thesis proved that dynamic environment promoted by fluidisation sustains biomass viability in long-term cell culture and leads 3D cell constructs with physiologically

relevant phenotype. Therefore, this bioreactor would constitute a simple and versatile tool to generate *in vitro* tissue models and test their response to different agents, potentially increasing the complexity of the system by modifying the scaffold or co-culturing relevant cell types.

Impact Statement

Currently, most *in vitro* cell and tissue models are based on two-dimensional (2D) culture in static conditions, where cells are grown in conventional tissue culture flasks fed with medium in a batch-wise fashion. Although this approach has proven fruitful for the present knowledge of biological systems, new considerations have demonstrated that this method generates misleading readouts (e.g. in drug screening and toxicity) since it does not accurately reflect the *in vivo* architecture nor environment.

Efforts have been made in the Tissue Engineering field to generate *in vitro* cell constructs in the three-dimensionality (3D) of native tissues to recapitulate the architecture and cell-cell and cell-extracellular matrix interactions to produce physiologically relevant models for basic scientific research as well as biosubstitutes for tissue therapy and regeneration. Most studies have focused primarily on the structure, but the surrounding milieu is pivotal to maintain viability and stable performance, since nutrients, waste removal, biochemical and biomechanical cues and signals are assured *in vivo* by blood and interstitial fluid perfusion. Because these *in vitro* models lack vasculature, bioreactors can replicate the biological perfusion.

Therefore, this thesis introduces a hydrodynamic environment, based on perfusion, promoted by a small-scale fluidised bed bioreactor prototype (sFBB) for long-term culture and testing of 3D cell constructs. This prototype offers a simple, reusable and cost-effective bioreactor that combines the capacity of expanding hydrogel encapsulated cells with probing the effect of external agents and stimuli (e.g. hydrodynamic forces, differentiation soluble factors) on cell phenotype and performance, making it an all-in-one device and reducing the need for additional equipment and downstream-associated costs. It is a versatile and robust device, capable of hosting different cell types and hydrogel formulations and expandable to a multiunit setup (up to 4 sFBB in parallel), enabling co-culture systems and multiple simultaneous observations, complexifying and speeding the R&D process.

Although its current scale does not provide the same high throughput analysis as microfluidics systems, the biomass volume it harbours allows a long-term and detailed assessment of cellular performance in a "per cell" sampling manner. Moreover, as an *in vitro* model, it reproduces the interactions in a more tissue/organ volume context, therefore, contributing to studies at the preclinical stage and committing to the 3Rs' principle proposed by Russell and Burch: replacing animal models with other methods, reducing the number of animals to a minimum and, refining the studies to minimise animal suffering.

Furthermore, this work has produced two manuscripts for future publication in reference scientific journals in the fields of Bioengineering and Biotechnology.

In conclusion, the developed prototype contributes to technological advances in the Tissue Engineering field with application to both academia and industry as a versatile device, with commercial potential, for producing physiologically relevant 3D cell constructs as *in vitro* models for studies in cancer biology, drug toxicity, cellular development, among others.

Table of Contents

Table of Figures

Table of Tables

List of abbreviations

Δp - Pressure drop

Δp_d – distributor pressure drop

Δp_f – fluidised bed pressure drop

2D – Two dimensional

3D – Three dimensional

A – area

AFP - α-fetoprotein

AGN - Aggrecan

ALP - Alkaline phosphatase

ATP – Adenosine Triphosphate

B - β-D-mannuronic acid

B – buoyant force

BAL – bioartificial liver

BMP2 - Bone morphogenic protein 2

C – concentration

C/EBPα - CAAT/enhancer-binding protein alpha

$CaCl_2$ – Calcium chloride

CAD – computer-aided design

C_D – drag coefficient

CDK4 - Cyclin dependent kinase 4

CFD – computational fluid dynamics

CPS - Cryoprotectant solution

CYP450 - Cytochrome P450

D – diameter

D_{AB} – diffusion coefficient

DMSO - Dimethyl sulfoxide

d_p – particle diameter

ECM - Extracellular matrix

EDTA - Ethylenediaminetetraacetic acid

ERK1/2 - Extracellular signal-regulated kinase

FBB – fluidised bed bioreactor

F_D – drag force

FDM - fused deposition modelling

G - α-L- guluronic acid

g – gravitational constant

GLU2 - Glucose transporter-2

H – height

H/D - Height-diameter ratio

H_b – height of the settled bed

HIF1α - Hypoxia inducible factor 1 alpha

H_L – height of the liquid

HNF-4α - Hepatocyte nuclear factors 4 alpha

H_t – height of the bioreactor

INHBA - inhibin beta A

J – mass flux

K_La – volumetric oxygen mass transfer

LETFs - Liver-enriched transcription factors

LPL - Lipoprotein lipase

MAP2 - Microtubule-associated protein 2

mRNA – Messenger RNA

MSCs – mesenchymal stem cells

mTOR - Mechanistic target of rapamycin

P – pressure

PEG - Polyethylene glycol

PPARγ2 - Genes peroxisome proliferator-activated receptor γ2

psd – particle size distribution

PSDA – plan-study-do-act

PVA - Polyvinyl alcohol

RCCS - Rotary cell culture systems

Re – Reynold's number

Re_t – Reynold's number at terminal velocity

RGD - Arginine-glycine-aspartic acid

sFBB – small-scale/benchtop fluidised bed bioreactor

SLA – stereolithography

SLS - selective laser sintering

TSC2 - Tuberous sclerosis complex 2

u – fluid linear velocity/ superficial velocity/ linear flow rate

u_0 – given linear velocity

u_f – maximum fluidisation velocity

u_{mf} – minimum fluidisation velocity

u_t – particle terminal velocity

V – particle volume

VEGF - Vascular endothelial growth factor

ε– fractional void volume/ bed porosity

ε_{mf} – void fraction at minimum fluidisation

μ – fluid viscosity

ρ – fluid density

ρ_p – particle density

ϕ – particle sphericit

CHAPTER 1

Introduction

1.1. Thesis outline

This thesis is divided into 6 chapters describing and discussing the results of a main project of design and developing a small-scale fluidised bed bioreactor for long-term culture and testing of 3D cell constructs:

- **Chapter 1** introduces the theoretical concepts of tissue engineering with a focus on 3D cell culture and perfusion systems, and the fundamentals on fluidised bed bioreactor technology and applications, which will lead to the scientific hypothesis and aims validated in the results chapter of this work.
- **Chapter 2** describes in detail all the general materials and methods used for the work produced, discussing the utilisation of some of the methods.
- **Chapter 3**, entitled "Designing a small-scale fluidised bed bioreactor for the dynamic culture of 3D cell constructs", focuses on the scaling down of the fluidised bed technology to a benchtop scale, testing the physical and biological performance of the prototype, and comparing it to the clinical scale model.
- **Chapter 4**, entitled "Applications of a small-scale fluidised bed bioreactor", is divided into 3 sub-chapters which will address different biological applications of the developed prototype to validate its versatility and compliance with diverse biological models. The first of these describes the effect of the dynamic environment on the proliferation and phenotype of alginate encapsulated tumour spheroids, while the second tests the potential for preservation of the undifferentiated phenotype of alginate encapsulated primary human mesenchymal stem cells. The third sub-chapter demonstrates the possibility of recovery cryopreserved in alginate encapsulated cells in the small-scale prototype.
- **Chapter 5**, entitled "Optimisation of the design of the small-scale fluidised bed bioreactor", describes the application of rapid cycling testing coupled with computational fluid dynamics, and rapid prototyping techniques to optimise the

design of the small-scale fluidised bed bioreactor, developing it into a commercial product.

- **Chapter 6** provides a general discussion of the results, potential solutions and future work for remaining questions raised from the data presented, and final conclusion of the thesis.

1.2. Tissue engineering

Tissue Engineering is a multi-disciplinary field where concepts of engineering are applied to life sciences to understand the functional and structural relationships between cells and the microenvironment in tissues, and transfer them to develop biosubstitutes that recapitulate that behaviour, to use in basic scientific research or regenerative medicine [1]. They aim to meet current challenges such as providing physiologically relevant and more accurate *in vitro* models for Research & Development; also to establish therapies for chronically damaged or diseased tissue which currently have no effective treatments, and to mitigate the critical shortage of donor organs [2].

These bioartificial constructs are developed as three-dimensional (3D) structures in a variety of forms comprising different cell types, biomaterials and growth factors. To fully replicate the cellular microenvironment, it is essential to deliver biochemical, physicochemical and mechano-structural cues provided not only by the 3D structure but also by the tight control of the external environment. This can be achieved through perfusion systems mimicking the blood circulation in the human body, which *in vitro* is assured by bioreactors that maintain: the chemostatic conditions, promote convective mass transfer, eliminate the formation of gradients and control hydrodynamic forces that could stimulate cell performance. The application of the tissue-engineered construct (i.e. for research or clinical therapy) will dictate the scale of the bioreactor.

However, advances in the field are directly dependent on technological progress as structures with increased complexity demand more accurate microenvironments, generally attained through innovative biomaterials, cell sources and perfusion mechanisms.

1.2.1. 3D cell constructs

Most of the current understanding of biological processes, their subsequent application and use for cellular models or therapies, is based on homogenous populations of cells cultured on flat surfaces of conventional tissue culture plates or flasks. This can be referred as two-dimensional (2D) culture where cells expand in a sheet/layer format, communicating only with the surrounding cells, producing limited extracellular matrix (ECM) and acquiring artificial polarity due to the orientation in the plastic [3]. Several studies have pointed out that in this system the architecture, cell-cell and cell-matrix contacts, biochemical and mechanical stimuli are lost due to "over-simplification" of the setup. For instance, fibroblasts cultured in 2D present a spread, flat morphology with ECM receptors in the ventral surface rather than the *in vivo* bipolar morphology with receptors throughout the entire surface [4]. Primary hepatocytes are a common example of a cell type which de-differentiates in 2D systems after a few days in culture, losing viability and liver-specific functions such as albumin production, urea synthesis or drug metabolism enzymatic activity [5].

Conversely, 3D cell structures replicate, to a certain extent, the *in vivo* architecture of the systems by spatially arranging cells in a physiologically relevant geometry. This provides a template for cells to adhere and expand, where the structure directly relates to function, as well as interconnectivity to promote cell-cell and cell-ECM interactions and bi-directional mass diffusion through the model [6].

The ECM, either produced by the cells or mimicked through a scaffold where they are embedded, is another key feature that drives cell behaviour in the 3D structure through biochemical and mechanical cues. Mammary epithelial cells embedded in interpenetrating networks of Matrigel® and alginate hydrogel acquired a malignant phenotype when ECM stiffness and the number of basement-membrane ligands were increased [7]. ECM composition also influences migration with fibroblast rapidly migrating in cell-derived 3D matrix and collagen, compared to basement-membrane extract matrix [8]. Although it is widely constituted by basal components such as collagen, fibrin, elastin, hyaluronic acid, fibrin, proteoglycans, growth factors and cytokines, ECM composition varies between tissues with, for example, cartilage mainly composed of collagen II and aggrecan and, heart tissue of collagens [9–11].

These models have empowered studies on cell adhesion, migration, proliferation and communication and been successfully applied for drug discovery and toxicity and cancer biology. For instance, 3D cell constructs have demonstrated higher sensitivity to drugs in liver, kidney and heart models, evidencing toxicity levels which have not been shown in 2D culture, leading to the progression to clinical trial of better drug candidates making the process more efficient and reliable and minimising the risk of failure [12–15]. In cancer, cell spheroids can serve as pre-clinical models of avascular solid tumours and metastases, replicating intervascular regions of sarcomas and carcinomas [16].

Hence, when conceptualising a 3D cell construct it is important to select the platform that will better replicate the *in vivo* microenvironment to generate the most reliable model. These are classified as scaffold-free and scaffold-based models below.

1.2.1.1. Scaffold-free 3D cell constructs

Scaffold-free systems are normally based on cellular spheroids described as spherically symmetrical aggregates with no artificial substrate for cell adhesion and formed through forced aggregation or proliferation. Several techniques can be employed to develop them: dynamic cell suspension in spinner flasks or microgravity in rotary cell culture systems (RCCS) [17,18]; hanging drop method through pipetting, low adhesion plates or gravity enforced [19,20]; culture in patterned surfaces [21]; bio-printing [22]; even microfluidics [23]. The simplicity of these structures enables co-culture systems and makes them an easily automated, mass-produced model for high-throughput analysis for drug screening and toxicity [24].

However, one of the limitations of spheroid culture is the absence of control over the size, shape and organisation of the constructs which could result in inadequate performance. As a spheroid expands its centre becomes more distant from the milieu increasing the concentration gradient of nutrients, gases and waste through the construct, a consequence of impaired diffusion. Thus, the outer most layer of the spheroid could be highly proliferative and metabolically active as it is in constant contact with the exterior, whereas layers at different depths from the surface are at different nutritional states and stages of the cell cycle with the core often becoming necrotic (Figure 1) [25].

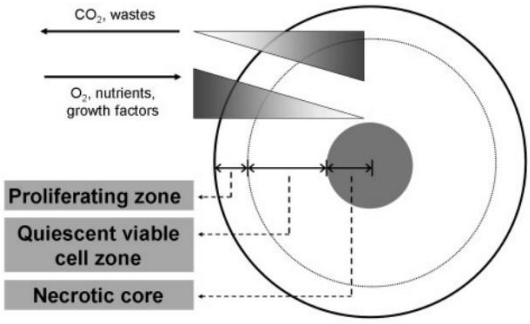

Figure 1 **-** Schematic representation of cellular spheroid mass transfer gradient. Formation of gradients through the cellular multilayers of the spheroids. Retrieved from Lin et al, 2008.

A recently growing technology of scaffold-free 3D systems is organoids. Organoids are complex multicellular structures with partial tissue function and structure. They are developed through manipulation of embryonic organogenesis mechanisms by controlled stepwise differentiation of embryonic or induced pluripotent stem cells, giving origin to embryonic germ layer–restricted or organ-specific organoids, or even specific cell types such as hepatocytes and cardiomyocytes [26,27]. The goal is to produce, *in vitro,* complex tissues that mimic exactly the native conditions, to be used as research models or replacements for diseased or ageing organs. At present, and similar to spheroids, this technology is not yet perfected to generate controlled and reproducible constructs, varying in size, shape and structure.

1.2.1.2. Scaffold-based 3D cell constructs

A scaffold is a natural or synthetic construct that provides structure and support for cell adhesion, proliferation, ECM deposition and differentiation. These are normally composed of biomaterials, i.e. materials that interact with biological systems with the purpose of evaluating, treating, enhancing or replacing tissue or organ functions [28]. Their chemical and physical properties will dictate the relationship with the biological system. Moreover, they can be classified according to the source (natural or synthetic), activity (inert, bioactive or bioresorbable) or chemical and atomic structure (metallic, ceramic, polymer and composite).

Naturally occurring biomaterials, derived from human, animal or plant sources, are often used for this purpose. They can be protein-based (collagen, gelatin, silk),

polysaccharide-based (cellulose, chitosan, alginate, hyaluronic acid) and decellularized tissue-derived biomaterials (decellularized cartilage, heart valves, liver) [29]. The ideal scaffolding would be the natural decellularised ECM matrices as the structural, mechanical and biochemical properties of the native tissue are preserved. However, limitations of this scaffold are associated with tissue availability, quality variability, intrinsic complexity and donor-related response to stimuli [30]. Alternatively, matrices composed of one or multiple ECM components (e.g. collagen type I, acid hyaluronic or basement-membrane extract commercially known as Matrigel®) have been purposed to provide the necessary biochemical cues in a more controlled environment. Polysaccharide-based scaffolds derived from plants (e.g. alginate, cellulose, agarose) or animal exoskeleton (e.g. chitosan) have also been widely used since they are regarded as inert, i.e. they have minimal interaction with the biological system they are inserted, in part, due to the absence of binding sites for cells. However, they can be functionalised with different groups to grant cell adhesion and other biochemical cues. They are extensively available and can be processed and produced in large scale.

Synthetic biomaterials benefit from well-defined and controlled chemical and physical characteristics which are tailored to the specific application and interaction and thus, reducing the complexity and variability of natural biomaterials [31]. Similarly, they can be cheaply and massively produced with low risk of containing pathogens. However, their main disadvantage is the relative absence of specificity towards organs or tissues, requiring high functionalisation and manipulation. Some examples of synthetic biomaterials are polyethylene glycol (PEG), polyvinyl alcohol (PVA), titanium and its alloys, and hydroxyapatite [32].

Either natural or synthetic, polymers have some of the most promising results when used as scaffolds due to their chemical and structural similarity to the native ECM and monomeric basic constitution, which, depending on the composition and links, can provide distinct hydrophobic, water-solubility, biological activity, biocompatibility, and degradation properties. Moreover, they have the ability to form hydrogels: 3D structures with physical and mechanical characteristics similar to the native tissues and organs.

1.2.1.2.1. Hydrogels

Hydrogels are hydrophilic 3D constructs of polymeric networks which have high water content (> 90%) and an adjustable polymer concentration. Due to their hydration and polymeric arrangement, hydrogels exhibit a viscoelastic mechanical behaviour comparable to native tissues [33,34]. Some of the most widely used polymers for hydrogel composition are alginate, agarose, hyaluronic acid, PEG and others.

They are normally formed through chemical and physical crosslinking methods. In chemical reactions, a crosslinking agent (e.g. polymer-polymer conjugation, photosensitive agents or by enzyme-catalyzed reaction) is added to the diluted polymer forming covalent bonds in the chains [35–37]. Conversely, physical crosslinking forms weaker and reversible hydrophobic, electrostatic, and/or hydrogen bonds [38,39]. The crosslinking density can control the mechanical compliance of the hydrogel, with increased concentration or exposure to the crosslinking agent increasing the stiffness of the hydrogel and vice-versa [40–42].

Another attractive feature of hydrogels as scaffolds for cell culture and further biomedical applications is the highly porous structure with an interconnected geometry that promotes cellular ingrowth, uniform distribution, increased surface area for mass transfer and assistance in vascularisation of the matrix [43–45]. Hydrogel biodegradability can also be tuned through the combination of cleavable crosslinks or moieties in the polymer backbone which can be digested, for instance, through enzymatic reaction [46]. Using ECM components (e.g. laminin, fibronectin) will also lead to natural biodegradation. Moreover, they can be modified to respond to external stimuli (e.g. temperature, light, pH, shear forces and small chemicals) resulting in changes in the properties of the hydrogel and becoming "smart hydrogels" [47].

1.2.1.2.1.1. Alginate hydrogels

Extracted from seaweed and brown algae, alginate is a polysaccharide of anionic monomers α-L- guluronic acid (G) and β-D-mannuronic acid (M). The characteristics of this natural polymer vary with the source: different algae produce alginates with

different molecular weight, ratio and arrangement of its monomers in homopolymeric regions (GG blocks and MM blocks) and heterogenic regions of MG blocks [48].

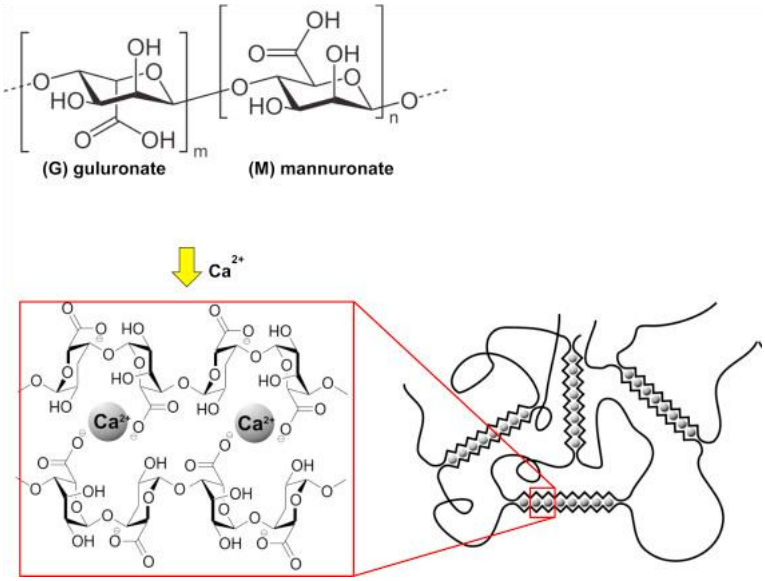

Figure 2 **-** Alginate crosslinking. Electrostatic binding of calcium ions (Ca^{2+}) to G residues establishing bonds between two adjacent chains and forming the egg-box model of alginate crosslinking. Retrieved from Bruchet M., 2015.

Physical crosslinking of soluble alginate into hydrogels is based on the high affinity of divalent cations (Ca^{2+}, Sr^{2+}, Ba^{2+}) to the GG blocks of the polymer, forcing adjacent chains containing this group to bind in an egg-box model and thus, forming the gel structure (Figure 2). The most common agent is calcium chloride ($CaCl_2$) which results in rapid crosslinking. For a slower and more controlled reaction, the crosslinking solution could contain phosphate groups which compete with the calcium ions for the carboxylate groups of the alginate. The rate of crosslinking and concentration of the agent highly influences the characteristics of the formed hydrogel, with slower rates and higher concentrations favouring uniform structures and improved mechanical integrity [49]. Subsequently, temperature is directly proportional to the reaction rate. The chemical characteristics of the extracted alginate also impact the formed hydrogel: generally, stiffness, stability, porosity and elasticity are increased with the increase of the G-content, length of G-blocks and molecular weight [50]. The hydrogel can be solubilised again, by reversing the crosslinking reaction, through the use of chelating agents for the divalent cations such as citrate and ethylenediamine tetraacetic acid (EDTA).

Given that alginate is considered an inert biomaterial, it does not possess binding sites recognised by human cells. However, it can be easily functionalised by introducing appropriate ligands which promote cell adhesion. A commonly used peptide sequence is arginine-glycine-aspartic acid (RGD) as various cell types display integrin receptors (e.g., $\alpha v\beta 3$, $\alpha 5\beta 1$) for this ligand [51]. On the other hand, as a bioinert material, alginate has been the only biopolymer which has passed most of the scientific and regulatory verifications certifying it as safe for human application [52].

The ability to be modified turns alginate hydrogels into an excellent scaffold for *in vitro* 3D cell culture and models. The structure can be achieved through microencapsulation, macroporous scaffolds or 3D bioprinting, where the polymer constitutes the bioink. Microencapsulation underlines the concept of immobilising cells within a micro-size spherical structure either compact (bead) or hollow inside (capsule). The principle is that droplets of alginate solution containing the biomass of interest are dispersed into a bath of crosslinking buffer, forming the hydrogel as they enter the bath and with the spherical shape determined from the surface tension during the impact of the droplet [53]. Although they are all droplet-based, different techniques can be used to encapsulate cells in beads or capsule: extrusion through a needle, coaxial fluid flow, electrostatic potential, vibrating or rotating capillary jet breakage [54].

The size of the hydrogel microbead/microcapsule, normally 100 - 1000 μm, depends on the droplet size, which subsequently is a function of the nozzle diameter, the alginate viscosity, the jet flow rate and the biomass (e.g. single cells or spheroids to encapsulate). As observed in cellular spheroids, the diameter of the beads could impact cell performance, since larger size beads (~1 mm) could impair the mass diffusion across the hydrogel forming a concentration gradient to the core, depriving it of nutrients and waste removal [55]. The properties of alginate hydrogels (e.g. high porosity, tuneable mechanical parameters) are preserved in this format with the advantage of the small diameter (i.e. micrometres) increasing the surface area of the beads, subsequently enhancing the bidirectional mass diffusion [56]. However, depending on the application, the microbeads/microcapsules might need reinforcement to preserve the mechanical and structural stability and prevent cells from escaping. Either coating the beads with poly-L-lysine or covalent stabilisation with Staudinger ligation will avoid the dissolution of

the hydrogel by long-term exchange reaction of divalent ions with monovalent cations present in milieu (i.e. culture medium or *in vivo* environment) [48,57,58].

Alginate encapsulation serves as a scaffold for 3D cell culture of single cells or cellular spheroids for basic research studies or *in vitro* models as well as delivery vehicles for cell, gene and drug therapy, and ultimately as biomass for the development of bioartificial organs due to the ability of mass production [52]. Regardless of the application, the alginate constitutes a mechanical barrier to shield cells from shear forces generated in culture methods and perfusion in the body and as an immunological barrier to prevent exacerbated reactions from the host immune system, and is practical for manipulation [59,60].

1.2.2. Dynamic culture

Conventional cell culture, either 2D or 3D, has been conducted under static conditions, where medium changes to provide fresh nutrients and remove the accumulated metabolites and waste products which occur, in a batch-wise fashion. This promotes mass transfer only through a diffusion mechanism and creates gradients that could limit proliferation and induce toxic effects, leading to loss of cellular function and viability.

Although 3D cell constructs replicate more accurately the *in vivo* architecture, the chemostatic microenvironment is maintained by the constant perfusion of blood through capillary vessels. Subsequently, since most 3D models lack incorporated vasculature, the provision of the dynamic environment *in vitro* can be assured through bioreactors, i.e. vessels that carry out biological reactions under a dynamic and tightly controlled environment. The perfusion environment generated by a bioreactor modulates the cell performance by providing convective mass transfer which overcomes the diffusional limitation of large cell constructs, accurately controlling the local microenvironment and providing mechanical cues and stimuli.

Under perfusion, chondrocytes seeded on PLLA/PGA scaffolds had their cell numbers and ECM deposition increased [61]. Other examples include in a 3D perfused model of breast carcinoma cells were found to migrate along flow streamlines [62]; perfused bone marrow stromal cells on mesh scaffolds differentiated into osteoblast-like cells and deposited higher contents of mineralised matrix compared to static conditions [63]; and

hepatocyte function was improved and maintained at constant values for 14 days in a microfluidics perfusion-incubator-liver-chip [64]. Therefore, perfusion of 3D cell culture will further enhance cell phenotype and performance being a valuable tool for applications such as drug screening, tissue engineering and cancer biology, but most importantly, for large biomass production or long-term culture since it will eliminate the heterogeneities of the micro- and macro-environments [65].

A wide range of bioreactors are capable of inducing this dynamic environment: stirred tanks, rotary cell culture systems, hollow fibre bioreactor, fluidised bed bioreactor, among others. The selection of the bioreactor design is dependent on the 3D cell construct and its inherent physiochemical environment.

1.2.2.1. Selecting a bioreactor design

Selecting a bioreactor design and operation mode is intrinsically dependent on the physiological environment necessary for the maintenance of cells and tissues as well as the desired biological outcome of the culture process. However, the first steps are to create a concept which can be easily assembled, built from a selection of non-toxic materials and that can keep the product sterile [66].

The cell or tissue type dictates the operating temperature, pH, oxygen and carbon dioxide levels; shear rate; the growth in suspension or requirement for adhesion; the culture medium composition and supply regime for maximising growth and avoiding starvation [67]. Moreover, metabolite quantity and stability and reaction kinetics can direct the operation mode to a batch, fed-batch or continuous/perfusion bioreactor, which differ from one another in rates of nutrient supply and metabolite removal.

The size and scale depend on the initial volume of cells, final yield and stage of the process, with systems in the range of millilitres adopted for prototypes and process development and litre-capacity vessels used in industries. The geometry of the vessel and design features such as impellers, baffles, flow distributors, spargers and heating jackets, are directly correlated with the intended magnitude of mass, gas and heat transfer, mixing efficiency, rheology, nutrient supply and sterility [68].

Based on these premises, several bioreactor designs have emerged to sustain cell culture requirements. For example, a stirred tank bioreactor, the most widely used design,

promotes efficient mixing, although producing higher shear stress rates due to the mechanical agitation promoted by the impellers [68]. Designs such as fluidised bed, hollow fibres or rotating vessel use different principles for agitation which induce low shear forces but have other constraints such as requiring cell immobilisation or having lower volumetric oxygen transfer. In tissue engineering, conventional designs do not always satisfy the needs of each type of tissue and hence, specific concepts for those applications have to incorporate special features that can replicate as much as possible the *in vivo* environment such as cyclic stretching for muscle tissue or compression for engineering cartilage [69,70].

1.2.2.2. Fluidised bed bioreactor

A fluidised bed bioreactor (FBB) operates on fluidisation principles where, in a vessel, a liquid (normally culture medium) moves upwards through a packed bed of immobilised cells (either in carriers or capsules), suspending them (Figure 3).

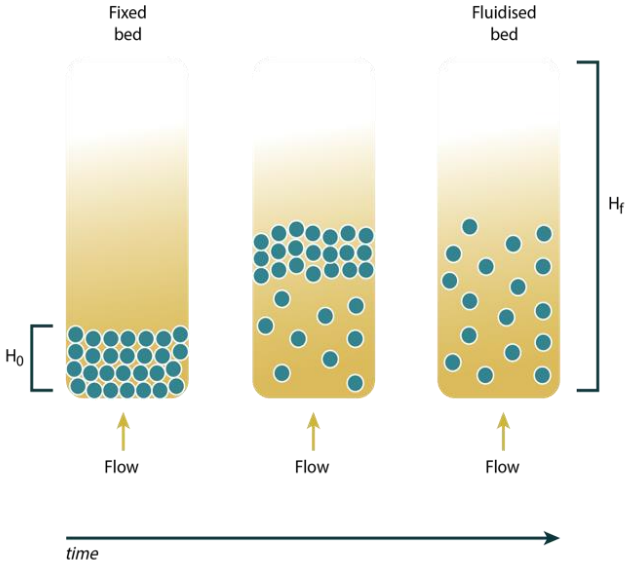

Figure 3 - Representation of expansion of solids bed in a fluidised bed bioreactor over time. H_0 is the height of the fixed bed and H_f the height of the fluidised bed at steady state.

Originally, this design could run as a gas-solid, liquid-solid or even gas-liquid-solid system. It was developed and long used in the petrochemical industry for catalytic

cracking of complex hydrocarbon chains into lighter ones. However, it gained more use as a liquid-solid system in biochemical processes since its application to waste-water treatment plants for the biodegradation of waste chemicals [71,72]. Here it was used it in a biological context.

1.2.2.2.1. Fluidisation principles

The phenomenon where settled solid particles acquire a fluid-like behaviour as a stream of gas or liquid passes through them is described as fluidisation [73]. Initially, a static packed bed with *H* height has a pressure drop of [74]:

$$-\Delta p = P_1 - P_2 = \rho g H \quad (1)$$

where P_1 and P_2 are the pressures measured at the bottom and top of the bed of solids, respectively; ϱ is the density of the fluid and g is the gravitational constant.
As the fluid travels through the bed, it exerts a drag force (F_D) on the particles expressed by:

$$F_D = \frac{\rho u^2 A C_D}{2} \quad (2)$$

with u as the fluid linear velocity, A the area and C_D the drag coefficient. C_D is a dimensionless number and a function of the solid geometry and Reynold's number (Re). To promote the fluidisation of the particles, breaking their continuous contact and suspending them, the drag force and buoyant force (B) of the fluid need to balance the gravitational force of the particles:

$$V \rho_p g = B + F_D \quad (3)$$

where V and ϱ_P are the volume and density of the particle, respectively. Under fluidisation conditions, the pressure drop across the bed reflects not only the hydrostatic pressure from Eq. (1) but also, the weight of the suspension and results in:

$$-\Delta p = H g (1 - \varepsilon)\left(\rho_p - \rho\right) \quad (4)$$

where ε is the fractional void volume, i.e. the porosity of the bed.

Hence, at low velocities, the fluid travels through the void spaces in between particles without disturbing the bed and thus, maintaining its packed or fixed state. The pressure drop across the bed increases proportionally with the fluid velocity, reaching a maximum when fluidisation starts. At this point, the fluid velocity is defined as the minimum fluidisation velocity (u_{mf}) (Figure 4). Beyond u_{mf}, as velocity increases, the pressure drop remains constant, but the bed continues to uniformly expand resulting in a homogenous fluidised bed in liquid-solid systems. In gas-solid fluidisation, beds present more instabilities like bubbling and channelling (preferential circulation of fluid through specific arteries) producing a more turbulent mixing [73,74].

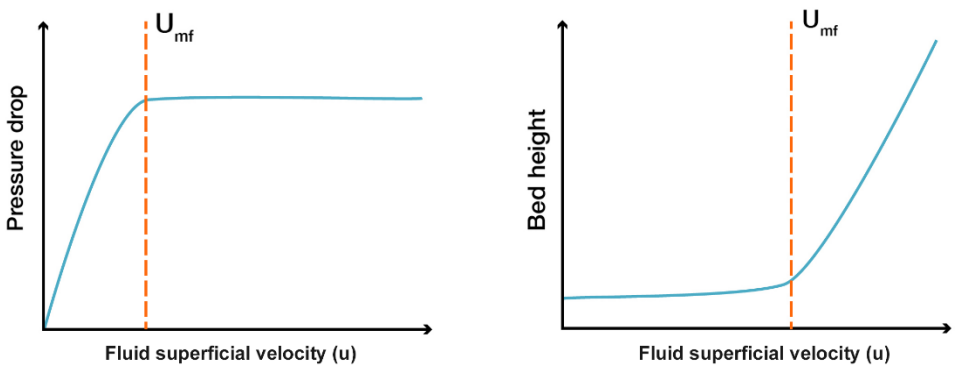

Figure 4 **-** Pressure drop across the bed (A) and bed height (B) as functions of fluid linear velocity in a fluidised bed.

However, if the flow rate rises to values where the drag force overcomes the weight of the solids, these can be washed out of the bed, i.e. elutriated, and the velocity immediately before this phenomenon occurs is denoted as maximum fluidisation velocity (u_f) [75]. To prevent elutriation, fluid velocity should be lower than u_f and the terminal velocity of the particle (u_t), which is the free-fall velocity of a particle in a fluid. Therefore, a fluid entering the system should have a given linear velocity u_0 and: $u_{mf} < u_0 < u_f < u_t$ [75].

Minimum fluidisation velocity is commonly determined experimentally in each system by measuring the pressure drop using a manometer or pressure transducers at given fluid flow rates [76–78]. This can be tested with increments in velocity and by slowly

defluidising the bed which is particularly relevant when it comprises solids with different characteristics [79,80]. Due to the non-ideal conditions of the experimental setup, u_{mf} can be defined over a range of velocities rather than an exact value.

Nevertheless, mathematical models have been developed to theoretically describe and determine u_{mf} and the pressure drop, although their generalisation is limited since they are often only valid for systems where they were established. The Kozeny-Carman equation is valid for laminar flow (Re < 2) where the fluid induces a viscous drag on the surface of the solids. Assuming the solids in the bed are spherical the model determines that:

$$u_{mf} = \frac{\varepsilon^3}{180(1-\varepsilon)} \frac{(\rho_p - \rho) g d_p^2}{\mu} \tag{5}$$

where d_p is the diameter of the particle [81]. Conversely, the most widely used model is the Ergun method, valid for a broader range of flow regimes (laminar and turbulent) and defines u_{mf} as:

$$(\rho_p - \rho) g = \frac{\rho u_{mf}^2}{\phi d_p \varepsilon_{mf}^3} \left[\frac{150(1-\varepsilon_{mf})\mu}{\phi d_p u_{mf} \rho} + 1.75 \right] \tag{6}$$

with ε_{mf} as the void fraction at the minimum fluidisation, ϕ the sphericity of the particle and μ the fluid viscosity [73,74,82].

Regardless of the model, another relevant hydrodynamic parameter is the fractional void volume or bed porosity ε. This is the volume in the interstices of solids that compose the packed bed and is dictated by size, shape and density of the particles as well as the particle-fluid velocity. Small and perfectly stacked particles will constitute a less porous bed than larger particles. Moreover, beds with solids of uniform dimensions have a different ε than those with different sizes, as smaller particles tend to fill the voids in between the larger ones [80,83].

The void volume of a bed increases with its expansion during fluidisation and is directly proportional to the fluid superficial velocity beyond u_{mf} [84]. To correlate bed voidage and the fluid superficial velocity, Richardson and Zaki proposed the following model:

$$\varepsilon^n = \frac{u}{u_t} \tag{7}$$

where ε is the bed voidage, n the bed expansion index, u the fluid linear velocity and u_t the particle terminal velocity. This model was established for homogenous, rigid, spherical particles in a liquid-solid system and is a function of Re_t (Re at the terminal velocity), with n defined according to different intervals of Re_t (Figure 5) [85–87]. However, reports that Richardson-Zaki model has inaccurately estimated bed voidage (e.g. for systems with elastic solids like hydrogels or low u_{mf}) are present in the literature and have led researchers to adapt and determine n for their specific systems [88–90].

Re_t<0.2	n=4.65+19.5d/D
0.2< Re_t <1	n=(4.35+17.5d/D) $Re_t^{-0.03}$
1< Re_t<200	n=(4.45+18d/D) $Re_t^{-0.1}$
200< Re_t<500	n=4.45 $Re_t^{-0.1}$
Re_t> 500	n=2.39

Figure 5 **-** Bed expansion index n as determined by Richardson-Zaki model.

Bed voidage influences the distribution pattern of particles during fluidisation [91,92]. At low void fractions, particle movement is constrained by neighbouring units and it mainly occurs near the wall of the vessel. Conversely, particles travel more freely at higher voidage values and predominantly in the core of the fluidiser, producing a bed with uniform behaviour throughout its height [91]. Also, it is reported that particles move faster and upwards in the centre of the vessel, whereas their velocity decreases as they travel downwards near the wall increasing the propensity for 'solids' holdup [92].

1.2.2.2.2. Fluidisation and design elements of FBB

Fluidisation performance is also intrinsically related to the construction of an FBB. This bioreactor is generally comprised of a cylindrical chamber with the fluid inlet point at the bottom and fitted with a flow distributor at a given distance from the inlet point. Considering the dimensions of the chamber, the height-diameter ratio (H/D) is an important design parameter in a bioreactor. Taller columns or those with small internal diameters exert greater wall effects on the solids, reducing their velocity, axial and radial mixing, especially at low flow rates, and require higher minimum fluidisation velocities

[93–95]. Conversely, in a wider column, the same effects are residual, with fewer bed fluctuations but lower expansion ratios and the manifestation of channelling at the top of the bed at higher superficial velocities [93]. Nonetheless, the height and diameter of the column should account for the total mass and expansion of the bed without elutriation of the particles.

The distributor consists of a porous media with random (e.g. sintered glass or metal) or organised perforations (e.g. perforated plate), which evenly distributes the fluid flow through the bed to ensure homogenous fluid-particle contact. It also physically supports the weight of the bed under static conditions. An effective design should promote a higher frictional pressure drop across the distributor (Δp_d) in relation to that across the fluidised bed (Δp_f), and uniform radial dispersion of the axial velocity of the fluid [81]. The purpose is to eliminate instabilities that could lead to channelling, circulation of pockets of concentrated particles interspersed with stagnation points, especially immediately above the distributor [74]. Although, even if Δp_d is sufficiently high, these instabilities might still occur due to imperfections in the distributor construction, the non-ideality of the system or the properties of the particles.

Parameters such as distributor hole size, shape, density and distribution, and the fractional open area significantly influence its performance and can modulate Δp_d [96–99]. For example, for the same open area, a distributor with decreased hole density will have a higher pressure drop; and smaller holes will reduce the distributor and channelling effects, as the flow is split over more channels [97]. The different designs might not alter the total velocity of the particles but can influence their circulation pattern [100]. On the other hand, the column dimensions may also impact the effect of the distributor, as $\Delta p_d/\Delta p_f$ decreases with height but increases with the width of the column [74]. However, these effects and distortions are particularly significant in beds of low-density particles and thus, for these applications the distributor design needs to be more precise [97].

The area underneath the distributor, from the inlet point to the bottom of the plate, designated the calming section functions as an equaliser of the flow, dispersing it as radially uniform as possible and reducing channelling before it reaches the distributor [74]. Partially or fully filling this section with large particles (> 1mm diameter) was demonstrated by several studies to further homogenised the fluid as the particles behave as a packed bed [79,83,93,97,101–103]. Although, manipulation of the distance between the inlet

and the distributor can exert the same effect, giving enough time for the fluid to homogenise at a given linear velocity.

The design of these elements and their interactions, in a specific system of solids and fluid linear velocity, can be pre-tested and iterated by computational fluid dynamics (CFD) which can simulate the fluid-particle circulating patterns and velocities.

1.2.2.2.3. Mass and heat transfer

Mass or heat transfer implies the movement of mass and/or thermal energy from one entity to another, usually evidenced by changes in concentrations and temperatures, respectively. The purpose of a bioreactor is maintaining these parameters as homogenous as possible maximising their transfer from the milieu to the cells and vice-versa to support cell viability and proliferation. Apart from the intrinsic properties of the medium and biomass (density, viscosity, morphology, size, concentration gradient, etc.), the degree of mixing can highly affect these transfers.

In an FBB, the heat transfer coefficient is sufficiently high for thermal equilibrium between liquid and solid surface to occur within a few particle layers of the bed [74]. Also, it is three orders of magnitude higher than the mass coefficient indicating the process of mass transfer is slower and thus, an easier parameter to use as a study reference, for instance, to determine the efficacy of the bioreactor.

As this bioreactor design requires immobilisation or entrapment of cells in microcarriers or scaffolds, the mass transfer model is a function of two mechanisms. The transport of a solute by the bulk motion of the fluid is a convection mechanism, while diffusion occurs at the liquid-solid interface and through the scaffold (if porous) driven by a concentration gradient. Fick's Laws describe the diffusion mechanism:

$$J = -D_{AB}\frac{dC}{dx} \tag{8}$$

$$\frac{dC}{dt} = D_{AB}\frac{d^2C}{dx^2} \tag{9}$$

where J is the mass flux, D_{AB} the diffusion coefficient, C the solute concentration, x the dimension where diffusion proceeds and t time. The first law (Eq. 8) assumes steady-

state and determines that diffusion flux is proportional to a concentration gradient where particles move from high concentration regions to low concentration. The evolution of concentration with time is described by the second law (Eq. 9).

However, each FBB design has its associated mass transfer equation as fluid, solid and geometry differ between processes and thus, each model does not represent others accurately [104].

1.2.2.2.4. Advantages and limitations of FBB

Fluidised bed bioreactors benefit from a higher degree of mixing due to the constant circulation of liquid through the solids, granting the fluid-like behaviour, with each particle experiencing the same environmental conditions and subsequently minimising the formation of heat, temperature and mass gradients. Moreover, the small size of the particles (normally in the magnitude of micro to millimetres) provides a high surface contact area between solids and fluid producing high heat and mass transfer coefficients [73,105]. Other advantages of FBBs concern the low hydrodynamic shear stress owing to the absence of mechanical agitation; ease of scaling; operation in a continuous process and low unit and maintenance cost.

Limitations of this type of bioreactor are associated with the absence of a systematic approach when conceiving these devices as they are usually application-specific with individual heat and mass transfer models. This absence of a design methodology can lead to deficient or over-fluidisation and consequent poor performance, channelling and particle entrainment [106]. Furthermore, for cell culture FBB requires the immobilisation of cells either on the surface or entrapped within particles, otherwise, cells would get easily elutriated from the vessel [74,88]. The immobilisation shields the biomass from shear stress, but it may limit the choice of cell type to be cultured or require specific technology to provide particles which grant adhesion points. Also, the constant fluidisation for long periods or high superficial velocities can lead to 'solids' erosion and demands for high pumping power [72].

1.2.2.2.5. Applications of FBB

As aforementioned, in biotechnology, the most widespread application of an FBB is in wastewater treatment and other environmental applications. Recent examples are the immobilisation of a population of microorganisms on activated carbon for the production of biohydrogen gas and the culture of microalgae on polyurethane foam for lipid extraction for biodiesel [107,108]. Since the 1980s this bioreactor design has been applied in animal cell technology for expression and production of recombinant proteins and cell expansion [109]. In the early 2000s, this technology started to be relevant in the context of a bioartificial liver. The advantage of this configuration is the perfusion environment it provides since it has been demonstrated that under perfusion homogenous cell seeding and higher cell densities are achieved [110,111].

1.2.2.2.5.1. Bioartificial liver

A bioartificial liver (BAL) is an extracorporeal device comprised of a bioreactor with immobilised hepatic cells able to perform liver biochemical functions such as protein synthesis, ureagenesis, glucogenesis and drug and toxin detoxification [112]. In comparison to purely artificial devices, which consist of mechanical or adsorptive filters only capable of detoxifying, the incorporation of biomass confers a superior performance on the system [113,114]. This technology is particularly pertinent for patients with acute or acute-on-chronic liver failure, a condition with poor prognosis and orthotopic transplant as the only effective treatment. Thus, a BAL could establish a bridge until transplantation or regeneration of the natural liver by replacing its function [114,115]. Briefly, this circuit is connected to a patient, collects blood (or it can be separated in plasma by plasmapheresis) which passes through the bioreactor where the biochemical exchanges occur and, returns free of toxins and full of hepatic metabolites to the donor (Figure 6).

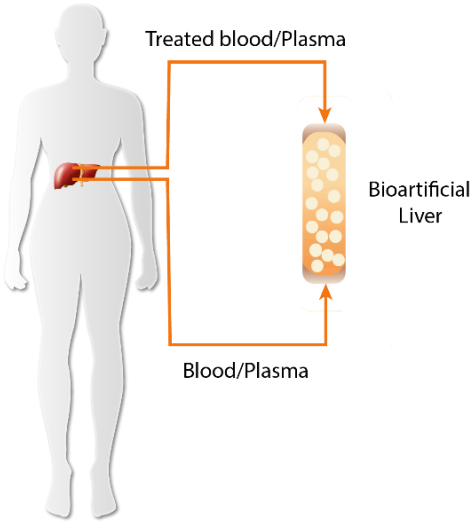

Figure 6 – Schematic of bioartificial liver device.

BAL devices differ from each other essentially in the bioreactor design, cell type and source, and immobiliser particle. The gold standard for clinical application is to use primary human hepatocytes as these are the cells responsible for the hepatic function, although their availability is limited and after isolation they start to immediately dedifferentiate, losing their phenotype and associated function [116]. Alternatively, xenogeneic hepatocytes, especially porcine, have been suggested but concerns of immunological responses, phenotypical differences in drug metabolism, for example, and potential for endogenous retroviral re-expression and in cross-species infection dispute this source as a viable substitute [117].

Hepatocyte cell lines benefit from unlimited proliferation, stable phenotype and low culture cost and thus, pose as the most advantageous cell type to be applied to a BAL. Among these, HepG2 and HepaRG cells, respectively hepatoblastoma and Hepatitis C patient-derived hepatocarcinoma cell lines, have been widely reported. Limitations of HepG2 cells include poor drug and ammonia metabolism and high lactate production in monolayer culture at least. HepaRG cells have a reduced proliferation rate, even though they present a more differentiated phenotype with the above-mentioned functions comparatively upregulated [112], but do not survive well in human plasma and die in liver-failure plasma.

Advances have also been made in deriving hepatocyte-like cells from stem cells (mesenchymal, embryonic and induced pluripotent stem cells), although in none of the studies it is yet possible to produce fully mature hepatocytes. Moreover, the complex

medium formulations and time of differentiation make this source currently unfeasible in terms of production costs for the BAL scale [118].

One of the most widely investigated bioreactor designs is the hollow fibre, where flow travels through membrane fibres and cells are adsorbed or anchored onto the outer surface. The membrane is a semipermeable material (cellulose acetate, polysulfone, polyethersulfone) enabling heat and mass transfer and creating a diffusion barrier between the cells and patients' blood or plasma [113]. However, non-uniform cell distribution, direct contact between cells and the patient's fluid, membrane fouling and its inherent molecular-weight cut-off limiting mass transfer, and difficulty in scaling-up are the main limitations of this design [116]. To overcome these problems the fluidised bed bioreactor has been proposed in several studies using single cells or spheroids encapsulated in alginate or modified alginate scaffolds as a better option for a BAL due to its improved mass transfer and immunological shield [119–124]. It also enables the cryopreservation of the biomass leading to a product that can be stored and be readily available on demand [125–127].

BAL supported by hollow fibre bioreactors have reached clinical trial phase with all the systems reporting safe implementation without associated complications or adverse effects but the efficacy of the treatment and improvement of clinical and chemical parameters varied due to the inherent characteristics of each device and trial (type and number of cells, number and condition of patients) [113,114]. In contrast, BAL using FBB are still under *in vitro* tests or pre-clinical stages to assess viability and biochemical performance of encapsulated cells subjected to plasma perfusion, the haemodynamic safety of the device and improvement of clinical and biochemical parameters in large animal models of acute liver failure [123,128–130].

1.2.2.2.5.1.1. UCLBAL

The UCLBAL is an ongoing BAL project composed of an FBB with more than 2 L of alginate encapsulated HepG2 cell spheroids, which are initially encapsulated as single cells and cultured in the same bioreactor design for up to 12 days [121,129,130]. Dynamic culture supports the growth of the cells into several spheroids inside the beads forming a 3D tissue-like structure with improved function and performance compared to monolayer and static cultured encapsulated cells. In this context, HepG2 spheroids

present cell density of more than 30 million cells/mL beads; enhanced deposition of extracellular matrix (collagen I, III, V and VI, fibronectin, laminin and vitronectin); active metabolism through glucose consumption and lactate production; synthetic function of proteins like albumin, α-fetoprotein and α-1-antitrypsin; increased expression of cytoprotective pathways; active detoxifying pathways through conjugation of bilirubin and the presence of CYP450 1A1/2; and maintenance of viability and function when exposed to liver failure plasma [121,131–133].

After culture to 'performance competence', the biomass is transferred to the BAL vessel where plasma is perfused for treatment. In pre-clinical trials, this system has demonstrated, in a porcine ischaemic acute liver failure model, improvement of coagulation, blood pH, intracranial pressure and oxygenation and reduction in vasopressor requirements, all important parameters in the clinical prognosis of the condition [130].

The successful outcome of the BAL pre-clinical trials has put this device on track to progress to clinical phase. However, process optimisation, validation and *in vitro* characterisation will always be a constant and for those studies, the current scale of > 2L of alginate beads will be impracticable.

The Liver Group attempted to scale down the FBB to harbour just a few millilitres of alginate beads, although that design did not maintain the same H_b/D ratio of the clinical model, thus not reproducing the same fluidisation patterns nor superficial flow velocity. Moreover, the device was composed of several individual parts of difficult assembly creating technical and operational constraints. This model was not an effective scale-down bioreactor and redesigning would be necessary. The goal would be to create a device that would be easy to operate, could harbour tens of millilitres of alginate beads and maintain the same hydrodynamic environment of the clinical scale FBB. If successful, the bioreactor would not be limited to serve as a pilot scale but could be explored as a versatile laboratory-scale equipment for culture of 3D cell constructs under perfusion conditions.

1.3. Hypothesis and aims

Three-dimensional (3D) cell culture has fuelled progresses in Tissue Engineering by closely replicating the *in vivo* environment and thus, producing *in vitro* models more physiologically relevant than conventional 2D culture in tissue culture flasks. Particularly, hydrogel encapsulation of cells (cell beads) can provide a 3D environment with physiochemical properties similar to those of the extracellular matrix (ECM). Moreover, their confinement in spheres or beads generates individual micro tissues or organoids within each particle enabling sampling of one biological replicate. Although a simple and versatile method of producing 3D cell constructs, encapsulated cells require an efficient transport of nutrients, growth factors and other molecules due to their complex structure (cell-cell, cell-matrix and cell-hydrogel contacts) which, because of lack of vasculature, is not an intrinsic process and the static condition of a tissue culture flask cannot efficiently provide it, even if the cell beads are surrounded by culture media. This can restrict the analysis to short-term conditions as cell viability and performance start to decline due to deficient mass transport.

Given that the majority of currently available devices for 3D cell culture either replicate static conditions, are tailored to a specific application or have a costly operation, by engineering a benchtop fluidised bed bioreactor we hypothesised that it would constitute a portable, simple and versatile tool able to generate a physiologically relevant dynamic/perfusion environment which could integrate the development of tissue-like *in vitro* structures with their response to different stimuli, agents and stresses in just one device.

To validate this main hypothesis, other hypotheses were progressively explored in each chapter:

1. A simpler and scale-down model of a clinical scale fluidised bed bioreactor designed by applying empirical similarity rules can effectively induce fluidisation of hydrogel spheres and generate an equivalent biomass yield.
2. The dynamic environment promoted by fluidisation sustains biomass viability in long-term cell culture leading to a more physiologically relevant phenotype of 3D cell constructs.

3. Design optimisation of the conceptualised prototype can follow a rapid-cycle testing using computational fluid dynamics to predict the hydrodynamic behaviour of the bioreactor when redesigning features such as the flow distributor.

Thus, the aim of the project was to develop a benchtop bioreactor that could host hydrogel encapsulated cells (cell beads) and operate under fluidisation principles to promote perfusion and maximise mass transport, consequently enabling long-term culture and sampling of the 3D cell constructs.

The work will be addressed in sequenced chapters whose aims will be:

1. To design a benchtop fluidised bed bioreactor with an operating volume of hundreds of millilitres which can host tens of millilitres of hydrogel encapsulated cells to enable prolonged monitoring and sampling.
2. To investigate the effect of a dynamic environment induced by fluidisation/perfusion on the viability, proliferation and performance of hydrogel encapsulated cells in the long-term; two cell models will be explored, one with epithelial phenotype and one with mesenchymal stem cell phenotype.
3. To optimise the designed prototype based on experimental results.

The next chapter will present the general materials and methods used throughout the work, except for the specific method of cryopreservation.

CHAPTER 2

Materials and methods

2.1. Monolayer cell culture

Materials

- Cell lines: HepG2 cells (ATCC)
- Primary cells: Human bone marrow-derived Mesenchymal Stem Cells (MSCs) isolated at UCL Great Ormond Street Institute of Child Health from infant donor samples
- Media:

  Minimum Essential Medium Alpha Modification with L-Glutamine, ribonucleosides and deoxyribonucleosides (αMEM-G) (GE Healthcare, #T1059.3017)

  Minimum Essential Medium Alpha Modification without L-Glutamine, ribonucleosides and deoxyribonucleosides (αMEM) (Sigma, #M4526)

  Fetal Bovine Serum (FBS) (Gibco, #10500-064)

  Human Fresh Frozen Plasma (FFP)

  Penicillin-Streptomycin (Gibco, #15070-063)

  Amphotericin B (Gibco, #15290-026)

  D-Glucose solution (Sigma, #G8769)

  Heparin sodium (500 IU/mL) (Leo Laboratories)

  Insulin (100 IU/mL) (Novo Nordisk, #041-7642)

  Linoleic Acid/Bovine Serum Albumin (Sigma, #L9530)

  Sodium Selenite (Sigma, #S5261)

  Hydrocortisone (Sigma, #H0888)

  Thyroid Releasing Hormone (TRH) (Sigma, #P1319)

- Cell harvesting:

  Hank's Balanced Salt Solution without Ca^{2+} and Mg^{2+} (HBSS) (Gibco, #14170-888)

  TrypLE™ Select Enzyme (Gibco, #12563029)

15 or 50 mL conical centrifuged tubes

syringes

21-gauge needles

Neubauer chamber

0.2 μm hydrophilic filter (Sartorius, #16534)

75 cm^2, 175 cm^2 or 500 cm^2 tissue culture flasks (Thermo Fisher)

2.1.1. Culture medium preparation

2.1.1.1. αMEM-G supplemented with 10% FBS

αMEM-G was supplemented with 10% FBS (v/v), 100 IU/mL penicillin and 0.1 mg/mL streptomycin, 1.25 μg/ml amphotericin B, 0.27 IU/mL insulin, 50 μg/mL linoleic acid, 0.017 μg/mL sodium selenite, 0.4 μg/mL hydrocortisone and 0.4 μg/mL THR.

2.1.1.2. αMEM-G supplemented with 10% FFP

αMEM-G was supplemented as described in *section 2.1.1.1.*, except for 10% FBS. Instead, 10% FFP (v/v) was added, as well as a final concentration of 80 IU/mL heparin and 25 mM D-glucose.

2.1.1.3. αMEM supplemented with 10% FBS

αMEM was supplemented with 10% FBS (v/v), 100 IU/mL penicillin and 0.1 mg/mL streptomycin and 1.25 μg/ml amphotericin B.

2.1.2. Cell culture and harvesting

HepG2 cells were cultured in αMEM-G supplemented with 10% FBS and MSCs in αMEM supplemented with 10% FBS. For both cell types, medium was replaced every 2 -3 days and, at approximately 80% confluence cells were harvested or passaged. To harvest, medium was discarded and monolayers washed with HBSS. Next, 1.5 mL per

25 cm^2 of TrypLE™ Select was added to each tissue culture flask, followed by incubation at 37°C for 5 – 10 min. Detached cell suspension was collected into a 15 or 50 mL conical tube, each flask washed with culture medium and the respective volume added to the same conical tube to inactivate the TrypLE™ Select. Subsequently, tubes were centrifuged for 4 min at 289 x g, supernatant discarded and pellet resuspended in an appropriate volume of fresh medium. MSCs pellet was disaggregated by pipetting up and down, whereas for HepG2 a syringe fitted with 21-gauge needle was used to pass the suspension 3 – 4 times. To determine cell density of the suspension and the desired reseeding number, cells were counted using a haemocytometer.

2.2. Alginate solution preparation

Materials

- High viscosity, G-rich, Sodium (Na)-alginate (Manugel GMB, FMC Biopolymer)
- Sodium chloride (NaCl) (Fischer Scientific, #S/3160/65)
- Sodium hydroxide (NaOH) (Fisher Scientific, #S/4880/53)
- 1 M 4-(2-hydroxyethyl)-1-piperazineethanesulfonic acid (HEPES) solution (Gibco, #15630)
- MilliQ water
- pH meter
- Silverson L5M-A Laboratory Mixer
- Viscometer (Brookfield DV-II+Pro) with a CP(E)-41 spindle

2.2.1. 2% alginate solution

1 M HEPES solution was diluted to 15 mM in 0.15 M NaCl solution and adjusted to pH 7.4 with 1 M NaOH. A 2% (w/v) Na-alginate solution was prepared in 15mM HEPES buffer using Silverson L5M-A Laboratory Mixer. Bulk viscosity of this final solution was measured in triplicate at 25°C and a shear rate of 10 s^{-1}, with a plate viscometer using a CP(E)-41 spindle.

2.3. Alginate hydrogel encapsulation

Materials

- 2% Na-alginate solution
- Collagen I extracted from rat tails
- HepG2 or MSCs cell suspension
- Glass beads, 10 – 50 μm diameter (Kisker Biotech, #PGB-05)
- Pluronic acid (Sigma, #P1300)
- HBSS (Gibco, #14170-888)
- Dulbecco's Modified Eagle's Medium (DMEM) (Sigma, #D5796)
- Sterile deionised water (dH_2O) (Baxter)
- Cross-linking buffer:
    - Calcium chloride ($CaCl_2$) (Sigma, #12022)
    - NaCl (Fischer Scientific, #S/3160/65)
    - NaOH (Fisher Scientific, #S/4880/53)
    - 15 mM HEPES solution
- Jet Cutter Encapsulation System (GeniaLab)
- Glass pyrex beakers
- Plastic bottomless beaker
- Rubber bands
- 200 μm nylon mesh
- Magnetic stirrer
- Stainless steel weighing spatula
- 24-well tissue culture plates

2.3.1. Crosslinking solution preparation

A 204 mM $CaCl_2$ solution was prepared in a 5x concentration (i.e. 1.02 M) 15 mM HEPES solution and pH adjusted to 7.4. Prior to use, the solution was sterilised for 15 min at 121°C.

2.3.2. Cell encapsulation in hydrogel discs

Cells harvested as per *section 2.1* were in suspension and mixed 1:1 with 2% (w/v) Na-alginate solution, resulting in a final mix of 1% (w/v) alginate. 200 μL of the final mix was spread as a thin layer onto the surface of a 24-well plate. Next, 250 μL/well of 50 or 204 mM crosslinking solution (diluted appropriately from the stock in HBSS) was added dropwise and incubated for 2 min. Lower concentrations of crosslinking solution generated softer gels, while stiffer ones were produced by 204 mM $CaCl_2$. The solution was pipetted out and each gel washed once with 500 μL of HBSS.

Similarly, hybrid alginate-collagen hydrogels were made by mixing equal parts of cell suspension, 2% (w/v) Na-alginate solution and collagen I solution (~ 850 μg/mL), resulting in a final mix of 0.67% (w/v) alginate. This final solution was thoroughly mixed with a pipette tip to guarantee homogeneity. Crosslinking method followed that aforementioned, except hybrid discs were incubated for 30 min at 37°C to crosslink collagen fibres before being washed once with HBSS. Medium change followed the same regime as alginate discs. Of note, the collagen I solution had been prepared by previous members of the group by dissolving rat tail tendons in 0.01 M acetic acid for 2-3 days at 4°C, centrifuging the mixture and collecting the supernatant.

Alginate and alginate-collagen gels were cultured in appropriate culture medium, replacing it every 3 days.

2.3.3. Cell encapsulation in hydrogel beads

Cell encapsulation in spherical beads used the JetCutter System as previously described [121]. Briefly, the mix to be encapsulated was prepared as per *section 2.3.2* and poured into a pressure vessel: 1% (w/v) alginate mix was prepared by 2% (w/v) Na-alginate and equal volume of cell suspension; and hybrid hydrogel mix was prepared by adding equal volumes of 2% (w/v) Na-alginate, collagen I and cell suspension. To both, 1.5% (w/v) glass beads (10 – 50 μm diameter) were added to reduce buoyancy of produced hydrogel beads. The vessel was capped, coupled to a stirring motor and final mix continuously stirred at 125 rpm. Next, air pressure was applied allowing the flow to go through and priming the system. It was calibrated to 0.33 mL/s, a rate extensively tested

to ensure sphericity of the beads. After calibration, liquid flow passed through a 350 μm nozzle positioned above a cutting wire disk (100 μm diameter, 60 wires and rotating at 3600 rpm), which cut the jet into droplets. These droplets fell into a glass pyrex beaker filled with 204 mM crosslinking buffer and 0.02% (w/v) pluronic acid to reduce the surface tension of the solution [134]. This was continuously agitated by a magnetic stirrer preventing droplets from aggregating and crosslinking them into individual beads. Once the pressure vessel was empty and all the mix had been used, beads were left an additional 5 min in solution and then, transferred to a bottomless beaker fitted with a 200 μm mesh to collect solids and drain away the liquid. Hydrogels were washed 3x for 5 min with DMEM to remove any excess calcium and finally, collected using a spatula and placed in culture medium until seeding. For hybrid hydrogel beads (alginate-collagen hydrogel), similarly to discs and before washing, beads were incubated at 37°C for 30 min in a covered petri dish. Moreover, alginate beads not containing any cells (empty beads) were produced using the same method, mixing equal volumes of DMEM and 2% Na-alginate solution.

2.4. Culture of encapsulated cells in hydrogel beads

Materials

- HepG2 cells encapsulated in alginate beads
- MSC encapsulated in alginate and alginate-collagen beads
- αMEM-G supplemented with 10% FFP
- αMEM supplemented with 10% FBS
- 6-well tissue culture plates
- 175 cm^2 tissue culture flasks
- 100 μm Falcon™ Cell Strainers
- 15 mL and 50 mL conical tubes
- Bioreactor:

    Glass column fitted with a sintered glass filter

    2 L, 3.5 L or 5 L Duran® laboratory bottles

    Safety caps GL45 thread (VWR)

1 mm bore, 0.5 mm wall AlteSil™ High Strength Silicone tubing (Altec)

2 mm bore, 1 mm wall AlteSil™ High Strength Silicone tubing (Altec)

3.2 mm bore, 1.6 mm wall AlteSil™ High Strength Silicone tubing (Altec)

4.8 mm bore, 2.4 mm wall AlteSil™ High Strength Silicone tubing (Altec)

4.8 mm bore, 1.6 mm wall Santoprene® tubing (Altec)

36.09 mm ID, 3.53 mm cross section silicon "O-ring" (Altec)

520U peristaltic pump fitted with 313 multichannel head (Watson Marlow)

Pure O_2 oxygen concentrator AirSep

Air pump

D405, 25mm, Dissolved Oxygen (DO) Sensor with glass housing (Broadley James, #D405-B070-PT-D9)

Flow meter

Female and male luer connectors

IN-Stopper (B|Braun)

Discofix® 3-way Stopcock (B|Braun)

0.2 μm Hydrophobic PTFE membrane filters (Sartorius)

2.4.1. Static culture of encapsulated cells in hydrogel beads

2.4.1.1. Static culture of HepG2 cell beads

After encapsulation of HepG2 cells (*section 2.3.3*), 3 mL of beads were transferred to a 15 mL conical tube and left to settle to the final volume, adjusting it accordingly. They were then added to a 175 cm^2 tissue culture flask with 138 mL of 10% FFP αMEM-G medium to keep a bead to medium ratio of 1:46. One flask was set per time point (days 4, 8 and 12). Medium change followed the regime: 50% on day 4 of culture, 60% on day 7, 70% on day 9 and 80% on day 11. Both ratio and medium changes had been previously optimised [121]. Flasks were cultured for 12 days in a humidified incubator (Galaxy) at 37°C and 5% CO_2.

2.4.1.2. Static culture of MSCs beads

Similarly to HepG2 beads, MSCs encapsulated in alginate or alginate-collagen beads were transferred to a 15 mL conical tube and left to settle to the intended volume. 3 mL of alginate MSC beads were seeded per 175 cm^2 tissue culture flask (~17000 cells/cm^2) with 138 mL of αMEM supplemented with 10% FBS for studies on the impact of static *vs* dynamic culture. Conversely, 0.4 mL of beads were seeded per well in a 6-well plate with 8 mL of medium to investigate the influence of alginate *vs* alginate-collagen hydrogels on MSCs performance. Encapsulated MSCs were cultured for 21 days and time points included days 7, 14 and 21.

In the co-culture model, 0.4 mL of MSCs beads were seeded at the bottom of the well and 0.2 mL of HepG2 cell beads in a cell strainer above, all in 8 mL of αMEM supplemented with 10% FBS. Culture lasted 14 days and time points included days 7 and 14.

In all studies cells were cultured in a humidified incubator (95%) at 37°C and 5% CO_2 and medium was replaced every 3 days.

2.4.2. Dynamic culture of encapsulated cells in hydrogel beads

2.4.2.1. Bioreactor setup

A dynamic environment was achieved through fluidisation of beads in a bioreactor, where the upward movement of perfused liquid through the bed of solids overcomes the force of gravity resulting in the expansion of the bed and suspension of beads in the fluid. The small-scale fluidised bed bioreactor (sFBB) comprised a 21 cm long and 3.5 cm diameter glass column fitted with 4 mm thick sintered glass distributor, placed 2 cm from the bottom. It was sealed with two GL45 thread safety caps and two 36.09 mm ID, 3.53 mm cross section silicone "O-rings": bottom cap included two vertical inlet points (28 mm length, 6 mm diameter), while the top one an outlet and a sampling port to retrieve beads. This bioreactor was connected in a closed loop to a reservoir through 4.8 mm bore, 2.4 mm wall silicone tubing and recirculation of liquid achieved using 520U peristaltic pump with 313 multichannel head (4.8 mm bore, 1.6 mm wall Santoprene®

tubing). Inside the reservoir, a coil of silicone tubing (2.5 mm bore and 0.5 mm wall) was fitted for active gassing due to the material's permeability. Subsequently, oxygen supply to the system was adjusted by a flow meter and monitored with an in-line polarographic DO sensor fitted in a glass housing, filled with perfusing media, before the inlet of the sFBB. To determine the oxygen concentration at the outlet point (after biomass consumption) another sensor was fitted to the outlet tubing (before the reservoir).

Before the inlet point there was also connected a Discofix® 3-way Stopcock to enable media changes. Medium samples were collected both at the inlet and outlet points of the sFBB via IN-Stopper ports. Figure 7 further exemplifies the setup of the system. Moreover, the setup was expandable into multiple parallel units (up to four sFBB), with each bioreactor recirculating individually due to a multichannel pump head. All bioreactors shared a common reservoir and the flow rate was set by the pump for all channels but each channel allowed individual adjustment of the clamping effect on the respective tube.

The main components of the system were reusable, washable and autoclaved at 121°C for at least 20 min.

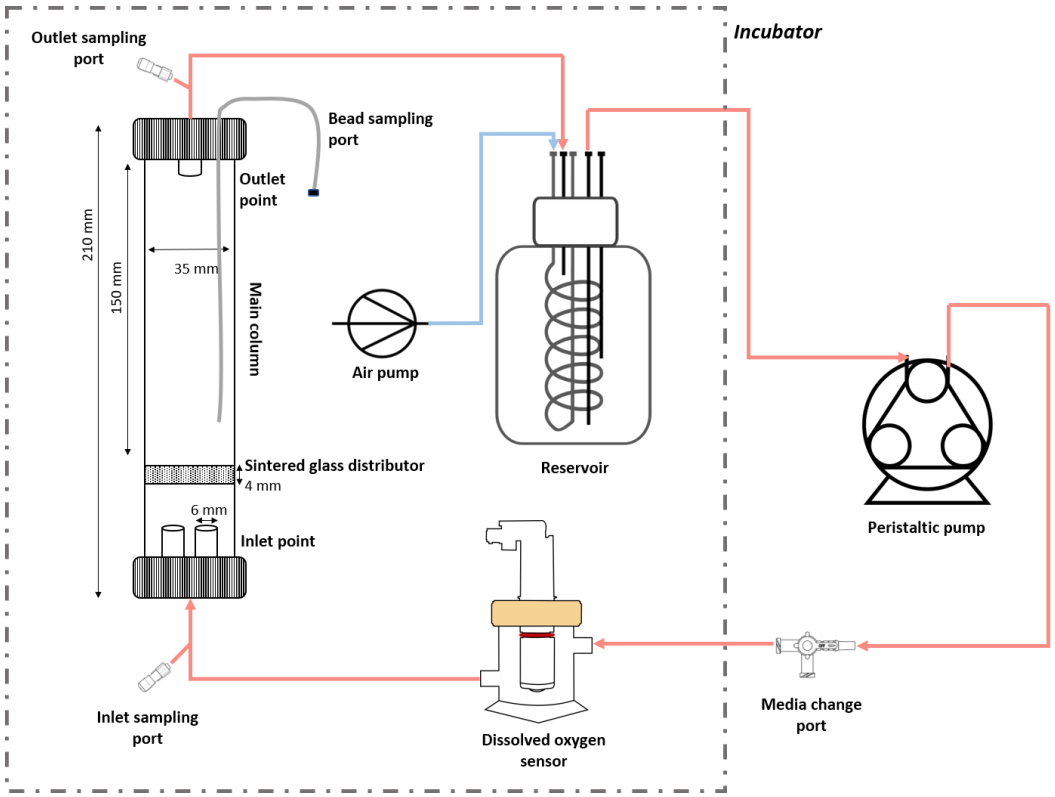

Figure 7 – Schematic representation of small scale fluidised bed bioreactor system setup.

2.4.2.2. sFBB culture of encapsulated cells

The small-scale setup described on *section 2.4.2.1* was assembled in a class II biosafety cabinet to guarantee aseptic conditions. After assembly, the reservoir was filled with sufficient medium to keep the ratio of cell beads to medium 1:46 and the system was primed up to half the volume of the sFBB main column. 30 to 40 mL of HepG2 or MSC cell beads were loaded by pouring in from the top of the bioreactor, the lid closed tightly and the circuit transferred to a research 5% CO_2 dry incubator (LEEC) at 37°C, with side openings for tubing to pass and fit the peristaltic pump placed outside. Medium was perfused from the bottom to the top of the sFBB and encapsulated cells fluidised to at least 1.6 times their initial bed height, measured with a ruler from the distributor surface to the top of the bed of beads. To keep fluidisation level constant, liquid flow rates were adjusted throughout culture, ranging from 6 mL/min to 19 mL/min. Moreover, the system was actively gassed with air-5% CO_2 at 150 – 200 mL/min by an air pump positioned inside the incubator and connected to the reservoir. As the oxygen level dropped to 15%, the air pump was replaced by an oxygen concentrator set to generate up to 35% DO. Culture periods, time points, media composition and media change regime followed those of static culture controls for the respective cell type.

2.4.2.3. Large scale dynamic culture of encapsulated cells

Similarly, encapsulated HepG2 cells were cultured in a scale-up fluidised bed bioreactor (FBB) as detailed in [130]. Briefly, a 4 L capacity vessel hosted 2.5 L of alginate encapsulated HepG2 cells and was attached in a perfusion circuit to a stirred tank bioreactor with single-use bioprocess container (SUB) containing 116 L of αMEM-G supplemented with 10% FFP. Culture lasted 12 days and with a media change regime identical to the small scale. The system was recirculated at 380 mL/min with a peristaltic pump. Temperature, pH, CO_2 and O_2 were controlled by proportional–integral–derivative dynamic system. This procedure was performed by other team members.

2.5. Time to reach equilibrium in the sFBB

Materials

- sFBB system: bioreactor with all features, silicone tubing, peristaltic pump and reservoir
- Alginate beads without cells (empty beads)
- 2 mM $CaCl_2$ in 155 mM NaCl solution
- Methylene blue 5mg/mL solution (ProVepharm)
- Bromophenol blue (BHD, #44305)
- 96-well polystyrene microplate
- FLUOstar Omega Filter-based multi-mode microplate reader (BMG Labtech)
- MARS data analysis software (BMG Labtech)
- Canon EOS 700D camera

Method

Colorimetric methods for mixing time studies use inert or reactive dye tracers in a volumetric context to describe the mixing dynamic of the system. As a global method (i.e., analysis of the whole volume), this practice requires a transparent vessel and enables identification of unmixed or stagnate zones, although measurements are subjective to operator's interpretations [135]. Combining it with local measurements (using probes) or imaging techniques describes more accurately the fluid dynamics inside the vessel.

To characterise sFBB mixing time, it was assembled as per *section 2.4.2.1* and filled with 500 mL of 2 mM $CaCl_2$ solution and 25 to 30 mL of alginate cell or empty beads. Flow rate set by a pre-calibrated peristaltic pump fluidised the bed of beads to a minimum of 1.6 times its initial height. 0.3 mL of methylene blue solution or 0.8 mL of 0.04 mg/mL bromophenol blue solution was injected through the inlet sampling port. Afterwards, a time course of the sFBB mixing profile was established by collecting fluid samples from the outlet sampling port every 0.5 min from 0 to 8 min, every 1 min from 8 to 15 min, and every 5 min from 15 to 30 min. Simultaneously, real-time visual observation of the mixing pattern was conducted by the operator. 100µL of each sample were then

transferred in triplicate to a 96-well plate to measure the absorbance at 666 nm or 592 nm for methylene blue or bromophenol blue, respectively.

2.6. Bed fluidisation in the sFBB

Materials

- sFBB system: bioreactor with all features, silicone tubing, peristaltic pump and reservoir
- HepG2 cells encapsulated in alginate beads
- 2 mM $CaCl_2$ in 155 mM NaCl solution
- Toluidine blue O (Sigma, #T3260)
- Bottomless beaker
- 200 μm nylon mesh
- Canon EOS 700D camera

Method

A colorimetric method based on stained particles, visual observations and video recording was followed to describe the overall behaviour of a fluidised bed. Therefore, 30 mL of encapsulated HepG2 cells were collected after 12 days of culture and washed 3 times with 2 mM $CaCl_2$. From those, 10 mL were stained for 10 min with 10 mL of 1 mg/mL toluidine blue solution in a bottomless beaker fitted with a 200 μm mesh. Thereafter, beads were washed thoroughly to remove excess dye. The sFBB was assembled as previously described (*section Bioreactor* setup*)* and filled with 500 mL of 2 mM $CaCl_2$ solution and 20 mL of non-stained cell beads. On top, 10 mL of stained beads were added slowly so as not to disturb or pre-mix the bed before fluidisation. The bioreactor was sealed, and a flow rate set to expand the bed to 2x its initial height. A video of fluidisation was recorded to identify the instants of expansion, homogeneity and points of stagnation or heterogenous mixing.

2.7. Mass transfer in alginate beads

Materials

- sFBB system: bioreactor with all features, silicone tubing, peristaltic pump and reservoir
- Day 4 HepG2 cells encapsulated in alginate beads
- Empty alginate beads
- 2 mM $CaCl_2$ in 155 mM NaCl solution
- Fluorescein isothiocyanate–dextran average molecular weight 150 kDa (Sigma, #FD150S)
- 96-well black, glass bottom microplate
- Nikon Eclipse Ti-E microscope with Hamamatsu Flash 4.0 sCMOS camera and Nikon C2 Confocal with PMTs for 3 channel simultaneous imaging
- Nikon TE200 microscope with a Nikon DS-Fi1c camera (with a 0.67x adapter) and DS-U2 PC control unit
- NIS-Element Microscope Imaging software

Method

Fluorescein isothiocyanate (FITC)–dextran has been widely chosen for diffusion rate and permeability studies as it is a neutral and hydrophilic molecular weight marker. Coupling it with confocal fluorescence microscopy, which provides real-time imaging and serial optical sections (z-stacks) of 3D specimens, enables analysis of particle diffusion to the core of alginate beads in a non-destructive manner.

For mass transfer of particles into beads, 10 µL of empty alginate beads were aliquoted per well in a 96-well black, glass bottom plate and washed twice with 2 mM $CaCl_2$. 100 µL of 0.03 mg/mL FITC-dextran 150 kDa solution prepared in 2 mM $CaCl_2$ were added and imaged immediately. Every minute for a total of 20 min, 10 slices of the bead were captured to provide information about diffusion to the core. Conversely, transfer of FITC-dextran out of empty alginate bead, required overnight incubation in 100 µL of 0.03 mg/mL fluorescent solution after being washed twice. The following day, immediately before imaging, dextran solution was replaced by 100 µL of 2 mM $CaCl_2$

solution and the bead imaged to capture 10 slices of the z-stack every minute for a total of 20 min. The same method was applied to study diffusion in HepG2 cell beads.

Mass transfer was also studied under dynamic conditions where the sFBB was assembled as described, filled with 200 mL of 2 mM $CaCl_2$ and 25 mL of empty alginate beads. Once the bed was fluidising 1.6 times its initial height (flow rate at 18.2 mL/min), 0.6 mL of 10 mg/mL FITC-dextran solution were injected through the inlet sampling port (final concentration of 0.03 mg/mL in the system). Beads were then sampled at fixed time points, aliquoted per well in a 96-well black, glass bottom plate and imaged with 6 slices captured per bead. Subsequently and after 45 min, for mass diffusion out of the same beads, the reservoir was emptied and replaced with fresh 50 mL of 2 mM $CaCl_2$ solution. This was perfused through the system and likewise, beads were sampled at fixed time points, aliquoted and imaged.

2.8. Alginate beads dimensions

Materials

- Alginate encapsulated HepG2 cells
- Dulbecco's phosphate-buffered saline with calcium and magnesium (DPBS-Ca^{2+}/Mg^{2+}) (Gibco, #14190-094)
- Microscope glass slides
- Microscope slide coverslips
- Nikon TE200 microscope with a Nikon DS-Fi1c camera (with a 0.67x adapter) and DS-U2 PC control unit
- NIS-Element Microscope Imaging software

Method

0.3 mL of HepG2 cell beads were washed twice with 1 mL of DPBS-Ca^{2+}/Mg^{2+} solution. They were transferred onto a microscope slide, imaged with Nikon TE200 microscope with a Nikon DS-Fi1c camera (with a 0.67x adapter) and DS-U2 PC control unit and five phase images were captured per condition (static and dynamic culture) and time point.

From each image 10 beads were selected, and their diameter aspect ratio measured using NIS-Element Microscope Imaging software.

2.9. Cell viability of encapsulated cells

Materials

- Encapsulated cells, both HepG2 and MSCs in beads and discs
- DPBS-Ca^{2+}/Mg^{2+} (Gibco, #14190-094)
- Fluorescein diacetate (FDA) (Sigma, #F7378)
- Propidium iodide (PI) (Sigma, #P4864)
- Microscope glass slides
- Microscope slide coverslips
- Nikon TE200 microscope with a Nikon DS-Fi1c camera (with a 0.67x adapter) and DS-U2 PC control unit
- NIS-Element Microscope Imaging software

Method

An *in situ* live/dead assay was performed using double staining of fluorescein diacetate (FDA) and propidium iodide (PI). While non-fluorescent FDA passively diffuses through cell membrane and enzymatic de-acetylation in the cytoplasm of living cells converts it to fluorescent FDA, PI only binds to DNA of cells with compromised membranes [136]. This method involves quantification of fluorescence intensities, although it is only an estimation, albeit with validated algorithm. Flow cytometry would provide absolute viability values; however, it would require releasing cells from the hydrogel and disaggregating them from the formed spheroid, compromising the viability. Thus, 0.3 mL of cell beads or discs in 24-well plate were washed twice with DPBS-Ca^{2+}/Mg^{2+} and left in 0.5 mL of the same solution. Next, each sample was stained with 10 μL of 1 mg/mL FDA and 20 μL of 1 mg/mL PI solutions and incubated for 90 s in the dark. Staining solution was removed, and samples washed twice with DPBS-Ca^{2+}/Mg^{2+}. They were then imaged using Nikon TE200 microscope with exposure times of 100 ms for FDA staining and 800 ms for PI. Five different captures (measuring approximately 100

beads) were obtained per condition and cell viability calculated based on fluorescence intensities detected by set macros in the NIS-Element Microscope Imaging software:

$$viability\ (\%) = \frac{FDA_{intensity}}{FDA_{intensity} \times PI_{intensity}} \times 100 \quad (10)$$

The validation of this method was done by another team member and is described in detail in [130].

2.10. Cell number of encapsulated cells

Materials

- Encapsulated cells, both HepG2 and MSCs in beads and discs
- HBSS (Gibco, #14170-888)
- Dulbecco's phosphate-buffered saline (DPBS) (Gibco, # 14040-091)
- Ethylenediamine tetraacetic acid (EDTA) (Applichem, #A1105 1000)
- NaCl (Fischer Scientific, #S/3160/65)
- 5 mL syringes
- 21-gauge needle
- Reagent A lysis buffer (Chemometec, #910-0003)
- Reagent B stabilisation buffer (Chemometec, #910-0002)
- NucleoCassette™ (Chemometec)
- Nucleocounter NC-100™ (Chemometec)

Method

Encapsulated cells in hydrogel beads or discs were washed once with HBSS solution. To release cells spheroids from the hydrogel, 4 mL of 16 mM EDTA in 155 mM NaCl solution adjusted to pH 7.4 were added to each 0.3 mL of beads or whole disc in a 15 mL centrifuge tube. The mix was vortexed until alginate was chelated and cells pelleted by centrifugation at 4000 rpm for 10 min. The pellet was resuspended in 2 mL of DPBS and disaggregated with 21-gauge needle in 5 mL syringe. A cell suspension was prepared with reagents A and B, in equal volumes (e.g. 300 µL cell suspension + 300 µL solution

A + 300 μL solution B) for automatic nuclei quantification using NucleoCassette™ in Nucleocounter NC-100™. This method quantifies nuclei based on propidium iodide staining.

2.11. Glucose consumption

Materials

- Medium samples collected from static and dynamic culture of encapsulated HepG2 cells
- Deionised water
- GM7 Micro-stat analyser (ANALOX Instruments)
- Glucose oxidase reagent (ANALOX, #GMRD-002A)
- 8 mM glucose standard (ANALOX, #GMRD-011)

Method

Glucose concentration in culture medium from static and dynamic conditions was determined based on the following reaction:

$$Glucose + O_2 \xrightarrow{Glucose\ oxidase} Gluconic\ acid + H_2O_2 \quad (11)$$

where the oxygen consumption rate is directly proportional to the substrate concentration. Based on an enzymatic reaction and detection through an electrochemical oxygen sensor, this method is sensitive to temperature variations and could result in false readings if equilibrium is not achieved.

GM7 Micro-stat analyser was primed with glucose oxidase reagent and pre-calibrated with 8 mM glucose standard solution. Media samples (10μL) were injected to determine glucose concentration. Each sample was measured at least in duplicate and diluted appropriately in deionised water for measurements higher than 30 mM, to ensure linearity of the assay. Glucose consumption was calculated according to:

$$Glucose\ consumption = [Glucose]_t - [Glucose]_{t+n} \quad (12)$$

where $[Glucose]_t$ is glucose concentration at the time medium was added or changed and $[Glucose]_{t+n}$ concentration at the desired time point.

2.12. ATP assay

Materials

- HepG2 cells or MSCs encapsulated in hydrogel beads
- αMEM (Sigma, #M4526)
- Hank's Balanced Salt Solution with Ca^{2+} and Mg^{2+} (HBSS-Ca^{2+}/Mg^{2+}) (Gibco, #)
- Adenosine 5'-triphosphate (ATP) disodium salt (Sigma, #A-7699)
- 96-well white polystyrene microplate (Corning)
- CellTiter-Glo® 3D Cell Viability Assay (Promega, # G9681)
- Vortex mixer
- FLUOstar Omega Filter-based multi-mode microplate reader (BMG Labtech)
- MARS data analysis software (BMG Labtech)

Method

Metabolically active cells produce adenosine triphosphate (ATP), which can be assessed and quantified through a luminescence signal:

$$Luciferin + O_2 + ATP \xrightarrow[Mg^{2+}]{\substack{Ultra-Glow^{TM} \\ rLuciferase}} Luminescence\ signal \quad (13)$$

This method, using CellTiter-Glo® 3D Cell Viability Assay, enables direct analysis of ATP in 3D microtissues without prior disaggregation, as the reagent has a high lytic capacity necessary for dissemination in 3D cell constructs. However, quantification of ATP levels requires a standard curve and linearity of the assay is limited to 10 μM.

To determine ATP content in encapsulated cells in hydrogel beads, the protocol was adapted from supplier's instructions [137]. Briefly, CellTiter-Glo® 3D Reagent was thawed overnight at 4°C. Before use, the reagent was incubated at room temperature (approximately 22°C water bath) for 30 min and mixed gently to obtain a homogenous

solution. A stock solution of 20 mM ATP was prepared in αMEM and further diluted to 10, 7.5, 5, 2.5, 1.25 and 0.625 μM for the standard curve. 100 μL/well of each standard was pipetted in triplicate in white-walled 96-well plate. Cell beads were collected, washed once with HBSS-Ca^{2+}/Mg^{2+} and equilibrated at room temperature for 5 min. Thereafter, 10 – 40 μL of beads were added per well and the volume made up to 100 μL with αMEM. Each sample was measured in triplicate and the volume of beads depended on previously determined cell number to ensure concentrations fell within the linearity of the assay. Subsequently, 100 μL of CellTiter-Glo® 3D Reagent was added to each well (including standards and samples) and the plate vigorously mixed for 5 min using a vortex set at shake level 3 to induce cell lysis. It was placed in a microplate reader, to record luminescence signals every 5 min for 1 h with a gain set at 2500. Luminescence values used for analysis were retrieved once the signal stabilised which corresponded to a 25 min time point. A standard curve was produced by plotting relative luminescence units (RLU) *vs*. standard ATP concentrations ([ATP]) and through linear regression, ATP concentration of each sample was determined. Further calculations estimated the "per cell" content of ATP (μmol ATP/million cells).

2.13. Enzyme-Linked Immunosorbent Assay (ELISA)

Materials

- Medium samples from static and dynamic culture of encapsulated HepG2 cells and MSCs
- 96-well Nunc Maxisorp Immuno coated plates (Fisher, #DIS-971-030J)
- Capture and detection antibodies and standards for target proteins (Table 1)
- Coating buffer:
  - Sodium carbonate anhydrous (Na_2CO_3) (VWR International, #10240 4H)
  - Sodium hydrogen carbonate ($NaHCO_3$) (MERCK, #K4295129150)
- PBS Tween:
  - NaCl (Fischer Scientific, #S/3160/65)
  - Potassium chloride (KCl) (VWR International, #26764.232)

Potassium dihydrogen orthophosphate (KH_2PO_4) (VWR International, #102034B)

Di-sodium hydrogen orthophosphate 2-hydrate ($Na_2HPO_4.2H_2O$) (VWR International, #103834g)

Tween® 20 (Sigma, #P1379)

- Non-fat milk powder (Marvel)
- 30% hydrogen peroxide (H_2O_2)
- O-phenylenediamine (OPD) tablets (KEMSUND, #4110)
- Sulphuric acid (H_2SO_4)
- MilliQ water
- FLUOstar Omega Filter-based multi-mode microplate reader (BMG Labtech)
- MARS data analysis software (BMG Labtech)

Table 1 – Supplier's information of proteins detected by ELISA.

	AFP	**Final Concentrations**
Capture antibody	Abcam, #ab10071	2 μg/mL
Standard	Abcam, #ab10072	200 – 6.25 ng/mL
Detection antibody	Generon, #CSB-PA09987B0Rb	2 μg/mL

Method

Sandwich ELISA is an immunological assay with colorimetric enzyme-linked detection system which detects and quantifies a specific secreted ligand in a liquid sample. This is achieved by immobilising the antigen of interest between a capture antibody and a detection antibody covalently linked to an enzyme. Adding a substrate triggers the enzymatic reaction which converts it to a colour detectable signal. This technique requires optimisation and validation of the antibody pair to avoid cross-reactivity and, appropriate dilution of samples to ensure they fall within the limits of the standard curve.

Firstly, 100 μL of capture antibody (Table 1) prepared 1:1000 in coating buffer (15 mM Na_2CO_3 and 35 mM $NaHCO_3$ in MilliQ water at pH 9.6) were added per well in a 96-well Maxisorp Immuno plate. It was sealed with an adhesive cover and incubated overnight

at 4°C. Next, the following solutions were prepared: PSB Tween with 137 mM NaCl, 2.7 mM KCl, 1.8 mM KH_2PO_4 and 10 mM $Na_2HPO_4.2H_2O$ in 1 L of MilliQ water, to which was added 500 µL of Tween® 20; and blocking buffer with a final concentration of 0.05 g/mL of non-fat milk powder in PBS Tween solution. The plate was washed 3 times with 200 µL of PBS Tween and incubated for 1 h at room temperature with 100 µL of blocking buffer. Meanwhile, samples were diluted appropriately in culture medium, as well as a serial dilution of standards (200 to 6.25 ng/mL, Table 1) to produce the standard curve. In triplicate, 100 µL of each standard and sample were pipetted per well and incubated at 37°C for 90 min. The plate was again washed as formerly described and incubated for another hour at 37°C with 100 µL of detection antibody (Table 1) prepared 1:1000 in blocking buffer. Next, a final washing step of 5 times 200 µL of PBS Tween was performed. 100 µL of OPD solution (3 tablets of OPD and 6 µL of 30% H_2O_2 in 12 mL of MilliQ water) were added per well at timed intervals. This reaction consisted in the oxidation of OPD by HRP using H_2O_2 as the oxidising agent, yielding a yellow product. Once sufficient colour developed (approximately 5 min), reaction was stopped with 50 µL of 2 M H_2SO_4. Absorbance was measured at 492 nm through a microplate reader and data analysed by MARS data analysis software.

2.14. Cell cycle analysis

Materials

- HepG2 cells or MSCs encapsulated in hydrogel beads
- HBSS (Gibco, #14170-888)
- EDTA (Applichem, #A1105 1000)
- Ice cold 95% ethanol (VWR International, #20821.33)
- DPBS (Gibco, # 14040-091)
- PI (Sigma, #P4864)
- Trisodium citrate (BHD, #102427X)
- BD LSRFortessa™ Flow Cytometer
- Flowing Software 2

Method

Cell cycle analysis can be achieved by DNA quantification, as progression through the cycle implies the doubling of the DNA content from G_1 phase (growing phase with diploid cells, 2N) to G_2/M phase (pre-mitosis/mitosis with tetraploid cells, 4N), passing by the intermediate state of S phase (DNA replication ranging between 2N to 4N). Thus, staining cells with PI and analysis by flow cytometry will proportionally correlate the amount of DNA with fluorescence intensity (i.e. more DNA, brighter signal). This method enables screening of a large number of cells. However, it only identifies the three mentioned phases, not distinguishing between G_0 (cells exiting the cycle) and G_1 phases nor provides information about cell cycle kinetics, as it is a single time point measurement [138].

For cell cycle analysis, cell beads containing up to 2 million cells were washed once with HBSS, cells released from beads with 4 mL of 16 mM EDTA solution and centrifuged at 4000 rpm for 10 min. The pellet was resuspended in 1.2 mL of DPBS and disaggregated using a 21-gauge needle in a syringe. Then, 3 mL of 95% ethanol were added dropwise to the cell suspension while vortexing to prevent cells from aggregating. This was incubated for 30 min at 4°C and then stored at -20°C. On the day of analysis, fixed cells were washed twice with 12 mL of DPBS, pelleted at 4000 rpm for 10 min to remove the ethanol and resuspended in 1 mL of 50 μg/mL PI solution prepared in 3.8 mM trisodium citrate. Cells were processed by BD LSRFortessa™ Flow Cytometer for at least 100,000 events and data analysed using Flowing Software 2 gating out the debris and doublets.

2.15. Gene expression analysis

Materials

- HepG2 cells or MSCs encapsulated in alginate beads
- RNase Away (Thermo Fisher)
- RNA extraction:

    Diethyl pyrocarbonate (DEPC) (Sigma, #D578)

    HBSS (Gibco, #14170-888)

    EDTA (Applichem, #A1105 1000)

DPBS (Gibco, # 14040-091)

TRIzol™ reagent (Thermofisher, #15596026)

Chloroform (BHD, #100776B)

Isopropanol (Sigma, #27049-0)

RNase-free glycogen (20 mg/mL) (Thermo Fisher, #R0551)

Trisodium citrate (BHD, #102427X)

Ethanol (Sigma, #32221)

HyClone water (Thermo Fisher, #SH30538.03)

PCR clean microfuge tubes 1.5ml DNAse/RNAse free

Microcentrifuge

Tube heat block

NanoDrop™ spectrophotometer

- RT-qPCR:

  MicroAmp Fast 96-well reaction plate (Applied Biosystems)

  Optical adhesive covers (Applied Biosystems)

  Primers (Table 2)

  Luna Universal one-step RT-qPCR (New England Biolabs; #E3005)

  7500 Fast real-time PCR system (Applied Biosystems)

Table 2 – Primers sequences.

Target	Forward primer	Reverse primer
Albumin	*5'-TGAGCAGCTTGGAGAGTACA-3'*	*5'-GTTCAGGACCACGGATAGAT-3'*
AFP	*5'-CCAACAGGAGGCCATGCTT-3'*	*5'-GAATGCAGGAGGGACATATGTTT-3'*
CEBP-α	*5'-GTGCGTCTAAGATGAGGGGG-3'*	*5'-GGAAGGAGGCAGGAAACCTC-3'*
HNF4-α	*5'-CCGGGTGTCCATACGCATCCT-3'*	*5'-CAGGTTGTCAATCTTGGCC-3'*
CYP3A4	*5'-AGCTTAGGAGGACTTCTTCAACC-3'*	*5'-AGCCAAATCTACCTCCTCACACT-3'*
CYP3A7	*5'-ATTACGCTTTGGAGGACTTCTTCT-3'*	*5'-CGTCTTCATTTCAGGGTTCTATTT-3'*
HIF-1α	*5'-CAAAACACACAGCGAAGC-3'*	*5'-TCAACCCAGACATATCCACC-3'*
VEGF-α	*5'-TCCACCATGCCAAGTGGTCC-3'*	*5'-AGGAAGCTCATCTCTCCTAT-3'*
CCD1	*5'- GCCTCTAAGATGAAGGAGAC-3'*	*5'- CCATTTGCAGCAGCTC-3'*
BMP2	*5'-CTTCTAGCGTTGCTGCTTCC-3'*	*5'-AACTCGCTCAGGACCTCGT-3'*
ALP	*5'-ATGAAGGAAAAGCCAAGCAG-3'*	*5'-CCACCAAATGTGAAGACGTG-3'*
PPAR-γ2	*5'-GCTGTTATGGGTGAAACTCTG-3'*	*5'-ATAAGGTGGAGATGCAGGCTC-3'*
LPL	*5'-GAGATTTCTCTGTATGGCACC-3'*	*5'-CTGCAAATGAGACACTTTCTC-3'*
AGN	*5'-TGAGGAGGGCTGGAACAAGTACC-3'*	*5'-GGAGGTGGTAATTGCAGGGAACA-3'*
Col 2	*5'-CAGGTCAAGATGGTC-3'*	*5'-TTCAGCACCTGTCTCACCA-3'*
NANOG	*5'-ATAGCAATGGTGTGACGCAG-3'*	*5'-GATTGTTCCAGGATTGGGTG-3'*
INHBA	*5'-GATGTACCCAACTCTCAGCCA-3'*	*5'-GCCGATGTCCTTGAAACTGAC-3'*
Survivin	*5'-AGGACCACCGCATCTCTACAT-3'*	*5'-AAGTCTGGCTCGTTCTCAGTG*
MAP2	*5'-GGAACCAACTCTCTCTGGATTT-3'*	*5'-GCATTCTCTCTTCAGCCTTCT-3'*
HPRT1	*5'-AGACTTTGCTTTCCTTGGTCAG-3'*	*5'-TCAAGGGCATATCCTACAACAA-3'*
GAPDH	*5'-GACCCCTTCATTGACCTCAAC-3'*	*5'- CTTCTCCATGGTGGTGAAGA-3'*

2.15.1. RNA extraction

To prepare RNA extraction, HBSS, DPBS and 4 mM EDTA solutions were treated with 0.1% (v/v) DEPC, autoclaved at 121°C for 20 min and stored at 4°C until usage to inactivate RNase enzymes. Total RNA was extracted according to TRIzol™ reagent method. Thus, a volume of cell beads containing at least 5 million cells were washed twice with cold HBSS, cells released from alginate beads by 4 mM EDTA solution and centrifuged at 200 x g for 4 min at 4°C. The pellet was washed with DPBS, centrifuged again and resuspended in 1 mL TRIzol™. To homogenise the lysate, the suspension was

pipetted up and down, transferred to a PCR-clean 1.5 ml microfuge tube and further processed or stored at -80°C. Afterwards, 0.2 mL of chloroform were added to each tube, shaken vigorously for 15 s, incubated at room temperature for 3 min and centrifuged at 12000 x g for 15 min at 4°C. This separated the suspension into three phases with the aqueous upper one containing RNA, which was transferred to a new PCR tube. Isopropanol (0.5 mL) was added and incubated for 10 min at room temperature to precipitate RNA. For samples with ≤ 1 million cells RNase-free glycogen (RNA carrier) was used to help co-precipitate RNA. Hence, 50 μL of 3 M trisodium citrate were added to the aqueous phase, followed by 1.5 μL of glycogen and 0.5 mL of isopropanol. This solution was mixed thoroughly (pipetted up and down) and incubated for 1 h at -20°C. Next, samples containing isopropanol or glycogen and isopropanol were centrifuged at 12000 x g for 10 min at 4°C for RNA to pellet. Supernatant was discarded using a micropipette, pellet washed 3 times with 75% ethanol (in HyClone water), vortexed briefly and centrifuged each time at 7500 x g for 5 min at 4°C. Samples were air dried for 10 min and subsequently, resuspended in 50 μL of HyClone water and heated for 15 min at 60°C in a heat block. Finally, samples were placed on ice and their RNA concentration and purity (ratios A260/280 and A260/230) measured using the NanoDrop spectrophotometer. They were stored at -80°C until downstream processing.

2.15.2. RT-qPCR

Gene expression in encapsulated HepG2 cells and MSCs was performed by reverse transcription quantitative polymerase chain reaction (RT-qPCR). This is a one-step method where reverse transcription and PCR occurs in the same well immediately after one another, minimising experimental variation and enabling high throughput screening; although, the sensitivity of the assay is reduced due to the impossibility of optimising each reaction separately.

RT-qPCR was performed using Luna Universal one-step RT-qPCR kit with total RNA templates standardised to 250 ng per well (in nuclease free water). The reaction mix contained 1x Luna Universal One-Step Reaction Mix, 1x Luna WarmStart® RT Enzyme Mix and forward and reverse primers (Table 2) at a final concentration of 0.4 μM. Firstly, 12.6 μL of reaction mix was pipetted into each well of the 96-well plate, topped with 7.4

μL of RNA template. All preparations and steps were performed on ice to avoid degradation of the samples. The plate was sealed with adhesive covers to prevent evaporation of the samples during PCR, followed by a centrifugation step at 2500 rpm for 1 min to remove bubbles and collect the liquid at the bottom. Next, the plate was transferred to a 7500 Fast real-time PCR system for the thermocycling process according to the manufacturer's protocol. Data was analysed through the $2^{-\Delta\Delta Ct}$ method where Ct values provided by PCR quantification (gene expression) were normalised to those of an endogenous control (housekeeping gene HPRT1 or GAPDH) (ΔCt) and compared to a control sample (such as, 2D cell culture or 3D static cell culture) for a final comparative gene expression value (ΔΔCt) and exponentiated as $2^{-\Delta\Delta Ct}$ to achieve the fold difference in relation to the control [139].

2.16. Protein expression

Materials

- HepG2 cells encapsulated in alginate beads
- HBSS (Gibco, #14170-888)
- EDTA (Applichem, #A1105 1000)
- DPBS (Gibco, # 14040-091)
- Protein lysis buffer:
    - Tris hydrochloride (Tris-HCl) (Sigma, #T5941)
    - NaCl (Fisher Scientific, #S/3160/65)
    - EDTA (Applichem, #A1105 1000)
    - Triton X-100 (Alfa Aesar, #A16046)
- Protease inhibitor cocktail (Cytosketelon Inc, #PIC02)
- Phosphatase inhibitor cocktail 2 (Sigma, #P5726)
- Phosphatase inhibitor cocktail 3 (Sigma, #P0044)
- Pierce™ BCA Protein Assay Kit (Thermo Fisher, #23225)
- Western blot:
    - SeeBlue™ Plus2 Pre-stained Protein Standard (Invitrogen, #LC5925)

NuPAGE™ LDS (lithium dodecyl sulfate) Sample Buffer (4x) (Invitrogen, #NP007)

NuPAGE™ Sample Reducing Agent (10x) (Invitrogen, #NP009)

NuPAGE™ 4 - 12% Bis-Tris Gels (Invitrogen, #NP0322)

NuPAGE™ MOPS SDS Running Buffer (20x) (Invitrogen, #NP0001)

NuPAGE™ Transfer Buffer (20X) (Invitrogen, #NP0006)

Primary and secondary antibodies (Table 3)

10x Casein Blocking Buffer (Sigma, #B6429)

Methanol (Fisher Scientific)

Ponceau S solution (Sigma, #P7170)

DPBS tablets

Tween® 20 (Sigma, #P1379)

Amersham™ ECL™ Western Blotting Detection Reagents (GE Healthcare, #RPN2106)

Deionised water

Filter paper

Blotting sponge pads

Amersham™ Protran™ Premium 0.2 μm Nitrocellulose Blotting Membrane (GE Healthcare, #10600004)

Gel knife

Novex™ Power Supply Adapters (Invitrogen, #ZA10001)

XCell SureLock™ (Invitrogen, #EI0001)

XCell II™ Blot Module (Invitrogen, #EI9051)

Power supply (BioRad)

- 96-well polystyrene microplate
- Tube heat block
- Tube rollers
- Orbital shaker
- FLUOstar Omega Filter-based multi-mode microplate reader (BMG Labtech)
- MARS data analysis software (BMG Labtech)
- FluorChem M system (ProteinSimple)
- ImageJ analysis software

Table 3 – List of antibodies used for protein expression by western blot.

	Supplier	Cat. #	Dilution
Primary antibody			
Phospho-p44/42 MAPK (Erk1/2) (Thr202/Tyr204)	Cell Signalling Technology	9101	1:1000
p44/42 MAPK (Erk1/2)	Cell Signalling Technology	9102	1:1000
Phospho-Akt (Ser473) (D9E) XP®	Cell Signalling Technology	4060	1:1000
Akt (pan) (C67E7)	Cell Signalling Technology	4691	1:1000
Phospho-mTOR (Ser2448) (D9C2) XP®	Cell Signalling Technology	5536	1:1000
Phospho-mTOR (Ser2481)	Cell Signalling Technology	2974	1:1000
mTOR (7C10)	Cell Signalling Technology	2983	1:1000
Raptor (24C12)	Cell Signalling Technology	2280	1:1000
Rictor (53A2)	Cell Signalling Technology	2114	1:1000
GβL (86B8)	Cell Signalling Technology	3274	1:1000
Anti β-tubulin	Abcam	ab6046	1:3000
Anti-GAPDH	Abcam	ab8245	1:50000
Secondary antibody			
Anti-rabbit IgG, HRP-linked	Cell Signalling Technology	7074	1:1000
Anti-mouse IgG, HRP-linked	Cell Signalling Technology	7076	1:1000

2.16.1. Protein extraction

Prior to extraction, protein cell lysis buffer was prepared comprising: 20 mM Tris-HCl, 150 mM NaCl, 5 mM EDTA and 10% (v/v) Triton-X in deionised water. A volume of cell beads containing at least 5 million cells, were washed with HBSS, de-encapsulated from alginate beads by 4 mL of 16 mM EDTA solution and centrifuged at 4000 rpm for 10 min. The pellet was resuspended in 1 mL protein cell lysis buffer containing protease and phosphatase inhibitors cocktails 2 and 3 (1:100 for all 3 inhibitors) and homogenised by pipetting up and down. This lysate was centrifuged at 14000 rpm for 4 min at 4°C. Supernatant was collected to a new tube, snap frozen in liquid nitrogen and stored at -80°C until downstream processing.

To determine protein concentration of each sample Pierce™ BCA Protein assay was performed following manufacturer's instructions. Briefly, 80 µL of the working solution,

made up by mixing 50 parts of solution A to 1 part of solution B, was added to 10 μL of protein lysate per well in a 96-well plate. Standard albumin solutions (2000, 1500, 1000, 750, 500, 250 and 125 μg/mL) were prepared in a similar way to produce a standard curve. Each sample was measured in triplicate and the plate incubated at 37°C for 30 min. Absorbance was measured at 562 nm by a microplate reader and total protein concentration was calculated by linear regression of the standard curve.

2.16.2. Western blot

Western blot is a sensitive technique that identifies specific single proteins in a sample. It is particularly useful when trying to determine the activation of a signalling pathway and post-translational modifications in response to external cues [140]. However, this is semi-quantitative as it only provides relative comparison of protein levels and not an absolute value [141]. For accurate quantification of protein mass spectrometry would be more quantitative but difficult to perform in multiple samples.

To prepare protein lysates for western blot analysis, samples were diluted appropriately in protein cell lysis buffer to standardise their concentrations. Then, to 65 μL of sample, 10 μL of reducing agent and 25 μL of LDS sample buffer were added to cause protein reduction. These were heated for 10 min at 70°C in a heat block. Meanwhile, the gel cassette was washed in deionised water, white tape at the bottom removed and locked in place in the XCell SureLock™ electrophoresis chamber. The chamber was filled with running buffer (diluted 1:20 in deionised water) and the comb removed. After heating, 25 μL of sample were loaded in the respective wells; and per gel (in one well only) 5 μL of protein ladder were added. Gel electrophoresis ran for 70 min at 160 V constant voltage. Once it finished, the cassette was cracked open and the gel carefully removed on top of pre-soaked filter paper and blotting pads in transfer buffer (diluted 1:20 in 20% (v/v) methanol). On top of the gel was positioned the nitrocellulose membrane, filter paper and blotting pads, all pre-soaked. This sandwich was transferred to the XCell II™ Blot Module, which was fitted inside XCell SureLock™. The blot chamber was filled with transfer buffer and the outer chamber with deionised water to help dissipate heat during transfer. It ran for 2 h at 30 V and at the end, the membrane was removed and stained with Ponceau S solution to verify the efficacy of the transfer. It was washed with

deionised water to remove the dye and blocked for 1 h in 25 mL of 1x casein solution (diluted 1:10 in deionised water) on an orbital shaker at room temperature. For protein staining, membrane was rolled into a 50 mL tube and incubated overnight at 4°C with 3 mL of primary antibody solution (diluted according to Table 3 in 1x casein solution). The following day, the membrane was washed 3 times for 10 min with DPBS-Tween (0.1% (v/v) Tween 20 in DPBS solution) and incubated for 1 h at room temperature in a 50 mL tube with 3 mL of secondary antibody solution (diluted according to Table 3 in 1x casein solution). Next, the membrane was washed as described, incubated for 1 min with a chemiluminescent detection reagent (mixing equal parts of solution 1 and 2) and imaged by FluorChem M system. To re-probe the membrane for endogenous control (β-tubulin or GAPDH), it was quickly washed and the same staining protocol performed. Data analysis used ImageJ to estimate the intensity of the detected bands, with each band normalised to its respective endogenous control.

2.17. Sirius red histochemistry for staining hybrid alginate/collagen I beads

Material

- MSCs encapsulated in alginate and alginate-collagen beads
- DPBS-Ca^{2+}/Mg^{2+} (Gibco, #14190-094)
- 4% (w/v) paraformaldehyde (PFA) (BHD, #294474) in DPBS, pH 6.9
- Weigerts Haematoxylin solution A (#S20013-E)
- Weigerts Haematoxylin solution B (#S20014-E)
- 1% (w/v) Sirius red solution saturated in aqueous picric acid
- Ethanol (Fisher Scientific)
- DPX mounting medium (Fisher Scientific, #D/5319/05)
- Deionised water
- X-tra™ adhesive slides (Leica Biosystems)
- Nikon TE200 microscope with a Nikon DS-Fi1c camera (with a 0.67x adapter) and DS-U2 PC control unit
- NIS-Element Microscope Imaging software

Methods

MSCs alginate and alginate-collagen beads were collected, washed with DPBS-Ca^{2+}/Mg^{2+} and fixed for 30 min with cold 4% PFA solution. Beads were then washed 3 times with DPBS-Ca^{2+}/Mg^{2+} and kept in the same solution at 4°C until processing.

To verify the presence of collagen fibres in the hybrid hydrogels, Sirius red staining was performed using MSC alginate beads as control. Cell beads were seeded in X-tra™ adhesive slides and left to dry. Next, each slide was stained for 7 min with Weigerts Haematoxylin (mixing solution A and B in equal parts), rinsed with deionised water, and washed for 5 min in running tap water. Following microscope examination to determine the haematoxylin staining of the cells, slides were stained with picro-Sirius red solution for 1 h. They were then rinsed in ethanol and mounted in xylene. Images of each slide were capture with Nikon TE200 microscope with a Nikon DS-Fi1c camera (with a 0.67x adapter) and DS-U2 PC control unit.

2.18. Immunofluorescence staining

Materials

- Monolayer cell culture
- 4% PFA solution
- DPBS-Ca^{2+}/Mg^{2+} (Gibco, #14190-094)
- DPBS (Gibco, #14040-091)
- Triton X-100 (Alfa Aesar, #A16046)
- Bovine Serum Albumin (BSA) (Sigma, #A9647)
- Primary and secondary antibodies (Table 4)
- Hoechst 33342 (Thermofisher)
- Nikon TE200 microscope with a Nikon DS-Fi1c camera (with a 0.67x adapter) and DS-U2 PC control unit
- NIS-Element Microscope Imaging software

Table 4 – List of antibodies used for immunofluorescence staining.

	Supplier	Cat. #	Dilution
Primary antibody			
Albumin	Dako	A0001	1:200
Secondary antibody			
Anti-Rabbit IgG-PE	Santa Cruz Biotechnology	sc-3739	1:500

Method

As medium was removed from the wells, cells washed with DPBS-Ca^{2+}/Mg^{2+} and fixed with cold 4% PFA solution for 15 min. After fixation, cells were washed twice with DPBS and permeabilised for 5 min with 0.1% (v/v) Triton X-100 prepared in DPBS. Samples were blocked with 3% (w/v) BSA solution (in 0.05% Triton X-100) for 1 h at room temperature and incubated overnight at 4°C with primary antibody diluted in 3% BSA solution (Table 4). Cells were then washed 3 times for 5 min with DPBS and incubated for 1 h at room temperature in the dark with secondary antibody diluted in blocking solution (Table 4). Samples were washed once with DPBS and nuclei stained with Hoechst 33342 for 2 min at room temperature in the dark. Finally, cells were washed 3 times for 5 min with DPBS and imaged with Nikon TE200 microscope at 460 nm emission and 100 ms exposure for Hoechst dye (blue) and 590 nm emission and 1 s exposure for IgG-PE secondary antibody (red).

2.19. Releasing encapsulated cells from alginate beads

Materials

- Day 14 and 21 alginate encapsulated MSCs from dynamic and static cultures
- HBSS (Gibco, #14170-888)
- 16 mM EDTA solution filtered sterilised
- Neubauer chamber
- 12-well tissue culture plates

Method

Alginate encapsulated MSCs from day 14 and 21 in dynamic and static culture were sampled and washed once with HBSS solution. Cells were released from the hydrogel through addition of 4 mL of 16 mM EDTA in 155 mM NaCl solution adjusted to pH 7.4 and filtered sterilised. The mix was vortexed until alginate was chelated and cells pelleted by centrifugation at 289 x g rpm for 4 min. The supernatant was removed, the pellet resuspended in 2 mL of HBSS and centrifuged again to remove alginate debris. The pellet was resuspended in medium and disaggregated through pipetting up and down several times. The cell suspension concentration was determined through cell counts using the Neubauer chamber. After, cells were seeded in a 12-well plate in triplicate at 23 000 cells/cm^2. They were left to adhere overnight in 0.5 mL of αMEM supplemented with 10% FBS at 37°C in a 5% CO_2 humidified incubator.

2.20. Differentiation of de-capsulated MSCs

Materials

- Day 14 de-encapsulated and alginate encapsulated MSCs from dynamic and static cultures
- HBSS (Gibco, #14170-888)
- StemPro® Adipogenesis Differentiation Kit (Gibco, #A10070-01)
- StemPro® Chondrogenesis Differentiation Kit (Gibco, #A10071-01)
- 4 % PFA solution
- DPBS (Gibco, # 14040-091)
- Oil Red O solution, 0.5% Isopropanol (Sigma, O1391-250ML)
- Alcian Blue staining solution (Merck, TMS-010-C)

2.20.1. Differentiation

Differentiation capacity of MSCs was assessed through directed adipogenesis and chondrogenesis using the StemPro® Adipogenesis and Chondrogenesis Differentiation kits. The kits were prepared according to manufacturer's specification where 10 mL of

the respective supplement were added to 100 mL of differentiation basal medium. After overnight culture of day 14 de-encapsulated MSCs (*section 2.19*) from dynamic and static culture, medium was removed, and each well was washed once with HBSS. Cells were then culture in respective adipogenesis and chondrogenesis differentiation medium for 14 days with medium changes every 3 days. The same procedure was applied to day 14 alginate encapsulated MSCs from dynamic and static culture which were seeded in the 12-well plate at the same density as the de-encapsulated cells.

At the end of the 14 days of differentiation, assessment of the phenotype was done through histological staining and gene expression following the method of *section 2.15*.

2.20.2. Histological staining

To validate the differentiated phenotype, de-encapsulated MSCs from dynamic and static culture, after the 14 days of differentiation, were washed once with DPBS and fixed for 20 min with 0.5 mL of 4% PFA solution per well. Each well was washed 3 times with 1 mL of DPBS.

Cells subjected to chondrogenesis were stained with 0.5 mL/well of Alcian Blue solution for 30 min. After, staining solution was removed and cells were washed 3 times with DPBS and preserved in DPBS until imaging. For adipogenesis, cells were also fixed with 4% PFA solution, washed and stained with Oil Red O for 45 min. Solution was aspirated and cells washed with DPBS. Stained cells were imaged with imaged with Nikon TE200 microscope.

2.21. Flow simulation

Models of the sFBB, with variations of design features, were drawn using computer-aided design (CAD) software SolidWorks v. 2018 (Dassault Systems). Analysis of the influence of these features in the fluid performance was carried out by computational fluid dynamics (CFD), using flow simulation package provided by SolidWorks, in which the numerical method follows the finite volume element model. Parameters and approximations of the system were defined equally for all simulated models:

- Fluid tested: water
- Flow type: laminar and turbulent
- Wall thermal condition: adiabatic
- Temperature: 37°C
- Pressure: 101325 Pa
- Boundary conditions: inlet set at uniform flow rate of 25.7 mL/min and the outlet at environmental pressure of 101325 Pa.
- Mesh: global mesh defined at refinement level 3

Results were retrieved for fluid velocity, pressure and shear stress.

2.22. Statistical analyses

Statistical analyses used GraphPad Prism 7.0 software. Student's t-test or multiple Student's t-test were used to compare two groups, whereas for sets of data with more than two factors (i.e. static vs dynamic culture and time) analysis using two-way covariance (ANOVA) was performed. In both analyses, significance level was set at $p < 0.05$ and corrections used the Holm-Sidak and Sidak methods, respectively, to assume that individual tests are independent.

Further details on number of samples and replicates, data and error description are referred in each figure legend in the results sections.

CHAPTER 3

Designing a small-scale fluidised bed bioreactor for the dynamic culture of 3D cell constructs

3.1. Introduction

3.1.1. Bioreactor scale

The scale of a bioreactor is subject to its application and can be classified as micro, benchtop and clinical or industrial scale. Microscale bioreactors operate in volumes of micro to millilitres and are being powered by the technological advances in the microfluidics field. This scale is particularly relevant at the basic research level for tightly controlled environments, costly compounds or high-throughput applications such as organoid formation, stem cell differentiation or drug screening [142]. The benchtop scale ranges from tens of millilitres to a couple of litres of operating volume, hosting considerable biomass to monitor the process throughout several time points and testing per sample performance. These bioreactors often serve as prototypes for scaling up or down the processes but can also stand as tools for basic research on, for example, the influence of perfusion, oxygen and nutrient transfer rate in cell culture along with *in vitro* modelling of tissues and diseases. Both micro and benchtop scales benefit from initial low investment and being portable. Conversely, industrial scale operates bioreactors of hundreds of litres with optimised cellular expansion processes for various applications such as vaccines and antibody production; or just to be directly producing a biomass used in the clinical context of cell and gene therapies [143].

Each of these stages can be scaled up or down for different purposes. Increasing the scale has normally an industrial and commercial purpose associated, whereas scaling down from a large size bioreactor creates a model for pre-testing improvements and optimisation of process parameters and even, other distinctly different applications for the system [144,145].

Although a common method in biotechnology, there is not a theoretical model to be followed when scaling a bioreactor. Used approaches comprise fundamental methods;

semi-fundamental methods; dimensional analysis and rules of thumb [146]. Fundamental methods are based on very complex mathematical models (mass transfer and momentum balances) that describe the influence of operational and design parameters on the bioreactor performance at different scales. The semi-fundamental methods are simplified equations applied to approximately describe the bioprocess and its scale dependent parameters. Even though these are significantly simpler than fundamental methods, their level of complexity is still high, requiring computational fluid dynamics and model simulations [147,148]. Instead, dimensional analysis and rules of thumb are more practically applied as they are defined based on similarities of parameters: the up or down scaling of a system is as successful as the number of parameters maintained or similar across the different scales [68]. However, it is impractical to keep all factors at their optimal levels when changing scale.

The main factors influencing or limiting the process are chosen to control the scaling and often include the design, geometry, hydrodynamic and kinetic parameters. In terms of geometry, the aspect ratio (the height of liquid divided by the diameter of the vessel, H_L/D) is a linear relationship in a bioreactor and should remain constant across scales, satisfying one similarity principle [144]. Another important factor to be kept constant is the volumetric oxygen mass transfer coefficient (K_La) since oxygen is a limiting nutrient in biological cultures due to its the low solubility in an aqueous medium and is consequently further reduced with the increase in scale [146]. Considering the hydrodynamic parameters of the system, mixing time, the residence time of solids, maximum shear stress and dimensionless numbers such as Reynolds, Sherwood or Schmidt should be kept constant independently of the bioreactor scale [68,74]. Nonetheless, to satisfy the similarities of selected factors it is necessary to alter other parameters to support the former, such as increasing the flow rate and agitation, introducing other fluid inlet points, or supplying more nutrients.

In a fluidised bed bioreactor even if the particle density, superficial velocity of the fluid and circulation pattern of the solids are maintained, the hydrodynamics of the fluidised bed might not be the same. The approach to scale-up or down is to identify similarities in the hydrodynamic performance of the bioreactor and transform them in dimensionless numbers and relations which can describe the motion of fluid and solids in the system. Thus, Glicksman et al. proposed a simplified set of ratios and factors [149]:

$$\frac{\rho_p}{\rho}, \quad \frac{u_0^2}{gD}, \quad \frac{u_0}{u_{mf}}, \quad \frac{H}{D}, \quad \phi, \quad psd \tag{14}$$

Where ρ and ρ_p are the density of the fluid and the particle, respectively, u_0 the given linear velocity, u_{mf} the minimum fluidisation velocity, g the gravitational constant, H and D the height and diameter of the bioreactor, respectively, ϕ sphericity of the particle and psd the particle size distribution. Several assumptions were established to obtain these ratios: incompressible fluid, interparticle forces omitted, coefficient of friction due to particle collision not included, and they are valid for a wide range of particle Reynolds number [74].

In all circumstances validation of the scaling is achieved experimentally by testing the performance of the bioreactor across scales.

3.2. Aim and hypothesis

It was hypothesised that based on the technology developed by the Liver Group for the UCLBAL, a scale-down prototype of the clinical FBB could be conceptualised through empirical similarity rules. This prototype should effectively induce fluidisation of alginate beads and have comparable biomass yield to the FBB. Thus, the aim was to create and design a versatile benchtop fluidised bed bioreactor for long-term culture of micro 3D cell constructs (alginate encapsulated cells). It was intended to provide a dynamic environment with an operating volume of hundreds of millilitres, which could subsequently host significant biomass for prolonged monitoring and sampling.

3.3. Results

3.3.1. Scaling-down UCLBAL fluidised bed bioreactor

To design a benchtop fluidised bed bioreactor (sFBB) based on the technology developed by the Liver Group for the UCLBAL, a scale-down model was conceptualised from 3 L volume fluidised bed bioreactor (FBB). The FBB was comprised by a chamber of 15 cm diameter and 35 cm height, loaded with 2.5 L of alginate beads and operated at a range of flow rates from 227.2 to 420.9 mL/min to promote a bed expansion of 1.6 to 2 times in height. From the empirical similarity rules for scaling down, the selected parameters to keep constant were the ratio between the height of the settled bed of alginate beads and the diameter of the column (H_b/D) and the linear flow rate (u) calculated from the following mathematical relations:

$$Cross\ section\ (A) = \pi r^2 \tag{15}$$

$$Linear\ flow\ rate\ (u) = \frac{volumetric\ flow\ rate}{A} \tag{16}$$

$$Volume\ chamber = A \times height \tag{17}$$

The design and hydrodynamic parameters of the FBB are shown below:

Table 5 – Calculated large scale fluidised bed bioreactor design and hydrodynamic parameters for developing a scale-down prototype.

FBB parameters	
A (m^2)	0.0177
u_{min} (m/s)	0.00021
u_{max} (m/s)	0.00040
H_b (cm)	14.15
H_b/D	0.94
H_t/D	2.33

Aiming to create an sFBB able to host a minimum of 30 mL of alginate beads and maintaining the estimated u interval and H_b/D, from Eq. 11 and H_b/D ratio, the iterated

minimum diameter for the small-scale model would be 3.5 cm. Considering the same H_t/D ratio, the minimum height for the column was calculated to be 8.2 cm, just enough to sustain the expansion of the bed to twice its settled height.

3.3.2. Manufacture and assembly of the sFBB

The sFBB prototype was intended to be simple to assemble and made of reusable and autoclavable materials (Figure 8). Therefore, the main body of the bioreactor was a custom-made glass column of 3.5 cm diameter and 21 cm height, fitted with a 4 mm thick sintered glass filter (technique used to melt glass particles without liquefying them, to form a porous solid material) as the distributor, and placed 2 cm from the bottom end of the column, constituting one assembled piece. Above the distributor, the column height extended to 15 cm giving more flexibility to the bioreactor to host higher volumes of alginate beads (up to 45 mL) and expand the bed to more than double its settled height, while still guaranteeing a safe height from the outlet to prevent bead escape (elutriation). Each end of the column had a screw thread for a GL45 lid to seal the sFBB. Commercially available polypropylene (PP) lids with two vertical inlet points, each with 6.8 mm internal diameter, were selected to seal the bottom end and allow the flow inside the bioreactor, whereas for the top a PP lid was fitted with a 4.8 mm bore silicone tube as the outlet point and a 15 cm long and 2 mm bore silicone tube for sampling beads. Of note, this prototype was conceptualised by previous members of the Liver Group although neither theoretically nor extensively tested, at the practical level.

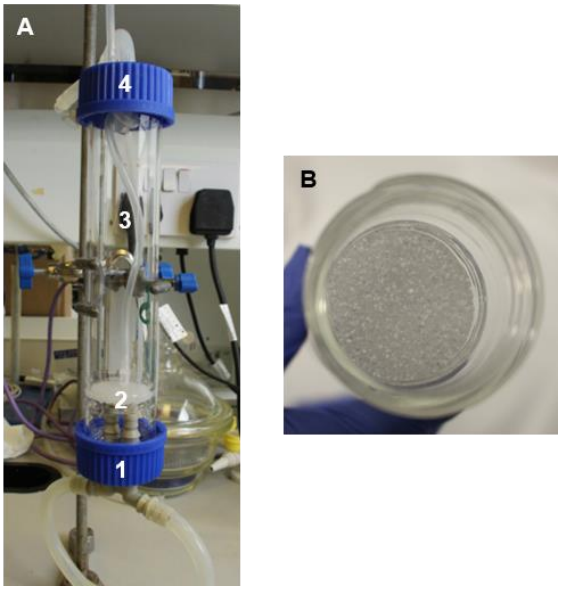

Figure 8 - Prototype of benchtop scale of fluidised bed bioreactor (sFBB). (A) 1 – Inlet tubes fitted in a PP lid; 2 – Sintered glass distributor; 3 – Glass column; 4 – Outlet fitted in a PP lid. (B) Focus on sintered glass distributor structure.

3.3.3. Experimental operation and performance of the sFBB

With the small-scale prototype developed, its function and operation had to be validated by assessing the fluidisation performance through equilibrium time, mixing pattern and bed expansion behaviour. For these tests, the sFBB system was assembled as per *section 2.4.2.1* in a simplified setup with recirculation through a peristaltic pump to a reservoir containing 2 mM $CaCl_2$ solution in 155 mM NaCl. It ran at room temperature on a benchtop.

3.3.3.1. Bed fluidisation and expansion

The fluidisation efficacy of the sFBB prototype was validated through bed expansion level and pattern. To facilitate observations and digital recording, a portion of alginate encapsulated HepG2 cells was stained with toluidine blue. Subsequently, 20 mL of unstained beads were introduced first in the sFBB topped by 10 mL of stained beads forming a 30 mL bed with the two distinct phases (Figure 9)

With recirculation of the fluid, a pulsing movement started to expand the bed a few millimetres high from the bottom while maintaining the two phases segregated, until a

burst of stained beads fluidised to the top (38 s). The upward movement of the fluid induced beads to mix in a bottom-top pattern, although in a heterogeneous fashion as noted by some low-velocity spots at the bottom of the bed (1:16 min). The double bed expansion (from 2.6 cm to 5.3 cm) was achieved after 2 min of fluid recirculation. Continuous observation identified a steadily fluidised bed, maintaining the expansion level, with beads moving downwards near the wall and upwards in the centre of the column. However, channelling effects were observed in sections of slow-moving alginate beads interspersed with flow channels rapidly transporting beads to the top. These inconsistencies were particularly evident immediately above the distributor and near the walls. Moreover, as the bioreactor operated air pockets accumulated underneath the distributor which when released dispersed beads in the bed to the point of a few of them escaping the chamber (elutriation).

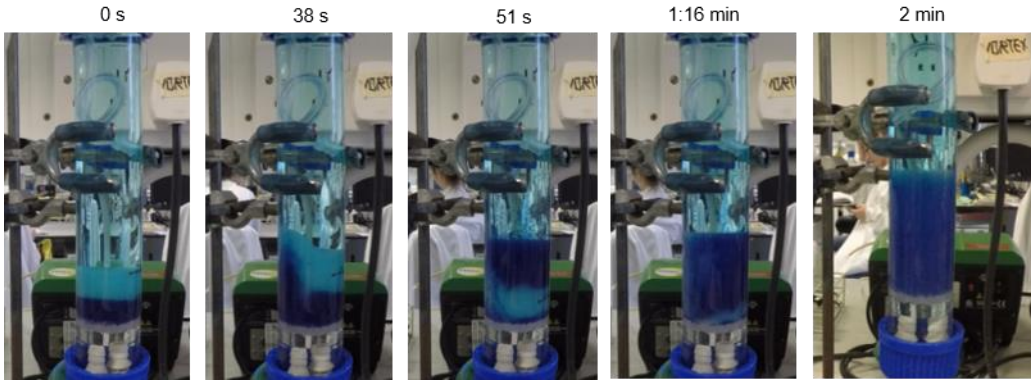

Figure 9 **-** Bed expansion level and pattern in the small-scale fluidised bed bioreactor prototype. Time line of a double fluidised bed of alginate encapsulated cells homogenously mixed.

Figure 10 – Fluidisation of alginate beads with different compositions in the sFBB. Left bioreactor contained 50% alginate cell beads and 50% alginate empty beads, while the bioreactor on the right was solely composed of cell beads.

Fluidisation was also analysed under different bed compositions. Alginate encapsulated cells have higher mass and density than empty beads as their mass is solely granted by the alginate and the incorporated glass particles responsible for the buoyancy of the beads. Thus, a bed of 100% cell beads will have a different density to that made of 50% cells beads and 50% empty beads. When comparing fluidisation levels, both beds expanded to twice the settled height at the same flow rate (Figure 10). However, it was observed in the mixed beads bed that blue stained cell beads were predominantly at the bottom of the bed, whereas unstained empty beads fluidised at the top creating a segregated colour pattern Figure 10, left column) unlike the even distribution in the cell beads bed. This phenomenon was a consequence of beads with different masses, with heavier particles fluidising at the bottom and lighter on top. To note, the same protocol could not be applied to a bed made only by empty beads as these did not retain any dye making it difficult to clearly observe the mixing pattern.

These results suggested the system was able to induce and sustain a stable and coherent fluidisation of alginate beads (either empty or encapsulating cells spheroids), although further analysis would be required to determine the impact of the identified inconsistencies in the biological performance of the bioreactor.

3.3.3.2. Equilibration time

One of the main factors determining the performance of the bioreactor is its efficacy in providing a homogenous environment which can be assessed through the mixing time, i.e. the time it takes for the system to attain a certain degree of homogeneity at a given mixing condition. Therefore, the prototype was loaded with approximately 30 mL of alginate empty beads and the flow rate set for double-fluidisation of the bed (31 mL/min). Upon a steadily expanded bed, methylene blue was injected through the inlet sampling port of the sFBB and fluid samples were collected at the outlet to measure the absorbance at each time point (Figure 11 A).

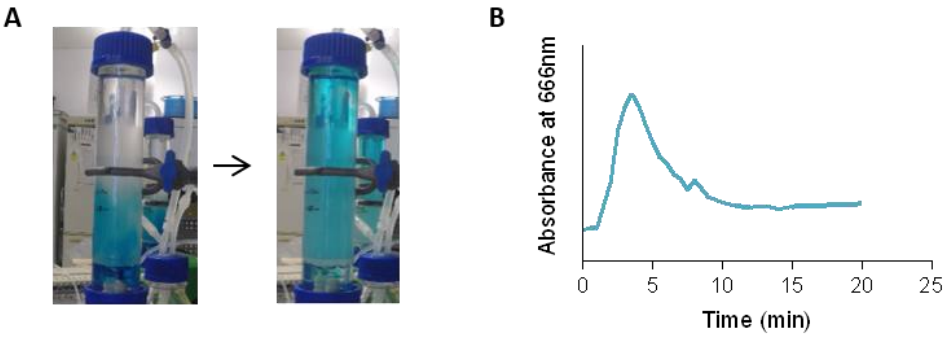

Figure 11 **-** Mixing time of the small-scale fluidised bed bioreactor (sFBB). Progression of methylene blue inside sFBB (A) and respective absorbances readings at 666 nm until homogenisation of the system (B).

From the measured absorbance profile (Figure 11 B), the first detection of colour was 2 min after injection and the peak achieved at 3.5 min, establishing the characteristic circulation time of the sFBB, i.e. the time particles take to flow through the bioreactor. Once the maximum absorbance was reached, values decreased and stabilised after 10 min of operation. This constituted the mixing time of the bioreactor where the system returned to equilibrium after a disturbance was introduced (dye injection). The small peak in absorbance detected at 8 min could be an effect of the recirculation of fluid carrying the bolus dye injection, entering the column and contributing to an increase in colour concentration. Moreover, from the visual analysis it was observed that the injected dye progressed through the bioreactor in a diffusing pattern, attaining a homogenous shade of blue after some recirculation loops. It also evidenced the pronounced axial flow distribution from the inlet points because the dye was mostly concentrated right between them and the distributor, taking some time to homogenise in all the calming section underneath the distributor.

The influence of other parameters on the mixing time was analysed for a more detailed characterisation of the system. Beds with different densities did not modify the equilibrium point of the bioreactor as observed in the absorbance readings from 100% cell beads and 50% cell beads + 50% empty beads beds (Figure 12 A). The maximum concentration of dye was detected at 2.5 min and the system was homogenised at 9 min. These profiles were not significantly different from Figure 11 B.

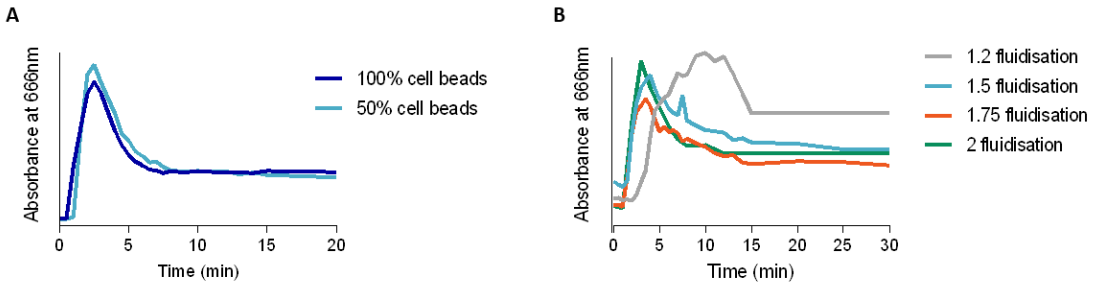

Figure 12 - Influence of operational patterns on mixing time in the sFBB. Determining the homogenisation of the system with beds of different composition (100% cell beads and 50% cells beads + 50% empty beads) (A) or fluidised at different expansion levels (from 1.2 to 2 times the settled height) (B). Absorbance readings measured at 666 nm.

Moreover, mixing conditions in a fluidised bed are a function of the induced flow rate which subsequently impacts the level of fluidisation. For the minimum 1.2-fold bed expansion (at 6.65 mL/min), colour was first detected at 3 min, but the maximum was only achieved at 10 min and equilibrium after 15 min (Figure 12 B). As the bed was progressively expanded to 1.5, 1.75 and 2-fold its settled height, maximum absorbance was attained at 4, 3.5 and 3 min, respectively, and the equilibrium reached at 13, 11 and 12 min. These results demonstrated the correlation between the mixing time and the fluidisation level, with low flow rates increasing the equilibration time of the system. Nevertheless, at the desired operating conditions, i.e. a bed constituted by alginate beads fluidising at least at 1.6 times, the system attained equilibrium at 10 to 12 min.

3.3.3.3. Mass transfer in the sFBB

An effective mass transfer is a crucial parameter in a bioreactor for sustaining viable and functional biomass. In the current system, the alginate hydrogel could constitute the main physical barrier for nutrients and other molecules to move in and out to enable the exchange process between the biomass and the milieu. This phenomenon would be driven by diffusion in both directions until equilibrium is achieved.

To determine the diffusion time, relative fluorescence intensity (intensity/area of the region of interest) of fluorescein isothiocyanate-labelled 150 kDa dextran (FITC-dextran) was quantified in the alginate bead and milieu through confocal microscopy (*section 2.7*).

Results were processed as the ratio of the inner and outer relative intensities with a value of 1 representing the equilibrium between the two phases.

Initially, only empty beads were assessed to eliminate any bias from the biomass. When exposed to FITC-dextran solution, diffusion inside the hydrogel followed a slow pattern maximising at 20 min but not equilibrating with the environment during the monitored time Figure 13). Conversely, dextran diffusion out of the bead occurred at a faster rate with equilibrium attained at 23 min.

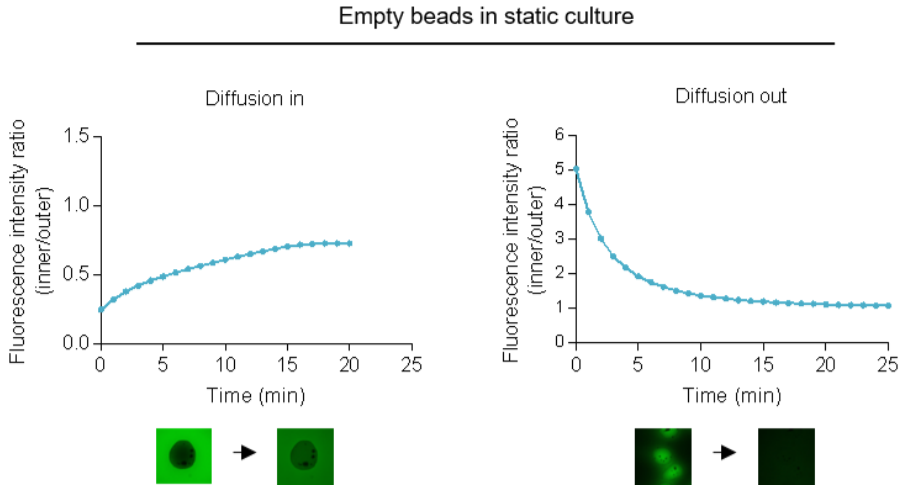

Figure 13 - Mass transfer across alginate empty beads under static environment. Diffusion times of FITC-labelled 150 kDa dextran from the surroundings into alginate empty beads and vice-versa. Values presented as ratio of the relative fluorescence intensity inside the bead to outside.

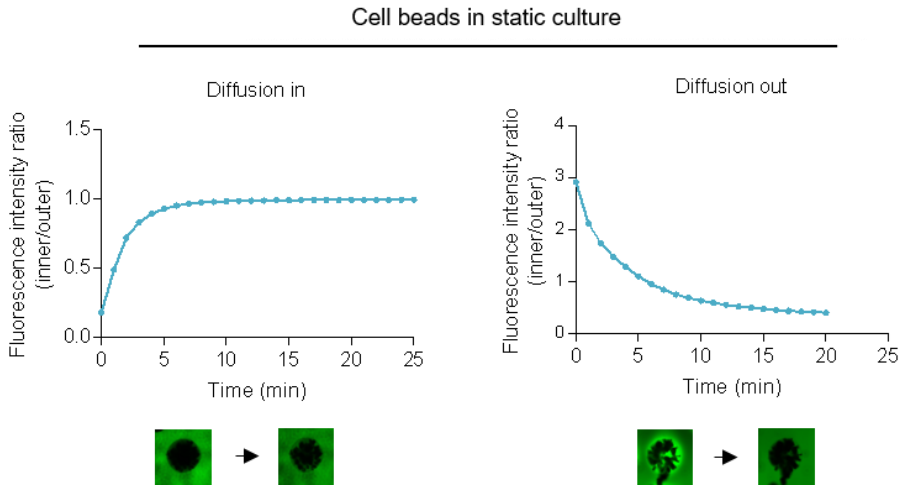

Figure 14 - Mass transfer across alginate encapsulated HepG2 cells under static environment. Diffusion times of FITC-labelled 150 kDa dextran from the surroundings into alginate cell beads and vice-versa. Values presented as ratio of the relative fluorescence intensity inside the bead to outside.

Under the same static conditions, diffusion was investigated in cell beads. In both directions mass transfer was faster compared to empty beads, almost certainly because the spheroids did not absorb dextran and reduced the available space in the bead (Figure 14). This meant solutes would reach the cell surface faster. Inside motion occurred in 8 min and the reverse process in 6 min, although dextran continued to diffuse out over time without increasing the surrounding fluorescence.

The identical method was applied to empty beads fluidised to double their settled height in the sFBB to study the impact of dynamic culture on the diffusion time. FITC-dextran was injected below the inlet point of the bioreactor and from samples collected therefore, it was observed that transfer into the beads peaked at 4 min but equilibrated with the milieu after 12 min and stabilising there after (Figure 15). In comparison with the static culture (Figure 13), where after 20 min equilibrium was not attained, the dynamic environment enabled faster mass diffusion across the alginate hydrogel. Moreover, the reverse mass transfer mechanism (out of the beads) stabilised with the milieu after 12 min, 7 min earlier than in static. Of note, given the obtained diffusion times and the complexity of the experiment it was not possible to investigate the mass transfer in cell beads under dynamic conditions. Furthermore, confocal microscopy of the alginate beads verified that particles diffused throughout reaching the core of the bead (Figure 16). Hence, the alginate hydrogel did not constitute an impairing barrier to mass transfer and diffusion was accelerated under dynamic culture.

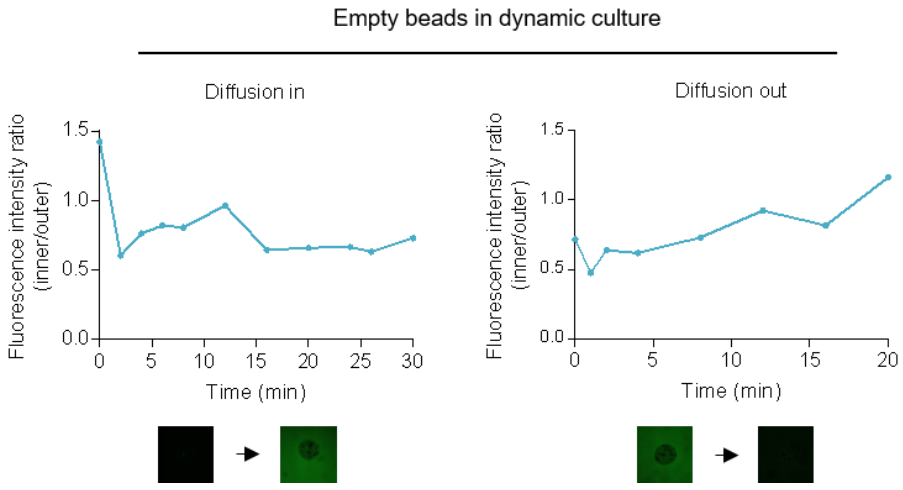

Figure 15 **-** Mass transfer across alginate empty beads under dynamic environment. Diffusion times of FITC-labelled 150 kDa dextran from the surroundings in the sFBB into alginate empty beads and vice-versa. Values presented as ratio of the relative fluorescence intensity inside the bead to outside.

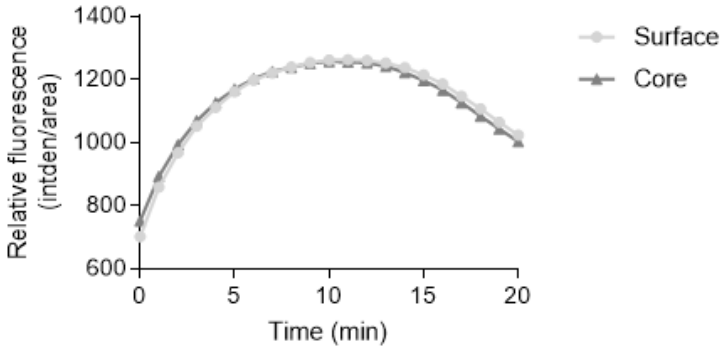

Figure 16 - Relative fluorescence intensity through alginate empty beads. Diffusion of FITC-dextran 150 kDa through alginate empty beads under static conditions imaged on the top slice and middle of a Z-stack. Values presented as intensity density (intden) per area.

3.3.3.4. Alginate bead integrity and shape factor

For long-term cell culture, the integrity of the alginate beads fluidised in the small-scale prototype has to be preserved to support the encapsulated cells. The impact of the shear stress caused by the continuous fluid flow inside the bioreactor on the beads was investigated by measuring their diameter and comparing it to those of beads in static culture. During a 12 day period of constant fluidisation, the diameter of the alginate beads encapsulating HepG2 cells did not alter significantly, except on day 12 where the average bead diameter was 606.9 ± 99.3 μm *vs.* to 573.6 ± 77.8 μm in static ($p < 0.001$) (Figure 17 A). This increase was likely an outcome of cell growth since spheroids formed under dynamic conditions were denser and larger than in static (Figure 17 B). Moreover, captured images supported their integrity by evidencing the spherical shape of the beads, also proved by the 0.96 shape factor (Figure 17 C). Thus, the constant flow inside the bioreactor did not produce sufficient shear stress to cause wear and/or disintegration of alginate beads.

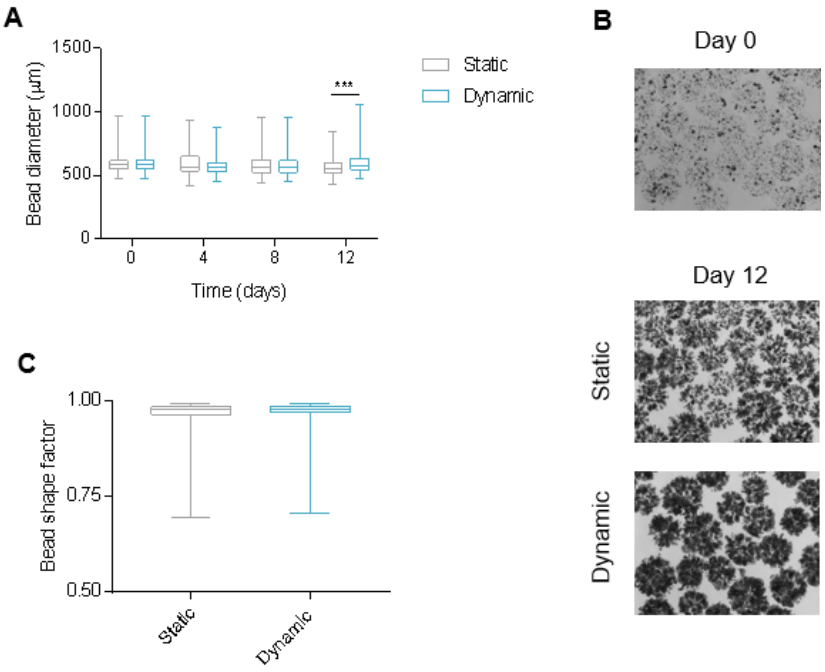

Figure 17 **-** Alginate beads integrity and diameter in the sFBB. (A) Diameter of alginate encapsulated HepG2 cell spheroid beads cultured under static and dynamic (sFBB) culture for 12 days. (B) Aspect ratio of beads on day 12 in static and dynamic culture. (C) Phase images captured on day 0 and 12 (C). Data presented in the box plot are average diameters with whiskers representing minimum and maximum measured values (n = 250). Statistical analysis was assessed by multiple Student's t-test with Holm-Sidak's method correction. ***$p < 0.001$.

3.3.4. Biological performance of sFBB compared to FBB

The physical parameters of the small-scale prototype indicated its capacity to fluidise a bed of alginate beads providing effective mixing and mass transfer with minimal shear stress to the hydrogels. Moreover, the final validation of the prototype consisted of its ability to host and expand viable biomass to a similar level to the clinical-scale FBB. Thus, culturing alginate encapsulated HepG2 cells during 12 days in the FBB and sFBB produced similar growth curves with final densities of 30.9 ± 0.56 and 27.3 ± 0.78 million cells/mL beads, respectively ($p < 0.0001$) (Figure 18 A). Cell viability in both devices was maintained above 97% with a difference of 1.5% on day 12 ($p < 0.001$) (Figure 18 B). These differences could be a consequence of the culture medium used in the FBB which is supplemented with amino acids providing more nutrients to the cells, although obtained values for the sFBB were still within the expected density and viability interval, therefore not constituting an underperformance of the prototype. Moreover, fluidisation

inconsistencies identified on *section 3.3.3.1* did not interfere significantly in the homogenous growth of spheroids in the beads (Figure 18 C).

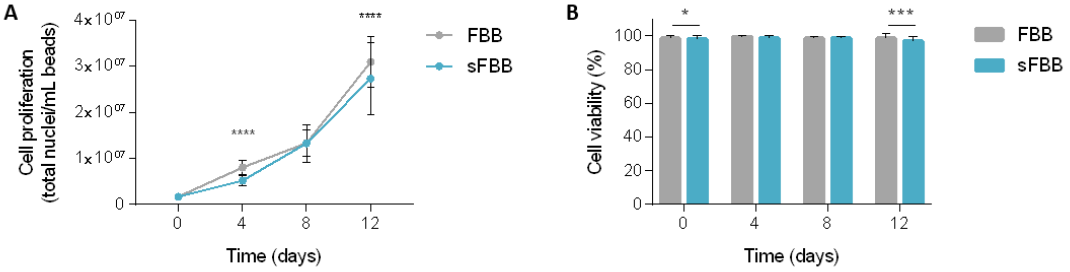

Figure 18 - Biological performance of the small-scale prototype (sFBB) compared to the clinical FBB. Cell proliferation curves (A) and corresponding viabilities (B) throughout 12 days of culture. Data presented are average ± standard deviation (SD) (n = 17 for FBB and n = 7 for sFBB). Statistical analsysis was assessed by multiple Student's t-test with Holm-Sidak's method correction. *p < 0.05, *** p < 0.001, ****p < 0.0001.

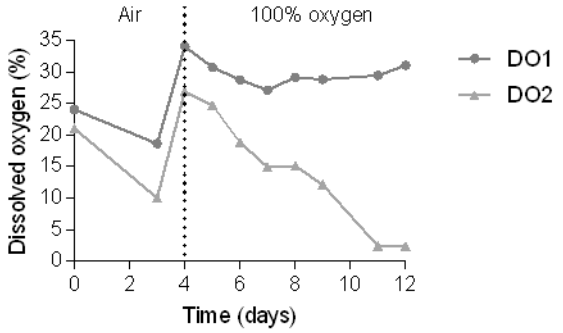

Figure 19 - Oxygen supply and consumption in the sFBB during culture of alginate encapsulated HepG2 cells. Dissolved oxygen (DO) levels were monitored at the inlet (DO1) and outlet (DO2) points of the bioreactor. Until day 3 active gassing was by supplying air to the reservoir at 250 mL/min. At day 4 the source was exchanged to pure oxygen at 70 mL/min. On day 8 flow rate was adjusted to 80 mL/min, day 10 to 95 mL/min and day 12 to 200 mL/min.

Also, oxygen levels were monitored during culture to determine whether the scale-down prototype was adequately gassed, and the oxygen demands of the cultured biomass met. The dissolved oxygen concentration at the inlet (DO1) indicated the supply from the reservoir which was aimed at 15% (limiting nutrient effect) to 35% (> 35% toxic level) [150],

whereas at the outlet point (DO2) readings could be correlated to oxygen consumption by the cell beads. It was observed that continuous gassing of the reservoir with adjusted flow rates effectively supplied the system with levels of oxygen within the intended interval (Figure 19). Moreover, this supply provided adequate gas concentration to the biomass to sustain their metabolic activity as suggested by the progressive decline in DO2 and correlated with the growth of the spheroids, i.e. as cells proliferated the concentration of oxygen declined.

Hence, these results corroborated the effective scale down of the FBB with the prototype supporting 12 days of continuous sterile culture of 3D cell constructs maintaining them highly viable and promoting growth to equivalent numbers to clinical scale data.

3.3.5. Expanding the setup into multiple parallel sFBB units

With the performance of the prototype validated, the possibility of expanding it into a setup of multiple parallel units was explored. This would be particularly beneficial to investigate several conditions simultaneously in a dynamic environment or to use the device as a co-culture system. The setup was incrementally expanded up to four sFBB fed by one reservoir, assessing first the influence on the mixing time. In systems with two or three bioreactors operating in parallel, the mixing time remained within 8 to 10 min interval, similar to one sFBB and demonstrating that the complexity of the setup did not influence this hydrodynamic parameter (Figure 20) setup but given the previous observations it could be extrapolated results would fall within the same time interval (~10 min).

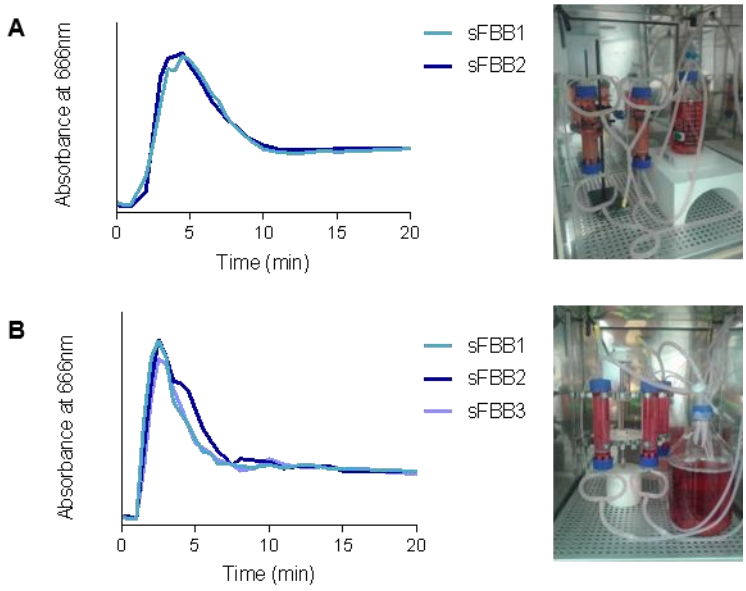

Figure 20 **-** Multiple sFBB setup ran in parallel. Mixing time profiles determined by absorbance readings at 666 nm until homogenisation of the system with setups of two (A) and three (B) bioreactors operating in parallel.

The biomass yield was assessed in the larger setup of four parallel bioreactors. In three independent experiments, while the global yield differed, final cellular densities were equivalent across all four bioreactors within each trial, supporting the consistency of the setup (Figure 21 A). Furthermore, in each bioreactor beds followed a similar expansion pattern in response to increments in fluid linear velocity to sustain a fluidisation level of at least 1.6 times (Figure 21 B).

This set of results certified the developed prototype as an expandable system which can provide a consistent and stable dynamic environment for long term-culture of hydrogel encapsulated 3D cell constructs.

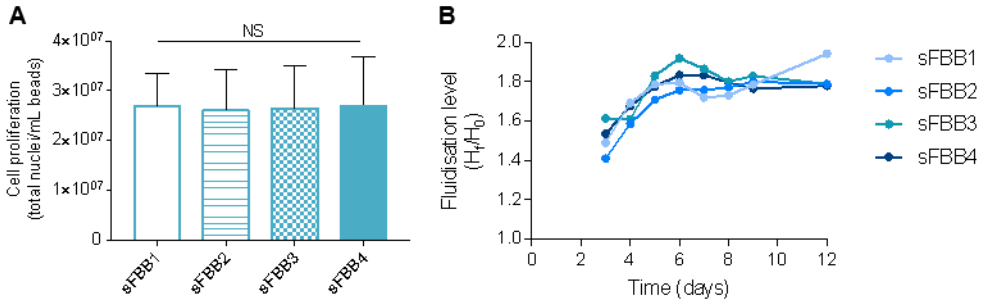

Figure 21 **-** Performance of multiple parallel sFBB setup. (A) Cell density on day 12 of culture in four sFBBs (sFBB1, sFBB2, sFBB3 and sFBB4) operating in parallel. Data presented as average ± SD (n = 3). Statistical analysis assessed by one-way ANOVA with Tukey's correction. NS – non-significant. (B) Representative fluidisation levels throughout culture of four sFBBs in parallel with adjusted flow rates: 18.8 mL/min from days 0-3, 22.9 mL/min from days 4-5 and 25.7 mL/min until day 12.

3.4. Discussion

Although the fluidised bed bioreactor could conceptually create a dynamic environment for 3D cell constructs (preferably in a spherical shape) that more closely replicates the *in vivo* perfusion, this design has not been widely explored for tissue engineering *in vitro* models. Therefore, the aim of this project was to develop a benchtop scale FBB (sFBB) that could be a versatile device for long-term culture and analysis of hydrogel encapsulated cells providing both the 3D structure and flow perfusion.

Using established FBB technology applied to the UCLBAL [121], a scale-down model based on empirical similarities of linear flow rate and H_b/D ratio, aiming to host a minimum volume of beads of 30 mL was a straightforward approach to produce the benchtop prototype. The designed sFBB effectively accommodated an operating volume of 140 mL, hosting up to 45 mL of alginate spheres with an initial diameter of 596 μm. This model focused on the volumetric capacity of the bioreactor and did not consider any specific fluidisation performance or bead characteristics. Although it could be argued that the fluidisation regime was implied in the linear velocity or in culturing the same biomass (i.e. alginate encapsulated HepG2 cells), a more detailed study of the performance of the clinical-scale FBB would have given fluidisation parameters such as u_0/u_{mf} ratio as the basis for scaling down.

While the current prototype stands as an obvious pilot scale for process optimisation of the clinical-scale FBB, the choice of scale concerned the design of a device for 3D cell culture that could host enough biomass for multiple observations per sample and time, and in relevant volumes relatable to *in vivo* conditions. These operating volumes will not support the high-throughput screenings as, for instance, microfluidics [151], but they will be useful in later stages when selected compounds are tested in a more *in vivo*-like environment and thus, contributing to the reduction of the number of animals in the study. Mostly, it was a proof-of-concept of a simple scale-down model with potential to be further scaled up or down for different applications.

This first prototype was projected to be simple and reusable with the lowest investment possible in custom-made features since it was necessary to first validate its feasibility, faithful reproducibility of the clinical scale and robustness. Therefore, all features were either readily available parts or manufactured with standard specifications. The main column was an all-together glass part fitted with a sintered glass distributor as a simple solution for an integrated setup avoiding potential leaks and misassembles. However, sintering generates pores of various sizes randomly distributed, and each disc has its own pore assortment [152]. This hinders the standardisation of the design for commercial purposes as well as an effective cleaning that eliminates any particles retained within the pores. But most importantly, the sintered glass did not create a reproducible fluidisation pattern and the inhomogeneities of the porous material (e.g. sections with wider pores or fewer pores) were likely to be responsible for the channelling effects observed in the bed and the accumulation of air pockets underneath [153]. Some systems do not include a flow distributor, reasoning on channelling effects created by this feature (i.e. preferential circulation of fluid through specific arteries generating points of fast moving particles interspersed with stagnant ones), and that without it the bioreactor still performs accordingly [154]. However, the majority describes the distributor and its design as the key parameter for the performance of the fluidised bed bioreactor. Lu et at. developed a distributor based on a turbine mechanism which induced a diversion-type vortex capable of fluidising the bed horizontally, exposing all microcapsules to the same level of perfusion and minimising wear [155]. Uniformity of the flow is not the only criteria for a better performance, as Wormsbecker et al. demonstrated that the punched plate distributor promoted a faster drying of solids than a perforated plate due to the

generated lateral mixing [96]. However, it has been observed that the effect of the distributor is subjected to the properties of the solid, for example, it is greater in beds of smaller particles [156].

The channelling effect may have also been a consequence of the inlet points. According to flow simulation data and the dye dispersion experiment, the flow out of the vertical tubes was mostly axially distributed and possibly a radial dispersion before the distributor is desired to homogenise the flow in all directions minimising the formation of stagnant points [92,157].

Other design considerations from experimental observations would include fitting a filter at the outlet point to avoid bead elutriation from disturbances or just to allow a safer fluidisation when culturing higher volumes of beads or expanding them more than two-fold. Also, a fixed port for loading and sampling beads would facilitate the sterile access to the biomass. Thus, the current prototype requires a design optimisation with special focus on the distributor and inlet points to produce a more homogenous fluidisation and also to simplify the operation of the device.

Nonetheless, fluidisation of alginate beads (with or without cells) to twice its settled height was achieved in 2 min and followed patterns consistent with those described in the literature where solids move upwards in the middle of the column and downwards near the walls due to the drag [158]. Similarly, Legallais et al. [159] observed the bottom-top mixing pattern and stabilisation of the expanded bed under 5 min. In their case, the process was independent of the volume of beads and perfusion flow. Even though different bed volumes were not described in the current results, preliminary tests in the sFBB verified effective fluidisation of 10 to 35 mL alginate beads but demonstrated that a minimum of 25 mL was necessary for a homogenously expanded bed without a fluctuating behaviour [160]. These characterisations were merely qualitative or semi-quantitative. For a detailed quantitative study of solids motion and associated velocities, a particle tracking velocimetry system would have to be adapted to the bioreactor with tracer particles (e.g. magnetic, radioactive or fluorescent nanoparticles) incorporated in the bed which would be imaged and analysed by complex systems [103,161].

An intrinsic parameter of the fluidised bed is the pressure drop at which expansion occurs. However, it was not possible to determine it experimentally because the pressure in the system fell below the detection limit of the available sensors (< 300 mmHg) and

was influenced by the peristaltic movement of the pump, thus, the small variations in pressure were indistinguishable from the noise of the sensors. The measured values suggested an upstream (at the inlet) pressure of 4 - 8 mmHg which falls within the interval obtained by Legallais et al. [159], although their operating bed volume was 10x higher than the one in the sFBB. Ideally, the pressure drop should be measured at both ends of the bed, but this would require special fittings in the bioreactor for the sensors, complicating the design.

The flow perfusion that effectively fluidised the hydrogel bed also promoted an average circulation time of particles of 3 min and a mixing time of 10 – 12 min. These were independent of the density of the bed and its expansion level, excluding the 1.2-fold expansion which was low enough to not be considered a relevant fluidisation, and the complexity of the setup with multiple parallel units. The registered equilibrium time and the absorbance profiles were similar to those reported in other studies verifying the compliance of the system to following a recirculation pattern [162]. This demonstrated the efficacy of the bioreactor in resolving disturbances and minimising concentration gradients. Similarly to the particle tracking technique, imaging methods coupled with fluid dynamic algorithms or with local probes in the bioreactor can be useful for a refined analysis of the mixing time and fluid velocity patterns identifying stagnant spots or poor mixing [135,163,164]. There, is an agreed tolerance of 5 - 10% in equal distribution when defining the degree of homogeneity of a bioreactor [68]. Other parameters to be studied which could influence the mixing time in the sFBB would be higher flow rates (outside the interval for double expansion), an extension of the setup and other solid properties such as diameter and hydrogel composition.

Moreover, under the dynamic conditions of the sFBB FITC-dextran diffused in 12 min into and out of alginate beads, whereas static diffusion across the same hydrogel was either slower or not determined for the monitored time, verifying the premise that mass transfer is faster in dynamic cell culture [165]. Interestingly, the diffusion times were similar to the equilibrium time of the bioreactor suggesting the governing mechanism in the system was the convection movement of the fluid, and the physical barrier imposed by the hydrogel did not impair mass transfer. The obtained values were in agreement with times described for molecules such as vitamin B12 or albumin (smaller than 150 kDa) in 2.2% alginate beads, while those in the current study were 1% [122]. These times are a

function of the diameter, composition and mechanical properties of the hydrogel as well of the size of the diffusing particles [124,166]. Nonetheless, 1% alginate beads have demonstrated permeability to larger molecules such as fibrinogen (~340 kDa) [167]. A time-wise study with different size molecules and hydrogels with various compositions would generate a diffusion profile for the sFBB and an application range as well as indicate whether there would be a cut-off weight for the alginate hydrogel impairing diffusion of large molecules.

Calculation of the mass transfer coefficient would support the obtained times and the performance of the bioreactor, however, there was a misfit of the generated data with the models suggested in the literature. For example, linearisation of the obtained data as proposed by David et al. [122] or Mobed-Miremadi et al. [168] was not possible because the estimation of dextran concentration from the retrieved relative fluorescence intensities did not follow a linear correlation. Calibration of the fluorescence intensity with pre-established dextran concentrations is required to effectively correlate the retrieved values with respective concentrations [168]. However, most models were developed for a specific system under investigation and do not accurately describe others. Studies have also shown that in fluidised bed bioreactors not only the intrinsic properties of the fluid and solids influence the mass transfer coefficient, but also design parameters can manipulate it: increasing the number of holes and pressure drop of the distributor increases the coefficient [104].

Finally, the shear stress induced by the continuous perfusion of fluid and consequent, fluidisation of beads was investigated indirectly through the integrity and sphericity of the micro hydrogels. They were preserved throughout 12 days and comparable to those under static culture (without any dynamic forces), an indicator that the hydrodynamic shear forces were low and did not damage the beads. Nonetheless, an experimental determination of the fluid shear forces with the aforementioned particle imaging techniques would more accurately characterise these effects in the bioreactor.

Normally high shear values are associated with high linear velocities and subsequently, improved mass transfer. These might be necessary to guarantee mass transfer across the hydrogel capsule, which in turn shields the cells from high shear stress environments minimising any detrimental effects [169]. The obtained data demonstrated that the low linear velocities and related shear stress in the sFBB did not hinder mass transfer across

the porous micro hydrogels. Yet, it would be valuable to determine the limits of the system, i.e. maximum fluidisation period and linear velocity, without negatively impacting the beads.

The hydrodynamic performance of the sFBB was then corroborated with its biological outcome. Although statistically different by day 12, the sFBB yielded comparable viable cell numbers to the clinical scale as the differences in viability and cell density were still within the intended interval. They could be attributed to biochemical (more complex culture medium and active gassing directly inside the FBB column) or design (the distributor in the FBB is a standard perforated plate) variations between the two bioreactors [121]. Such differences have also been reported in other scale-down bioreactors either, for example in viable cell number or metabolic activity, due to uncontrolled parts of the process or just a consequence of inherent biomass variability [170,171].

Moreover, the system confirmed robustness and reproducibility when expanded into a setup of 4 sFBB in parallel produced equivalent final cell densities and fluidisation levels. The small disparities in fluidisation could reflect the variability of the sFBB distributor design or back pressure in the system generating different pressure drops in each bioreactor. Nonetheless, these suggest the designed prototype could be used to study multiple conditions simultaneously or ultimately in co-culture systems.

However, this was just the first assessment of the biological performance of the sFBB. Further studies between the two scales, comparing the metabolic activity of the grown spheroids or their 3D structure, would give more parameters to validate the scale-down process. In addition, exploring other cell types and hydrogel compositions, and promoting studies of biochemical (e.g. growth factors, drug metabolism) or environmental (e.g. oxygenation, shear stress) effects under dynamic culture conditions will verify the ability of the prototype to generate a more *in vivo*-like milieu and consequently, be a versatile device for engineering *in vitro* tissue models which better replicate the *in vivo* structures.

Indirect evidence of the metabolic status of the cells was the reduction in dissolved oxygen concentration in the culture medium after the fluidised bed, suggesting the cells were consuming it and thus, were metabolically active [172]. The gassing was done directly to the reservoir via a silicone oxygenator producing microbubbles and not to the column, which due to the low solubility of oxygen in liquid phases and the extension of the setup

could pose a problem. To improve efficiency, minimising oxygen loses and maximising its uptake by the cells, oxygen releasing capsules could be mixed in the bed of cell beads [173,174]. It would create a more compact setup, although these capsules would risk being removed during the sampling of the cell beads.

Dissolved oxygen was the only environmental parameter continuously monitored during culture. Temperature, pH and CO_2 levels were imposed by the incubator conditions where the prototype was operated but without any additional monitoring. For tighter control, sensors for all these parameters would have to be set in-line in the device, increasing the number of associated instruments and eliminating the purpose of the simple and portable benchtop bioreactor. Nonetheless, one solution for including them in a simpler setup would be adherent optical spot sensors onto the glass column.

3.5. Conclusion

In this chapter, a benchtop fluidised bed bioreactor was effectively scaled down from the technology developed for the UCLBAL, based on empirical similarity rules, proving the established hypothesis. The sFBB successfully fluidised beds of micro alginate beads, creating a perfusion environment which promoted homogenous mixing and mass transfer across the hydrogels without any damage to the beads. It induced proliferation of alginate encapsulated HepG2 cells into viable cell spheroids during 12 days in setups of just one or multiple bioreactors in parallel, highlighting the robustness and reproducibility of the prototype. On the other hand, the current design indicated heterogeneities in the distributor and minimal radial flow which should be addressed in further optimisations (addressed in Chapter 5). Moreover, studies with different cell types, hydrogel compositions and culture periods should be explored to determine the application of the bioreactor to various biological models.

In summary, the current prototype has demonstrated potential as a simple and cost-effective device for long-term culture and analysis of 3D cell constructs with prospects of engineering *in vitro* models which better reproduce the *in vivo* conditions. The potential applications of the sFBB will be addressed in the next chapter.

CHAPTER 4

Applications of a small-scale fluidised bed bioreactor

The potential of the developed sFBB prototype in *Chapter 3* was explored as a bioreactor for biomass expansion but also as a testing platform of the impact that different external agents and stimuli (e.g. hydrodynamic forces, differentiation growth factors) have on the cellular performance of hydrogel encapsulated cells. Moreover, its ability to serve as a pilot scale for the clinical scale FBB and eventually other processes that could benefit from this operation mode was also investigated. Thus, this chapter will follow the structure depicted in Figure 22.

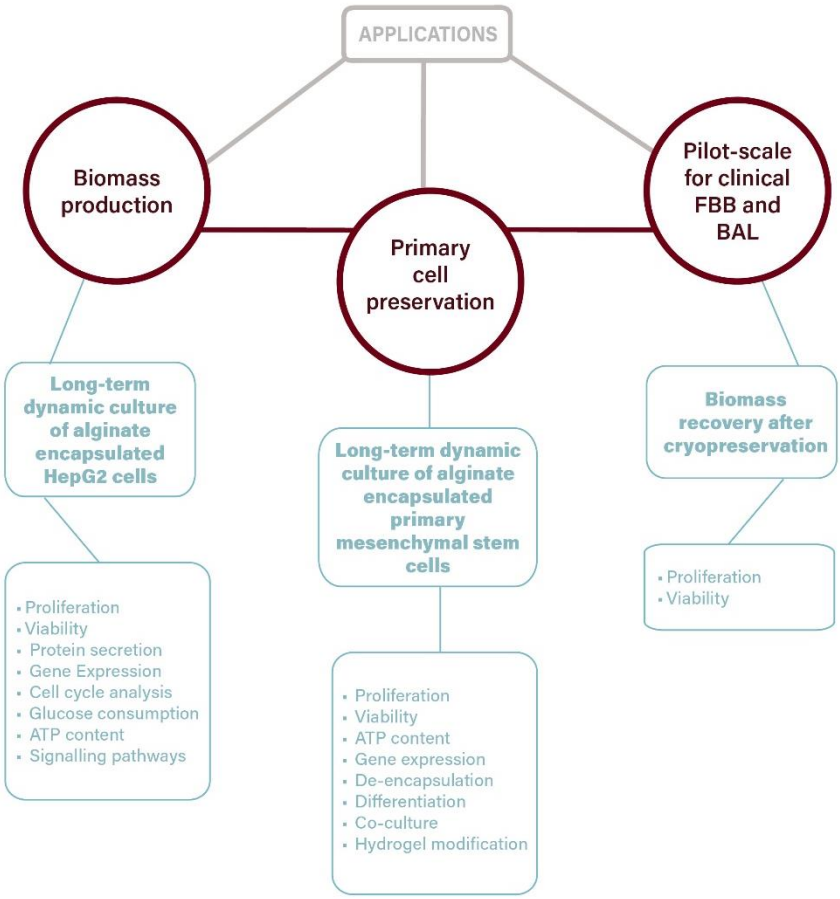

Figure 22 – Chapter 4 outline and structure.

4.1. Long-term dynamic culture of hydrogel encapsulated hepatoblastoma cells in a small-scale fluidised bed bioreactor

4.1.1. Introduction

HepG2 is a well-characterised cell line derived from a hepatoblastoma of a 15-year-old Caucasian male. It has been widely used as a cancer model and an *in vitro* alternative to hepatocytes due to its high availability, unlimited proliferating ability and stable phenotype. These cells retain several features of hepatocytes as synthesis of plasma proteins (e.g. albumin, anti-trypsin, prothrombin), triglyceride and lipoprotein metabolism, insulin signalling and others [175,176].

However, HepG2 cells present features associated with an immature phenotype. A hallmark of this cell type is α-fetoprotein (AFP) a highly expressed protein throughout the developmental stage of the liver, which declines rapidly during postnatal life, and is associated with proliferation and thus, the pathological progression of hepatocellular carcinomas. Another feature is its poor urea cycle and drug metabolism compared to primary hepatocytes, particularly the activity of phase I enzymes like the cytochrome P450 (CYP450) [177,178]. This cytochrome is composed of several families including the CYP3As responsible for the oxidation of more than 50% of clinical drugs for their progression into phase II metabolism. HepG2 cells have an upregulated activity of CYP3A7, which similarly to AFP is highly expressed in human foetal liver, being converted to CYP3A4 in the first postnatal weeks and continuing as the most abundant form in the mature phenotype. These two isoforms differ from one another in enzymatic reactions and substrate specificity [179].

The impaired hepatic function in HepG2 cells is in part due to the low expression of liver-enriched transcription factors (LETFs). LETFs are DNA-binding proteins which bind to a specific sequence within the regulatory element of a gene enabling its expression and regulation [180]. These include the hepatocyte nuclear factors (HNF) 1, 3, 4 and 6 and the CAAT/enhancer-binding proteins (C/EBPs) which act in complex auto- and cross-regulatory networks and play an important role in liver development and differentiation [181].

HNF4, particularly the isoform HNF4-α, has been described as the master regulator of hepatic function in the adult liver as it was found to bind to more than 40% of the promoters of activated genes including the regulation of HNF-1α [181]. Its expression is associated with liver homeostasis by inhibiting proliferation, regulating glucose, fatty acid and cholesterol metabolism, drug metabolism and overall maintenance of the differentiated phenotype of hepatocytes [182,183]. In fact, mutations or disruptions to HNF4-α expression have resulted in accumulation of lipids and bile acids, maturity-onset diabetes and epithelial-to-mesenchymal transition in mature hepatocytes, all leading to metabolic disorders and increased mortality [181,182,184,185]. Moreover, its down-regulation has been reported in liver cirrhosis, chronic liver failure and hepatocellular carcinomas [182,186]. Studies in HepG2 cells where the overexpression of HNF4-α was induced resulted in decreased tumorigenesis, enhanced ammonia metabolism and CYP enzyme activity [187,188].

The C/EBPα, also an important regulator of adipogenesis, is involved in the terminal differentiation of hepatocytes, preserving their homeostasis and the regulation of drug metabolism particularly the balance between CYP3A7 and CYP3A4 [189,190]. However, its more prominent role accounts for regulating the energy metabolism of the liver through lipid metabolism, gluconeogenesis, urea cycle for ammonia detoxification and bilirubin detoxification [189]. C/EBPα knock-out models have highlighted the generation of pseudoglandular structures in the liver parenchyma and the absence of hepatic glycogen storage, resulting in hypoglycemia and death shortly after birth in mice [191,192]. Similar to HNF4-α, its expression in tumour cells is diminished revealing the potential of C/EBPα as a novel clinical target for liver cancer due to its growth inhibition effect which moderates hepatocyte proliferation *in vivo* [193–195].

Nonetheless, HepG2 cell performance can be upregulated by manipulating the culture conditions, specifically organising the cells in 3D constructs. HepG2 spheroids, either encapsulated or not, had improved expression of albumin, cholesterol, urea, phase I and II drug metabolism enzymes and transporters [196–198]. Another 3D HepG2 culture using a collagen-scaffold coated with fibronectin demonstrated the same upregulated expressions at the mRNA level including the C/EBPα transcription factor [199]. Moreover, in these conditions cells polarised and formed bile canaliculi-like structures which demonstrate further resemblance to hepatocytes [196,200].

4.1.1.1. Glucose metabolism

Glucose metabolism is one of the main functions of liver cells, where free glucose enters the hepatocytes and is phosphorylated to glucose 6-phosphate following several metabolic routes like glycogen synthesis, hexosamine pathway, pentose phosphate pathway and oxidative pathway [201]. The selection of the pathway is normally associated with the oxygen availability driving it towards the oxidative pathway under normoxia and glycolysis under hypoxia. Additionally, hepatocytes can synthesise glucose from stored glycogen (glycogenolysis) and other precursors such as lactate (gluconeogenesis) therefore, requiring a bidirectional transport of glucose mediated by glucose transporter-2 (GLU2) whose expression is regulated by LETFs including HNF4-α.

Conversely, in liver cancer cells, glucose metabolism is predominantly governed by glycolysis independently of oxygen availability, a phenomenon referred to as the Warburg effect [202]. This mechanism results in higher glucose consumptions coupled with increased production of lactate and diminished energy generation, as it produces 2 molecules of ATP per molecule of glucose, compared to up to 36 molecules generated by oxidative phosphorylation in normal cells. However, this inefficiency is compensated by the faster metabolisation rate in glycolysis which ultimately yields equivalent ATP levels to glucose oxidation in the mitochondria [203]. Moreover, glycolysis kinetics acts as a tumour adaptation mechanism by responding to ATP demands from alterations in the microenvironment [203,204].

These effects have been observed in HepG2 cells where glucose uptake is higher than in primary human hepatocytes and its metabolism is processed through glycolysis independently from the glucose concentration in the medium [205,206].

4.1.1.2. Signalling pathways

Several extracellular cues trigger cellular responses modulated by the extensively investigated extracellular signal-regulated kinase (ERK1/2) pathway. These include osmotic pressure, growth factors, hypoxia, matrix detachment and even mechanical stimuli (Figure 23) [207,208]. The mechanism is activated when a ligand binds to the respective cell surface receptor, activating the GTPase Ras which recruits Raf to the membrane for phosphorylation [209]. The activated Raf subsequently phosphorylates

MEK1/MEK2 which in turn activate ERK1/2 through phosphorylation at the threonine and tyrosine residues. Activated ERK1/2 is translocated from the cytoplasm to the nucleus for regulation of several substrates involved in cell proliferation, differentiation, adhesion, migration and survival [209,210]. For instance, ERK1/2 is activated during proliferation of mature hepatocytes after partial hepatectomy by assisting in the progression of the G_1 to the S phase of the cell cycle through upregulation of cyclin D1 and cyclin-dependent kinase 1 [211]. Cyclin D1 is a protein that interacts with cyclin dependent kinase 4 (CDK4) for cell progression from G_1 to S phase of the cell cycle. Therefore, its expression gradually increases through G_1 phase until the G_1/S boundary, where it declines to allow cells to enter the S phase. Cyclin D1 has been identified as a mediator of cell growth and proliferation in hepatocytes [212]. However, due to this regulatory role in the cell cycle, its overexpression has been reported and associated with cancer cell proliferation [213].

Hyperactivation of ERK1/2 was observed in patients with advanced and aggressive non-small-cell lung cancer prognosis correlated with lymph node metastasis [214]. Moreover, epithelial-to-mesenchymal transition and resistance to chemotherapy were identified in hepatocellular carcinomas expressing BMP4 regulated by ERK1/2 pathway [215]. This anti-apoptotic effect could be promoted by downregulation of pro-apoptotic or upregulation of anti-apoptotic molecules/proteins [207]. However, the intensity and duration of the ERK1/2 activation (transient or prolong), dependent on each cell type and extracellular stimuli, mediates the specificity of the ERK1/2 action which has been reported to extend from proliferation inhibition to pro-apoptosis effect [207,216–218].

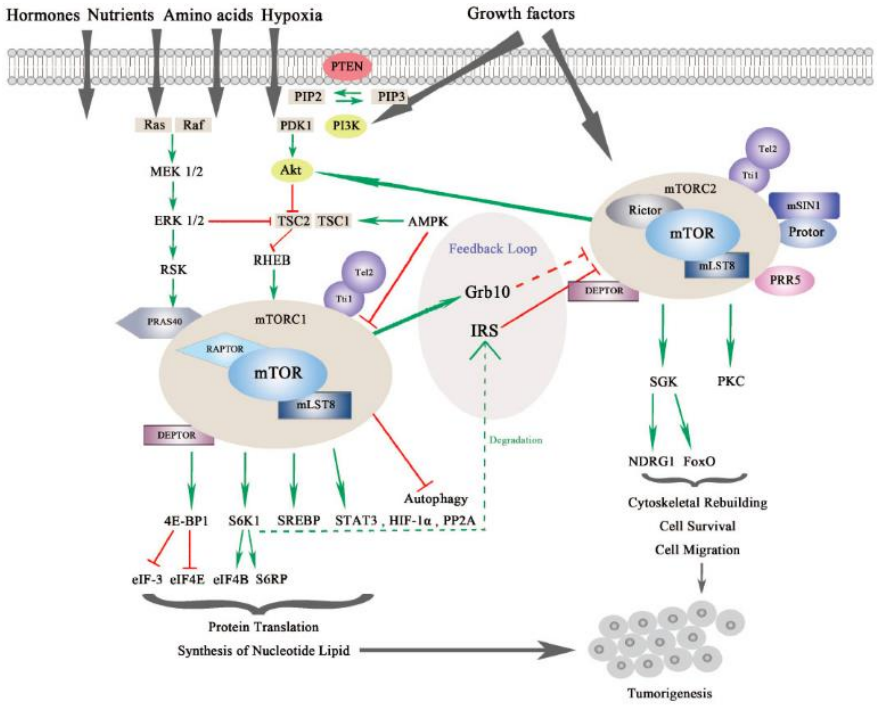

Figure 23 - Cross-talk between ERK1/2, mTOR and Akt signaling. Signalling pathways involved the extracellular signals and nutrient metabolism, normally hyperactivated in cancer cells. Image retrieved from Tian et al, 2019.

Another pathway regulated by the availability of nutrients is the mechanistic target of rapamycin (mTOR) composed of two complexes mTORC1 and mTORC2 (Figure 23) [219]. Both complexes are defined by three main components: mTOR, GβL and Raptor in mTORC1 or Rictor in mTORC2. Raptor and Rictor, in their respective complexes, facilitate substrate recruitment and correct the subcellular localisation of mTOR [220]. Although GβL is present in both subunits, its role has been described as a positive regulator of mTORC1 by stabilising its interaction with Raptor and stimulating the kinase activity towards the substrates S6 kinase 1 (S6K) and eIF-4E binding protein 1 [221]. mTORC1 plays an important role regulating metabolism by balancing the catabolic and anabolic processes in the cell based on the environmental concentration of nutrients, oxygen and energy to promote protein, lipid and nucleotides synthesis, ultimately leading to cell growth [222]. Conversely, mTORC2 is associated with proliferation control and cell survival acting on substrates which regulate cytoskeletal remodelling and cell migration, but most importantly mTORC2 activation phosphorylates Akt in the PI3K signalling [223].

Akt is a serine/threonine kinase which regulates several functions including angiogenesis, cell metabolism, growth and survival. It exerts its cell survival mostly by

inhibiting pro-apoptotic processes such as the release of Cytochrome c from the mitochondria triggered by several pro-apoptotic Bcl-2 family members [224,225]. The influence on cell growth highlights the continuous cross-talk between Akt and mTOR as Akt activation phosphorylates and inhibits tuberous sclerosis complex 2 (TSC2), a negative regulator of mTORC1 expression [226]. However, the inhibition of TSC2 does not depend on the mTORC2 regulation of Akt [220].

Similarly to ERK1/2, aberrant expression of mTOR/Akt mechanism has been implicated in cancer cell survival and progression, mostly due to mTOR being a downstream substrate of both ERK and Akt (Figure 23) [227]. For instance, overexpression of Rictor associated with high Akt activity has been observed in breast cancer [228]; and metabolic changes in glucose metabolism in cancer have sustained mTORC1 activation [229].

4.1.2. Hypothesis and aims

It was hypothesised that the dynamic environment promoted by fluidisation sustains biomass viability in long-term cell culture leading to a more physiologically relevant phenotype of 3D cell constructs. Therefore, the aim was to encapsulate HepG2 cells in alginate beads and culture them parallel in the sFBB and conventional static cultures evaluating their viability, proliferation, phenotype and performance throughout.

4.1.3. Materials and methods

Specific methods followed in this sub-chapter are referred in detail in Chapter 2 and include: *2.9. Cell viability of encapsulated cells, 2.10. Cell number of encapsulated cells, 2.11. Glucose consumption, 2.12. ATP assay, 2.13. Enzyme-Linked Immunoabsorbent Assay, 2.14. Cell cycle analysis, 2.15. Gene expression and 2.16. Protein expression.*

4.1.4. Results

4.1.4.1. *Cell proliferation and viability of alginate encapsulated HepG2 cells in dynamic and static culture*

HepG2 cells were encapsulated as single cells in alginate beads and cultured for 12 days in the sFBB (dynamic) and conventional tissue culture flasks (static). During the first 4 days, the two conditions yielded equivalent biomass densities with the static even producing 1.51 million cells/mL beads more than the dynamic (Figure 24 A). As the culture progressed, cells proliferated exponentially in the sFBB whereas the proliferation rate was slower in static culture. By day 12 cell density was 13.4 ± 0.73 and 27.3 ± 0.78 million cells/mL beads in static and dynamic culture, respectively. This represented a 2-fold increase in yield in the dynamic culture, also evident from the captured images where denser and larger spheroids were observed (Figure 25).

Cells remained highly viable in both conditions (above 90% level). However, a small drop was observed at the later time points for cells under static culture from an initial 98.3 ± 2.1% to 92.6 ± 3.3 % by day 12, while those in sFBB were 97.3 ± 2.3% (Figure 24 B). Overall, results suggested that the dynamic environment induced cell proliferation while supporting high viability.

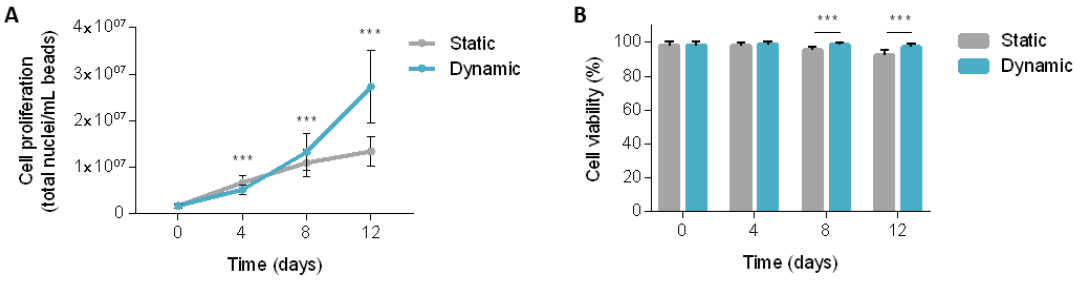

Figure 24 **-** Biological performance of alginate encapsulated HepG2 cells in dynamic (sFBB) compared to conventional static culture. Cell proliferation curves (A) and corresponding viabilities (B) throughout 12 days of culture. Data presented are average ± standard deviation (SD) (n = 7). Statistical analysis was assessed by multiple Student's t-test using the Holm-Sidak method correction. *** $p < 0.001$.

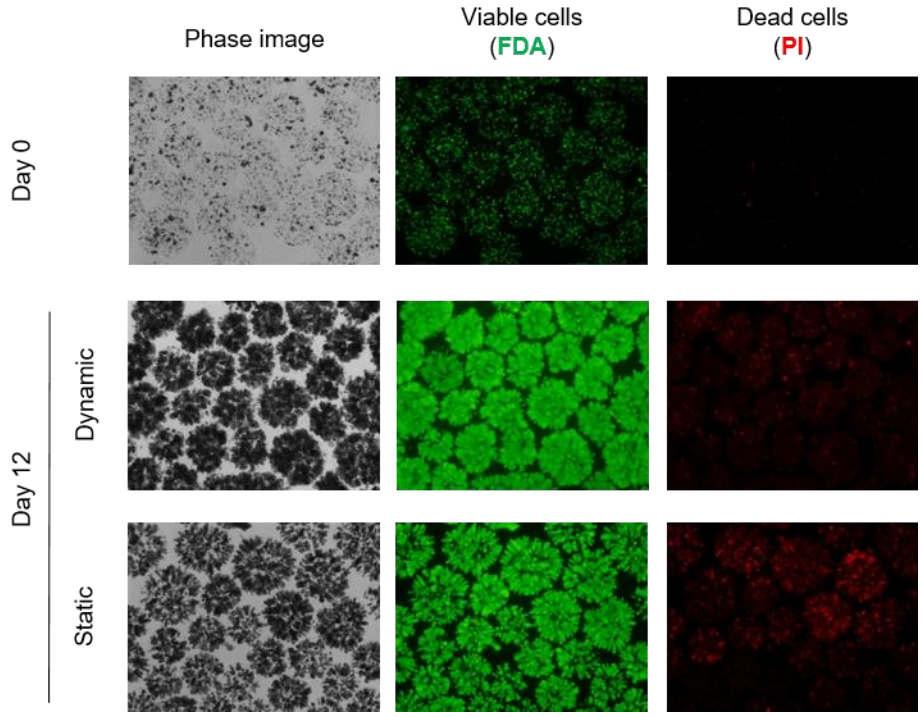

Figure 25 - Alginate encapsulated HepG2 cells cultured in dynamic and static culture for 12 days. Captured images of cell beads from the beginning (day 0) and end (day 12) of culture to observe their morphology (phase image) and determine viability (live cells stained with FDA and dead cells with PI).

4.1.4.2. Synthetic function of encapsulated HepG2 cells under dynamic culture

The effect of perfusion was also evaluated on cell function. As hepatic cells, HepG2 secrete several proteins including α-fetoprotein (AFP), a specific marker of this cell line, making it possible to correlate the synthetic capacity with functionality. Thus, AFP expression by alginate encapsulated cells under dynamic and static cultures was quantified with ELISA. Initially (day 4) similar expressions of AFP were observed in both conditions (22.03 ± 4.88 and 15.57 ± 0.93 μg/million cells per 24 h in static and dynamic, respectively) (Figure 26). But as the culture progressed, protein secretion increased in the two environments, although only significantly in static culture with 49.17 ± 9.11 μg/million cells in 24 h compared to 21.11 ± 6.55 from dynamic ($p < 0.01$). These results might indicate a superior function under static culture, or eventual a transition in phenotype, but further investigation on the gene expression upregulation would be necessary to draw more conclusions.

To note, that at this stage, it was only possible to analyse AFP secretion because the culture medium was supplemented with 10% human plasma, which would mask any analysis of cellular production of albumin and other hepatic proteins.

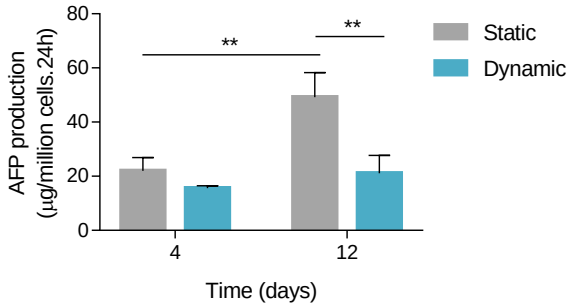

Figure 26 – AFP production by alginate encapsulated HepG2 cells cultured in static and dynamic conditions. Production normalised per million cells and 24 h was assessed on days 4 and 12 of culture. Data presented are average ± SD (n = 3). Statistical analysis was assessed by multiple Student's t-test using the Holm-Sidak method correction. ** $p < 0.01$.

4.1.4.3. Hepatic phenotype of 3D cell constructs under dynamic culture

A more in-depth phenotypical characterisation of the encapsulated HepG2 cells was assessed by the expression of hepatic markers at the mRNA level to determine the impact of the dynamic culture on gene expression. The analysis was carried out in a stepwise manner comparing first the gene expression between monolayer and 3D cell constructs (the encapsulated cells in static culture) (Figure 27 A and C) and then the effect of static and dynamic culture on the constructs (Figure 27 B and D). Markers included albumin and AFP proteins, members of the cytochrome P450 family CYP3A7 and CYP3A4 and transcription factors HNF4-α and C/EBP-α, data for each marker was normalised to monolayer.

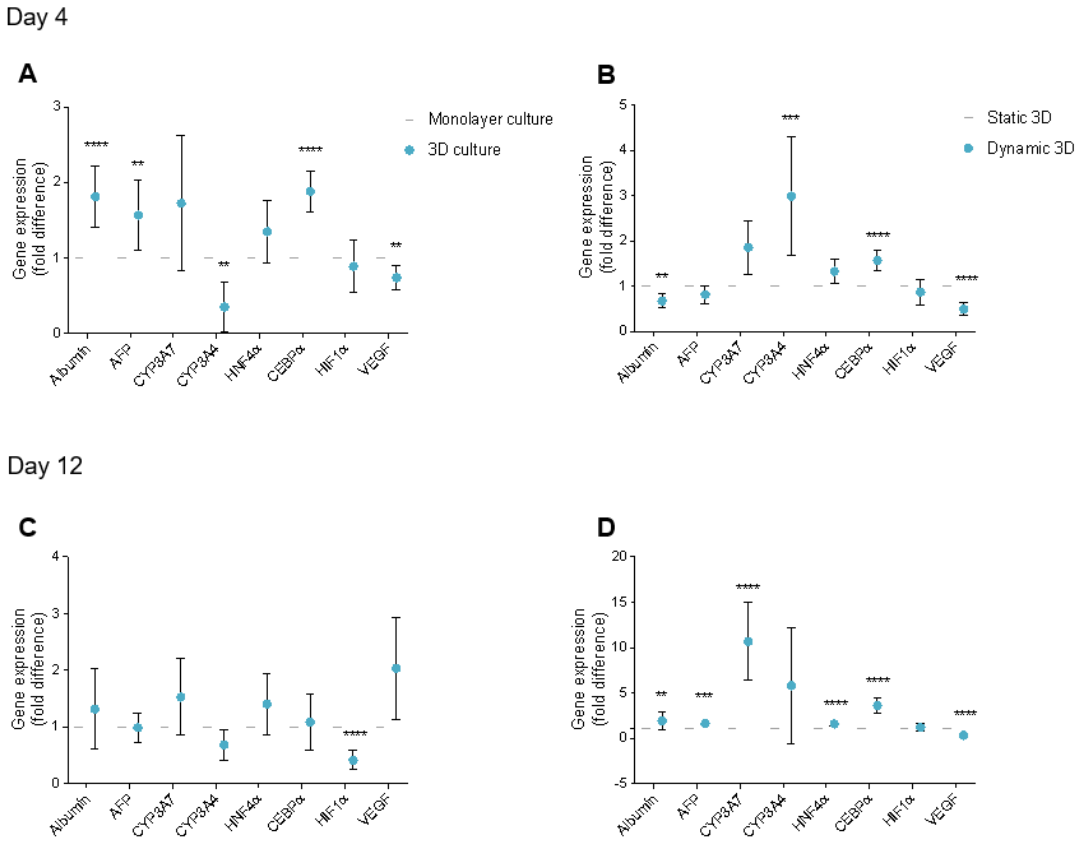

Figure 27 - Gene expression of alginate encapsulated HepG2 cells on days 4 (A and B) and 12 (C and D). Quantification of hepatic (Albumin, AFP, CYP3A7, CYP3A4, HNF4α and CEBPα) and hypoxia (HIF1α and VEGF) markers in 3D culture relative to conventional 2D culture (monolayer) (A and C) and, in dynamic (sFBB) 3D culture relative to static 3D culture (B and D). Calculation followed $2^{-\Delta\Delta C_t}$ method using HPRT1 as endogenous control. Data presented are average ± 95% confidence interval (n = 4). Statistical analysis was assessed by multiple Student's t-test using the Holm-Sidak method correction. ** $p < 0.01$, *** $p < 0.001$, **** $p < 0.0001$.

Initially, HepG2 cells grown in 3D structures exhibited a significant upregulation of albumin ($p < 0.0001$), AFP ($p < 0.01$) and C/EBP-α ($p < 0.0001$) and downregulation of CYP3A4 ($p < 0.01$) compared to monolayer, supporting that 3D structures replicate a more *in vivo* like phenotype (Figure 27 A). The culture of encapsulated HepG2 cells in the sFBB further increased the expression of C/EBP-α ($p < 0.0001$) and inverted the decrease of CYP3A4 by a 3-fold upregulation ($p < 0.001$) (Figure 27 B). Although not statistically significant, there was also an upregulation trend in HNF4-α and CYP3A7. Conversely, albumin was downregulated in the dynamic environment.

After 12 days of culture, HepG2 spheroids maintained the gene expression trend of day 4 but at reduced levels without any significant upregulation (Figure 27 C). However,

supporting them under perfusion conditions upregulated significantly all the assessed genes, except for CYP3A4 even though its expression was increased by 6-fold (Figure 27 D). These results suggest that, from an early stage, the dynamic environment induces an upregulated hepatic phenotype in the encapsulated spheroids independently of the cell number and, is further enhanced as the culture advances and cells proliferate, displaying an overall upregulation of the hepatic phenotype.

To note that a previous study from the Liver Group had identified several differences at the gene expression level between 3D structure and monolayer demonstrating an adaptive response from the former to enhanced performance [121].

4.1.4.4. Hypoxia in 3D cell constructs under dynamic culture

Hypoxia is a prominent feature in tumour spheroids as a result of their abnormal proliferation, metabolic activity and vascularisation. In cell culture hypoxia could be generated by a poor supply of oxygen and thus, compromise cell performance. To try to explain the slow proliferation of the HepG2 encapsulated spheroids in static culture, mRNA expression of hypoxia inducible factor 1 alpha (HIF1α), master transcription factor of the oxygen homeostasis in cells upregulated under hypoxic conditions, and vascular endothelial growth factor (VEGF), a target of HIF1α responsible for promoting angiogenesis and neovasculature, were assessed. On day 4, 3D constructs presented an unaltered expression of HIF1α and a downregulation of VEFG by 0.74-fold in comparison with monolayer HepG2 cell (Figure 27 A). The later was further reduced in constructs under dynamic conditions (Figure 27 B).

By day 12, HIF-1α expression in HepG2 spheroids was lower than in monolayer ($p < 0.0001$) but with an increase in VEGF, although not to a significant upregulation (Figure 27 C). When adding the perfusion effect, there was no difference in HIF1α expression between static and dynamic, but VEGF was significantly downregulated (Figure 27 D). These data might indicate a poor supply of oxygen in the static environment which is only reflected by HIF1α substrates (VEGF expression). Alternatively, another mechanism could be governing its expression and this result is connected to the angiogenic process characteristic in solid tumours, thus, supporting a more tumour associated phenotype.

4.1.4.5. Cell cycle of HepG2 cell spheroids under dynamic culture

To highlight the effect of the dynamic environment in a mechanistic form, cell cycle progression of the encapsulated HepG2 spheroids was evaluated to corroborate the proliferation pattern. Analysis of the DNA content of the formed spheroids both in static and dynamic conditions (Figure 28 A and B, respectively) demonstrated that there were no differences between both environments, with most of the cells in G_0/G_1 phase. There was a small increase in the number of cells in G_1 on day 1 (3% and 1% in dynamic and static, respectively) probably a consequence of the confinement of the cells in the hydrogel bead. As proliferation advanced on day 4 the percentage of cells in S and G_2 phases maintained the levels observed in day 0, progressively declining until day 12. Furthermore, the expression of cyclin D1, an important cell marker of the G_1 to S phase transition, at the mRNA level was similar between 3D constructs and monolayer HepG2 cells (Figure 29 A), and encapsulated spheroids in static and dynamic cultures (Figure 29 B). These verified the previous FACS analysis further demonstrating that the augmented cell proliferation in the sFBB was not explained by a simple change in cell cycle kinetics.

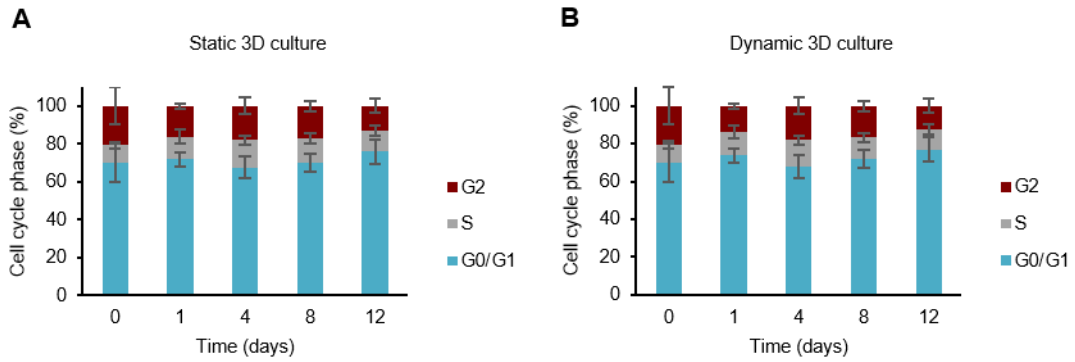

Figure 28 - Cell cycle analysis of alginate encapsulated HepG2 cells in dynamic (sFBB) and static culture. Determining percentage of cells in G_0/G_1, S and G_2 phases on days 0, 1, 4, 8 and 12 through quantification of DNA content by PI staining. Data presented are average ± SD (n = 4).

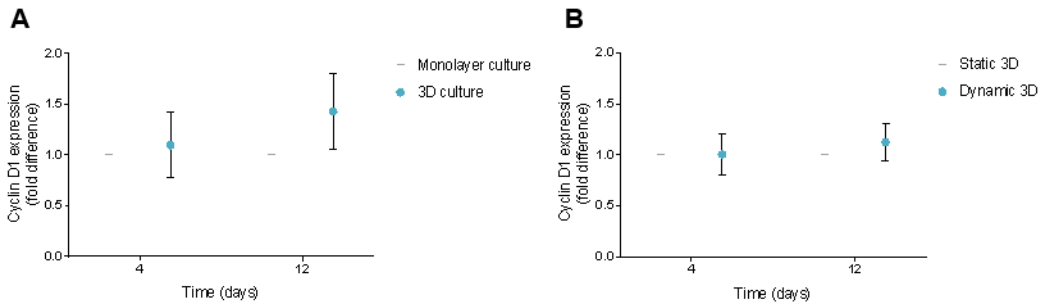

Figure 29 **-** Cyclin D1 expression by alginate encapsulated HepG2 cells on days 4 and 12. Quantification mRNA expression of cyclin D1 in 3D culture relative to conventional 2D culture (monolayer) (A) and, in dynamic (sFBB) 3D culture relative to static 3D culture (B). Calculation followed $2^{-\Delta\Delta C_t}$ method using HPRT1 as endogenous control. Data presented are average ± 95% confidence interval (n = 4).

4.1.4.6. Glucose and ATP metabolism of HepG2 cell spheroids under dynamic culture

It was hypothesised that encapsulated spheroids followed different metabolic patterns in the two environments, which would be consistent with the discrepancies observed in cell proliferation. Thus, glucose consumption and cellular ATP content were analysed. In static culture, encapsulated spheroids consumed less glucose on day 4 than day 12 with an increase of 24.2 µmol/million cells per 24 h which emulated the rise in cell number and the associated metabolic demands (Figure 30). Conversely, dynamic spheroids maintained a stable consumption of glucose between days 4 and 12 and inferior to the one in static particularly on day 12, even if not statistically significant.

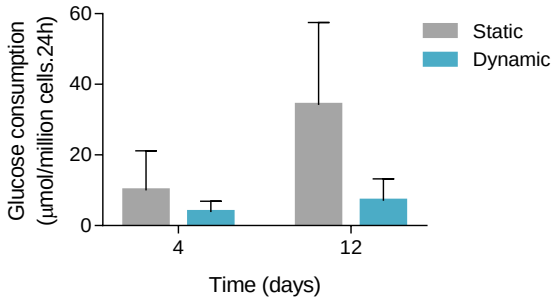

Figure 30 – Glucose consumption by alginate encapsulated HepG2 cells in dynamic (sFBB) and static culture. Analysis performed on days 4 and 12 normalised to million cells per 24 h. Data presented are average ± SD (n = 3).

In contrast, the cellular ATP content was higher on day 4 (14.5 ± 2.5 and 16.5 ± 2.8 nmol/million cells in static and dynamic, respectively) than on day 12 (9.7 ± 4.1 and 7.8 ± 2.5 nmol/million cells) (Figure 31). Similar to glucose consumption, there were no significant differences between spheroids cultured in static or dynamic environments. Thus, although results highlighted cells were metabolically active, they could not explain or reflect the promoted proliferation in the sFBB, since cells under perfusion did not have a higher glucose consumption or ATP content compared to those in static.

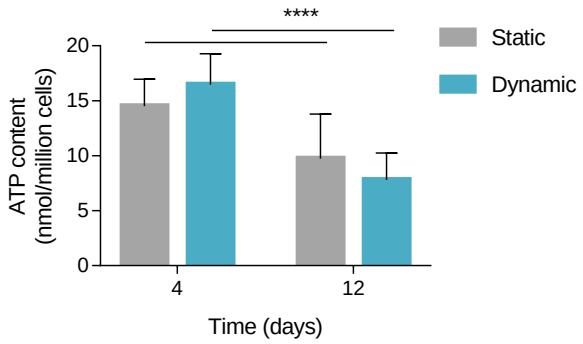

Figure 31 – Adenosine triphosphate (ATP) content in alginate encapsulated HepG2 cells in dynamic (sFBB) and static culture. Analysis performed on days 4 and 12 normalised to million cells. Data presented are average ± SD (n = 3). Statistical analysis was assessed by 2-way ANOVA with Sidak method correction. **** $p < 0.0001$.

4.1.4.7. Activation of signalling pathways in HepG2 cell spheroids under dynamic culture

Several pathways have been extensively associated with regulating cell proliferation based on nutrient, growth factors and cytokine availability.

The mammalian target of rapamycin (mTOR) is a master regulator of cell proliferation based on nutrient availability. Therefore, its activation by phosphorylation was investigated exploring the hypothesis that in dynamic culture, nutrient availability would be higher due to the elimination of gradients by improved mass transfer, as each cell would be exposed to the same concentration of nutrients. The analysis was conducted on HepG2 spheroids cultured both in static and dynamic conditions and on days 4, 8 and 12 (Figure 32).

Activation of the mTOR complex 1 (mTORC1) did not demonstrate significant alterations throughout culture time nor between static and dynamic, with a minimal

trend of higher phosphorylation in static than dynamic (Figure 33 A). The Raptor protein, which binds to the mTORC1 mediating its signalling to downstream targets, indicated increased expression in both conditions, although markedly higher in dynamic than static on day 12 (Figure 33 C). As for mTOR complex 2 (mTORC2) phosphorylation was higher on day 4, decreasing and stabilising for the remaining culture period without any marked differences between static and dynamic (Figure 33 B). A stable pattern was also observed in Rictor expression without any obvious increases or reductions in the conditions or throughout time (Figure 33 D). GβL protein expression increased in both cultures until day 8, continuing on day 12 in dynamic but declining in static (Figure 33 E). Moreover, no alterations were observed in the expression of total mTOR (t-mTOR) protein (Figure 32).

Investigation continued to Akt activation (Figure 32). Its expression in HepG2 spheroids peaked in dynamic culture on day 4, progressively diminishing through time to comparable levels of the static culture (Figure 33 F). This initial activation could be correlated with the higher expression of mTORC2 on day 4 as well.

Following on the external stimulation activation not only through nutrient availability but also exploring if the hydrodynamic forces in the bioreactor would influence the proliferation rate, the extracellular signal-regulator kinase (ERK1/2) phosphorylation was analysed. Activation of ERK1/2 increased over time in static culture but progressively decreased in spheroids in the dynamic environment, almost to non-phosphorylated (deactivated) levels by day 12 (Figure 33 G). Total ERK1/2 protein did not change throughout the experiment in either condition (Figure 32), determining the effect was activation related and not a decrease in the total protein expressed. These data evidenced that the dynamic environment dephosphorylated ERK1/2 in the long-term.

Collectively the results indicate the cell proliferation in dynamic culture could not be explained by hyperactivation of the investigated pathways for the monitored time. Although, they could suggest a switch in the phenotype due to the increases in the Raptor and GβL and decrease in Akt suggesting a more homeostatic metabolism rather than cell survival, most importantly due to the significant dephosphorylation of ERK1/2.

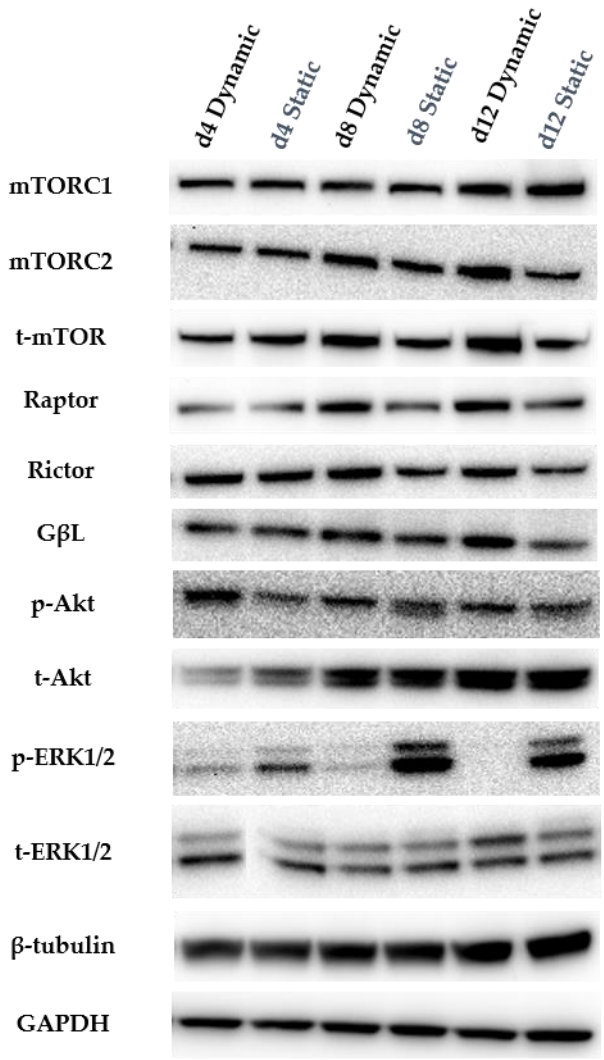

Figure 32 **-** Representative Western blots of nutrient signalling pathways in alginate encapsulated HepG2 cells in dynamic (sFBB) and static culture. Analysis of phosphorylated p-mTORC1 and p-mTORC2 and total (t) mTOR, total Raptor, Rictor and GβL, phosphorylated (p) and total (t) Akt, phosphorylated (p) and total (t) ERK1/2 and total β-tubulin and GAPDH as loading controls, on days 4 (d4), 8 (d8) and 12 (d12).

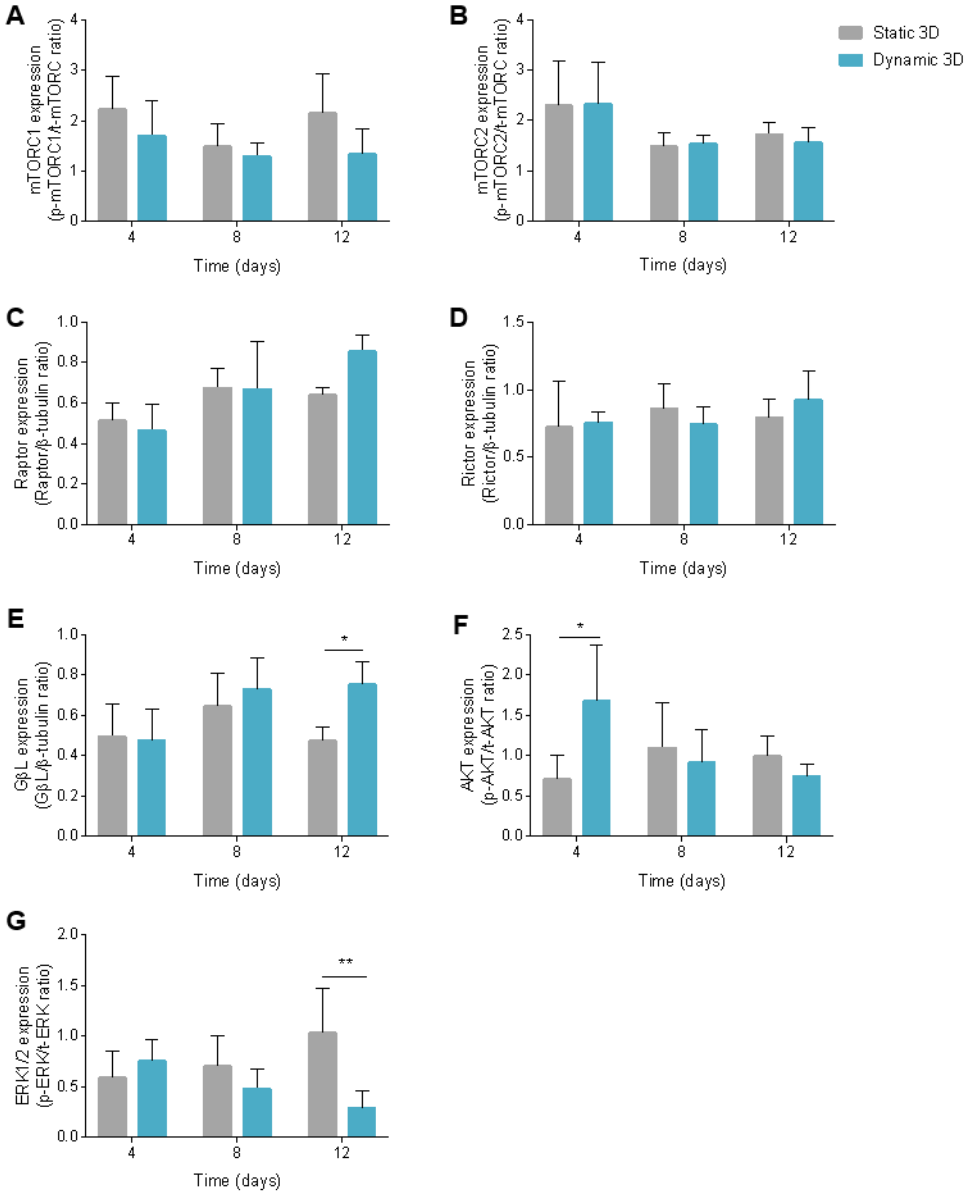

Figure 33 **-** Quantification of Western blot analysis from Figure 32 of nutrient signalling pathways in alginate encapsulated HepG2 cells in dynamic (sFBB) and static culture. Activation of protein determined by the phosphorylated/total protein ratio for mTORC1 (A), mTORC2 (B), Akt (F) and ERK1/2 (G) and total protein expression of Raptor (C), Rictor (D) and GβL (E) on days 4, 8 and 12 of static and dynamic culture. Data presented are average ± SD (n = 4). Statistical analysis was assessed by 2-way ANOVA with Sidak method correction. * $p < 0.05$, ** $p < 0.01$.

4.1.5. Discussion

The dynamic culture of alginate encapsulated HepG2 cells in the sFBB prototype developed in *Chapter 3* promoted cell proliferation resulting in the formation of several highly viable spheroids per bead. Proliferation rate was particularly increased during

the last 4 days of culture producing a final cell density double the one obtained in conventional static culture. These results further validate the application of the prototype as a bioreactor for long-term 3D cell culture and corroborate previous studies that highlighted the superiority of dynamic environments for cell proliferation and growth [131,230,231]. The improved performance is often associated with a more efficient mass transfer between the biomass and the milieu, which was observed through the dextran diffusion experiments in *Chapter 3*. Others have also demonstrated that the hydrodynamic shear stress produced in perfusion systems provides physiologically relevant biomechanical stimuli for cell expansion [232].

Although cell proliferation was evident from nuclei counts and imaged spheroids, cell cycle kinetics analysis did not verify the same profile since there were no significant increases in the percentage of cells in S or G_2 phase in dynamic compared to static culture, and no upregulation of cyclin D1 expression at the mRNA level. Increased cyclin D1 was detected at the protein level in alginate-collagen encapsulated MCF-7 cells in a rotary cell culture system after 48 h [231]. Conversely, Hongo et al. have observed suppression in the expression of cell cycle-related genes in HepG2 cells after seven days of culture in a radial-flow bioreactor, defining it as the stable phase with similar characteristics to the normal liver [233]. Achieving stability could describe the expression levels of day 12 but does not explain those observed at the early time points in this study. However, modifications might not be verified at the gene amplification stage but only at post-translation and hence, protein expression of cyclin D1 could provide more information.

Another investigation reported an arrest in the G_0/G_1 phase of HepG2 cells in 3D static and dynamic cultures as a consequence of the higher mortality of these cells in the respective setup [234,235]. This is not the case for the 3D constructs in the present study since they continued to proliferate and remained highly viable throughout. Moreover, there were no declines in the S and G_2 phases nor suppression of cyclin D1 expression indicating no downregulation of the proliferative capacity of the cells. Nonetheless, alterations in the cell cycle could still be occurring only not detected through the applied methods. Coupling DNA staining with cyclin markers or staining cells with S phase markers such as BrdU would improve the accuracy of the analysis, since the spheroids cultured in the clinical scale FBB have stained positive for BrdU and Ki67 [121].

A factor which could contribute to cell cycle arrest is the mechanical confinement generated by the hydrogel encapsulation. Nam et al. reported that tumour cells encapsulated in alginate hydrogels exhibiting fast stress relaxation progress through cell cycle and proliferate quicker than those in hydrogels of slow stress relaxation, where they are mainly arrested in G_0/G_1 phase [236]. Additionally, the surrounding cells and extracellular matrix of multicellular spheroids produce a similar mechanical effect. Although an investigation of the alginate bead mechanical properties was not conducted, it could be speculated that the increased percentage of cells in the G_1 phase results from the confinement of the spheroids in hydrogels of slow stress relaxation. This effect could be further supported by the results of G_2 arrest (data shown in Appendix 1). Incubating encapsulated spheroids with 1 μM Nocodazole for 24 h reduced the percentage of cells in the G_1 phase by 12% (from 73% to 61%), whereas in monolayer only 27% of HepG2 cells were in G_1 (a decrease of 45%).

Encapsulated HepG2 spheroids in dynamic conditions displayed a consistent protein synthesis ability throughout the culture period. Conversely, in static culture, cells demonstrate increased AFP production 2-fold from day 4 to 12 suggesting a superior secretory performance of these encapsulated spheroids. Another possibility would be an alteration of the immature phenotype under hydrodynamic conditions and thus, a more in-depth phenotypical analysis was conducted at the gene expression level.

Initially, the 3D structure granted an upregulation of hepatic markers (albumin, AFP and C/EBPα) compared to cells in 2D, consistent with literature descriptions of HepG2 cells cultured in other 3D configurations after three days. In the dynamic culture, C/EBPα was further upregulated and the CYP3A4 downregulation reversed indicating that the influence of the dynamic environment is exerted from the start independently of the number of cells. In the long-term, gene expression under static conditions approached that of the monolayer, whereas in the hydrodynamic environment there was an overall increased upregulation of the markers, representing an improved cell performance under dynamic conditions. A similar effect was observed in the hepatic differentiation of induced pluripotent and embryonic stem cells with cells acquiring a more hepatocyte-like phenotype under perfused conditions [237,238].

The overall gene upregulation by day 12 might suggest a transition in the spheroids' phenotype in hydrodynamic conditions. Although there was an upregulation of the AFP

gene expression (despite not agreeing with the previous protein secretion results) along with CYP3A7 (the other marker of the immature HepG2 phenotype) in dynamic spheroids, they also displayed higher levels of CYP3A4 and the transcription factors HNF-4α and C/EBPα normally less expressed in HepG2 cells; both are associated to a more mature phenotype.

HNF-4α and C/EBPα are master regulators of the hepatic functions and differentiated status of primary hepatocytes. Research has demonstrated the importance of these factors in the final differentiation stage of stem cells into mature hepatocytes, as their expression induced liver specific functions (e.g. production of albumin, cytochrome P450 and glucose-6-phosphatase) and their absence resulted in poorly differentiated cells [239,240]. Both transcription factors have also been identified in the regulation of several hepatic genes including the CYP3A family, with studies reporting that a decrease in HNF-4α subsequently decreases CYP3A4 expression, and overexpression of C/EBPα has led to an increase in CYP3A4 mRNA levels [183,241]. Moreover, C/EBPα regulates serum albumin expression in hepatoma cells by binding to the promoter gene [242]. Therefore, the upregulation of the proteins and cytochrome P450 genes will be directly correlated to the increased expression of the transcription factors.

The reported diminished expression of HNF-4α and C/EBPα in hepatoma cells is associated with their poorer performance and highly proliferative capacity, including upregulation of cyclin D1 [243–246]. Overexpression or forced activation of the HNF-4α and C/EBPα has been targeted as a tumour suppression mechanism resulting in inhibited cell proliferation, halted epithelial-to-mesenchymal transition, increased expression of subsequent hepatic markers as albumin, cytochrome P450 isoforms, and overall reduction of tumour burden [187,243,247]. Hence, the expression of the transcription factors is likely associated with a transition into a more hepatic functional phenotype probably due to the combined effect of the hydrodynamic environment and the complexity of the formed spheroids. The analysis of other markers involved in the ammonia and urea cycles and phase II of the drug metabolism, for example, would provide more parameters to clarify the improvement in the phenotype. Also, longer culture periods would give more information on the evolution of the phenotype as the current study only extended to 12 days.

The metabolic analysis of the encapsulated spheroids highlighted further differences between cells cultured in the two conditions. Media composition was identical in static and dynamic cultures containing 4.5 g/L of glucose, however, encapsulated HepG2 cells in dynamic culture presented a stable but lower glucose consumption than static, which in turn displayed an increasing trend. These were not the anticipated results since the exponential growth in the bioreactor should require a higher glucose uptake to cope with the proliferative demand. Iyer et al. demonstrated that HepG2 cells consumed less glucose in an environment with high glucose concentration (4.5 g/L) than with 1 g/L, always through glycolysis but proliferation was not sensitive to the glucose concentration in the medium, yielding comparable final cell densities in both conditions [205,248],. Although it does not fully explain the observed differences as the media concentration was the same in both conditions, the convective forces in the bioreactor diminish the formation of gradients and increase mass transfer, leading to higher glucose availability in the cells microenvironment and creating an effect of higher concentration, consequently reducing glucose consumption.

Another study has proposed a dynamic mechanism of glycolysis activation in cancer cells as an adaption to energy fluctuations in the environment: for conditions which are spatially and temporally homogeneous ATP is mostly produced by oxidative stress; in environments where the amplitude or frequency of the stimuli increases, the baseline ATP is produced by oxidative stress but the fluctuations demands are supplied by glycolysis [204]. This adds to the previous hypothesis suggesting that the increase in glucose consumption in static culture on day 12 results from fluctuations of an heterogeneous milieu more subjected to concentration gradients and inefficient mass transfer.

However, the lower glucose uptake by cells in dynamic culture could support the possible transition to a more physiologically relevant phenotype suggested by the gene expression analysis, since HepG2 cells are known to have higher glucose uptakes than hepatocytes. Analysis of the glucose consumption by monolayer HepG2 cells and hepatocytes would be valuable to verify this hypothesis

The intracellular ATP content was expected to follow a similar trend to glucose consumption but instead decreased over time and did not reflect the same differences between the two cultures. Zhang et al. observed similar behaviour in the dynamic

culture of cytokine-induced killer cells with the intracellular ATP content peaking at initial time points and gradually diminishing until day 14 [249]. By additionally assessing indicators of glycolysis and oxidative phosphorylation, they attributed the ATP reduction to a higher consumption to sustain metabolic processes such as proliferation. This could imply that the observed results in HepG2 spheroids are a consequence of a similar phenomenon even though, the metabolic functions exerted by static and dynamic spheroids are distinct (e.g. the cells in dynamic culture invest more energy in proliferation than those in static culture). Speculation on whether cells under static culture could be using the same amount of energy but for protein secretion, associating the higher production of AFP, was not supported by the overall cellular protein content since there were not substantial differences between dynamic and static conditions (Appendix 2). Investigation of other parameters such as the intracellular glucose and NADH content as well as the activity of glucose transporters, hexokinase 2, and other enzymes involved in glycolysis and oxidative phosphorylation would be essential to further understand the metabolic activity of the encapsulated spheroids [250].

The higher proliferation of 3D cell constructs in the sFBB could derive from an increased nutrient availability, a consequence of the enhanced mass transport promoted by the hydrodynamic forces, and thus, the activation of the mTOR signalling pathway was investigated. mTORC1, associated with cell growth and homeostasis, and mTORC2, activated under cell survival conditions, were phosphorylated both in dynamic and static encapsulated spheroids without any significant differences nor fluctuations throughout the time course. The respective associated proteins Raptor and Rictor did not display any statistically significant expressions and GβL was upregulated on day 12 spheroids in dynamic culture. These results demonstrated that there is not an evidently favoured activation towards cell growth nor cell survival mode between dynamic and static but nutrient availability is not a limiting factor in either of the conditions. Whilst not statistically confirmed, Raptor expression displayed an increasing trend in dynamic spheroids, and together with GβL expression, might suggest that over time there is a stronger influence of mTORC1 in the metabolic activity of the spheroids under hydrodynamic culture, consequent of the homogenous environment. To further clarify this possibility it would be valuable to analyse the phosphorylation of Raptor and expression of mTOCR1 substrates such as S6K and 4EBP since studies have reported

upregulation of S6K expression in 3D cell constructs in dynamic environment but no significant alterations to mTORC1 activation [251]. Moreover, the fact that mTOR is constitutively expressed in tumour cell lines and implicated in hepatocarcinogenesis, differences might only be noticeable at the downstream cascade [252,253].

Upstream from mTORC2 is Akt whose activation at the start of dynamic culture could have triggered cell proliferation in a transient stimulus since its phosphorylation was reduced throughout time, perhaps due to a possible increase in the mTORC1 expression, which exerts negative feedback in Akt activation. Similar to mTOR, Akt is abnormally overexpressed in cancer cell lines, but the phosphorylation in the dynamic culture could arise from a stress response to the hydrodynamic forces in the bioreactor activating the cell survival mode. Alternatively, the insulin supplemented to the culture medium stimulates Akt activation through the improved hydrodynamic delivery of nutrients and growth factor compared to the static environment.

Related to mTOR/Akt pathway and its overexpression implicated in cell survival and proliferation of cancer cells is ERK1/2. Its activation has also been detected under pulsative flow fluid conditions [254]. Therefore, the mechanical stimulus of the hydrodynamic forces inside the sFBB could be another factor activating ERK1/2 and driving cell proliferation. Although the alginate bead shields cells from damaging shear stress, the hydrodynamics forces could propagate mechanical stimuli through the hydrogel network and porous structure impacting on the cellular microenvironment and cell performance [255]. Interestingly, ERK1/2 phosphorylation was weak from the beginning in dynamic culture progressively diminishing until almost no signal was detected on day 12. In static culture, an opposite outcome was observed: phosphorylation increased over time with a more intense expression of ERK2 than ERK1. These activation patterns were inversely correlated with the respective cell proliferation curves, revealing that the dynamic culture did not promote ERK1/2 phosphorylation and consequently was not responsible for governing proliferation. A similar result, although not as extensive, was obtained by Jackman et al. during the development of cardiomyocytes and attributed to an inhibitory effect of S6K to PI3K [251].

The deactivation, together with the previous gene analysis and reduced glucose consumption, could further support the transition to a more functional hepatic phenotype of HepG2 spheroids cultured in dynamic environment. In fact, it has been

demonstrated that in hepatoma cells there is a higher expression of ERK2 than ERK1 as in the case of spheroids in static culture, while normal hepatocytes have a more balanced ERK1:ERK2 ratio [211]. Also, other reports have identified a direct interaction between ERK1/2 activation and HNF−4α expression in HepG2 cells with the activation inhibiting HNF−4α [218]. This is consistent with their described roles in proliferation promotion and inhibition, respectively, and is in accordance with the results obtained in this study where there is a decline in ERK1/2 and upregulation of HNF-4α in the dynamic environment. Moreover, ERK/Akt/mTOR signalling was previously identified as downregulated in 3D culture of colon cancer cells compared to 2D cultures suggesting a rewiring in the metabolic activity, a phenomenon which could be similarly occurring once the perfusion component is introduced [256]. Within the investigated pathways, AMPK expression would provide further indications on the nutrient content and survival status of the cells, as its activation is a metabolic checkpoint normally associated to starvation conditions [222,251].

Of note, none of the observed metabolic alterations were hypoxia-related since HIF-1α was downregulated from the start both in static and dynamic conditions and, further reduced as dynamic culture progressed supporting an efficient oxygen delivery.

Collectively, these results demonstrate that the trigger for cell proliferation in the sFBB could have been a transient activation of the Akt which might be converted into a sustained mTORC1 regulation of the glucose metabolism, and a deactivation of ERK1/2 disconnecting the cell survival mode and proliferation in a homeostatic manner.

4.1.6. Conclusion

The current bioreactor sustained the viability of alginate encapsulated HepG2 cells and promoted their proliferation into several multicellular spheroids, as expected from the previous data from the FBB at clinical scale. It hosted sufficient biomass volume to enable long-term sampling measuring several readouts for a more in-depth analysis of the impact of the hydrodynamic environment on cell performance. This analysis uncovered that the dynamic environment promoted an upregulation of the hepatic phenotype, a consistent and low glucose consumption and the deactivation of the ERK1/2 signalling,

possibly owing to an increased nutrient and signal delivery promoted by the hydrodynamic mixing, and consequent homogenous milieu. This indicates an improved performance of the encapsulated spheroids under dynamic conditions with a probable transition from the tumour phenotype to more physiological relevant hepatic functionality. Further support of this theory would be given by investigating other markers as well as testing other cell types to validate the versatility of the device.

4.2. Impact of long-term dynamic culture on hydrogel encapsulated primary stem cells in a small-scale fluidised bed bioreactor

4.2.1. Introduction

Stem cells are immature cells with a remarkable self-renewal capacity and differentiation into a multitude of lineages originating different cells types. Multipotent stromal cells (MSCs) are multipotent stem cells harboured in several adult tissues (e.g. dental pulp, amniotic fluid, adipose tissue, Wharton's jelly) but firstly isolated from bone marrow [257,258]. To identify isolated MSCs from a mixed cell population and as a standardised minimal criteria, the International Society for Cellular Therapy, after analysis from different sources, established MSCs to be: (1) plastic adherent; (2) possess specific surface markers (positive for CD73, CD90, CD105 and negative for CD14, CD34, CD45 and human leucocyte antigen-DR; and (3) able to differentiate *in vitro* into adipocytes, chondrocytes and osteoblasts [259].

Other markers characteristic of the undifferentiated phenotype, not exclusive to MSCs but to stem cells in general, are Nanog and inhibin beta A (INHBA). Nanog is a transcription factor associated to pluripotency and its expression in MSCs has proven to increase cell proliferation rate and differentiation potential, inhibit spontaneous differentiation, restore contractile function and reverse effects of stem cell senescence [260–262]. Similarly, INHBA, a member of the transforming growth factor-β (TGF-β) family and characteristically more highly expressed in multipotent stem cells, is reported to regulate

cell proliferation and differentiation with a key role in early stages of osteogenesis and chondrogenesis [263,264].

The multipotent differentiation potential, preferably into specialised mesoderm cells, can be easily induced through culture in suitable medium and supplementation of growth factors. For adipogenesis, a combination of dexamethasone, indomethacin, insulin and isobutylxanthine successfully promotes lineage commitment demonstrated by the accumulation of lipid droplets within the cells and corroborated through Oil Red O staining as well as expression of adipocyte-specific genes peroxisome proliferator-activated receptor γ2 (PPARγ2), adipocyte protein 2 and lipoprotein lipase (LPL) [265]. The standard protocol for chondrogenesis includes growth factors such as insulin, pyruvate, ascorbate 2-phosphate, dexamethasone and TGF-β3, where after a period of 14 days, cells display a rounded shape with extensive extracellular matrix rich in proteoglycans like aggrecan (AGN) and type 2 collagen (Collagen 2) [266]. It can be validated by Alcian Blue staining which stains the glycosaminoglycans chains of the proteoglycans. Osteogenesis is induced by ascorbic acid, β-glycerophosphate and dexamethasone, presenting mineral aggregations of calcium and increasing activity of alkaline phosphatase (ALP) up to 10-fold [265]. The mineralised nodules stain positive for Alizarin Red and gene expression of runt-related transcription factor 2 (Runx2), osteonectin and bone morphogenic protein 2 (BMP2) also verify the differentiation into osteoblasts.

Furthermore, trans-differentiation of MSCs into ectodermal and endodermal lineages has proven successful. Transformation of MSCs into mature neurons which express markers of nervous systems cells such as nestin (Nes), microtubule-associated protein 2 (MAP2) and neuron-specific enolase is possible through stimuli from β-mercaptoethanol, epidermal growth factor (EGF), nerve growth factor (NGF), fibroblast growth factor (FGF), among others [267]. Moreover, MSCs subjected to compounds such as insulin, EGF, FGF, nicotinamide can be effectively differentiated into hepatocyte-like cells secreting albumin, AFP and expressing HNF-4α, and insulin-producing β-islet-like cells [268].

MSCs offer great potential for cell therapy, regenerative medicine and tissue engineering as they are easily available, have fewer ethical issues compared to other stem cells (e.g. embryonic stem cells), are expandable *in vitro* maintaining a stable phenotype, but mostly because of their trophic activity and homing ability to injury sites [257]. Their

secretome is composed of a multitude of molecules which can promote proliferation and differentiation of other cells types and exert antifibrosis, antiapoptosis, angiogenesis, and immunomodulation properties [269,270]. Several *in vitro* studies have identified the presence of these soluble factors in conditioned medium from cultured MSCs. Recently, extracellular vesicles (microvesicles and exosomes) have been recognised as carrying vehicles of these factors and micro RNAs also responsible for the MSC paracrine effect [271].

The immunomodulatory effects of MSCs were observed through inhibition of effector T-cell activation and proliferation, reduction of the number of neutrophils binding to vascular endothelial cell or limitation of mast cell degranulation and secretion of their pro-inflammatory cytokines [272–274]. MSCs have also been responsible for modifying the immune response of macrophages from the pro-inflammatory M1 phenotype to a more regenerative, pro-angiogenic, anti-inflammatory M2 phenotype [275]. This has motivated the development of intravenous injections of MSCs for modulation of the immune response in conditions as graft-versus-host disease. These cells also secrete factors (e.g. vascular endothelial growth factor (VEGF), FGF2, metalloprotease 1, TGF-α, EGF, NGF) which promote angiogenesis and impact on endothelial cell survival, proliferation and migration; and reduce fibrosis during tissue regeneration [268].

In tumour environments, MSCs have demonstrated a dual contribution to tumour progression and suppression. These cells migrate to damaged tissue, sites of inflammation and irradiated tumours following a gradient of chemo-attractants. Once onsite, they can integrate the microenvironment, differentiating into tumour-associated fibroblast and supporting the tumour progression [276]. Conversely, it can also inhibit the immune response through direct interaction with T-lymphocytes with cell-cell contacts established by surface ligands [277]. Given their homing ability, paracrine effects and capacity to be genetically modified, MSCs are good targets to be genetically engineered or primed with drugs or nanoparticles to exhibit anticancer activity. Transducing MSCs to express TNF-Related Apoptosis Inducing Ligand (TRAIL) have counteracted tumour progression in two orthotopic models of Ewing sarcoma through caspase activation [278]. Moreover, MSCs demonstrated to be promising vectors for delivery of cisplatin, a common anticancer drug. Priming them with this drug had no adverse effects on cell morphology, adhesion, viability or differentiation potential [279].

However, to safely deliver MSCs, maintain their viability and paracrine function *in vitro* and *in vivo*, preserving their regenerative or therapeutic potential, 3D cell encapsulation has been widely investigated. It provides a 3D biomimetic environment which parameters such as, composition, structure, stiffness and porosity can direct cellular fate. For instance, co-encapsulation of MSC and human chondrocytes in a bio-printed nanofibrillated cellulose and alginate hydrogel were implanted *in vivo* with stem cells enhancing chondrocyte proliferation and formation of cartilage clusters [280]. Moreover, arginylglycylaspartic acid (RGD)-modified alginate encapsulated MSCs transplanted to infarcted myocardium induced angiogenesis, arrested remodelling of left ventricular and reduced infarct area [281]. Studies have shown that these microcapsules maintain their integrity for several months when transplanted *in vivo* and thus, enabling long-term factor release essential for tissue repair and vascularisation processes [282,283]. Multicellular encapsulated MSCs spheroids have also demonstrated superior retention *in vivo* and responded to inflammatory cytokines [284].

To achieve high cellular expansion and/or improved functionality, bioreactors could be applied to culture encapsulated MSCs for clinical expansion or *in vitro* models. The tight regulation of the microenvironment parameters in a bioreactor (e.g. temperature, pH, gas supply) offers the possibility of extending MSC self-renewal and multipotency capacity, influence secretome and result in improved therapeutic effect [285,286]. Perfusion systems have increased cell functionality of populations whose cell numbers decreased over time [287]. Additionally, an active hydrodynamic culture can induce differentiation cues important for preconditioning cells and accelerate differentiation protocols [288].

4.2.2. Hypothesis and aims

It was hypothesised that the dynamic environment promoted by fluidisation would sustain long-term cell culture of hydrogel encapsulated human primary multipotent stem cells (MSCs) that could be used for cell therapy or tissue engineering. Therefore, the aim was to culture alginate encapsulated MSCs in parallel in the sFBB and conventional static cultures assessing their performance and functionality and, test the

versatility of the sFBB as a device for *in vitro* culture suitable for any cell types that could benefit from a perfusion environment.

4.2.3. Materials and methods

Specific methods followed in this sub-chapter are referred in detail in Chapter 2 and include: *2.9. Cell viability of encapsulated cells, 2.10. Cell number of encapsulated cells, 2.11. Glucose consumption, 2.12. ATP assay, 2.15. Gene expression, 2.7 Sirius red histochemistry staining for hybrid alginate/collagen I beads, 2.18 Immunofluorescence staining, 2.19. Releasing encapsulated cells from alginate beads and 2.20 Differentiation of de-capsulated MSCs.*

4.2.4. Results

4.2.4.1. Dynamic culture of alginate encapsulated bone marrow-derived human multipotent stromal cells

4.2.4.1.1. Cell proliferation and viability

Bone marrow-derived human multipotent stromal cells (MSCs) were encapsulated as single cells in alginate beads and cultured under dynamic and static conditions, respectively in the sFBB and conventional tissue culture flasks, for a maximum of 21 days. Independent of the system used, cells did not spread to their monolayer spindle morphology, remained round and declined in number throughout the culture period. This proved they did not proliferate in these conditions, probably due to the absence of adhesion cues in the hydrogel.

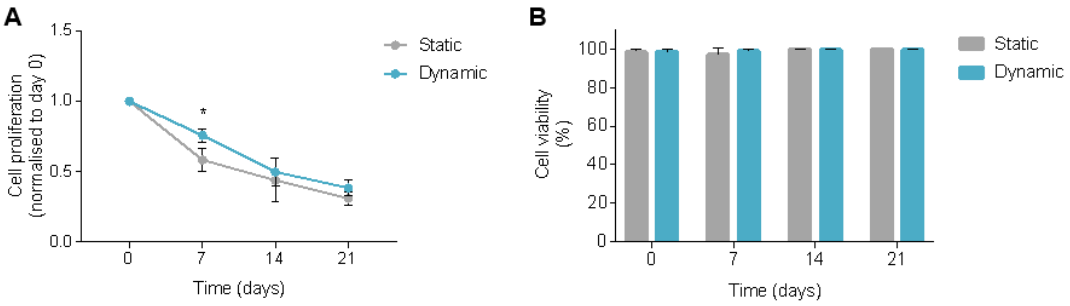

Figure 34 **-** Biological performance of alginate encapsulated MSCs in dynamic (sFBB) compared to conventional static culture. Cell proliferation curves (A) and corresponding viabilities (B) throughout 21 days of culture. Cell proliferation data was normalised to the initially seeded cell number on day 0. Data presented are average ± SD (n = 3). Statistical analysis was assessed by multiple Student's t-test using the Holm-Sidak method correction. * $p < 0.05$.

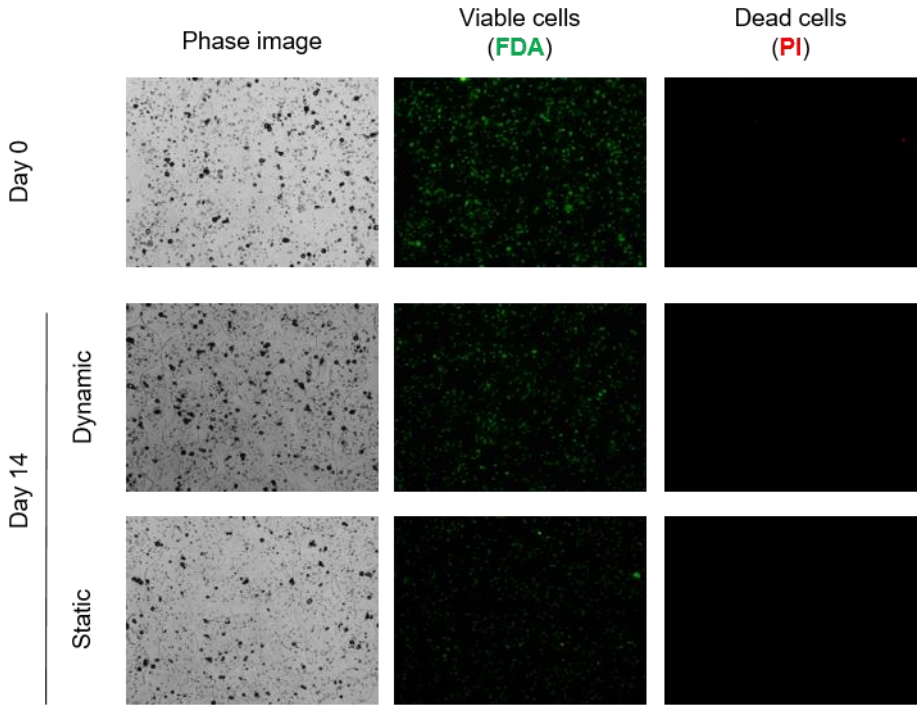

Figure 35 **-** Alginate encapsulated MSCs cultured in dynamic and static culture for 21 days. Captured images of cell beads from the day 0 and 14 of culture to observe their morphology (phase image) and determine viability (live cells stained with FDA and dead cells with PI). Images captured at 4x magnification.

However, cell loss in the sFBB was decelerated with a 26% decrease in the number of nuclei on day 7 compared to 42% in static ($p < 0.05$) (Figure 34 A). The discrepancy between dynamic and static tapered by the end of the 21 days, although the dynamic

environment displayed a minimal superiority in final cell density. Conversely, this loss was not reflected in the estimation of cell viability in either of the two cell conditions, with viabilities remaining above 97% throughout the 21 days (Figure 34 B). The microscope images indicated that there was not an increase in PI intensity, but the density of FDA-stained nuclei was reduced at later time points (Figure 35), consistent with the diminished number of cells and suggesting that the majority of dead cells (possibly already disintegrated) did not stain for either of the dyes and thus, not contributing to the calculation method.

After 21 days, MSCs in static and dynamic culture were released from the hydrogel (de-encapsulated), seeded on conventional tissue culture plates and left in culture for an additional 8 days. De-encapsulated cells attached and spread onto the surface of the plate, displaying their characteristic fibroblast-like morphology (Figure 36). This was a preliminary indication that neither the encapsulation nor the de-encapsulation method damaged the cells irreversibly. Also, there were no differences in cell attachment nor morphology between MSCs cultured in static or dynamic environments. After 8 days, microscopic observation highlighted that cells which had been in static culture were more elongated and larger in area than the ones from dynamic culture. The latter also formed a denser monolayer corroborated by preliminary cell numbers: 2.28 $x10^5$ vs. 1.54$x10^5$ cells/mL.

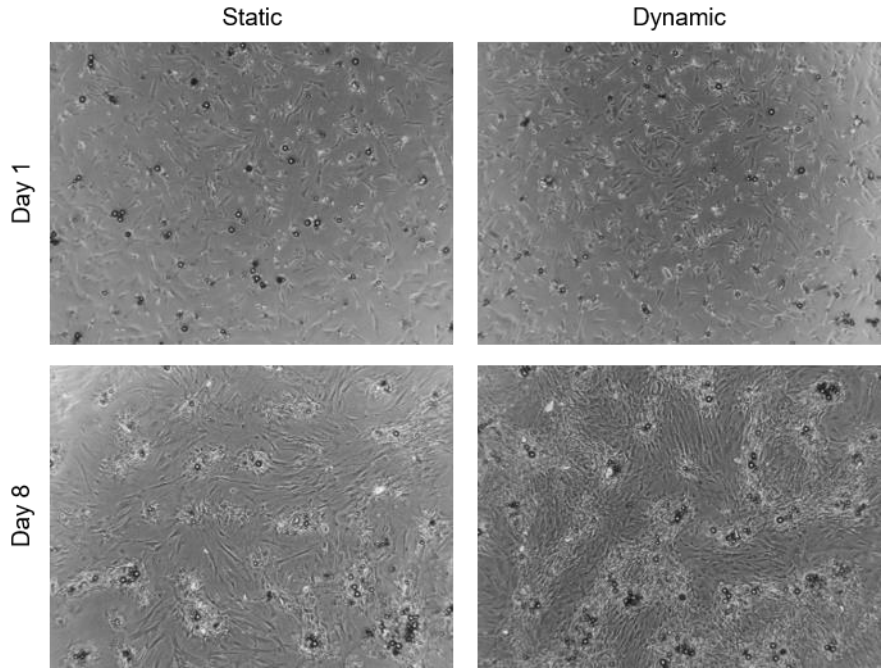

Figure 36 - De-encapsulation and reattachment of day 14 alginate encapsulated MSCs cultured in dynamic (sFBB) and static conditions. Release of MSCs from the alginate beads through chelation with 16 mM EDTA, seeded on a tissue culture plate and left in culture for an additional 8 days (day 8). Images captured at 10x magnification.

Similarly, to HepG2 spheroids, the ATP content of the encapsulated MSCs did not differ between dynamic and static cultures (Figure 37). It peaked on day 14 to 25.3 and 30.2 nmol/million cells, respectively, dropping on day 21 to levels equivalent to day 7 (7.5 vs 7.2 nmol/million cells). This maximum at day 14 could be related to a metabolic activation for cell survival mode.

Collectively, these data demonstrated that despite the absence of biochemical adhesion points, MSCs encapsulated in alginate beads were metabolically active up to 21 days. The hydrodynamic mixing in the sFBB further supported the maintenance of the cells by decelerating the cell loss process.

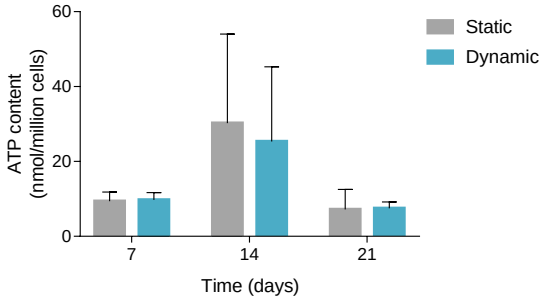

Figure 37 - ATP content in alginate encapsulated MSCs in dynamic (sFBB) and static culture. Analysis performed on days 7, 14 and 21 normalised to million cells. Data presented are average ± SD (n = 3).

4.2.4.1.2. Gene expression of alginate encapsulated MSCs

To determine the influence of the dynamic culture on the performance of MSCs, gene expression was analysed including genes related to the undifferentiated phenotype (NANOG and INHBA) as well as osteogenic (BMP2 and ALP), chondrogenic (AGN and Collagen 2), adipogenic (PPARγ2) and neurogenic (MAP2) lineages. Encapsulated MSCs exhibited marked upregulation of undifferentiated markers during the 21 days of culture compared to the control sample (MSC monolayer) (Figure 38). On day 7 both NANOG and INHBA expressions were more prominent in cells from the dynamic environment, approaching levels in the static condition for the remaining days of culture. NANOG attained its maximum by day 14 (7-fold) whereas INHBA exhibited a stable expression of approximately 2-fold compared to the control.

Survivin, a master regulator of MSCs functions and promoter of proliferation, displayed a diminished expression as culture progressed although less accentuated in dynamic condition, especially on day 7 where its expression was comparable to MSC monolayer. In addition, Cyclin D1 was markedly upregulated in static and dynamic conditions since day 7. The expression was even higher in static, but this difference was suppressed by day 21. Hypoxia was assessed by HIF-1α expression which remained downregulated in static, whereas in dynamic a marked downregulation was only observed on day 21. Its effector, VEGF, had an overall upregulated expression which declined over time both in static and dynamic cultures, particularly in static on day 14.

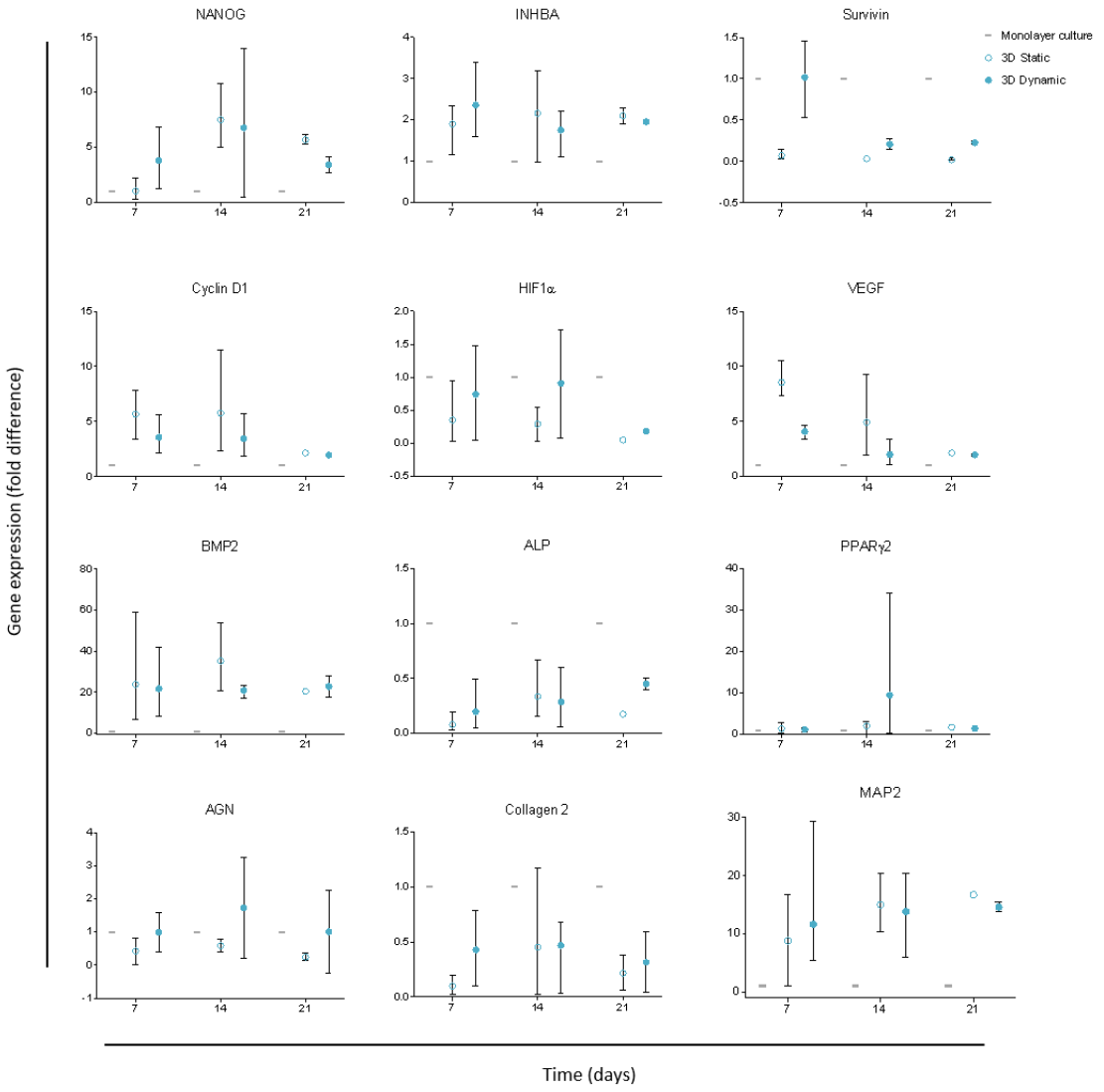

Figure 38 **-** Gene expression of alginate encapsulated MSCs cultured in dynamic and static conditions for 21 days. Quantification of undifferentiated (NANOG and INHBA), cell function (Survivin), proliferation (Cyclin D1), hypoxia (HIF1α and VEGF), differentiation (osteogenesis: BMP2 and ALP, adipogenesis: PPARγ2, chondrogenesis: AGN and Collagen 2, neurogenesis: MAP2) markers in MSCs in 3D dynamic and static culture relative to conventional 2D culture (monolayer) on days 7, 14 and 21. Calculation followed $2^{-\Delta\Delta C_t}$ method using GAPDH as endogenous control. Data presented are average ± range (n = 2).

Regarding differentiation stimuli, the markers highly upregulated in encapsulated MSCs were BPM2 and MAP2, without any significant differences between static and dynamic conditions. Their expression was also approximately consistent throughout the 21 days. All the remaining genes were either downregulated or comparable to the control MSC monolayer. These results could suggest a predominance of the undifferentiated phenotype in alginate encapsulated MSCs, although the

microenvironment and biophysical characteristics of the hydrogel could imprint some information on the cells upregulating genes of specific lineages.

4.2.4.1.3. Differentiation potential of alginate encapsulated MSCs

To validate the differentiation potential of these encapsulated MSCs, on day 14 samples were collected, de-encapsulated, seeded on a plate and subjected to differentiation towards the chondrogenic and adipogenic lineages. Moreover, alginate beads from static and dynamic conditions were also cultured in differentiation media.

Unfortunately, it was not possible for those from dynamic to be differentiated in the sFBB due to the volume of differentiation medium required. They were then sampled and seeded onto a plate. Other lineages were not induced due to time constraints.

De-encapsulated cells attached, spread and acquired the fibroblast-like morphology (Figure 39). 24 h after de-encapsulation, attached cells and alginate encapsulated cells were placed in differentiation medium (both chondrogenic and adipogenic) and alterations in cell morphology were first noticeable 4 days later. For chondrogenesis, there was a cohesive monolayer of round-shaped cells interspersed with others more elongated; while in adipogenesis cells also lost their elongated shape but were not as round as those in chondrogenic medium. At the end of the differentiation period, 14 days later, cells subjected to chondrogenesis were round, had an increased area and stained positive for Alcian Blue validating the lineage. In adipogenesis, cells were larger in area with an irregular shape and contained lipid droplets in the cytoplasm; the Oil Red O staining verified the phenotype. Of note, all images contain some debris from the de-encapsulation process that was not possible to remove.

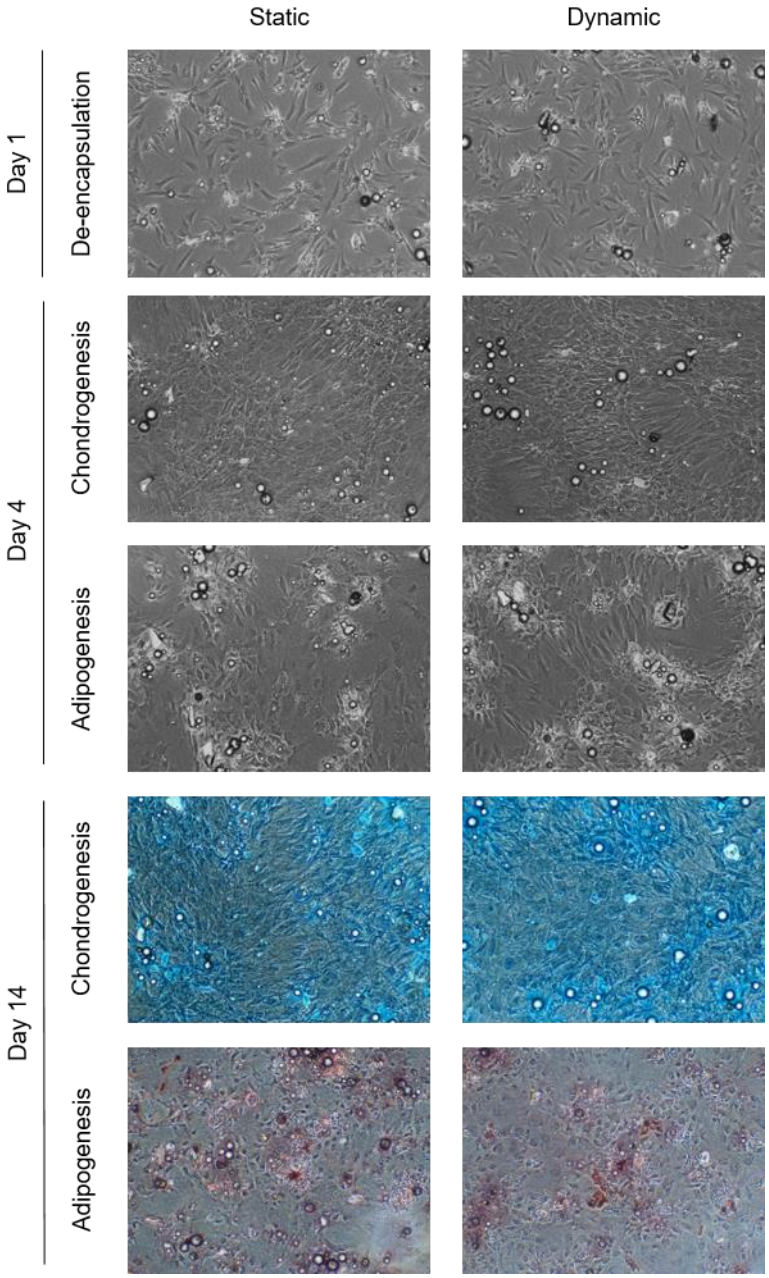

Figure 39 - Differentiation of de-encapsulated MSCs previously cultured in dynamic and static conditions. Alginate encapsulated MSCs cultured for 14 days were de-encapsulated, seeded on a tissue culture plate and left to attach for 24 h (day 1). Then, chondrogenesis and adipogenesis were induced through differentiation medium for an additional 14 days. Corroboration of the phenotype was made through histological staining of Alcian Blue (chondrogenesis) and Oil Red O (adipogenesis). Images were captured at 10x magnification.

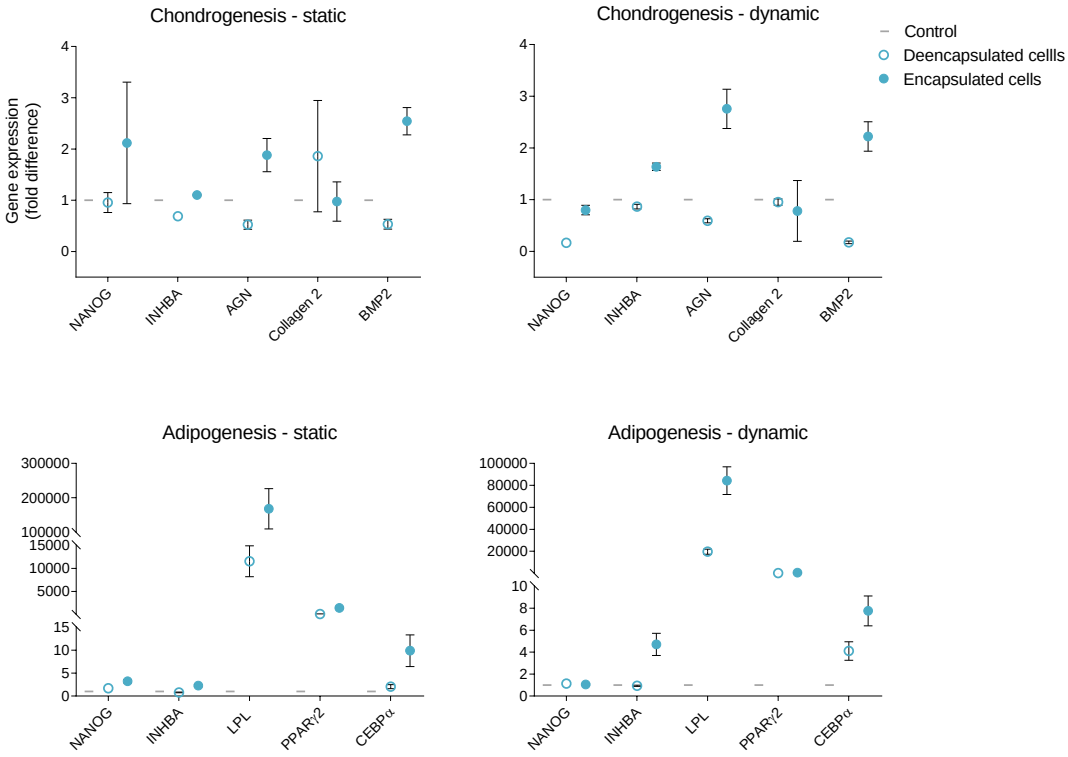

Figure 40 - Gene expression of differentiated encapsulated and de-encapsulated MSCs previously cultured in dynamic and static conditions. After 14 days of differentiation, expression of undifferentiated (NANOG and INHBA), chondrogenic (AGN and Collagen 2) and adipogenic (LPL, PPARγ2 and CEBPα) were assessed in encapsulated and de-encapsulated MSCs relative to day 14 alginate encapsulated MSCs cultured in dynamic or static conditions (control), from where they were respectively sampled. Calculation followed $2^{-\Delta\Delta C_t}$ method using GAPDH as the endogenous control. Data presented are average ± range (n = 1).

Gene expression was also performed to corroborate the previous results and verify the differentiation process of the encapsulated cells. Interestingly, de-encapsulated cells did not exhibit upregulation of chondrogenesis markers AGN and Collagen 2, except for Collagen 2 in MSCs de-encapsulated from alginate beads cultured in static conditions (Figure **40**, chondrogenesis – static and dynamic), even though the change in morphology and positive staining validated the lineage. Conversely, differentiated alginate encapsulated MSCs had an increased expression of AGN and BMP2.

As for adipogenesis, de-encapsulated MSCs displayed a marked upregulation of LPL and PPARγ2 genes as well as adipogenesis transcription factor C/EBPα without any accentuated differences between those which came from the static or dynamic culture (Figure **40**, adipogenesis – static and dynamic). Similarly, to chondrogenesis, encapsulated MSCs had higher expressions of these markers compared to de-

encapsulated cells, with the static demonstrating a distinct upregulation relative to dynamic (168000 vs. 84000-fold for LPL and 1444 to 452-fold for PPARγ2, respectively). This upregulation of lineage markers in alginate encapsulated cells relative to de-encapsulated cells did not have an obvious explanation. Moreover, differentiation under dynamic conditions would be valuable to highlight whether the hydrodynamic mixing would benefit the process.

Overall, MSCs were successfully released from the hydrogel bead and positively differentiated into two distinct lineages with minimal influence of the culture method to which they had been previously exposed. Nonetheless, further replicates are needed to corroborate these results.

4.2.4.2. Co-culture of alginate encapsulated MSCs and HepG2 cells

To understand the trophic potential of MSCs, a co-culture model with HepG2 cells was established. Cell beads were cultured in a 1:1 cell density ratio in 6-well plates with MSC beads at the bottom of the well and HepG2 cell beads in a cell strainer above. A preliminary test in monolayer verified that the two cell types did not interact directly, with MSCs surrounding colonies of HepG2 cells (Figure 41). The albumin stained cells constitute HepG2 cells surrounded by MSC nuclei (Hoechst-stained). Based on these results, it was determined that the best co-culture model for alginate encapsulated cells using these two cell types would be to encapsulate them separately and assess their paracrine effect on each other. This would also validate the potential use of alginate encapsulated MSCs as a delivery vector.

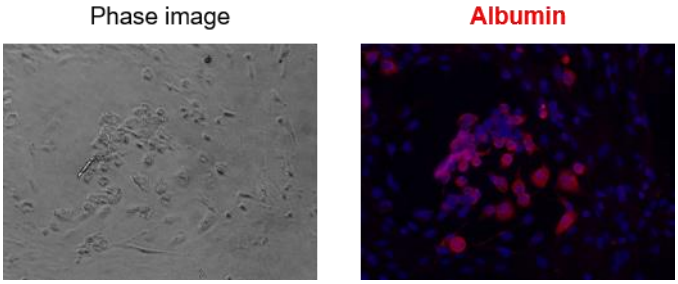

Figure 41 **-** Co-culture of MSCs and HepG2 cells in monolayer. Phase image and immunofluorescence staining of albumin positive cells (red) and nuclei (blue) highlighting the HepG2 cells in a colony form surrounded by MSCs. Images were capture at 10x magnification.

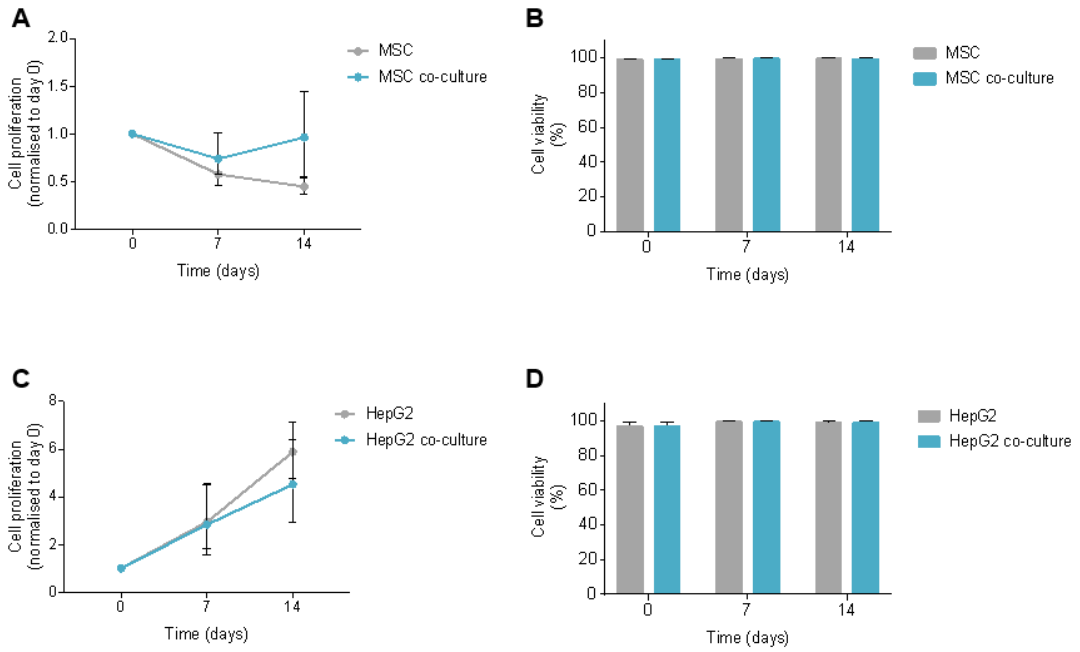

Figure 42 **-** Biological performance of alginate encapsulated MSCs in co-culture with alginate encapsulated HepG2 cells. Cell proliferation curves of MSCs (A) and HepG2 cells (C) and corresponding viabilities (mean and standard deviation (B and C, respectively) throughout 14 days of culture. Cell proliferation data was normalised to the initially seeded cell number on day 0. Data presented are average ± range (n = 2).

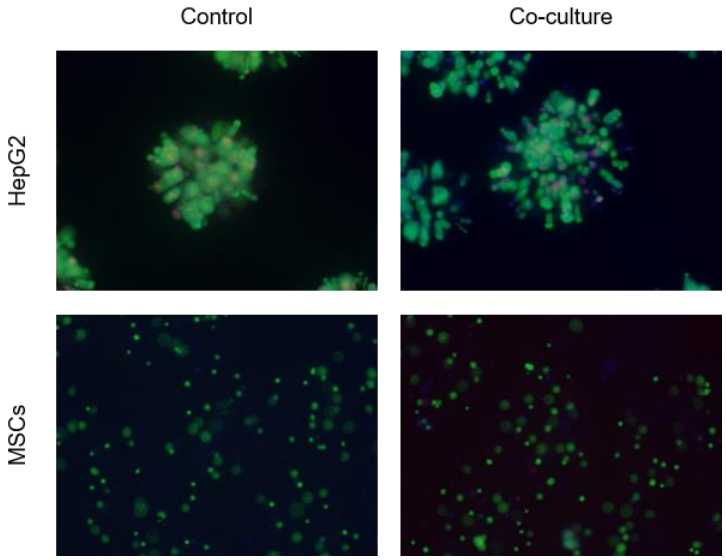

Figure 43 **-** Viability of alginate encapsulated MSCs co-cultured with alginate encapsulated HepG2 cells. Captured images of cell beads from day 14 of culture to determine viability of encapsulated HepG2 alone and in co-culture and, encapsulated MSCs alone and in co-culture. Live cells stained with FDA (green), dead cells with PI (red) and nuclei stained with Hoechst dye (blue). Images captured at 10x magnification.

Alginate encapsulated MSCs were co-cultured with alginate encapsulated HepG2 cells in a 1:1 cell density ratio for 14 days in static conditions. Total nuclei count demonstrated that MSCs in co-culture had a decelerated cell loss comparatively to encapsulated MSCs alone (26% *vs.* 42% loss, respectively, on day 7), even recovering to their initial cell number by day 14 (Figure 42 A). As for HepG2, they continued to proliferate throughout the 14 days, although at a slower rate between days 7 and 14 for cells in co-culture. Final cell density for those in co-culture was 4.5-fold over the initial number, whereas for the control (encapsulated HepG2 alone) it was 5.9-fold (Figure 42 C).

Cell viability was not affected and did not reflect the alterations verified in cell numbers (Figure 43), similarly to the results described in *section 4.2.4.1.* Both HepG2 cells and MSCs had viabilities above 98% throughout the culture period (Figure 42 B and D).

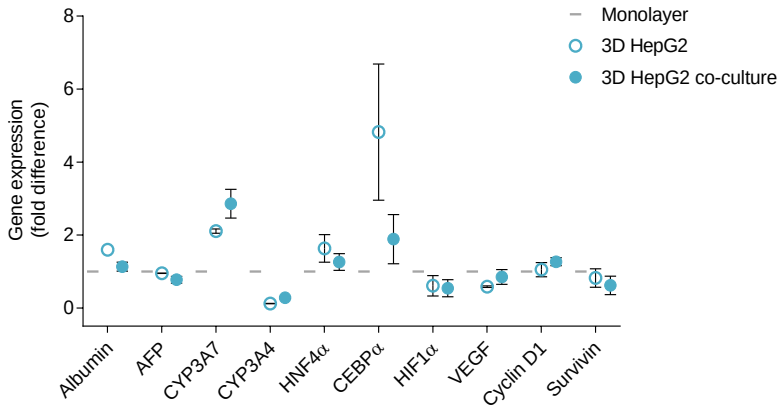

Figure 44 - Gene expression of day 14 alginate encapsulated HepG2 cells co-cultured with alginate encapsulated MSCs. Expression of hepatic and hypoxia markers in alginate encapsulated HepG2 cells cultured alone (3D HepG2) or in co-culture with MSCs (3D HepG2 co-culture) relative to 2D monolayer culture (control). Calculation followed $2^{-\Delta\Delta C_t}$ method using GAPDH as the endogenous control. Data presented are average ± range (n = 1)

Paracrine effects of this co-culture system were investigated at the gene expression level. The set of genes screened for assessment of HepG2 and MSC performance were the same as in previous *sections 4.1* and *4.2.4.1.2*, respectively. There were no significant differences in gene expression between encapsulated HepG2 and those in co-culture, except for the reduced C/EBPα in co-culture (Figure 44). Conversely, the effects of HepG2 cells on MSCs were more significant: BMP2 and MAP2 were markedly reduced in co-cultured MSCs compared to MSCs alone; HIF-1α expression also decreased on day

14, while for the same time point Survivin was highly upregulated (Figure 45). Even though these results were representative of only one experiment, there was evidence that HepG2 cells modulated alginate encapsulated MSCs through paracrine effects in the long term.

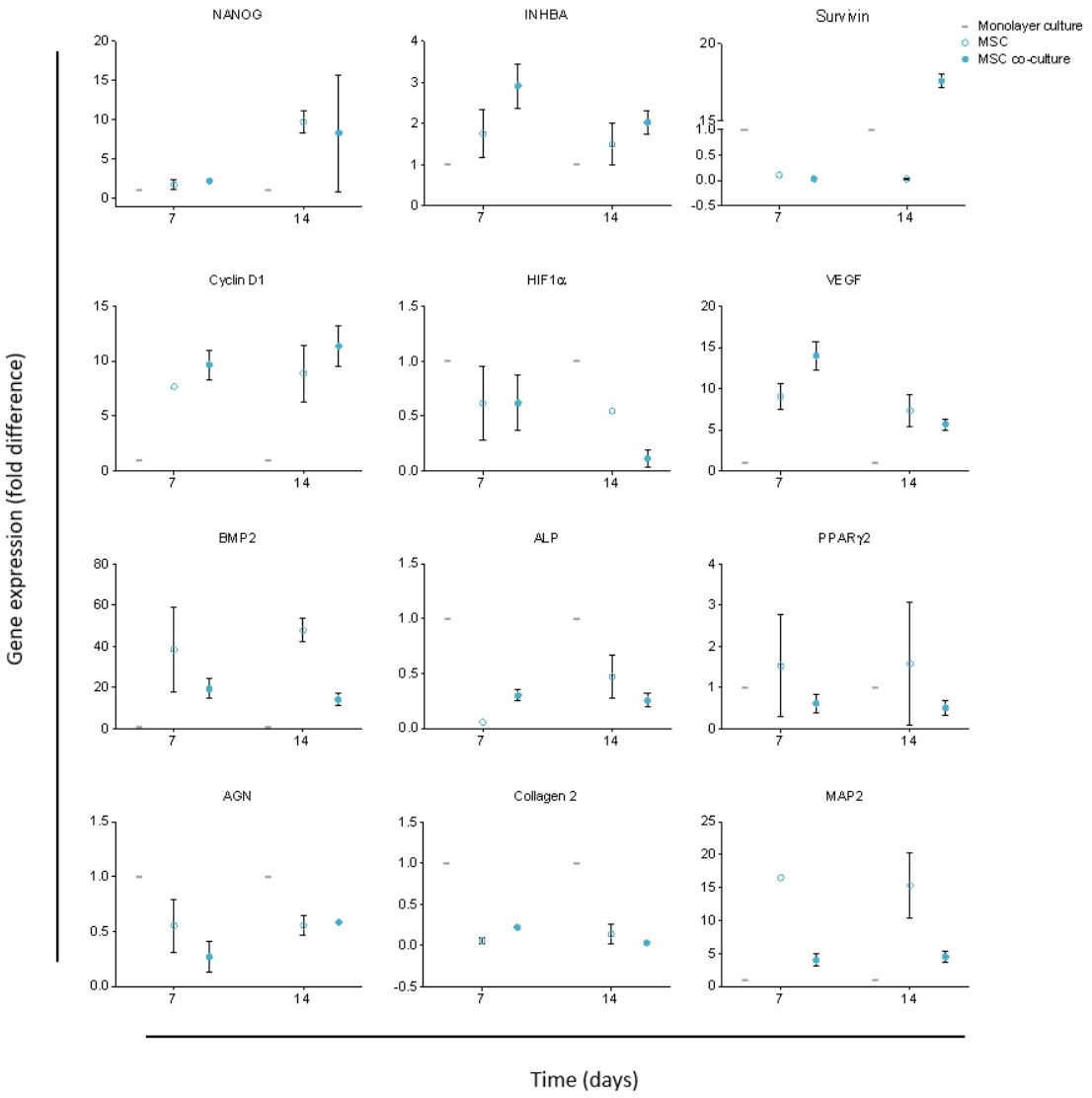

Figure 45 **-** Gene expression of alginate encapsulated MSCs co-cultured with alginate encapsulated HepG2. Expression of undifferentiated (NANOG and INHBA), cell function (Survivin), proliferation (Cyclin D1), hypoxia (HIF1α and VEGF), differentiation (osteogenesis: BMP2 and ALP, adipogenesis: PPARγ2, chondrogenesis: AGN and Collagen 2, neurogenesis: MAP2) markers in alginate encapsulated MSCs cultured alone (3D MSC) or in co-culture with HepG2 (3D MSC co-culture) relative to 2D monolayer culture (control) on days 7 and 14. Calculation followed $2^{-\Delta\Delta C_t}$ method using GAPDH as the endogenous control. Data presented are average ± range (n = 1).

Unfortunately, due to time constraints, it was not possible to transfer this model to the sFBB to investigate the impact of dynamic culture on the system and validate the prototype as a co-culture device.

4.2.4.3. Hydrogel manipulation for cell performance optimisation of encapsulated MSCs

To improve MSCs performance and adjust the microenvironment created by encapsulation, the characteristics of the hydrogel were manipulated. The stiffness could be adjusted by crosslinking the alginate with $CaCl_2$ solution of different concentrations, since increasing concentrations increases the stiffness, and thus, solutions of 50 mM and 200 mM (the concentration used in all the previous studies) were tested. Also, a biochemical adhesion cue was introduced by producing a hybrid hydrogel of alginate and collagen I in a 1:1 volume ratio.

A preliminary study on the influence of these parameters on MSCs was conducted in hydrogel discs produced in tissue culture plates (Figure 46). The morphology of MSCs was not altered by the $CaCl_2$ concentration and inherent stiffness. Cells remained individually separated and round, although a higher number of dark cells in the disc crosslinked with 200 mM $CaCl_2$ were observed. These dark cells did not stain positive for FDA or PI suggesting they had already disintegrated. Another observation was that a few MSCs were able to escape the softer gel easier than the stiffer one, adhering to the bottom of the plate and proliferating.

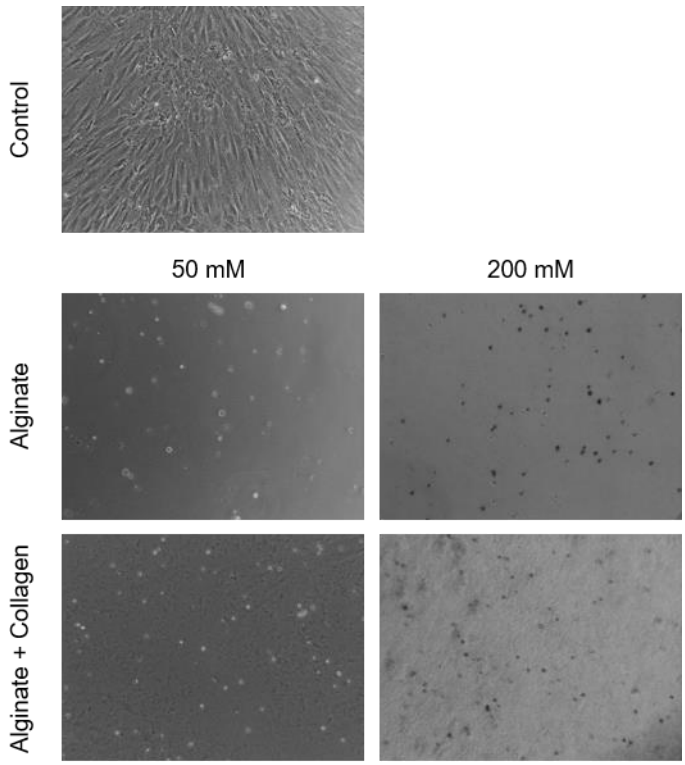

Figure 46 - Modifying alginate hydrogel for encapsulated MSC culture. Crosslinking Na-alginate discs with 50 and 200 mM CaCl2 solution and introducing Collagen I to create a hybrid hydrogel (alginate + collagen) with biochemical adhesion cues. Images captures after 14 days of culture at 10x magnification.

When introducing collagen I, there was not a drastic change in morphology nor the number of disintegrated cells. However, it was noticeable that after 14 days a few MSCs were able to align and elongate along collagen fibres (Figure 47 A). Because crosslinking the alginate with 50 mM $CaCl_2$ would not produce individual spherical beads using the current method, MSCs encapsulation in hybrid alginate and collagen I (alginate + collagen) beads was only attempted crosslinking the alginate with 200 mM $CaCl_2$ solution, followed by the collagen in an incubation step of 30 min at 37°C. This generated a hydrogel with a final alginate percentage of 0.67% (w/v) instead of the previous 1% (w/v). Unfortunately, due to experimental constraints of non-adjusted flow rate for a different hydrogel mix composition, the produced beads had irregular shapes and sizes demonstrating that the protocol required further optimisation. Nonetheless, MSCs were encapsulated and beads contained collagen fibres as validated by a Sirius Red staining (Figure 47 B).

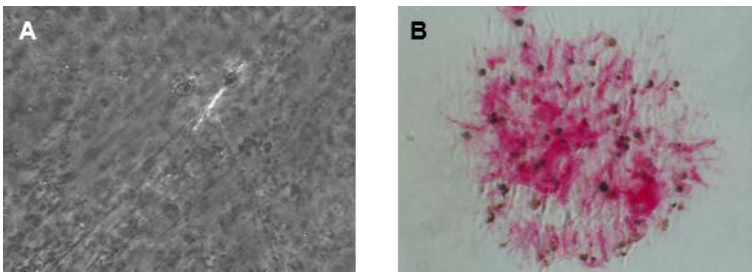

Figure 47 **-** Collagen distribution in hybrid alginate and collagen I hydrogel. (A) MSC cell encapsulated in alginate + collagen disc spread along collagen fibres. Image captured at 20x magnification. (B) Sirius red staining of alginate + collagen bead to verify the distribution of collagen within the gel. Cell nuclei were stained with haematoxylin. Image captured at 10x magnification.

Alginate + collagen encapsulated MSCs were cultured in static for 21 days using alginate encapsulated MSCs as control. The biochemical adhesion cue did not prevent cell loss nor decelerated it with cell numbers diminishing in a similar rate to the control to a final loss of 75% (Figure 48 A). As observed previously, viability did not reflect this decrease in cell numbers since the remaining cells were highly viable (above 97%). The only significant difference was on day 0 with alginate MSCs being 96% viable and cells in alginate + collagen beads 86% (Figure 48 B). This result demonstrated that the production of the hybrid beads induced more damage to the cells, further highlighting the need for method optimisation. Moreover, the images captured for viability quantification highlighted more elongated cells in alginate + collagen beads on day 21 (Figure 49), consistent with observations from the hydrogel discs.

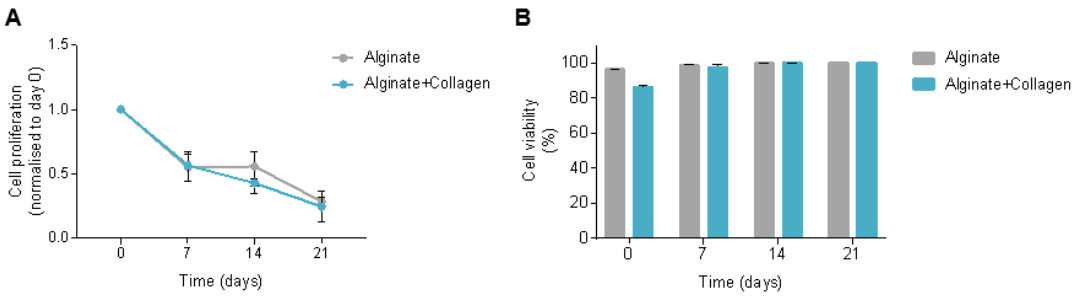

Figure 48 **-** Biological performance of MSCs encapsulated in alginate and alginate and collagen I beads. Cell proliferation curves (A) and corresponding viabilities (B) throughout 21 days of culture. Cell proliferation data was normalised to the initially seeded cell number on day 0. Data presented are average ± range (n = 1).

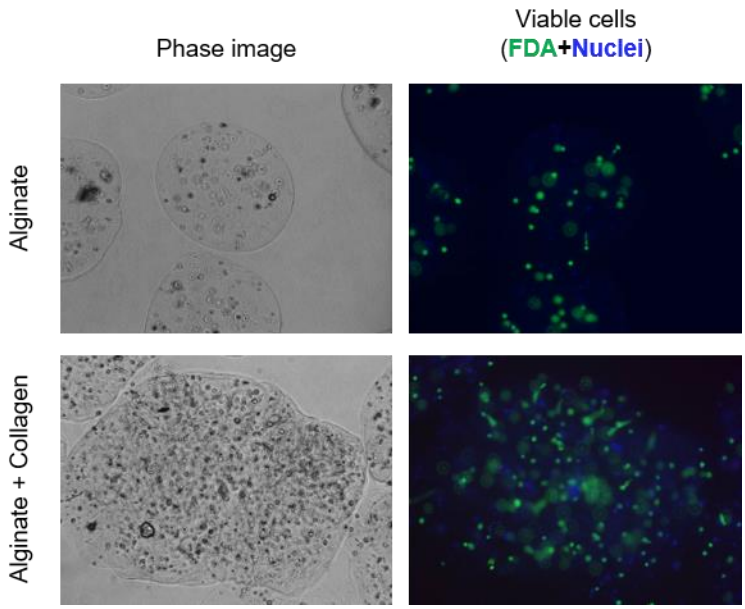

Figure 49 - Viability of MSCs encapsulated in alginate and alginate and collagen I beads. Captured images of cell beads from day 21 of culture to determine viability of encapsulated cells and highlight elongated shape of some MSCs in alginate + collagen beads. Live cells stained with FDA (green), dead cells with PI (red) and nuclei stained with Hoechst dye (blue). Images captured at 10x magnification.

ATP content of MSCs encapsulated in these hybrid beads was also assessed. Results indicated that cells were metabolically active displaying a stable ATP content throughout the 21 days, with levels on day 7 higher than the control (14.1 vs 7.5 nmol/million cells, respectively) (Figure 50). However, few conclusions could be taken since this only corresponded to one experimental replicate.

Collectively, these data suggested that modification of the hydrogel by reducing its stiffness and including biochemical cues might improve the performance of encapsulated MSCs, although the protocol requires extensive optimisation. Once again due to time constraints, it was not possible to reproduce this experiment in the sFBB.

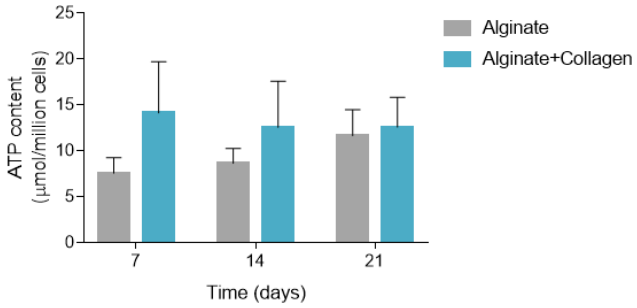

Figure 50 - ATP content in MSCs encapsulated in alginate and alginate and collagen I beads. Analysis performed on days 7, 14 and 21 normalised to million cells. Data presented are average ± range (n = 1).

4.2.5. Discussion

Alginate encapsulated single multipotent stromal cells were maintained metabolically active in culture for 21 days. Encapsulation of single cells has demonstrated to harbour a reduced number of apoptotic and dead cells compared with monolayer and MSC spheroids (encapsulated and non-encapsulated) [289]. However, in this study there was a continuous decline in cell number which was decelerated under the hydrodynamic conditions of the sFBB, highlighting that the dynamic environment contributes in part to sustain primary stem cells in culture. A similar profile had been observed in proteosteoblasts seeded on a polyurethane scaffold where dynamic culture decelerated the cell loss process in comparison to conventional static conditions, due to a more efficient chemotransportation through the porous scaffold [290].

This progressive decline in cell number is likely triggered by programmed cell death, specifically anoikis due to the absence of matrix support and cell adhesion. Although activation of specific markers (e.g. caspase-3, focal adhesion kinase, vinculin, integrin-linked kinase) needs to be investigated to support this hypothesis [291,292], all subsequent results and cellular behaviour could potentially be associated and characteristic of a MSC apoptotic phenotype.

Literature has reported several studies on the proliferation of MSCs under dynamic conditions [293,294]. Vessels such as spinner flasks or rotating cell culture system were able to form MSC spheroids which remained viable and proliferated during 7 days [295]. When using hydrogel systems, Tang et al. demonstrated a higher proliferation of 3D

encapsulated MSCs in the dynamic environment compared to the 3D static and monolayer controls [296]. However, unlike here, they used a collagen scaffold which enabled integrin-based cell adhesion.

Other hydrogel systems which induced MSC proliferation resorted to RGD peptide-modified alginate, gelatin-chitosan-polyethene glycol (PEG) hybrid polymer, fibrin gel and further combinations of these biomaterials to promote interactions between cells and the microenvironment that lead to activation of signalling cascades associated with survival and proliferation [297–301]. Maintenance of cell number and viability of encapsulated MSCs has also been achieved in thiol-modified hyaluronic acid and PEG diacrylate hydrogel where cells interact with the polymer through surface markers CD44 and CD168 and not integrin-based bonds [302].

Besides biochemical signals, mechanical properties of hydrogel impact cell fate. Lee at al. demonstrated that faster relaxing hydrogels induced chondrocytes to form an interconnected cartilage matrix, whereas for slower relaxation there was an upregulation of genes related to cartilage degradation and cell death [303]. Moreover, Goldshmid et al. described that MSCs proliferation was favoured in 3D hydrogels with lower storage modulus (G′ = 100–250 Pa) when compared to higher modulus materials (G′ = 500–2000 Pa) [304]. These mechanical properties (e.g. stiffness, porosity) may also enable more cell-cell contacts which boost MSC viability and their paracrine function [305,306]. Higher initial cell loads could produce a similar effect by enabling more interactions between neighbouring cells as observed through the sustained and controlled erythropoietin secretion by alginate encapsulated MSCs initially seeded at 20 million cells/mL [307].

These findings reinforce the notion that maintaining the cell number or inducing proliferation in hydrogel encapsulated MSCs will only be achieved in more biomimetic conditions, through modification of the hydrogel mechanical and biochemical characteristics, providing a matrix for attachment and interactions that could suppress the potential anoikis process. Although not successfully produced in this study, alginate and collagen I hybrid hydrogels have effectively maintained cells during the 21 days of culture and, even demonstrating the potential for adhesion. Therefore, optimisation of the hybrid hydrogel manufacturing method shows promising results for the present system. Cell viability, proliferation and performance would be further enhanced through culture under dynamic conditions.

Other evidence supporting the beneficial impact of the hydrodynamic environment of the sFBB, particularly during the first 7 days of culture, was the upregulation of stemness markers, NANOG and INHBA, and the preserved expression of Survivin. NANOG and INHBA have been extensively associated with the maintenance of self-renewal and potency of stem cells, therefore their high expression verified the undifferentiated phenotype [262,264,308]. Contrary to Pitrone et al. study which states NANOG downregulation is associated to diminished adipose stem cell proliferation and differentiation rate, these results evidenced a different mechanism between the upregulation of NANOG and the decline in cell number [308]. Furthermore, Singh et al. proved that downregulation or inhibition of Survivin in MSCs was directly related to a decrease in cell number, suppression of migration capacity to wound site and reduced ability to differentiate into the 3 characteristic lineages [309]. In agreement with these findings, Survivin expression on day 7 under dynamic conditions supported the decelerated cell loss and potentially constituted a sign of function preservation.

Additionally, after 21 days in dynamic culture, MSCs released from alginate beads maintained their spindle morphology and appeared to proliferate, while those from static culture displayed an enlarged area morphology similar to senescent cells [310]. β-galactosidase staining could have verified the senescence phenotype. These are very preliminary results and more replicates are essential to draw definitive conclusions.

However, there are evidences supporting the referred results since it has been reported that MSCs cultured in non-adherent conditions can be successfully reseeded, reacquiring adherent growth and differentiating into the 3 characteristic lineages independently of the increase in apoptotic cells in the cell population [311].

In the current system, MSCs phenotype and differentiation potential were not governed by the hydrodynamic mixing but rather by the hydrogel microenvironment, since no significant differences in the gene expression were observed between dynamic and static conditions. The absence of biochemical cues in the hydrogel probably overrides any of the other external signals. Nonetheless, in general, softer hydrogels have been linked to directing MSC differentiation towards neurogenic and adipogenic lineages, while stiffer gels appear to favour commitment to osteogenesis and chondrogenesis, although it is all subjected to the hydrogel composition and range of stiffness tested [312–315]. Similarly and interconnected with the hydrogel mechanical properties, the biophysical characteristics

of the secreted extracellular matrix (ECM) also influence stem cell differentiation [316]. Ferreira et al. have demonstrated that MSCs assembled an extensive proteinaceous pericellular matrix in hydrogels inefficiently crosslinked directing them towards adipogenesis, whereas for those efficiently crosslinked there was degradation of the hydrogel matrix promoting osteogenesis [302].

Herein, gene expression analysis indicated an upregulation of BMP2 and MAP2 suggesting the potential to differentiate into two distinct lineages: osteogenesis and neurogenesis, respectively. Although mechanical characterisation of the alginate beads and ECM expression were not investigated, these findings could be contradictory as the two lineages are oppositely driven. However, BMP2 is involved in the activation of a common precursor of osteogenesis and adipogenesis and directing the differentiation towards one of the lineages depends on culture conditions [257,317]. This increased expression of BMP2 in alginate encapsulated MSCs could mean a predisposition for differentiation without committing to a specific lineage. For a more accurate corroboration of the osteogenic lineage Runx2 expression should be analysed. Also, MAP2 has been constitutively identified in MSCs and, similarly to BMP2, its expression might not be associated with neurogenesis but only a facilitated phenotype for future differentiation [318]. Thus, the observed gene expression could just demonstrate preservation of the MSC undifferentiated phenotype with a predisposition for an eventual commitment to a lineage upon stimulation with the adequate factors. The successful differentiation into adipocytes and chondrocytes of de-encapsulated MSCs corroborated this argument to some extent.

Interestingly, the histological staining of differentiated de-encapsulated MSCs validated the chondrogenic phenotype, but gene expression did not present any marked upregulation of the specific markers (AGN and Collagen 2). It was noted that specifically, the Collagen 2 primer was not adequate due to the observed inconsistencies in the melting curve. Therefore, a wider panel of makers for chondrogenesis should be analysed for phenotype validation at the mRNA level. Another unexpected experimental difference was the higher expression of differentiation markers in encapsulated MSCs rather than in de-encapsulated cells. No conclusions can be drawn from this as it was only one experimental replicate, further repetitions are essential to confirm the results, and the MSC population in the beads could be abnormally

responding to the differentiating signals due to the probable activated apoptotic process. However, a valuable experiment would be to induce differentiation of modified alginate encapsulated MSCs under dynamic conditions since it could constitute a more efficient process with faster diffusion of the soluble factors, possibly decreasing the time and volume of reagents required for lineage commitment.

The paracrine potential of alginate encapsulated MSCs was evaluated through co-culture with alginate encapsulated HepG2 cells. Results determined that MSCs were highly influenced by HepG2 cells. The latter sustained MSCs by decelerating cell loss and upregulating Survivin on day 14 and, reduced the impact of the hydrogel microenvironment on the upregulation of BMP2 and MAP2. In reverse, the influence on HepG2 cells was mainly centred on slowing proliferation rate between days 7 and 14, with subsequent diminished final cell density, and the downregulation of C/EBPα. Several studies have described the influence of these two cell types on each other. Li et al. observed that fusing HepG2 cells with MSCs created an *in vitro* metastasis model with increased cancer-associated and malignant properties [319]. Conversely, conditioned media from encapsulated MSCs in a collagen/Matrigel scaffold effectively inhibited HepG2 proliferation and tumour initiation through secretion of IL-24 [320]. A dual effect was determined by Liau et al. where MSCs have assisted in the recovery of injured HepG2 cells through secretion of VEGF and HGF and, in response to the injured phenotype, MSCs exhibited early markers of hepatogenesis [321]. Differentiation induction was also observed in co-culture of MSCs with primary hepatocytes in a growth factor-free media with MSCs displaying characteristics of hepatic progenitors [322]. Here, there was no indication of the tumour phenotype progression, but rather a support of encapsulated MSCs followed by an impaired proliferation rate of HepG2 cells. It could be speculated that there was a commutative process where firstly the HepG2 influence on MSCs is greater since their performance is not maximised due to absence of adhesion points, but as they become more functional (evidenced by the stabilisation of cell numbers and upregulation of Survivin), they then exert their influence on HepG2 cells affecting proliferation. Obviously, more replicates, longer co-culture periods, modifications to the hydrogel and screening of a wider panel of makers (e.g. hepatic differentiation markers for MSCs, cancer-related signalling pathways) would unravel the behaviour and extent

of the paracrine effect. Moreover, transferring the model to the sFBB setup would further improve the process and validate the system as a co-culture device.

None of the conditions tested in this study (3D static, dynamic or co-culture) induced hypoxia as demonstrated by the downregulation of HIF-1α. However, several reports have highlighted the importance of hypoxia on MSCs performance by enhancing proliferation, retaining stem cell properties and increasing differentiation capacity, while cells under normoxia exhibit premature senescence and reduction in population doublings [323–325]. Thus, depending on the application for MSCs, suppression of oxygen delivery could be considered. Still, there was no impairment on its VEGF effector since its mRNA expression level was upregulated in all conditions throughout culture periods, verifying the endogenous secretome of MSCs.

Overall, the ability to de-encapsulate MSCs from hydrogel beads without irreversible damage and preserving their capacity to proliferate and differentiation into distinct lineages, although requiring extensive optimisation of the 3D matrix composition, demonstrate the potential for these beads to serve as vehicles for cell therapy or tissue engineering. They could either be preserved undifferentiated to mimic the *in vivo* niche or pre-differentiated into specialised cells.

4.2.6. Conclusion

Here, the hydrodynamic environment of the sFBB sustained viable and metabolically active alginate encapsulated MSCs in culture up to 21 days. Although cell numbers declined, the dynamic conditions decelerated that process in contrast to conventional static culture. Nonetheless, both conditions preserved the stem cell phenotype highly expressing undifferentiated markers, reattaching to tissue culture plates once released from the hydrogel beads and responding to differentiation cues, successfully following adipogenesis and chondrogenesis. As for paracrine function, when in co-culture with alginate encapsulated HepG2 cells, MSCs reduced the proliferation rate of HepG2 cells after 14 days but most significantly, HepG2 supported the culture of encapsulated MSCs by stabilising their cell number and inducing expression of Survivin.

In conclusion, hydrogel encapsulation of MSCs demonstrated potential for optimisation of both the hydrogel composition as well as the co-culture system to improve cell performance which could then be further potentiated in the dynamic environment of the sFBB.

4.3. Small-scale fluidised bed bioreactor as a BAL pilot scale for studies on improving biomass recovery after cryopreservation

4.3.1. Introduction

Whether it is a single cell suspension, a 3D cell construct or whole tissues, preservation of the biomass produced in a bioreactor is essential for the progress of tissue engineering and regenerative medicine in order to stock readily available products. This can be achieved through cryopreservation: exposing the biomass to sub-zero temperatures arresting any biological activity present without compromising it or its structure and thus, enabling long-term preservation of the constructs, usually in liquid nitrogen at -196°C [326]. Once the biomass is thawed, its performance should be comparable with performance prior to cryopreservation. Cryopreservation and subsequent thawing results in a phase change of the water content in the intra- and extra-cellular environment, from liquid to solid, which leads to chemical alterations in the cells and also to mechanical constraints and injury, endangering cell survival.

Cryoinjury can occur as soon as the temperature falls a few degrees below the optimal temperature of the cell and, while the exact mechanism is not yet established, literature has proven there is a direct correlation with the cooling rate. At slow rates the driving force of injury are osmotic pressure effects: as water diffuses out of the cell due to ice nucleation extracellularly, the intracellular solute content can increase to toxic levels, but also extreme dehydration can irreversibly compromise the cell membrane integrity [327]. Conversely, at fast cooling rates, water diffusion is slower than ice nucleation and thus, ice forms intracellularly causing mechanical disruption to the cell. Thus, each cell has

its optimal cooling rate which induces a balanced osmotic pressure to dehydrate the cells enough to minimise intracellular ice formation but not excessively avoiding denaturation [326].

Designated as cryoprotectants and commonly classified according to their cell membrane permeating capabilities (permeating e.g. dimethyl sulfoxide and glycerol, and non-permeating e.g. sucrose and trehalose), these agents can modulate the cryopreservation process by lowering the glass transition temperature of the cell, maintaining its glassy state for longer and consequently, minimizing the cryoinjury induced by ice formation [328]. However, they are cytotoxic when used at high concentrations, high temperatures and long exposures, hence limiting their application [329].

Another component used to minimise injury and maximise post-thaw recovery, are antioxidants because oxidative stress is an important impairing outcome of cryopreservation. For instance, adding vitamin E, glutathione, catalase or monothioglycerol to the preservation media of sperm cells has reduced the levels of reactive oxygen species and improved cell viability, DNA integrity, motility and velocity when compared to control groups without any antioxidants [330–333].

Thawing is as crucial as freezing and can cause the same extent of damage to the biomass. Osmotic stress and recrystallisation are the main detrimental phenomena during warming, but as in freezing, they can be minimised by tailoring the thawing rate [327]. Moreover, before post-thaw recovery removal of cryoprotectant and equilibration of the osmotic pressure by incrementally washing the biomass is necessary for it to return to its isotonic environment.

The established protocols have been successful in cryopreserving small volumes of single cell suspensions. However, preservation of engineered 3D constructs or tissues with similar methods has yielded low recovery due to their complex biophysical structure comprised of multiple cells, extracellular matrix, scaffold structure and interactions between cells, cells and matrix, and cells and scaffold. The heterogeneity and macroscopic dimensions of these assemblies generate different thermophysical properties and non-uniform spatial distribution of osmotic gradients, cryoprotectant concentrations and cooling rates which result, for example, in some regions being insufficiently dehydrated, others overexposed to cryoprotectants and others even

rapidly cooled forming intracellular ice [334]. Furthermore, expansion and contraction of the extracellular matrix or biomaterials during freeze/thaw may compromise their chemical and physical properties [335,336]. A better understanding of mass and heat transfer and the exact mechanisms behind cryopreservation is necessary for establishing efficient protocols.

4.3.2. Hypothesis and aims

It was hypothesised that the sFBB could serve as a scale-down model for the Liver Group FBB for process optimisation. Thus, the aim was to scale-down the cryopreservation protocol and replicated the biomass post-thaw recovery pattern attained in the FBB.

4.3.3. Materials and methods

Materials

- Alginate encapsulated HepG2 spheroids
- αMEM-G supplemented with 10% FFP
- DMEM (Sigma, #D5796)
- Glucose (Sigma, #G8270)
- Cryoprotectant solution (CPS):
    - Belzer UW® Cold Storage Solution (Bridge to Life)
    - Dimethyl sulfoxide (DMSO) (Sigma, #34869)
    - Cholesterol (Sigma, #C3045)
    - Catalase (Sigma, #E3289)
    - Trolox (Sigma, #238813)
- Peristaltic pump (Watson Marlon)
- Water bath
- -80°C freezer
- Controlled Rate Freezer (CRF) Kryo 750 (Planer)
- CryoStore™ 2500 Conical EVA Freezing Bag (Origen, #CSD2500Y9)

- Polypropylene bottles

4.3.3.1. Cryopreservation of alginate encapsulated HepG2 spheroids

A total of 1.3 L of biomass was produced in the clinical scale FBB at a final cell density of 26.1 million cells/mL beads. Cell beads were transferred into a large container, left to settle and the excess medium removed. With the container in an ice water bath, beads were cooled down until 10°C and, at that point, cold CPS solution, containing 76% (v/v) UW® solution, 24% (v/v) DMSO and 0.02% (w/v) cholesterol, was mixed in a 1:1 volume ratio with the biomass. Once the beads settled again, the majority of CPS was discarded, leaving only a volume equivalent to 20% of the total bead volume (for 1.3 L, 260 mL of CPS remained). Following, antioxidants, catalase (114000U/mL prepared in water) and Trolox (604.3 mM prepared in ethanol) were added to the mix to a final concentration of 500 IU/mL and 1.7 mM, respectively. This final mix was continuously stirred and pumped into the 2 L conical shape cryobag (Appendix 3) at 80 mL/min. The bag was sectioned into 3 parts and transferred to the CRF Kryo 750 and the cooling profile induced was the following:

- Cool down from 4°C to -50°C at -1°C/min,
- Holding step at -50°C for 2h
- Cooling at -0.5°C/min from -50°C to -120°C

The bag was stored in a liquid nitrogen tank in vapour phase until thawing.

For the thawing process, the bag was taken from the tank and moved into a -80°C freezer to enable initial controlled warming and prevent a temperature shock if moved directly into a water bath. Once the temperature reached -80°C, the cryobag was transferred into a 37°C water bath for complete thawing. Thawed cell beads were washed 3 time: first with cold 1 M glucose DMEM, second with cold 0.5 M glucose DMEM and third with room temperature DMEM. All washes were performed in a 2:1 ratio (2.6 L of washing solution to 1.3 L of biomass). At each washing step the solution was mixed and left to equilibrate for 5 min, draining and discarding the excess between steps.

As for the alginate encapsulated HepG2 spheroids expanded in the sFBB, the cryopreservation procedure followed the same protocol, except the biomass was placed in a polypropylene bottle (Appendix 3) frozen in 40 mL batches at a depth equivalent to

the sections in the bag (~3 cm). Moreover, it did not require pumping of the biomass into each bottle.

4.3.3.2. Recovery of cryopreserved alginate encapsulated HepG2 spheroids

Recovery of thawed cell beads from took place in the respective growth vessel: biomass produced in the clinical scale FBB was again loaded into it, as it was the one produced by the sFBB. In both systems cell beads were left to recover until pre-cryopreservation levels of cell density and viability were achieved, in a 1:46 volume of beads to medium ratio in αMEM-G supplemented with 10% FFP. The cell counts and viability assay followed the methods described in *Chapter 2* (*sections 2.9* and *2.10*).

4.3.4. Results

4.3.4.1. Biomass recovery for the bioartificial liver

HepG2 cells were encapsulated as single cells in alginate beads and cultured in the large-scale fluidised bed bioreactor for 14 days until several spheroids formed and a final cell density of 26.1 ± 0.71 million cells/mL beads was achieved (day -1, Figure 51 A). At the end of the culture period the 1.3 L of biomass were pre-equilibrated in a 1:1 volume ratio at 4°C with a cryoprotectant solution (CPS) composed of 76% (v/v) UW® solution, 24% (v/v) dimethyl sulfoxide (DMSO), 0.02% (w/v) cholesterol, 1.7 mM Trolox and 500 IU/mL Catalase in Belzer UW solution. The biomass was then cryopreserved in a controlled rate freezer (CRF) set to induce an average freezing rate of -0.35°C/min and thawed in a water bath at 37°C.

After thawing the total cell number diminished to 19.5 ± 0.14 million cells/mL beads at a 95% viability (day 0, Figure 51 B), indicating that the cryopreservation process itself induced cell damage and subsequent loss.

Once the biomass was thawed, it was loaded again into the FBB for recovery. The decline continued the following 24 h attaining a minimum of 6.5 million viable cells/mL (10.4 million cells/mL beads at 62.3% viability), a reduction of 60%. After this point, cell

number and viability started to recover achieving the pre-cryopreservation level on the 5th day (24.5 million cells/mL beads at 99% viability).

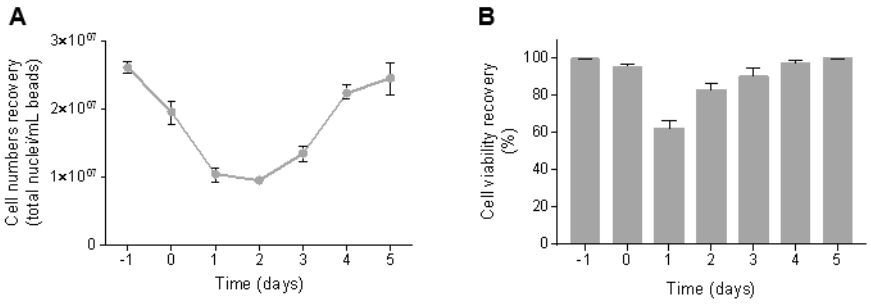

Figure 51 - Biomass recovery in the clinical scale FBB after cryopreservation. Cell numbers (A) and viability (B) recovery profile after cryopreservation of alginate encapsulated HepG2 cells to serve as biomass for Bioartifical Liver device. Day -1 referes to the day of freezing, day 0 to warming and days 1 to 5 are the days of recovery. Data presented are average ± range (n = 1).

4.3.4.2. Biomass recovery in the sFBB

The same protocol was applied to alginate encapsulated HepG2 cells cultured in two parallel sFBB at a final density of 17.3 and 21.4 million cells/mL beads both at 99% viability. To mimic the scale-up procedure, biomass was cryopreserved in containers with the same geometric depth as in the large scale, with 40 mL per container.

The recovery in the sFBB followed the same profile as in the FBB, with a reduction in cell number and viability immediately after thawing, validating the effect of cryoinjury and further declining in the first 24 h of recovery. Complete recovery was attained on day 5 of culture: 22.5 and 23.3 million cells/mL beads at 97% and 96% viability, respectively (Figure 52). The obtained data demonstrated a correlation between the initial cell density and the recovery pattern. Lower cell numbers only declined a maximum of 26% on day 1 compared to 30% for densities of 21.4 million cells/mL beads. Similar behaviour was observed in viabilities with reduction of 17% in lower density and 25% at higher cell density. This evidence supports the notion that constructs with an increased number of cells and complex structures were more susceptible to cryoinjury.

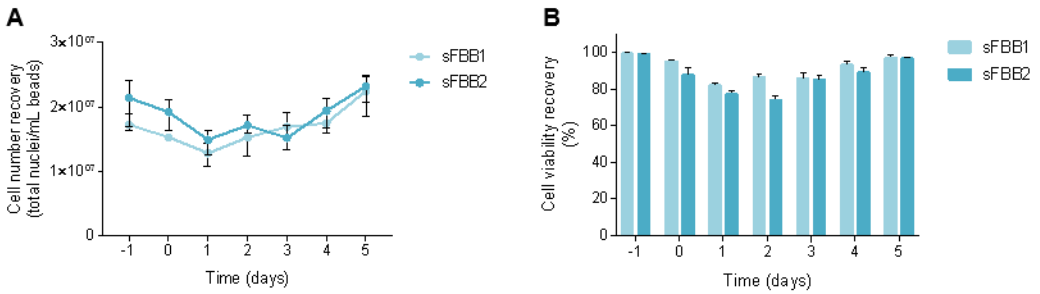

Figure 52 **-** Biomass recovery in the benchtop scale fluidised bed bioreactor (sFBB) after cryopreservation. Cell numbers (A) and viability (B) recovery profile after cryopreservation of alginate encapsulated HepG2 cells in two parallel sFBBs (sFBB1 and sFBB2). Day -1 referes to the day of freezing, day 0 to warming and days 1 to 5 are the days of recovery. Data presented are average ± SD (n = 1).

4.3.5. Discussion

The sFBB designed in *Chapter 4* validated its application as a pilot scale for the FBB developed by the Liver Group by mimicking the recovery profile of cryopreserved alginate encapsulated HepG2 spheroids. After thawing, biomass was recovered to pre-cryopreservation levels after 5 days in culture.

Cryopreservation is essential to convert the BAL into an "off-the-shelf" clinical device/product since patients diagnosed with acute-on-chronic liver failure have a poor prognosis with a narrow window for treatment and recovery. Ideally, within 2 days from the diagnosis the BAL should be made available but to fulfil that requirement, the current cryopreservation protocol requires optimisation to reduce the post-thawing recovery time. Given this demand, the sFBB presents itself as the ideal device for the optimisation tests as it enables simultaneous observations in a scaled-down manner.

The current protocol was built on principles identified by previous members of the Liver Group. Massie established the need to include an ice nucleating agent such as cholesterol to reduce supercooling and latent cryoinjury, resulting in an improved recovery in cell number, viability and function after 72 h [125]. Also, the production of reactive oxygen species and activation of caspase were observed and minimised by the addition of antioxidants (Trolox and Catalase) to the CPS [337]. For large volumes cryopreserving the biomass with extra CPS (i.e. 20% of the total volume to be cryopreserved) minimised the toxicity of the cryoprotectant and high solutes concentration [127].

The encapsulation of the spheroids in hydrogels constitutes itself an improved mechanism against cryoinjury since several studies have demonstrated that hydrogel encapsulation confines the ice crystal growth within the pores and shields from abrupt osmotic shocks [125,336]. Alginate encapsulated neurospheres had a shorter post-thaw recovery and were significantly less fragmented in comparison to cryopreserving the same non-encapsulated spheroids [338]. Encapsulating aggregates of human embryonic stem cells (hESCs) adhered onto microcarriers proved to yield a higher recovery post-cryopreservation maintaining their undifferentiated phenotype without using feeder cells [169]. These capsules may also serve as ice nucleating agents and to further investigate that effect and the contribution of the CPS used in this study there is an on-going collaboration with experts at ISIS Neutron and Muon Source resorting to neutron scattering spectroscopy.

Improvements to the protocol could be centred at the freezing or thawing stages. Modifying the freezing stage includes adjusting the cryoprotectant concentrations and CPS composition as well as the freezing rate [339]. However, previous investigations have determined the most effective method was to pre-equilibrate the CPS at 1:1 volume ratio with the biomass to attain enough dehydration and a final DMSO content of 12% [126]. Furthermore, the freezing rate has been extensively tested in the context of a Master student's project, where the multi-stage profile set by the CRF induced the most consistent biomass freezing rate (measured at several points) with a minimal supercooling effect. Thus, the focus should be directed to the warming and post-thawing recovery as it has been underexplored before revisiting the freezing stage.

Most warming procedures resort to convective heat (e.g. from water baths) to thaw the samples. Although the external temperature is controlled, the internal temperature of the thawing biomass fluctuates highly due to the generated convective currents. Thus, inductive heat produced by magnetic nanoparticles could constitute the solution to a uniform, controlled and rapid warming, particularly for large volumes [340]. Another method to reduce injury during warming would be to include in the CPS low molecular mass ice recrystallization inhibitors (IRIs) which are capable of reducing the average ice crystal size in the extracellular environment minimising the damage induced by recrystallisation [341]. Other adjustments could take place at the removal of the cryoprotectant and restoration of the osmotic equilibrium by continuously perfusing the

biomass in the sFBB with solutions of decreasing solutes concentration instead of interrupted washes. Moreover, medium change during recovery might be imperative to remove the accumulation of toxic metabolic products (e.g. lactate) which could exert an inhibitory effect on cell recovery.

Nonetheless, to further improve the current protocol a more in-depth understanding of the cryoinjury mechanism in the context of the alginate encapsulated HepG2 spheroids is required, for instance, whether it is an apoptosis or necrosis driven mechanism and which signalling pathways trigger them. Several studies highlighted that low recovery post-cryopreservation is due to the apoptotic mechanism activated by p53. p53 was activated via p38 MAPK pathway in cryopreserved sperm and in a network including ROS production, ROCK activation and change in F-actin in hESCs [342,343]. Moreover, adding ROCK and p53 inhibitors to the post-thawing medium on day 1 significantly improved hESCs recovery by 20% [344]. Besides the cryoinjury mechanism, other parameters need to be assessed to determine the impact of cryopreservation on the spheroids function and performance such as gene expression, energy metabolic activity (e.g. glucose consumption, ATP content), protein synthesis and other hepatic-specific functions (e.g. drug metabolism, urea cycle, ammonia detoxification) during recovery and *in vitro* experiments in liver failure plasma [132]. The optimisation of the cryopreservation protocol of the BAL biomass is currently being developed within the Liver Group by another PhD student.

The obtained results also corroborated literature reports that constructs with increasing cell numbers and structure complexity pose more risks of cryoinjuries than single cells, since cell death and loss was not as abrupt for samples with lower initial densities, subsequently, recovering faster. Overall, the data in this study, whilst limited to draw any definite conclusions, provides a "proof-of-concept" of the utility of the sFBB as a pilot scale and as an all-in-one complete system for culture, recovery and testing hydrogel encapsulated 3D cell constructs.

4.3.6. Conclusion

Herein the sFBB validated its role as a pilot scale for the FBB by replicating the post-thaw recovery pattern of cryopreserved alginate encapsulated HepG2 spheroids. Results also determined that the current cryopreservation protocol requires optimisation to meet the clinical demands of an "off-the-shelf" BAL through a rapid post-thaw recovery. This could implicate adjustments to freezing and warming rates but also additional compounds to the CPS and recovery media. Therefore, this scale-down bioreactor will serve as a testing platform due to its reduced operating volume and capacity to run several units in parallel allowing for multiple simultaneous observations.

The proliferation of alginate encapsulated HepG2 cells into highly viable spheroids with a final cell density 2-fold above the control static culture; the preservation of viable and undifferentiated alginate encapsulated MSCs in dynamic culture for 21 days; and the recovery of biomass in 5 days after cryopreservation corroborated the sFBB application as cellular expansion and long-term testing platform for 3D cell constructs and pilot scale model for the clinical FBB. This further validates the potential of the prototype as a versatile commercial device setting the grounds for the necessary design improvements that will be explored in the next chapter.

CHAPTER 5

Optimisation of the design of the small-scale fluidised bed bioreactor

5.1. Introduction

5.1.1. Design optimisation

One of the steps of the engineering process of developing a device includes design optimisation. At this stage, the aim is to improve the performance of the design from its initial implementation. Optimisation enables redefinition of parameters that do not perform to their maximum capacity; reduction of costs to make the product more competitive; or reconfiguration of the design as the best way to achieve the intended nominal level, for example, what is the smallest configuration of a bioreactor which can hold a desired operating volume [345]. This is often a time-consuming process with a step-by-step approach to identify the combination of parameters that fit the best solution.

Independently of the purpose, design optimisation involves defining the optimisation model, solving it and analysing the results [346]. When establishing the model, it is necessary to correctly identify the objective, design variables and constraints. The objective is the improvement intended for the system (e.g. increasing biomass yield, reducing mixing time, etc) and it serves as comparison criteria to determine whether the modified design achieved the desired goal [347,348]. Design variables are the parameters to be altered in order to attain the objective. However, they cannot be modified indefinitely as there are restrictions, such as physical space, operating times or costs, which will limit the modifications to a set of possible solutions. Recognising these constraints leads to designing attainable objectives, increasing the feasibility of the project.

To solve the optimisation model, an analysis model is created where input variables are fed into the system to calculate outputs which will be analysed to verify the compliance with the objectives and constraints [346,347]. The inputs include design variables as well as boundary conditions, material properties and other characteristics necessary for the definition of the model. Based on the produced results, considerations about the

optimality, feasibility, sensitivity and improvement of the model are made to decide if the goal has been achieved or further actions will be necessary [348]. Often this is an iterative process, where from obtained results, new inputs are fed into the system to generate an improved model until optimal values that correspond to the objectives are attained.

There are different approaches to design optimisation and consequently, to solving the analysis model which can be classified as expert-based, design of experiments-based and algorithm-based. The expert-based approach capitalises designers' experience and judgement to create the optimal design. It is normally coupled with simulation techniques, like computational fluid dynamics analysis, to technically and numerically support the final decision [349]. This gives incremental improvements and does not require highly specific skills, thus, being the most applied in industry. Conversely, it can be time-consuming and limited to the expert's knowledge, failing to identify unknown but potentially better designs.

Design of experiments (DoE) is an empirical technique that determines the relationship between design variables and their impact on the performance of a design. It uses statistical methodology to analyse and predict performance under all conditions within the limits of the experiment with only a fraction of all possible experimental combinations of design variables (fractional factorial experiment) [350]. This is a widely applied method to optimise bioreactors, although it can generate a large pool of results [351].

The approach currently gaining more popularity is the use of algorithms since they partially automate the optimisation process and widen the search of the best design. The genetic algorithm is one of the most applied and it creates a population of several designs, composed of specific design variables, evaluates them and passes hereditary traits from the "good" designs to the next generation based on a process similar to natural selection [345]. Algorithm-based optimisation enables solving more complex models but requires advanced mathematical and computational skills.

5.1.1.1. Computational fluid dynamic analysis s of the initial sFBB prototype

Computational fluid dynamics (CFD) is an integrated engineering tool that numerically solves equations of fluid motion to produce quantitative analyses of fluid phenomena in a given system. The Navier-Stokes equations are the most widely used to describe the behaviour of a moving fluid by correlating its velocity, pressure, temperature, density and viscosity and assuming conservation of mass, momentum and energy [68]. Therefore, CFD is a useful tool to theoretically evaluate and characterise a bioreactor design and respective hydraulic conditions including velocities distribution, pressure and shear stress [147].

All accurate CFD simulations require firstly the creation of the correct geometry of the bioreactor since any small imprecision may cause considerable differences in the flow behaviour. The model is designed in computer-aided design (CAD) software and transposed to the CFD package. There, the geometry needs to be divided into smaller cells such that each cell constitutes a small control unit where the numerical calculations are solved [352]. This process is described as meshing and creates the computational domain. Once completed, the domain is discretised, i.e. at each cell, the partial differential equations of the governing physical models are transformed into analytical solutions for the intended variable (e.g. fluid velocity, pressure, temperature).

Approaches for discretisation include finite difference, finite element or finite volume methods. The finite difference determines the solution of the intended variable as the difference between values at various points in the grid, transforming them into derivatives of Taylor series [353]. Conversely, both the finite element and volume methods use integral forms to solve the equations. In the finite element, there is a sub-division of the domain into a finite number of sub-elements (nodes) where the variable variation is estimated and each of the calculated solutions are used to describe the behaviour of the variable in the whole domain [354]. As for the finite volume instead of nodes, small control volumes are created where the integration of the equation occurs and results in a balance equation guaranteeing the conservation of the fluxes [355]. This method is the most common in CFD packages of several programs because it does not require a uniform mesh like in the finite difference, and the boundary conditions can be applied non-invasively since they are located within the control volume.

With the geometry and mesh created, the discretisation, governing physical models and boundary conditions defined, the simulation starts solving iteratively the system as a steady-state or transient, if a time-dependent evolution of the variable of interest is necessary.

5.1.2. Rapid-cycle testing

Rapid-cycle testing is a fast, iterative method to implement changes in a product or process. One methodology commonly associated with this approach is the plan-do-study-act (PDSA) principle developed as a continuous improvement procedure [356]. Established in the automobile industry, its purpose is to apply small changes in a quick and easy fashion using simple monitoring tools to measure their effect over time and in successive rapid cycles. Each stage of the PDSA principle involves [357]:

- Plan – establishing the objectives and what is necessary to implement the process and achieve the desired outputs;
- Do – implementation of the process; this stage can have its own PDSA mini cycle until implementation is done without problems;
- Study – retrieve the outputs of the process and compare them with the objectives to determine how compliant they are;
- Act – analyse the results to determine the cause of observed differences and define which changes need to be implemented in the next cycle.

Consecutive PDSA cycles are carried out until the intended objectives and optimisation is achieved.

This method promotes continuous improvement of the product and prevents error repetition. Moreover, it provides both temporary and permanent corrective action, by fixing the problem and investigating its source and thus, providing sustainability of the improved process.

5.1.3. Rapid prototyping

Rapid prototyping is the process of producing a 3D model in a faster and low-cost manner, eliminating the need for expensive tools or heavy manpower. It can be applied at any stage of the product development although with particular relevance at the

prototyping level as it accelerates product development, provides early-stage validation and hands-on experience to the end-user generating practical feedback [358].

Several techniques can be used for rapid prototyping including stereolithography (SLA), selective laser sintering (SLS), fused deposition modelling (FDM), binder jetting, and others [359]. These are broadly referred to as 3D printing and require a pre-established CAD model which will guide the manufacturing process.

SLA is the oldest 3D printing technique and forms solid parts by curing liquid photopolymer resin using a laser beam. Models are built layer-by-layer as a platform is lowered in a resin tank to where the laser is directed and draws a cross-section of the 3D model, hardening the material [360]. To finalise, the printed parts are rinsed in a solvent to remove any excess of resin. This technique builds models with extreme detail and accuracy although it requires embedding support structures in the CAD project to sustain the model during printing.

Also based on laser power, SLS builds 3D models by sintering small particles of powdered material (plastic, metal, ceramic, or glass) into solid structures. A bed of powder is heated just below the melting temperature of the raw material and the laser scans a cross-section of the model fusing the particles together. The bed is lowered, and a new layer of powder is added to build the next layer of the model. This technique does not need support structures since the unsintered particles sustain the design throughout manufacture. However, all SLS printed parts will have a grainy surface and depending on the application may need polishing.

In FDM 3D models are built from thermoplastic materials, where a filament is fed into a heated printer extruder head and a nozzle deposits the melted material onto a base forming the object layer-by-layer. Once each layer is finished, the head moves vertically to build the next layer. Raw objects formed through FDM have an uneven surface with the lines of each layer showing quite evidently and thus, most parts need finishing to have a smooth surface [361]. Similar to SLA, support structures need to be printing along with the model, but conversely, it cannot produce small, detailed features.

The properties of the raw material and the end purpose of the manufactured models dictate the selection of the 3D printing technique to be used in a specific application. For instance, resin models cannot withstand high temperature sterilisation and are generally

thinner and more brittle than plastic, therefore its application for components that need to be autoclaved or are under pressure could be limited [362].

Although not included in the rapid prototyping methodologies, laser cutting can serve as a fast manufacturing method to form or finalise a projected component. As the name suggests, it uses a high-power laser beam to scan the material surface and trim a structure or cut complex shapes that could not be easily done through conventional methods. It is a high precision method with smooth finishing and which can cut micro size holes [363]. There are several laser cutting techniques differing from each other on laser operating modes (pulse or continuous wave), energy and assistance by gas [364]. The application of each technique depends on the laser source (CO_2, neodymium, etc), material's physical properties and thickness of the workpiece. However, all of them require a CAD model to direct the laser into position.

5.2. Hypothesis and aims

It was hypothesised that the design of a prototype could be optimised following a rapid-cycle testing approach and resorting to rapid prototyping techniques. Thus, based on the results obtained from *Chapter 3* and *4*, the aim was to produce an improved design of the conceptualised sFBB, focusing on the inlet structure and distributor design, using computational fluid dynamics to predict the hydrodynamic behaviour of the bioreactor before implementing the planned modifications.

5.3. Results

5.3.1. Computational fluid dynamic analysis s of the initial sFBB prototype

As a baseline and control model for the design optimisation of the sFBB, CFD modelling of the initial prototype was simulated using SolidWorks software to estimate the fluid velocity, trajectory, pressure and shear stress. The geometry created in the CAD model was adjusted to an approximated design of the distributor as porous media, because of

its irregular design, was difficult to reproduce (Table 6). Simulations considered water as the fluid running in the system since culture medium properties are not drastically different. All initial conditions and parameters are specified in Table 7.

Table 6 – Porous media conditions defined in the database in SolidWorks.

Porous media	
Porosity	0.5
Permeability type	Unidirectional
Resistance calculation formula	$k = \mu/(\rho.D^2)$
Pore size (m)	0.000375

Table 7 – Initial conditions set for computational flow simulation in SolidWorks®.

Initial conditions	
Temperature (°C)	37
Pressure (Pa)	101325
Gravity (m/s2)	9.81
Fluid	Water
Inlet flow rate (mL/min)	12 - 25
Global mesh refinement (level)	3
Local mesh fluid cells refinement (level)	4
Local mesh solid cells refinement (level)	3

Models only simulated the fluid behaviour since including the bed of micro hydrogels would require complex equations. Therefore, all analyses were conducted for 12 and 25 mL/min flow rates, as these related to the superficial velocity interval maintained for the scaling down. The retrieved velocity profiles for both flow rates corroborated that faster velocities were obtained at higher flow rates (Figure 53).

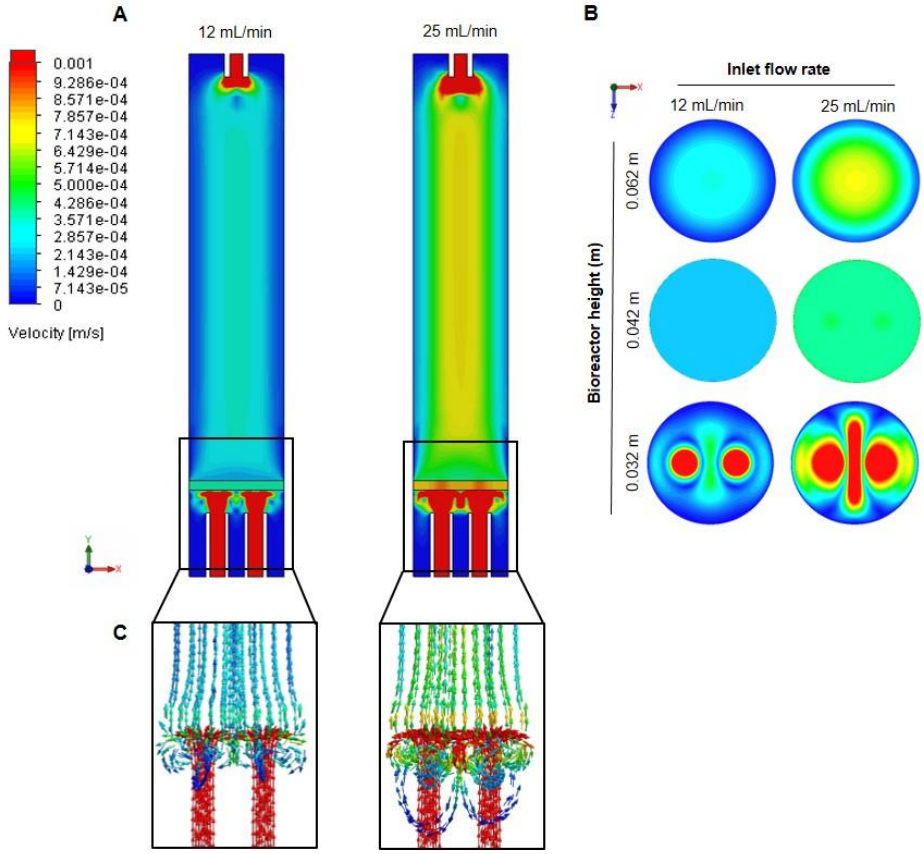

Figure 53 **-** Fluid velocity inside the prototype benchtop scale fluidised bed bioreactor. (A) Velocity cut plots of the middle plane of sFBB at inlet flow rates 12 and 25 mL/min, as well as (B) top plane plots distancing 0.032, 0.042 and 0.062 m from the bottom of the bioreactor. (C) Fluid trajectory of focusing on the inlet-distributor region. Values presented in m/s.

The minimum and maximum velocities attained in the system were 3.75×10^{-9} and 2.14×10^{-8} and, 0.021 and 0.043 m/s for 12 and 25 mL/min, respectively. This demonstrated that the intended linear flow rates set as scaling down parameters were within the interval estimated by CFD analysis. Velocity profiles suggested that higher velocities were achieved at the inlet and outlet points (Figure 53 A) with the flow being almost homogenous at the cross section immediately above the distributor (Figure 53 B, 0.042m). As the flow progressed through the column, the colour gradient indicated flows were faster in the centre of the column compared to near the wall where a stagnant layer was formed (dark blue layer; Figure 53 B, 0.062m). Flow trajectory plots demonstrated that most of the flow was axially oriented (along Y-axis) and the radial flow primarily occurred in the calming zone between the surface of the inlet point and the distributor. Because the distributor was designed as a porous media, the software could not analyse velocity on its top and bottom surfaces. The XY-plot set along the edge of the top and

bottom surfaces of the distributor (red and blue lines, respectively; Figure 54) highlighted fluctuations in fluid velocity which were consistent with a porous media definition and possibly the source of observed channelling in the experimental validation mentioned in *Chapter 3*.

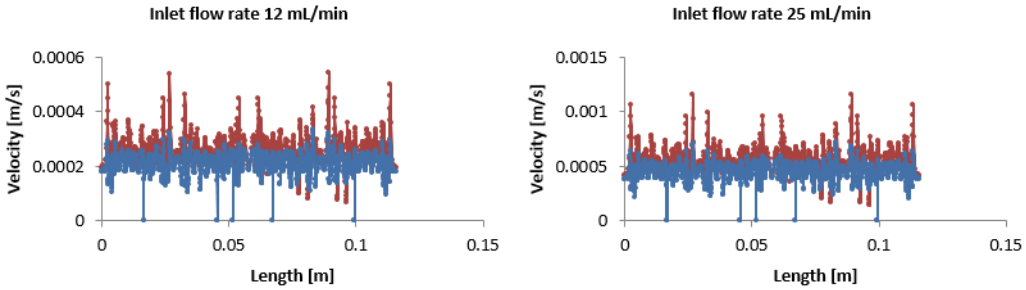

Figure 54 **-** Fluid velocity at the edge of the distributor of the benchtop scale fluidised bed bioreactor. XY-plot of flow velocity along the edge of the top (**red**) and bottom faces (**blue**) of distributor of the sFBB at inlet flow rates 12 and 25 mL/min. Values plotted as length of the circle (m) vs. fluid velocity (m/s).

In terms of pressure, there was a drop inside the bioreactor of 2231 Pa (2%) with the inlet at 101253 Pa and pressure decreasing progressively along the column to 99022 Pa at the outlet point (Figure 55). However, the estimated values were still within the interval of atmospheric pressure. Given the small pressure variability, the pressure drop across the distributor was 38.5 Pa at the simulated steady state. Moreover, the pressure was not a function of the inlet flow rate, as there was no difference between the two analysed flow rates.

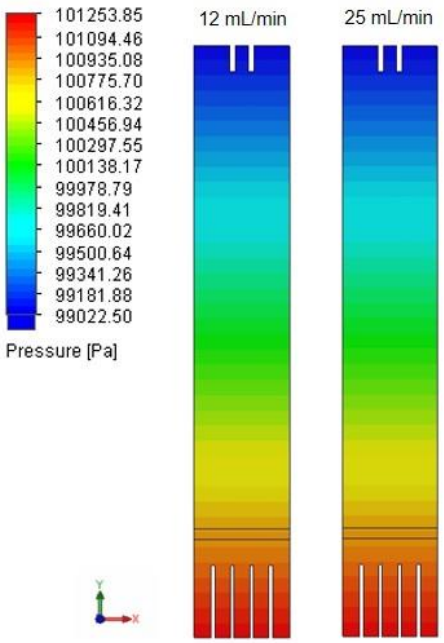

Figure 55 - Fluid pressure inside the prototype benchtop scale fluidised bed bioreactor. Pressure cut plots of the middle plane of sFBB at inlet flow rate 12 and 25 mL/min. Values presented in Pa.

While pressure is a force exerted perpendicular to the surface, shear stress is the force vector component parallel to the wall of the bioreactor. At the wall surface, shear stress was minimal, with stronger points in the regions immediately below and above the distributor (Figure 56). This was expected due to the faster fluid velocities obtained for the same area, with shear profiles higher below than above the distributor (Figure 57). Nonetheless, numerically shear stress values were still low. Complete analysis of the whole design calculated the highest shear stress in the system of 0.23 Pa at the outlet. This impact was solely on the surfaces of the prototype and not on the alginate beads as they were not included in flow simulation.

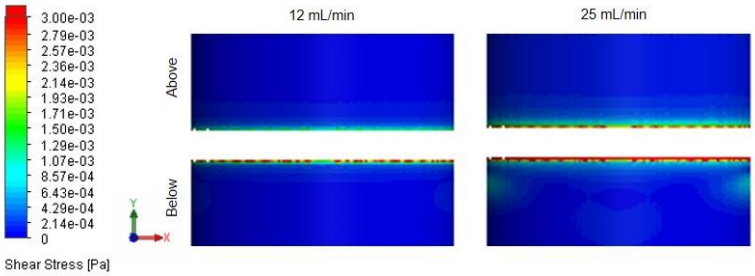

Figure 56 - Fluid shear stress on the inner wall of the prototype benchtop scale fluidised bed bioreactor. Flow shear stress surface plots in the sFBB at the distributor region (above and below) for inlet flow rates 12 and 25 mL/min. Values presented in Pa.

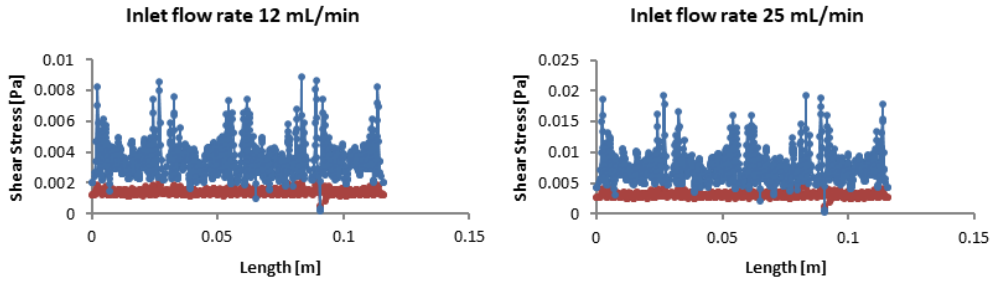

Figure 57 **-** Fluid shear stress at the edge of the distributor of the benchtop scale fluidised bed bioreactor. XY-plot of flow shear stress along the edge of the top (**red**) and bottom faces (**blue**) of distributor of the sFBB at inlet flow rates 12 and 25 mL/min. Values plotted as length of the circle (m) vs. shear stress (Pa).

5.3.2. Redesigning sFBB prototype

From *Chapters 3 and 4*, the conceptualised sFBB verified its potential as a device for long-term 3D cell culture and testing, since it effectively fluidised alginate encapsulated cells (tumour spheroids or primary single cells), sustaining cell viability, inducing proliferation and maintaining the native phenotype. Although, it was evident that the design needed optimisation for safer and easier handling and standardisation, to establish it as a commercial product. The focus of the optimisation was redesigning the distributor to homogenise the fluidisation and eliminate stagnation spots, and the inlet point to promote more radial dispersion of the flow. Other features which needed to be included were a filter at the outlet point to avoid elutriation (beads flowing out of the bioreactor) and fitting a side port to enable loading and sampling the beads in a more sterile procedure.

To combine all the desired features with the purpose of creating a prototype still under development, a concept of 3 separate parts was projected. It comprised the inlet and outlet cups and the main column, all fitted with flanges where tri-clamps would be adapted to assemble the structure, keeping it sealed. This concept, rather than an all-together piece as the first prototype with the fitted sintered glass distributor, allowed inserting a filter on the column-outlet junction and adapting a distributor on the inlet-column junction to experimentally test different designs and evaluate their performance. Also, each part could be individually cleaned in a more thorough and effective manner.

CAD models of the intended prototype were drawn as demonstrated by Figure 58 and Figure 59 with respective dimensions. The H_b/D ratio of the main column was maintained since it was a scaling down parameter and proved to fit the specific fluidisation conditions. The lengths of the inlet and outlet cups were conceived to allow enough space for fluid equilibration and eventual adjustments without compromising the design.

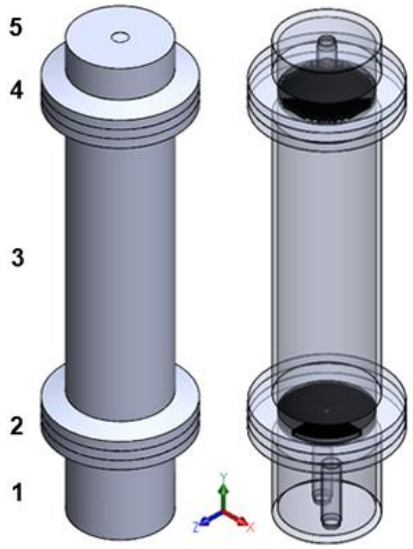

Figure 58 **-** CAD 3D models of the optimised prototype. Complete sFBB model with transparency detail for inside view of the concept (right model). 1 – inlet cup with flanges; 2 – distributor; 3 – main column with flanges; 4 – filter; 5 – outlet cup with flanges.

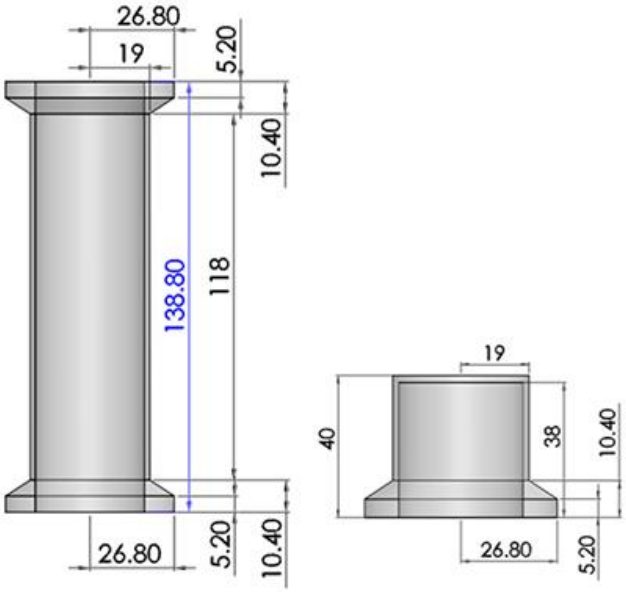

Figure 59 **-** CAD 3D models of the main column and inlet/outlet cup of the optimised sFBB prototype. Transparent model for inside view with specified dimensions. Dimensions are expressed in mm.

For optimising the designs of the distributor and inlet, the rapid-cycle testing approach of the PDSA method was used. Firstly, the concept was produced as a CAD model through SolidWorks® software and included in the complete assembly of the redesigned prototype. Secondly, the hydrodynamic behaviour was assessed through CFD simulation and, based on the obtained results, and comparatively with previous designs, a decision was made: either to pursue and implement it experimentally, or continue to optimise it. All analysed geometries followed the initial conditions described in Table 7, except simulations were only ran for inlet flow rate of 25 mL/min. Similar to the previous CFD models, simulations only referred to fluid behaviour and did not include the bed of alginate beads.

5.3.2.1. Redesigning flow inlet

The inlet feature of the initial sFBB prototype was constituted by two vertical points of entry which dispersed the flow mostly in the axial direction. To also promote more radial dispersion, geometries were considered where the flow would be directed horizontally as it entered the bioreactor. The rationale was if the fluid was evenly dispersed in all directions before the distributor, then it would homogenously cover the bottom surface of the disc, facilitating the distribution on top and assisting in minimising any channelling effects.

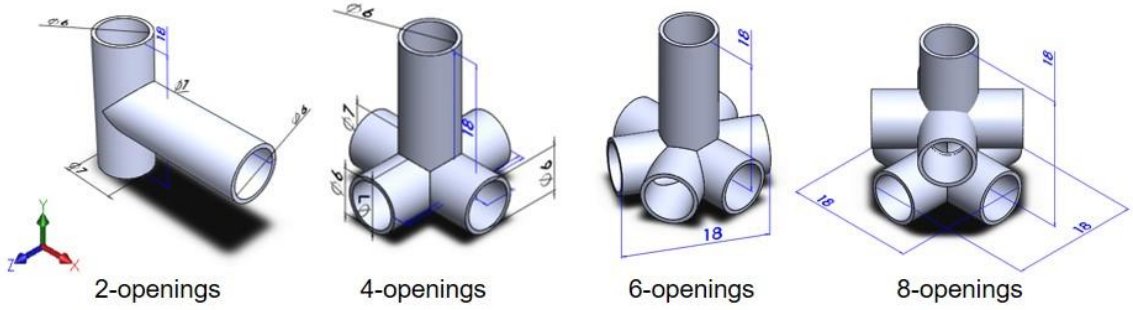

Figure 60 **-** CAD 3D models of the inlet geometries. Geometries tested for the optimised sFBB prototype differed in the number of openings. Dimensions are expressed in mm.

Therefore, the first geometry considered was two horizontal entry points resembling a T-shape, supplied by a common tube and splitting in opposite directions inside the bioreactor (inlet cup) (Figure 60, 2-opening geometry). This feature was modelled with 6 mm internal diameter, 18 mm height and 18 mm length, based on the internal diameter of the original inlet of the first prototype, which was designed from available components and proved to achieve an appropriate fluidisation of the beads. From the flow simulations, the fluid was dispersed evenly from both points at a maximum velocity of 0.012 m/s (Figure 61 A), directed towards the wall where the projection produced turbulence and radial movement, but dissipated and aligned axially as it moved vertically until the bottom surface of the distributor with velocity ranging from 0.0004 to 0.00065 m/s (Figure 61 B, 38 mm). On average it distributed the fluid throughout the volume of the calming zone at higher velocities compared to the vertical inlet, especially near the wall (Figure 61 C). The very focused dispersion in only two directions generated maximum shear stress of 0.012 Pa on the wall but did not propagate across the surface (Figure 62 A). Moreover, the fluid depressurised as it entered the inlet cup/calming zone to a homogenous 101325 Pa (Figure 62 B).

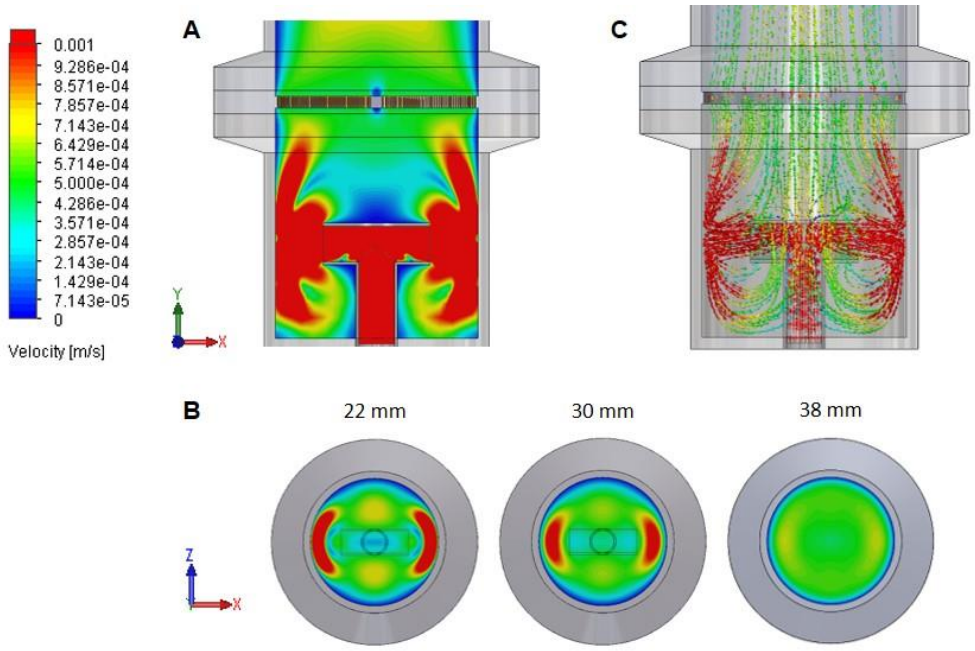

Figure 61 - Fluid velocity inside the inlet cup of the optimised sFBB prototype with a 2-opening inlet. Velocity cutplots of the XY-plane through the centre of the model (A) and the XZ-plane at 22, 30 and 38 mm distances from the bottom of the sFBB (B). (C) Corresponding flow trajectory depicted by coloured directional arrows. Values are presented in velocity as m/s.

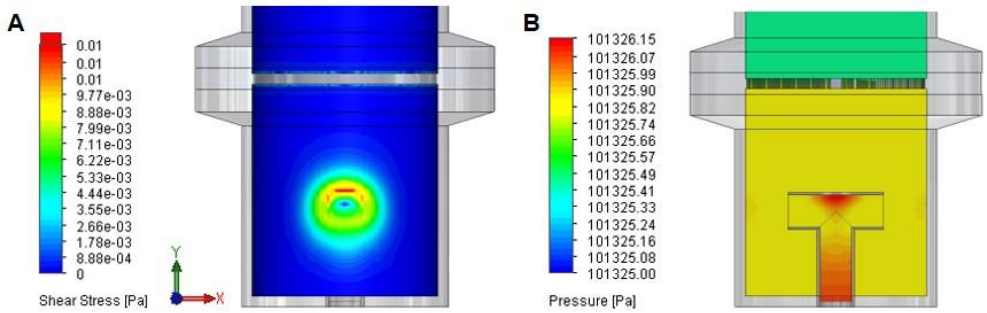

Figure 62 - Pressure and shear stress inside the inlet cup of the optimised sFBB prototype with a 2-opening inlet. (A) Fluid shear stress on the inner wall of the model facing one of the openings of the inlet. (B) Pressure cutplots of the XY-plane through the centre of the model. Values are presented in Pa.

Based on these results, the design was re-iterated to comprise more entry points to disperse the flow in more directions: 4 points oriented 90° from each other with the same dimensions as previously (Figure 60, 4-opening). In this geometry, the fluid was again dispersed horizontally through all openings and directed to the wall promoting radial movement at a maximum 0.009 m/s (Figure 63 A). It also produced turbulence but to a smaller extent and a reduced area of impact on the wall with a maximum shear stress of 0.0048 Pa, lower than the 2-opening (Figure 64 A). The flow dispersion in several directions promoted faster velocities also in the region between each opening and thus, contributing to a higher degree of mixing beneath the distributor (Figure 63 B, 38 mm), equilibrating velocities to 0.0004 - 0.00065 m/s. Compared with the previous geometry, it produced slower velocities near the wall but a larger volume of fluid with equivalent velocities (Figure 63 C). The number of openings did not influence the pressure inside the bioreactor as it was maintained the 101325 Pa (Figure 64 B).

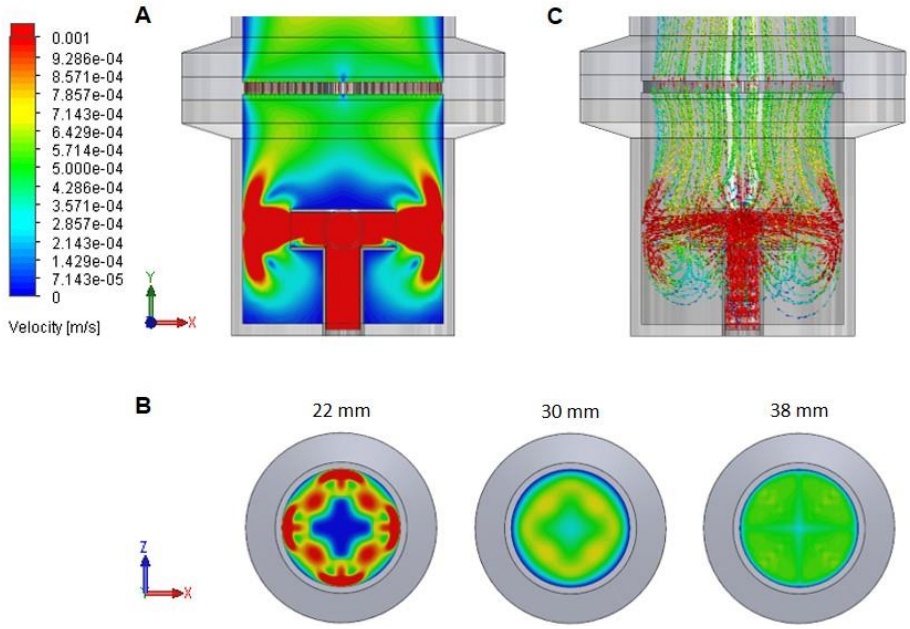

Figure 63 - Fluid velocity inside the inlet cup of the optimised sFBB prototype with a 4-opening inlet. Velocity cutplots of the XY-plane through the centre of the model (A) and the XZ-plane at 22, 30 and 38 mm distances from the bottom of the sFBB (B). (C) Corresponding flow trajectory depicted by coloured directional arrows. Values are presented in velocity as m/s.

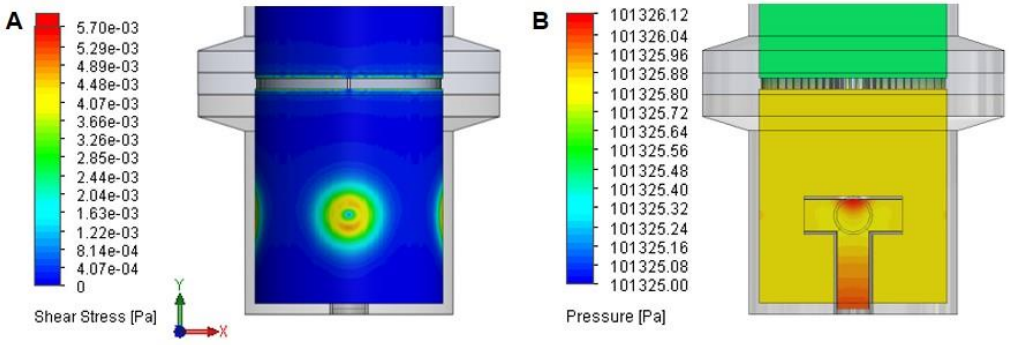

Figure 64 - Pressure and shear stress inside the inlet cup of the optimised sFBB prototype with a 4-opening inlet. (A) Fluid shear stress on the inner wall of the model facing one of the openings of the inlet. (B) Pressure cutplots of the XY-plane through the centre of the model. Values are presented in Pa.

Expanding the geometry to 6 openings with the same dimensions and oriented in a 60° angle (Figure 60, 6-opening), maintained the homogenous injection of fluid from each point at a maximum velocity of 0.007 m/s and the radial dispersion (Figure 65 A and C). However, the fast flow velocities were more confined to their horizontal projection and

a smaller extension to the surrounding areas, consequently, producing slower flows in the calming zone and lower shear stress on the wall, in the range of 0.002 Pa (Figure 66 A). Nonetheless, fluid velocities beneath the distributor still attained the interval of 0.0004 to 0.0006 m/s (Figure 65 B, 38 mm). The operating pressure in this model differed by 0.75 Pa from the former two (Figure 66 B).

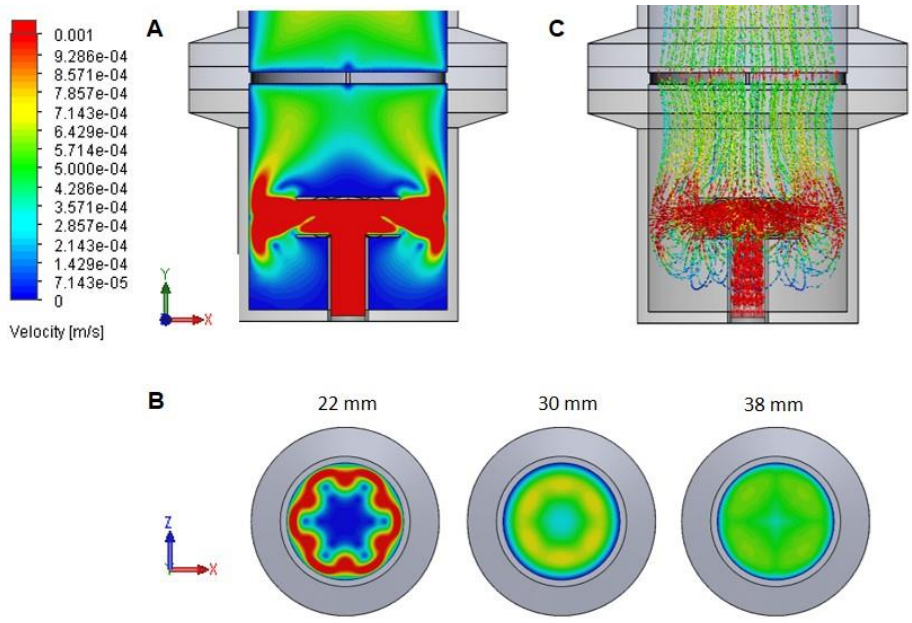

Figure 65 - Fluid velocity inside the inlet cup of the optimised sFBB prototype with a 6-opening inlet. Velocity cutplots of the XY-plane through the centre of the model (A) and the XZ-plane at 22, 30 and 38 mm distances from the bottom of the sFBB (B). (C) Corresponding flow trajectory depicted by coloured directional arrows. Values are presented in velocity as m/s.

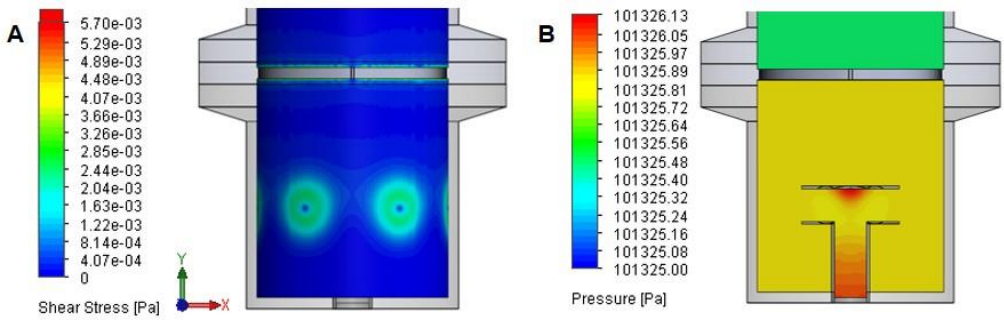

Figure 66 - Pressure and shear stress inside the inlet cup of the optimised sFBB prototype with a 6-opening inlet. (A) Fluid shear stress on the inner wall of the model facing one of the openings of the inlet. (B) Pressure cutplots of the XY-plane through the centre of the model. Values are presented in Pa.

Finally, to maximise the number of openings and mixing in the calming zone space, the last geometry tested included 8 openings, divided into two levels where openings of the second level aligned with the space in between the openings of the first level (orienting them in a 45° angle from each other) (Figure 60, 8-opening). Results demonstrated the fluid was only dispersed from the top openings suggesting the inlet flow rate was not enough to disperse through all openings (Figure 67). Because it operated only with 4 openings the fluid behaviour and pattern, and associated velocities, were similar to the previously described 4 openings and thus, there was no clear advantage in this geometry (Figure 68).

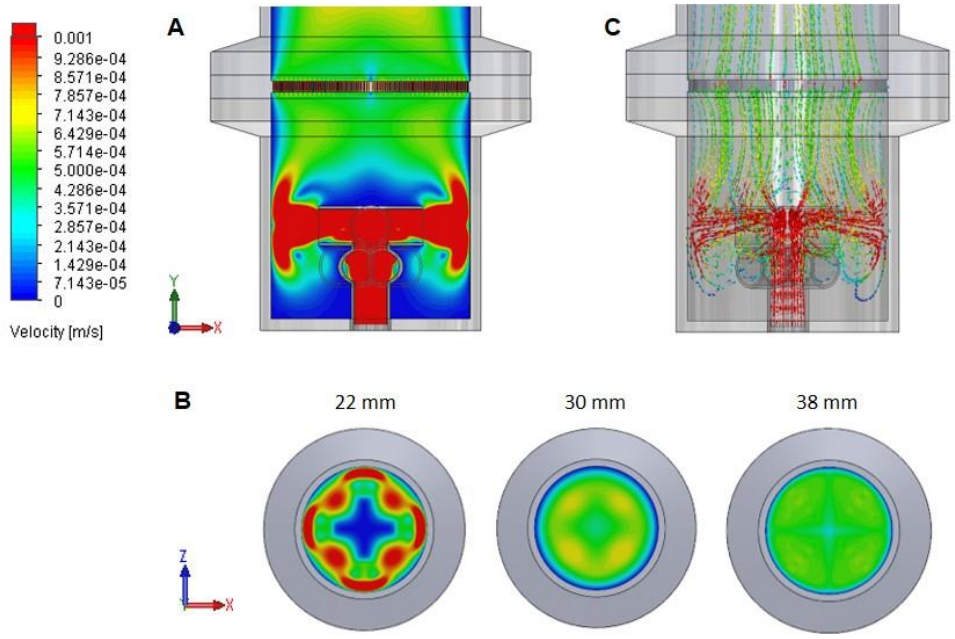

Figure 67 - Fluid velocity inside the inlet cup of the optimised sFBB prototype with a 8-opening inlet in 2 layers of 4 openings. Velocity cutplots of the XY-plane through the centre of the model (A) and the XZ-plane at 22, 30 and 38 mm distances from the bottom of the sFBB (B). (C) Corresponding flow trajectory depicted by coloured directional arrows. Values are presented in velocity as m/s.

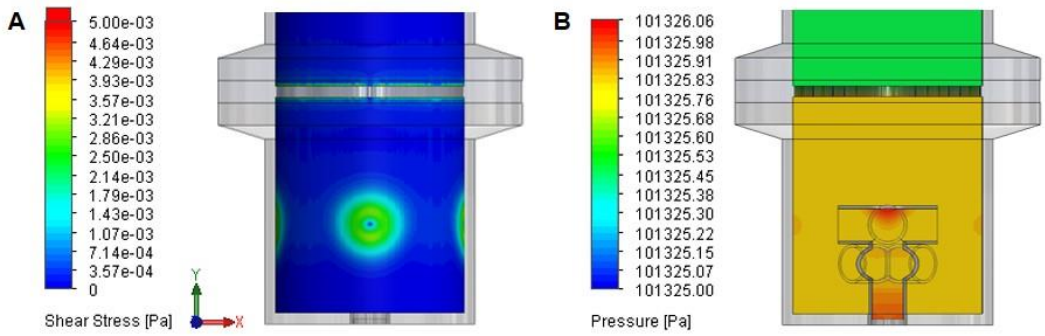

Figure 68 **-** Pressure and shear stress inside the inlet cup of the optimised sFBB prototype with a 8-opening inlet in 2 layers of 4 openings. (A) Surface plot of fluid shear stress on the inner wall of the model facing one of the openings of the inlet. (B) Pressure cutplots of the XY-plane through the centre of the model. Values are presented in Pa.

Indications from the data, and accounting for manufacture feasibility, the inlet design which demonstrated the most potential was the 4-opening inlet with flow radially dispersed while maintaining low shear stress and progressing to the distributor in a range of velocities compatible with the superficial velocity used as a scale down parameter.

Another parameter influencing the performance of the inlet was its position in the bioreactor, specifically the distance from the distributor for efficient and homogenous flow distribution. Therefore, the impact of the distance between the inlet and distributor on the fluid behaviour was analysed with the 4-opening inlet. Independently of the distance, the movement of the fluid inside the bioreactor displayed the horizontal projection against the wall which promoted a radial dispersion of the flow above the inlet, although creating a stagnant film around the inlet feature (Figure 69). For distances up to 20 mm the fluid radial dispersion promoted an effective mixing in the calming zone, minimising the areas with low velocity/stagnant flow and enabling the fluid velocities to homogenise to 0.0004 - 0.0006 m/s before reaching the distributor. Comparative to the 28 mm distance, positioning the inlet 20 mm apart from distributor reduced the stagnant fluid film around the wall between these two features.

As the inlet was placed closer to the distributor the space for mixing and homogenisation was reduced and the area underneath the inlet became a fluid dead-zone. For distances shorter than 13 mm, velocities underneath the distributor were slower than for distances up to 20 mm, except for the areas surrounding the projection of the flow against the wall.

The proximity of these high velocity regions to the distributor, not allowing the fluid to equilibrate all over the volume to a homogenous interval, could cause channelling effects in the fluidising bed where beads would move faster immediately above those regions. In contrast, the position of the inlet did not impact the pressure in the bioreactor nor the fluid shear stress on the wall.

Overall, flow simulations suggested that the most advantageous inlet design was a 4-opening geometry positioned up to 20 mm from the distributor to radially disperse the fluid promoting effective mixing throughout the calming zone and homogenous velocity when reaching the distributor to induce a consistent bed fluidisation.

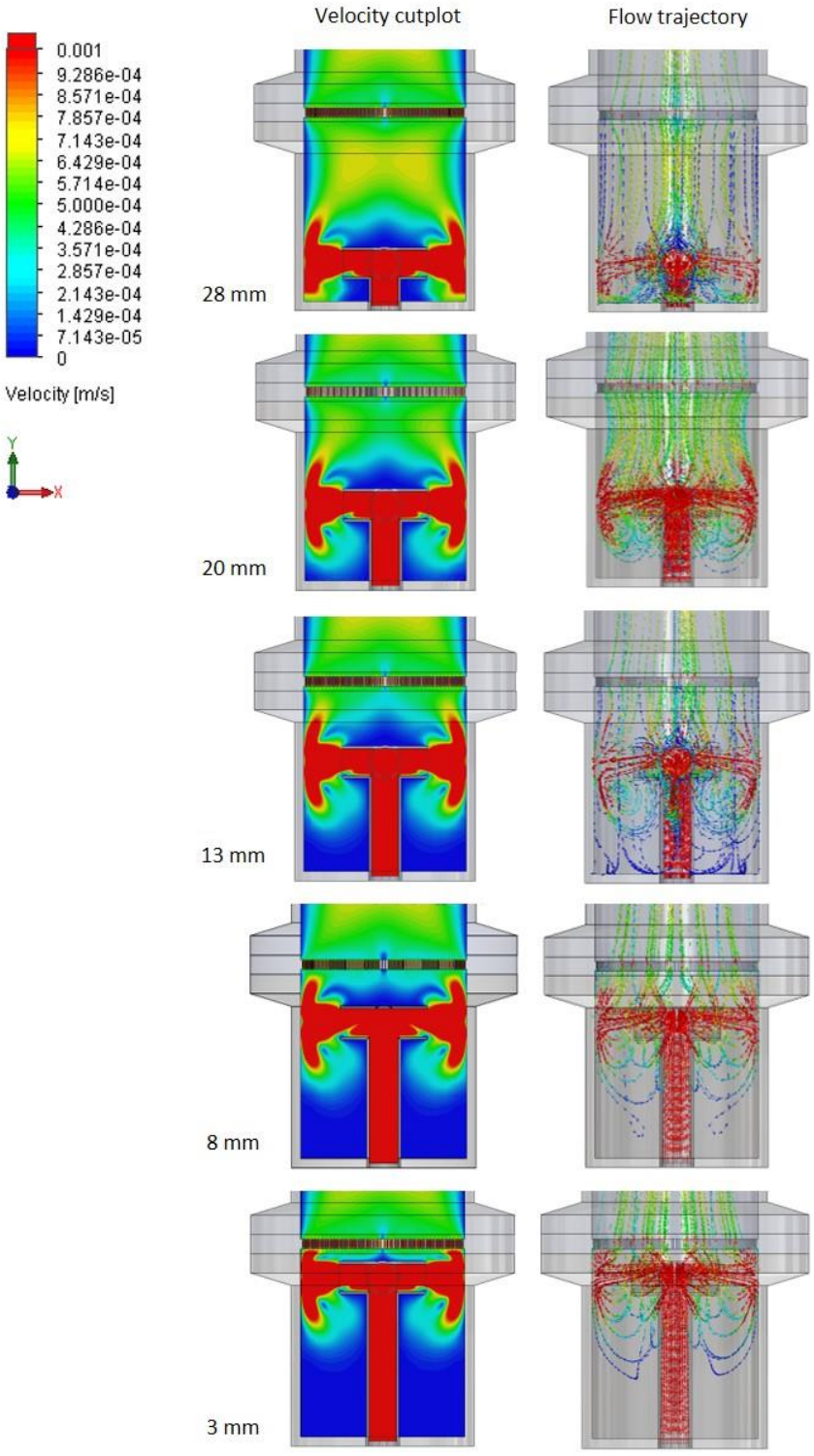

Figure 69 **-** Fluid velocity inside the inlet cup of the optimised sFBB prototype with a 4-opening inlet positioned at different distances from the distributor. Velocity cutplots of the XY-plane through the centre of the model and corresponding flow trajectory depicted by coloured directional arrows with inlet distancing from the distributor at 28, 20, 13, 8 and 3 mm. Values are presented in velocity as m/s.

5.3.2.2. Redesigning flow distributor

With the inlet design tested, the next step was redesigning the flow distributor. The purpose was to create a structured pattern that would induce a homogenous fluidisation, eliminating the observed stagnation points near the wall, specifically, immediately above the sintered glass. Note that in all the following simulations the applied inlet was the 4-opening geometry placed 20 mm apart from the distributor.

The simplest and conventional design of a flow distributor is a perforated plate consisting of a structured version of a sintered glass with perforations/holes of established shape, diameter and distribution. Resorting to pattern tooling of SolidWorks®, a 2 mm thick disc was created with 967 holes of 0.3 mm diameter, spaced 1 mm apart in a 60° stagger angle (Figure 70). These dimensions were established to prevent the smallest alginate beads from falling through the distributor. The total open area of this design was 7.4%.

From the flow simulation data, it was observed that the fluid behaviour in the calming zone (the area between the inlet and the distributor) was equivalent to that previously obtained and not influenced by the distributor design.

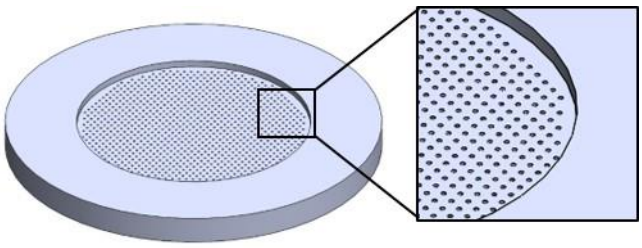

Figure 70 - Perforated plate distributor. 3D CAD model of the perforated plate of 2 mm depth with 967 holes of 0.3 mm diameter, spaced 1 mm apart in a 60° stagger angle.

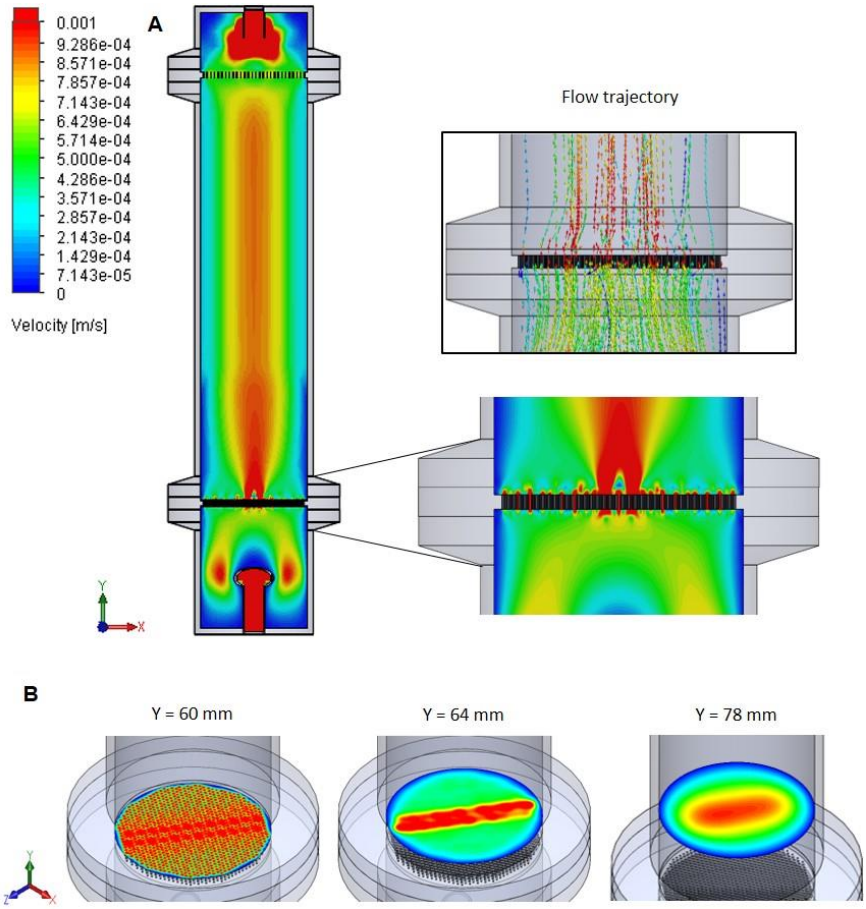

Figure 71 **-** Fluid velocity inside the optimised sFBB prototype with a 4-opening inlet and a perforated plate distributor. (A) Velocity cutplots of the XY-plane through the centre of the model with focus on the distributor area and corresponding flow trajectory plot depicted by coloured directional arrows. (B) Velocity cutplots of the XYZ planes on the surface of the distributor and 4 and 18 mm above it. Values are presented in velocity as m/s.

The velocity profile above the perforated plate presented a heterogeneous distribution where orifices in the centre section extending along the whole diameter of the plate dispersed flow at higher velocities than the remaining holes (Figure 71 A). The maximum velocity attained at the exit of the holes was 0.012 m/s, although the majority distributed fluid at 0.002 to 0.004 m/s (Figure 71 B). This behaviour generated focalised points of fast flow interspersed by low velocity ones which could potentially cause channelling effects. Moreover, the concentration of high velocities in the centre propagated vertically throughout the column, suggested a convergence between the distributor effects and the upward movement forced by the outlet, which would increment the inherent phenomenon of fast and upwards movement of beads in the centre of the column and slow and downwards near the wall. CFD results highlighted a

ring of slow fluid, almost stagnant, around the perimeter of the plate indicating the current design would not disperse liquid with enough velocity to overcome the stagnation points observed experimentally on the top of the surface of the distributor and immediate adjacent wall. Overall, the average velocity in the bioreactor was 0.000586 m/s with the distributor directing the fluid axially.

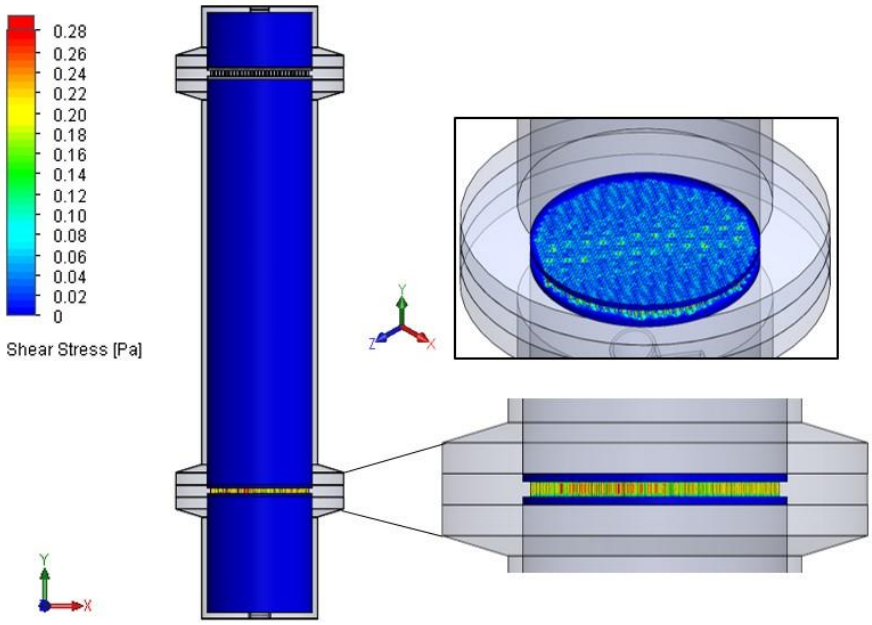

Figure 72 - Fluid shear stress inside the optimised sFBB prototype with a 4-opening inlet and a perforated plate distributor. Surface plots on the inner wall of the bioreactor and distributor surfaces, with focus on the distributor area. Values are presented in Pa.

Shear stress levels were minimal in the system, mainly verified on the top surface of the distributor and the immediately adjacent column wall with average levels of 0.00244 Pa and 0.000502 Pa, respectively (Figure 72).The maximum shear stress, 0.52 Pa, was attained within one of the orifices of the distributor and hence, would not cause any significant effect on the alginate beads inside the bioreactor.

As observed before, the system depressurised from the inlet to the outlet with a pressure drop of 10.42 Pa occurring at the distributor (Figure 73). Pressures remained stable in the contiguous volumes of each side of the perforated plate.

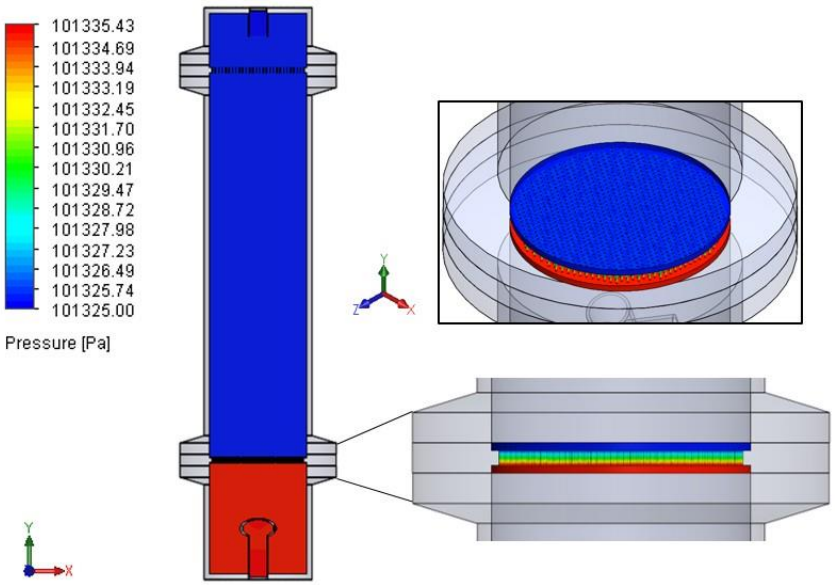

Figure 73 - Pressure inside the optimised sFBB prototype with a 4-opening inlet and a perforated plate distributor. Pressure cutplots of the XY-plane through the centre of the model with focus on the distributor area. Values are presented in Pa.

Based on the data and to minimise the stagnant fluid film near the wall, with the final purpose of eliminating channelling effects above the distributor, a second iteration on the distributor design was conceptualised. A ring of 210 holes of 0.3 mm diameter distancing 0.8 mm from each other was designed on the perimeter of the plate (Figure 74). On each hole, a shell with 0.15 mm height and 0.1 mm thickness was fitted covering half the diameter of the orifice to direct the flow towards the wall and promote active mixing in that region. To validate this concept a preliminary flow simulation with a plate only containing these openings was tested. The results corroborated the intention of the design with the fluid being directed against the wall and projected towards the centre of the column (Figure 75).

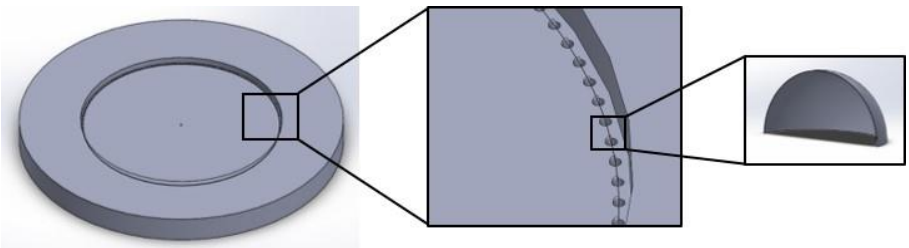

Figure 74 - Ring of shell holes on the perimeter of the distributor. 3D CAD model of distributor with 2 mm depth and holes of 0.3 mm diamater distancing 0.8 mm from each other, and half the diameter covered with a 0.1mm thick shell of 0.15 mm height.

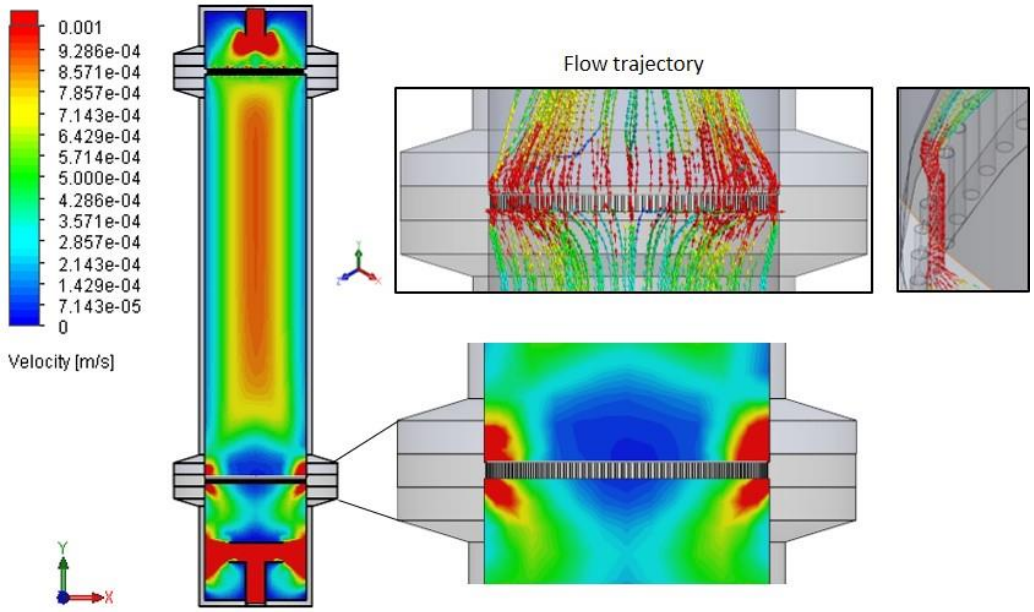

Figure 75 - Fluid velocity inside the optimised sFBB prototype with a 4-opening inlet and a distributor with shell holes. (A) Velocity cutplots of the XY-plane through the centre of the model with focus on the distributor area and corresponding flow trajectory plot depicted by coloured directional arrows. Values are presented in velocity as m/s.

The remaining surface of the plate was composed of 0.2 mm wide slots separated by 0.2 mm wide solid rings to increase the open area of the distributor while maintaining the cut-off size to prevent alginate beads from falling through the plate (Figure 76). Thus, the open area of this design was 47.4%.

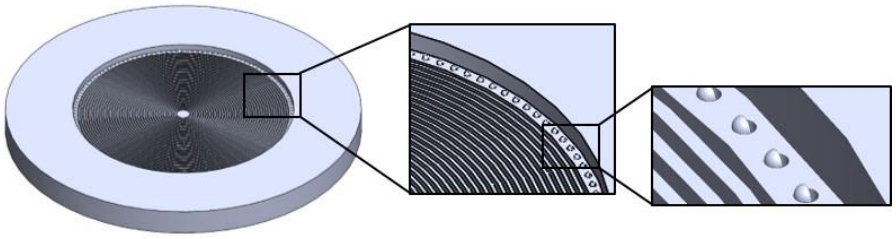

Figure 76 - Distributor with ring of shell holes and 0.2 mm slots. 3D CAD model of distributor with 2 mm depth, ring of shell holes as in Figure 74, and 0.2 mm wide slots separated by 0.2 mm wide solid rings.

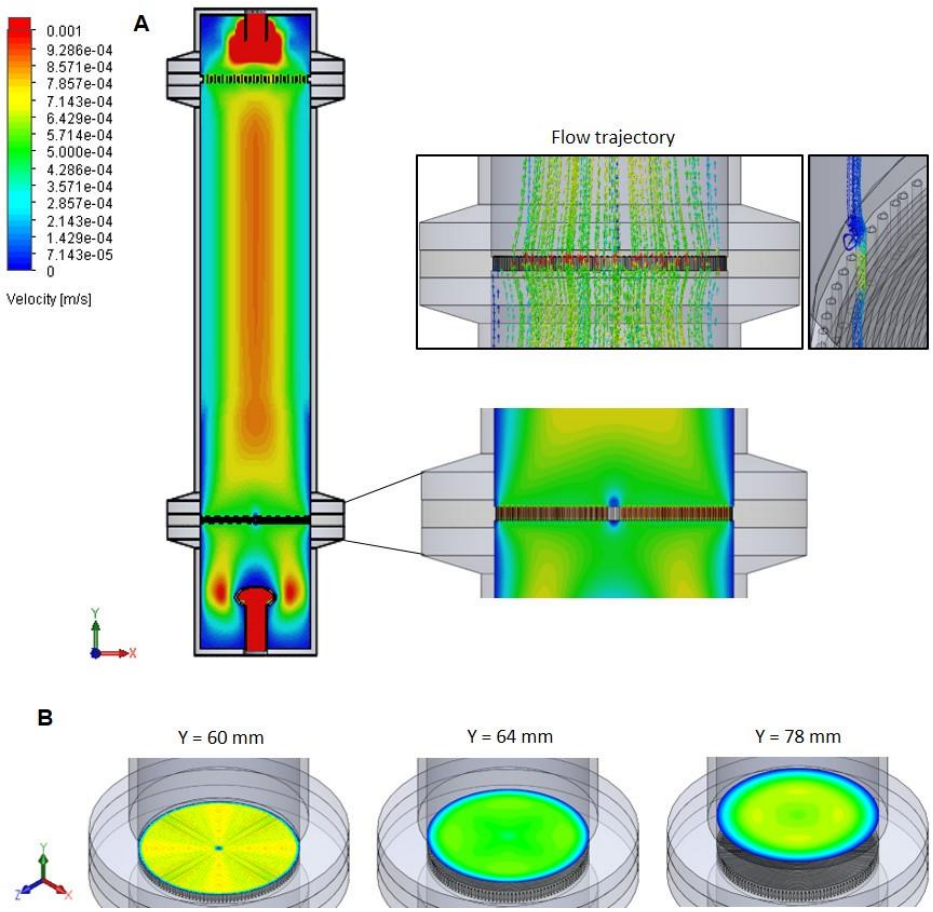

Figure 77 **-** Fluid velocity inside the optimised sFBB prototype with a 4-opening inlet and a distributor with a ring of shell holes and 0.2 mm wide slots. (A) Velocity cutplots of the XY-plane through the centre of the model with focus on the distributor area and corresponding flow trajectory plot depicted by coloured directional arrows. (B) Velocity cutplots of the XYZ planes on the surface of the distributor and 4 and 18 mm above it. Values are presented in velocity as m/s.

The increased open area produced a homogenous velocity pattern on the surface of the distributor without any noticeable points of fast flow (Figure 77 A). The maximum superficial velocity within a slot was 0.0012 m/s with fluid dispersing on the surface mostly at 0.0007 m/s and scattered points ranging from 0.0005 to 0.001 m/s (Figure 77 B). However, the shell covered holes on the perimeter of the disc did not minimise the stagnant film, although, they caused turbulence and directed the fluid towards the wall (Figure 77 A, flow trajectory). This was a consequence of the already low velocity at which the flow entered the distributor due to the presence of a stagnant layer underneath these holes.

The overall average velocity in the system was comparable to the perforated plate with the fluid also generally axially dispersed: 0.000579 *vs* 0.000586 m/s, respectively.

Conversely, the pressure drop across the current design was lower, only 0.4 Pa (Figure 78).

This hydrodynamic behaviour generated shear stress levels lower than those of the perforated plate ranging from 0.007 to 0.01 Pa in the central area of the distributor surface, although an average of 0.00069 Pa through the whole surface (Figure 79). Due to the projection of fluid against the wall contiguous to the distributor, the maximum shear stress in that area was 0.00312 Pa and an average of 0.000227 Pa.

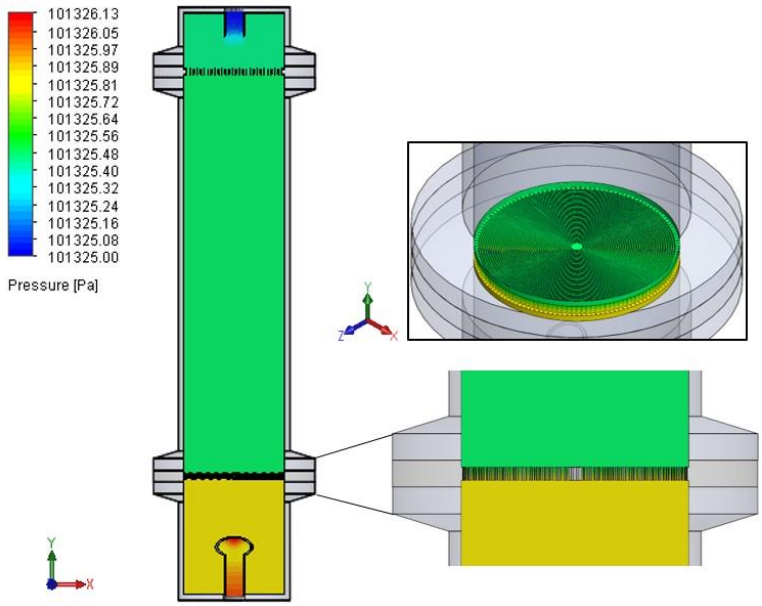

Figure 78 - Pressure inside the optimised sFBB prototype with a 4-opening inlet and a distributor with a ring of shell holes and 0.2 mm wide slots. Pressure cutplots of the XY-plane through the centre of the model with focus on the distributor area. Values are presented in Pa.

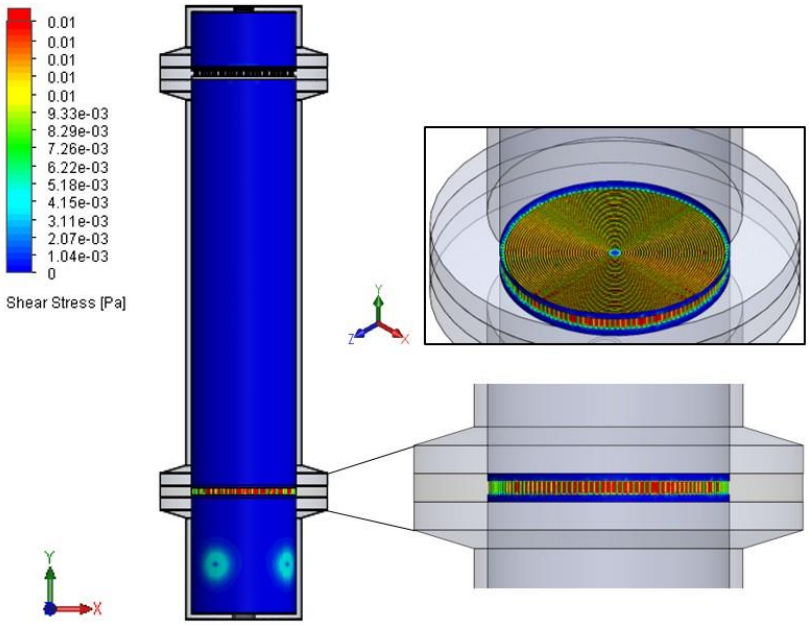

Figure 79 - Fluid shear stress inside the optimised sFBB prototype with a 4-opening inlet and a distributor with a ring of shell holes and 0.2 mm wide slots. Surface plots on the inner wall of the bioreactor and distributor surfaces, with focus on the distributor area. Values are presented in Pa.

A third iteration on the distributor design eliminated the shells concept as they did not succeed in reducing the stationary fluid and would be impractical to manufacture without a custom-made mould. Therefore, the distributor was solely composed of 0.2 mm wide slots interspersed with 0.2 mm solid rings and structural beams of 0.5 mm width arranged in a cross along the diameter of the disc (Figure 80). This additional feature reduced the open area by 0.5%.

The distribution of the flow with this design followed the same pattern with the velocity through the slots attaining a maximum of 0.012 m/s and ranging from 0.0005 to 0.01 m/s on the surface of the disc (Figure 81 A). Because of the structural beams, the CFD simulation highlighted stationary and low velocity fluid above and around these features, respectively (Figure 81 B). Conversely to the previous design, this distributor was able to reduce the stagnant film on its perimeter and contiguous wall, demonstrated by the thinner dark blue ring around the edge of the plate. This advantage did not impact the average velocity in the system which was 0.000581 m/s.

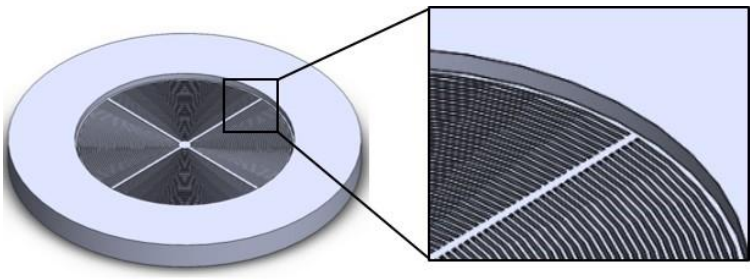

Figure 80 - Distributor with 0.2 mm slots. 3D CAD model of distributor with 2 mm depth, 0.2 mm wide slots separated by 0.2 mm wide solid rings and 4 supporting beams along the radius with 0.5 mm width.

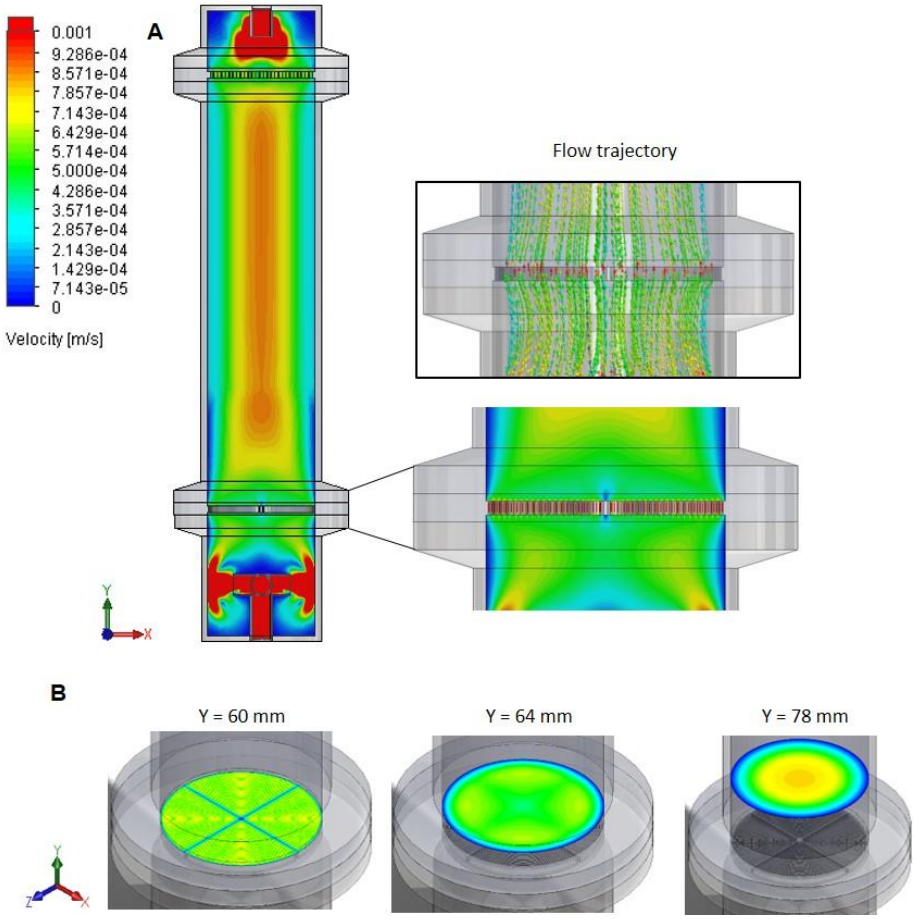

Figure 81 - Fluid velocity inside the optimised sFBB prototype with a 4-opening inlet and a distributor with 0.2 mm wide slots. (A) Velocity cutplots of the XY-plane through the centre of the model with focus on the distributor area and corresponding flow trajectory plot depicted by coloured directional arrows. (B) Velocity cutplots of the XYZ planes on the surface of the distributor and 4 and 18 mm above it. Values are presented in velocity as m/s.

Regarding shear stress on the distributor, surface levels remained between 0.007 and 0.01 Pa with a maximum of 0.015 Pa near the structural beams (Figure 82). On the contiguous wall, the average was 0.000436 Pa and maximum of 0.00573 Pa. These values, although higher than those from the previous design, were still in the low range spectrum of shear stress. Moreover, this design maintained the pressure drop of 0.4 Pa (Figure 83).

From the preliminary theoretical assessment, the final concept of 0.2 mm wide slots distributed the flow in a more homogenous velocity pattern across the distributor surface which suggested that it could induce a consistent and even fluidisation of the hydrogel bed.

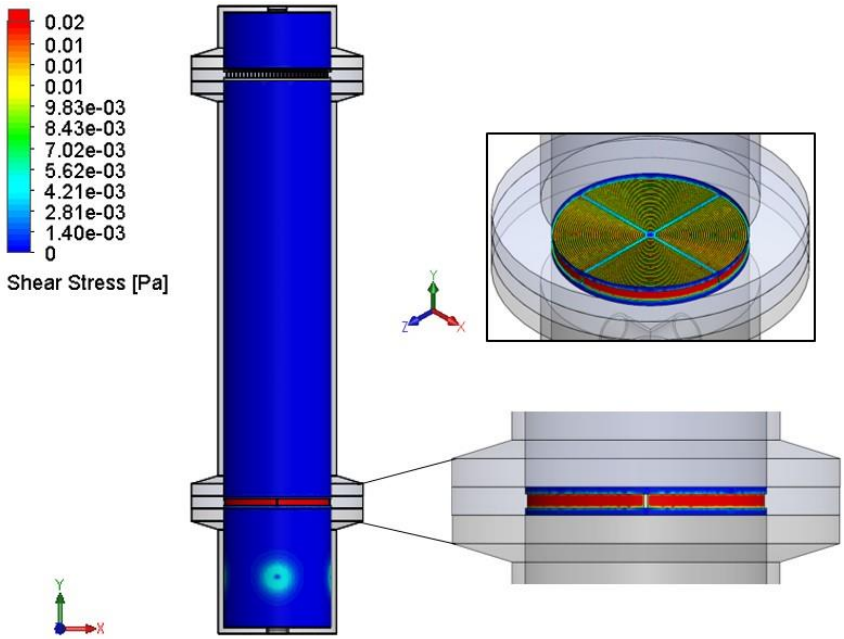

Figure 82 **-** Fluid shear stress inside the optimised sFBB prototype with a 4-opening inlet and a distributor with 0.2 mm wide slots. Surface plots on the inner wall of the bioreactor and distributor surfaces, with focus on the distributor area. Values are presented in Pa.

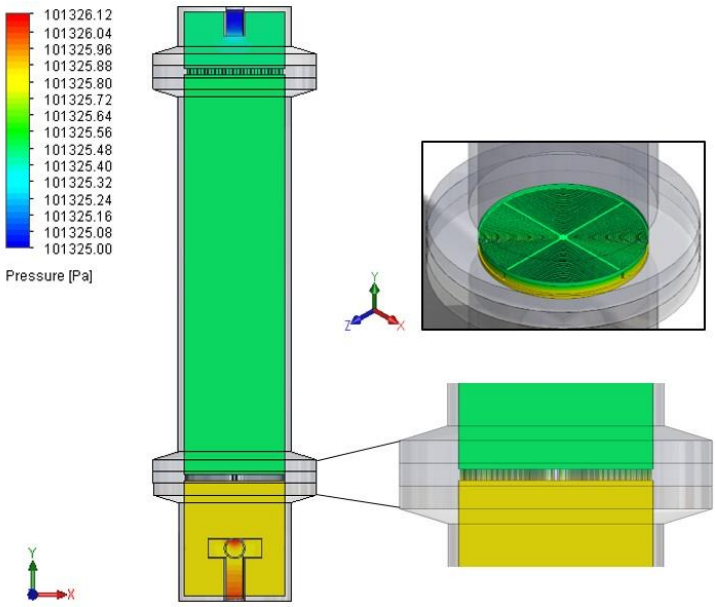

Figure 83 **-** Pressure inside the optimised sFBB prototype with a 4-opening inlet and a distributor with 0.2 mm wide slots. Pressure cutplots of the XY-plane through the centre of the model with focus on the distributor area. Values are presented in Pa.

5.3.2. Manufacturing the optimised prototype

The improved design required an experimental test to validate the CDF theoretical results and assess the bioreactor performance and therefore, each integrating part had to be manufactured. As a prototype with tailored features, customisation was necessary although in a cost-effective approach considering the device was still in the experimental/testing phase subjected to modifications and not a final commercial product. The main body of the bioreactor was a simple multi-element concept which would not suffer alterations independently from testing different distributors and inlets designs. Thus, the 3 main parts were customised in glass, with flanges of standard dimensions fitted at the extremities to enable using commercially available tri-clamps to assemble and seal the bioreactor (Figure 84 A). The main column featured the sampling port also made of glass with 2 mm outer and 1 mm inner diameters to prevent any blockage of the beads (Figure 84 B). Communication with the bottom of the alginate bed and the exterior was finalised by adapting high-strength silicone tubing.

On the opposite end of the flanges, the inlet and outlet cups were conceived with a GL45 screw-thread for standard lids to effectively close the system (Figure 84 D). Each lid was

also custom-made in polypropylene with fixed stainless-steel 316 protrusions where silicone tubing could be adapted to complete the recirculation circuit (Figure 84 C).

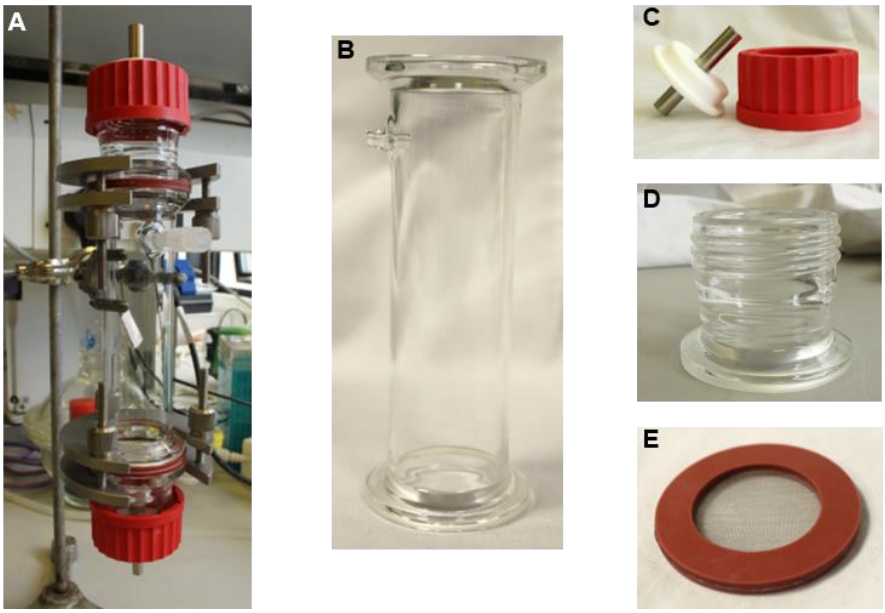

Figure 84 - Manufactured optimised sFBB prototype. A – Assembly of complete setup of the second sFBB prototype; B – Main glass column of the bioreactor with fitted flanges and 2 mm outer and 1 mm inner diameter sampling port; C – Polypropylene lid with stainless steel protrusion; D – Inlet/outlet cup fitted with a flange and a GL45 thread for screwing in the lids; E – Top filter composed of stainless steel mesh and flat silicone washers.

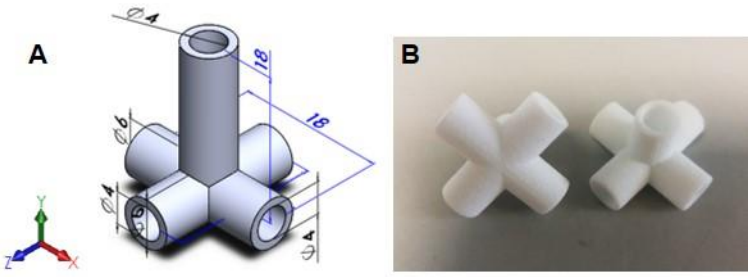

Figure 85 - 4-opening inlet with 4 mm inner diameter. (A) 3D CAD model with dimensins in mm. (B) Fabricated model in nylon polymer through selective laser sintering.

The inlet point conceived in the CAD model and tested in the CFD simulations had four exit points oriented 90° from each other. All models ran with an inlet of 6 mm internal diameter as a reference from the initial vertical inlet. However, given the experimental

low flow rates the sFBB operated on, a 4 mm diameter was considered to enable the operation at lower flow rates without compromising the fluid behaviour (Figure 85 A). From the flow simulation, a 4 mm inner diameter did not significantly change the fluid behaviour as velocities beneath the distributor still equilibrated to 0.0004 - 0.0006 m/s (Figure 86 B). The dispersion of the flow from the inlet attained a maximum speed of 0.03 m/s compared to 0.02 m/s from the 6 mm one (Figure 86 A). This suggested that at low flow rates, a narrower diameter would maintain the performance and thus, enable accurate operation at a wider range of flow rates.

Moreover, it generated an average shear stress on the inlet cup wall of 0.00102 Pa with a maximum of 0.034 Pa (Figure 87 A). The pressure was still maintained at 101325.85 Pa (Figure 87 B).

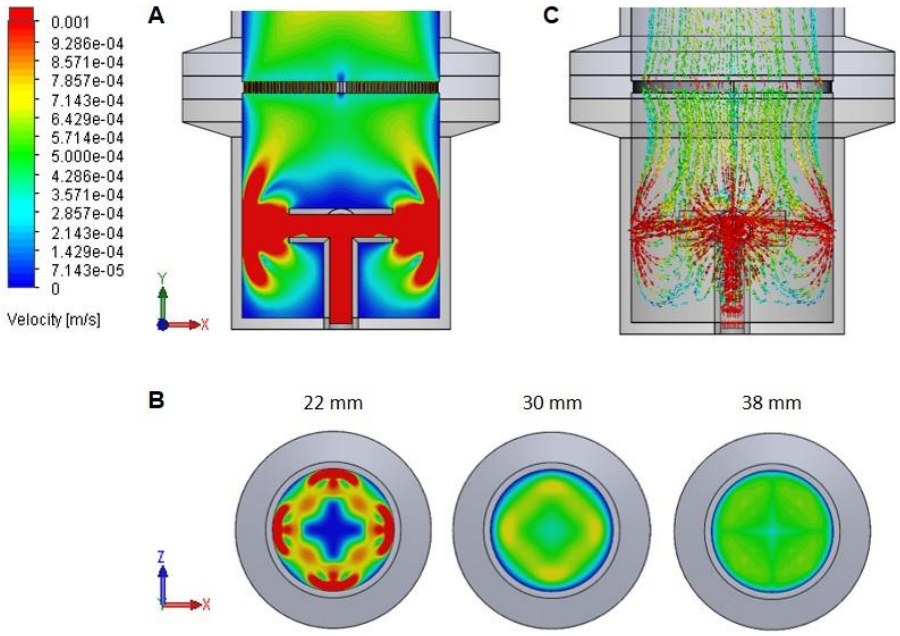

Figure 86 **-** Fluid velocity inside the inlet cup of the optimised sFBB prototype with a 4-opening inlet with 4 mm inner diameter. Velocity cutplots of the XY-plane through the centre of the model (A) and the XZ-plane at 22, 30 and 38 mm distances from the bottom of the sFBB (B). (C) Corresponding flow trajectory depicted by coloured directional arrows. Values are presented in velocity as m/s.

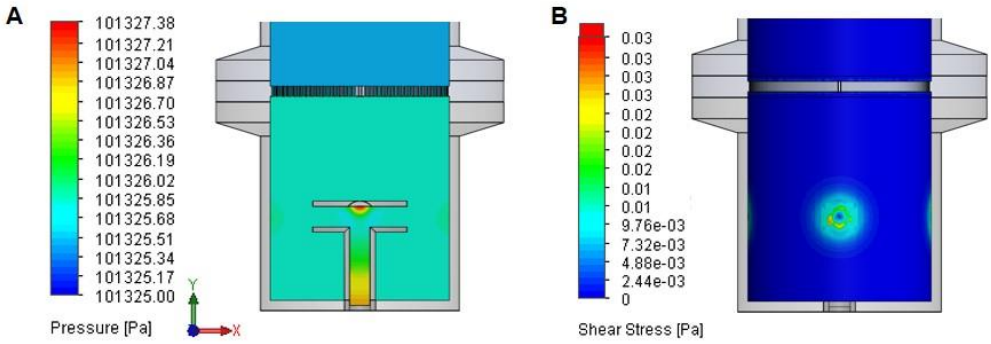

Figure 87 - Pressure and shear stress inside the inlet cup of the optimised sFBB prototype with a 4-opening inlet with 4 mm inner diameter. (A) Surface plot of fluid shear stress on the inner wall of the model facing one of the openings of the inlet. (B) Pressure cutplots of the XY-plane through the centre of the model. Values are presented in Pa.

Due to the geometry and small size of the inlet, the fastest and most economical way to produce it was through 3D printing. Specifically, selective sintering laser would produce an accurate geometry from a resistant material without adjusting the design with support structures. This feature was sintered from nylon powder creating a strong final product which could withstand autoclaving cycles or ethanol-sterilisation and be adapted to the stainless-steel part of the lid (Figure 85 B). Moreover, because of this modification, the stainless-steel protrusions in the inlet lid had an internal diameter of 4 mm, while the one for the outlet was 6 mm.

The fine structure of the 0.2 mm wide slot distributor posed the greatest manufacture challenge. This feature could not be produced by 3D printing since FDM nozzles had a wider diameter than the slots of the design and SLS would not produce a smooth surface, generating imperfections which could distort the flow as well as wear the fluidising alginate beads because of the constant impact with a rough surface. An attempt to resort to SLA demonstrated that the slots were too narrow for that technique since the melted structure merged together when solidifying forming one compact part without openings (Figure 88 B).

Hence, 3D printing was discarded as a manufacturing tool, and the focus was drawn to laser cutting. Because the laser beam is narrow and focused, this could be a promising, low-cost approach. A first trial cutting 0.1 mm metal sheets demonstrated that the intended dimensions were impossible to replicate on the current material as the structure easily disintegrated or burnt during cutting. Also, the restriction to only cut 0.1

mm thick sheets constituted an issue as on its own this distributor would be very fragile, notwithstanding the weight of the settled bed of alginate beads. Given these constraints, the design was adjusted to the requirements of the manufacturing process. While the slots maintained their 0.2 mm width to prevent beads from falling through the distributor, the interval between them was increased to 0.8 mm as well as the width of the structural beam to 1 mm to create a robust feature and allow for effective heat dissipation of the material during the incidence of the laser (Figure 88 A). An additional aperture in the centre of the plate in cross-shape of 0.2 mm width and 0.6 mm length was included to minimise the dead fluid spot in the middle of the column.

Moreover, other possibilities of raw materials were explored. Aluminium oxide ceramic is a widely used composite in dental and bone implants due to its high mechanical strength, wear resistant, good biocompatibility and ability to sustain ethanol-sterilisation certifying its use for sterile cell culture conditions. It could also be laser cut from pieces of a few millimetres deep, constituting a more robust part. Although, given the availability of the material and the designed dimensions of the distributor, the imposed thickness of the feature was 1 mm rather than the initially projected 2 mm.

Before, laser-cutting the material, a CFD simulation with all the modifications was run to verify the performance of the adjusted model. This design reduced the open area to 20% and generated focalised points of high velocity flow immediately on the surface of the distributor, but not as pronounced as in the perforated plate (Figure 89 A). The highest velocity out of the slots was 0.0016 m/s and dispersion on the surface covered a wider range of velocities from 0.00009 to 0.0006 m/s (Figure 89 B). Nonetheless, velocities equilibrated to the 0.0004 to 0.0006 m/s range a few millimetres above the surface (~ 4 mm) and the average velocity inside the bioreactor was still 0.000583 m/s. This new pattern generated a maximum shear stress level on the distributor surface and contiguous wall of 0.024 Pa but an overall average of 0.00324 Pa (Figure 90). The pressure drop across the distributor, 0.46 Pa, was similar to the previous designs (Figure 91). Overall, from the CFD preliminary results, the modified distributor did not perform markedly differently from the initial concept, achieving the same range of velocities and promoting fluid movement on the perimeter of the plate. This design was successfully laser cut in the 1 mm thick aluminium oxide ceramic without any impairments (Figure 88 C).

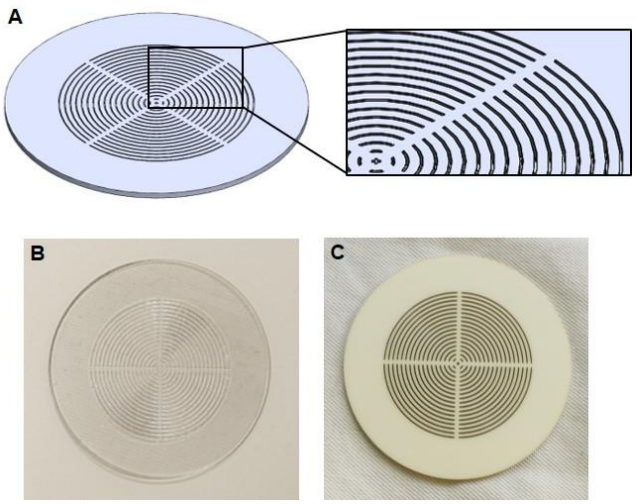

Figure 88 **-** Distributor of 1 mm depth with 0.2 mm wide slots spaced at 0.8 mm and with supporting beam of 1 mm width. (A) 3D CAD model of distributor. (B) Model 3D printed through stereolitography. (C) Distributor laser cut in aluminium oxide.

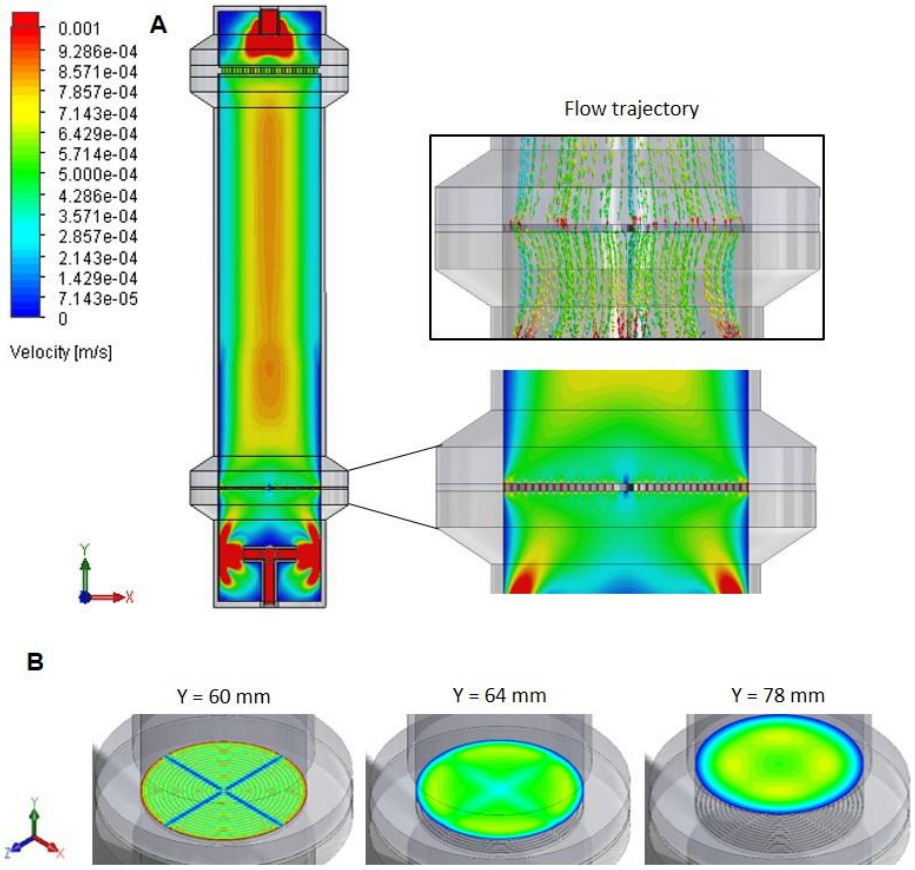

Figure 89 **-** Fluid velocity inside the optimised sFBB prototype with a 4-opening inlet and a distributor with 0.2 mm wide slots spaced at 0.8 mm. (A) Velocity cutplots of the XY-plane through the centre of the model with focus on the distributor area and corresponding flow trajectory plot depicted by coloured directional arrows. (B) Velocity cutplots of the XYZ planes on the surface of the distributor and 4 and 18 mm above it. Values are presented in velocity as m/s.

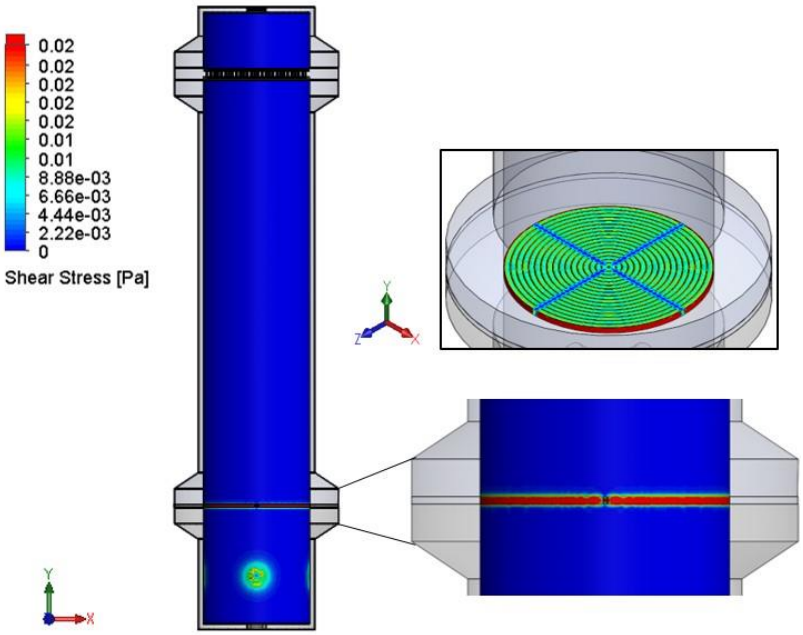

Figure 90 - Fluid shear stress inside the optimised sFBB prototype with a 4-opening inlet and a distributor with 0.2 mm wide slots spaced at 0.8 mm. Surface plots on the inner wall of the bioreactor and distributor surfaces, with focus on the distributor area. Values are presented in Pa.

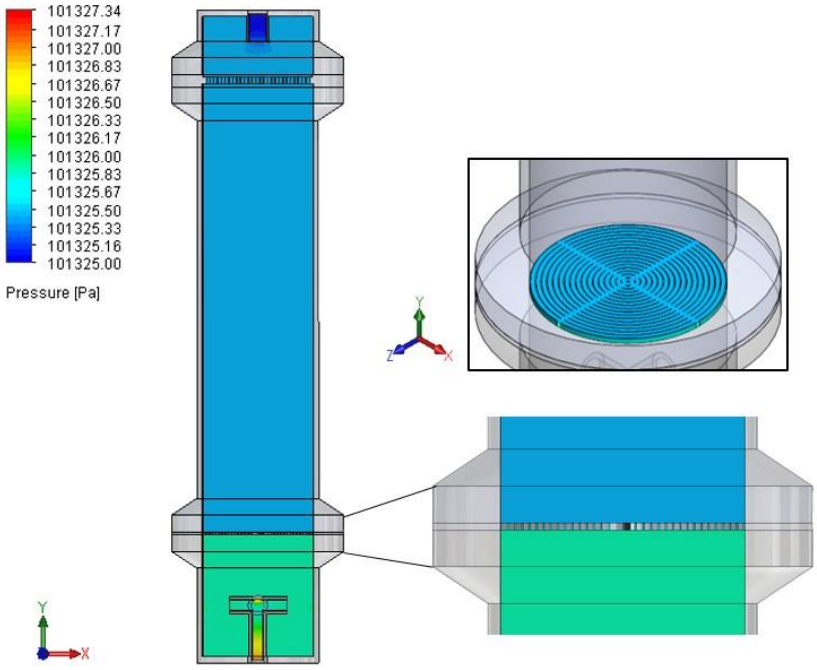

Figure 91 - Pressure inside the optimised sFBB prototype with a 4-opening inlet and a distributor with 0.2 mm wide slots spaced at 0.8 mm. Pressure cutplots of the XY-plane through the centre of the model with focus on the distributor area. Values are presented in Pa.

The final element of the setup was a filter to prevent bead elutriation. For this, a woven wire mesh of stainless steel 316 with 0.212 mm aperture and 0.09 mm wire diameter was placed in between two silicone flat washers and placed before the outlet (Figure 84 E). The washers were adapted to provide proper sealing to the assembly, and they were also used at the distributor point.

Maintaining the setup assembled and sealed were U-shape aluminium tri-clamps with the exact dimensions of the flanges and which adjusted vertically allowing variation in the thickness of the parts fitted in between.

5.3.3. Experimental validation of optimised sFBB prototype

5.3.3.1. Bed expansion of optimised sFBB prototype

With the prototype manufactured, experimental validation was necessary to determine the performance of the bioreactor. The new prototype was assembled as illustrated in Figure 84 A.

Firstly, the fluidisation efficacy of the optimised sFBB design was investigated by progressively increasing the flow rate generated by the pump and measuring the respective fluidised bed height. The bed continued to expand with increased flow rates and double expansion of the bed was reached at 25.7 mL/min with a similar profile of the sintered glass of the initial prototype (Figure 92).

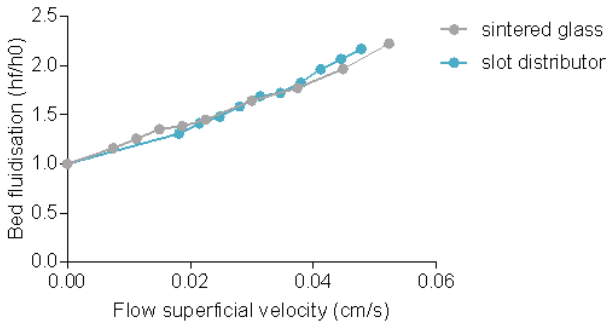

Figure 92 **-** Bed expansion in optimised sFBB prototype. Plot of increments in flow superficial velocity and corresponding bed expansion determined by the ratio of the fluidised bed (H_f) and the settled bed (H_0).

To study further the fluidisation of the bed and corroborate the results obtained from CFD simulations, bed expansion pattern of stained alginate HepG2 beads was determined using the method applied on *section 4.3.4.1*. Fluidisation of the bed was attained as previously verified with beads moving from the bottom to the top of the bed as it started to expand (Figure 93). There was continuous motion, especially immediately above the distributor and contiguous wall, where the projected slot induced a fast movement of beads preventing the stagnation points observed in the first prototype (Figure 94).

However, after 2 min of operation the bed was not completely homogenised as had been observed with the sintered glass. Opposite the highly fluidised area, there was a considerable portion of the bed that experienced very slow flows, displaying almost no fluidisation and causing a heterogeneous expansion (Figure 95). Only after 4 min of fluidisation the bed presented a more evenly mixed pattern. This phenomenon was attributed to a misassemble of the setup or eventually a high sensitivity to inclination of the column which could not be compensated by a thin (1mm thick) distributor, as once the bioreactor was rotated along its support axis (the clamp which was holding it) there was an inversion between the fluidised and the stagnant area. Yet, this distributor design was still able to effectively induce a limited expansion of the bed.

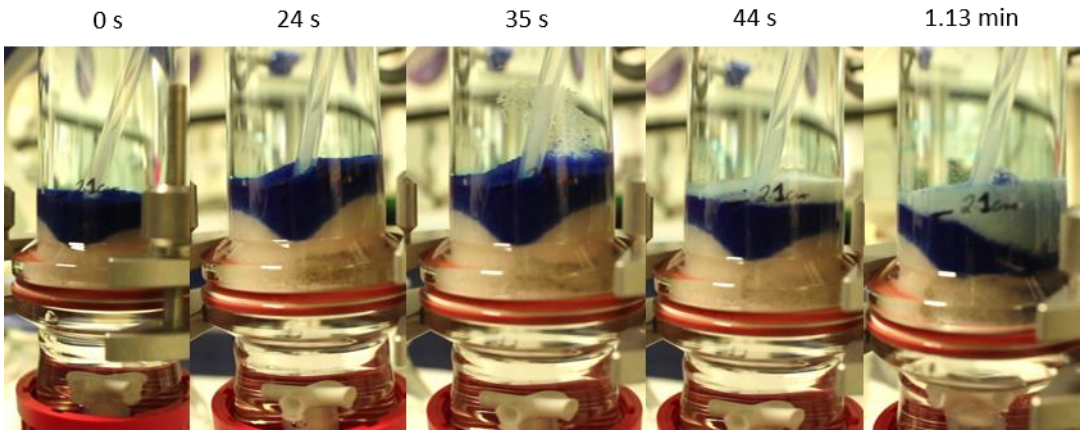

Figure 93 **-** Bed expansion pattern in the optimised sFBB prototype. Fluidisation process of alginate encapsulation beads was set for double expansion at 25.7 mL/min. These images depict the start of the process.

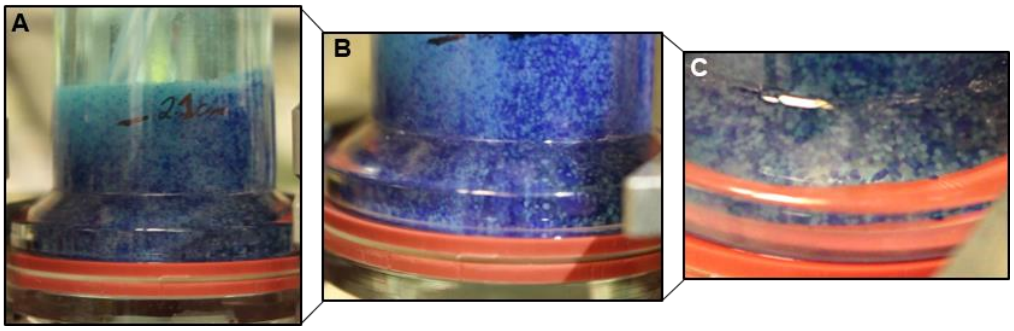

Figure 94 - Highly fluidised beads on the distributor surface and contiguous wall.

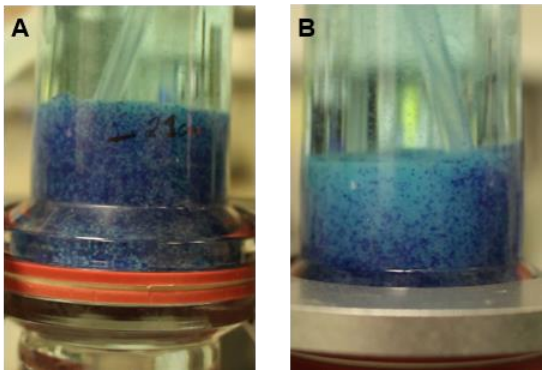

Figure 95 - Heterogenous bed fluidisation in optimised sFBB prototype. Section of bed with continuous movement of beads (A), opposite an almost stagnant area highlighted by the low degree of mixing between stained and non-stained beads (B).

5.3.3.2. Equilibration time of optimised sFBB prototype

The characteristic times of the new design were also explored to understand its impact on the circulation and mixing. As in *section 4.3.4.2*, times were monitored through a tracer dye except in this case bromophenol blue was used to avoid staining the distributor and inlet with methylene blue (Figure 96). The circulation time inside the bioreactor was 2 min. This was comparable with those attained in the prototype with the sintered glass distributor, indicating the time the fluid takes to travel through the bioreactor was not a function of the distributor, even if the distributor did not disperse the fluid homogenously through its surface as was observed by not promoting a homogenous fluidisation of the bed. Similarly, the mixing time was independent of the distributor design with the system attaining equilibrium 13 min after the injection of the dye. This demonstrated that the flow albeit impaired by the distributor still moves

through the path that offers the least resistance completing the recirculation circuit. The obtained mixing time was approximate to the interval of the initial prototype (10 – 12 min).

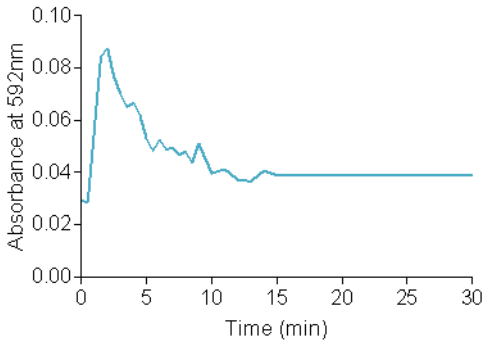

Figure 96 - Equilibration time in the optimised sFBB prototype. Progression of bromophenol blue in the system determined by measured aborbances at 592 nm.

5.3.3.3. Biological performance of the optimised sFBB prototype

The final validation of the optimised design required assessing its biological performance, i.e. how it sustained cell viability and induced proliferation compared to the initial prototype.

Thus, alginate encapsulated HepG2 cells were cultured for 12 days in parallel in the initial sFBB (with the sintered glass distributor) and in the new design with the 0.2 mm wide slot distributor. This culture followed the same protocol and method as in the previous chapters. The final cell density obtained in the initial prototype was 23.8 ± 2.37 million cells/mL, whereas in the optimised design it only reached 15.6 ± 2.91 million cells/mL (Figure 97 A). This difference was significant from day 8 onwards. Cell viability was also different between the two prototypes with the former sustaining 99.1% of the cells viable and the latter 92.8% (Figure 97 B). These discrepancies were supported by the captured images of the alginate beads in culture (Figure 98). Beads in both bioreactors maintained their shape and integrity with those from the initial bioreactor displaying a similar density of spheroids in all beads. Conversely, in the optimised design beads did not have equivalent cell densities, with some beads filled with large, developed spheroids evident from the darker masses inside, while others were mainly

composed of smaller spheroids or even single cells which did not expand. It also resulted in the reduced viability attained in this prototype as correspondingly low cell density beads also displayed a stronger fluorescence signal for dead cells (PI staining).

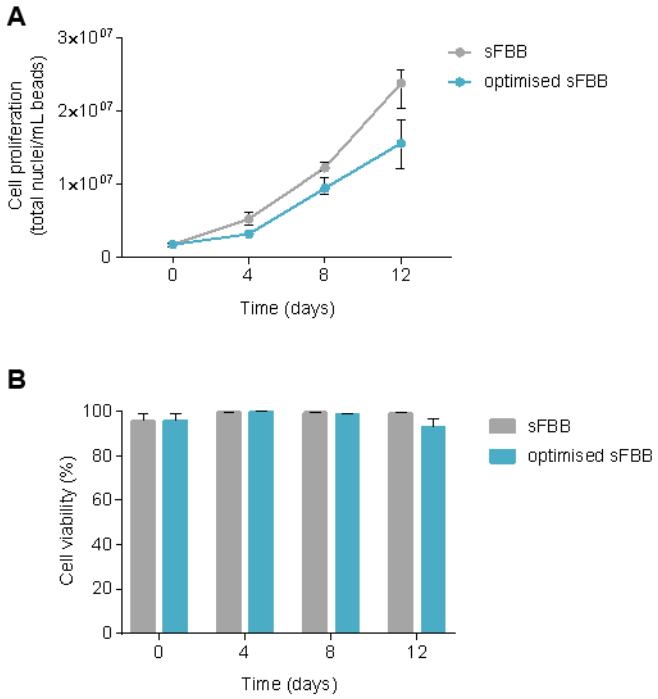

Figure 97 - Biological performance of the optimised sFBB prototype compared to the initial sFBB. Cell proliferation curves (A) and corresponding viabilities (B) throughout 12 days of culture. Data presented are average ± range (n = 1).

These inconsistencies were a result of the heterogeneous fluidisation of the bed where zones, opposite the highly fluidised areas, displayed limited movement of the beads. This phenomenon persisted during culture and was momentarily overcome by increasing the fluid flow rate which was able to break the stagnant area. However, as the bed settled to its new expansion level, the same heterogeneous pattern was observed. It emphasised that the source of the problem was intrinsic to the new design rather than a misassembled setup.

Overall, the tests conducted demonstrated that the current design underperformed the initial prototype mostly as a consequence of the designed distributor, which will need further optimisation for the bioreactor to be established as a robust and reproducible commercial device.

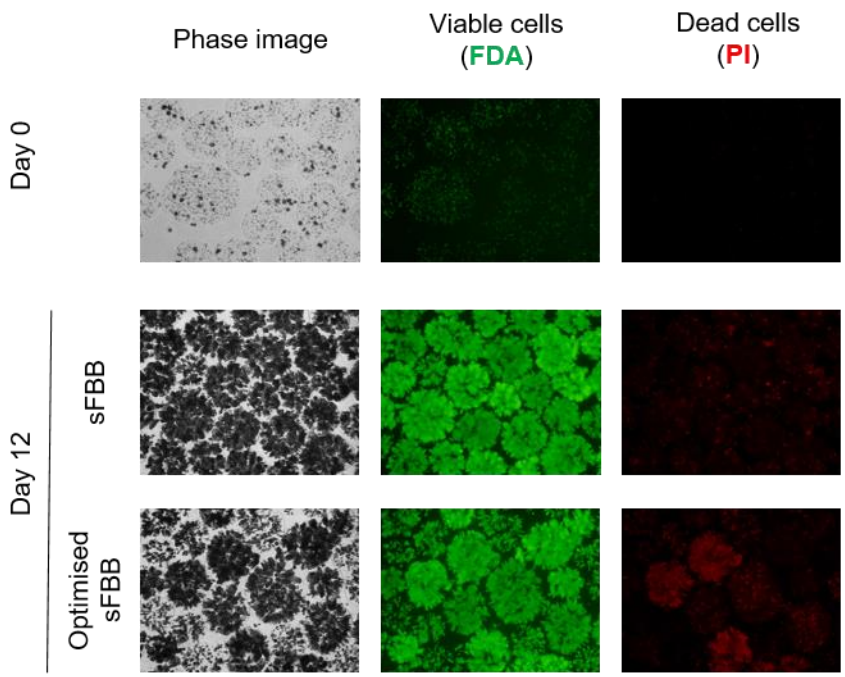

Figure 98 - Alginate encapsulated HepG2 cells cultured in the optimised sFBB prototype for 12 days. Image of cell beads were captured on days 0 and 12 of culture from the initial and optimised sFBB prototype. Viable cells stained for FDA and dead cells stained for PI.

5.4. Discussion

Establishing a prototype as a commercial product takes several design iterations until all parameters are operating at their optimal performance. For the sFBB that implied generating a consistent and homogenous fluidisation within a bioreactor composed of standardised features.

To achieve this aim design optimisation followed a rapid-cycle testing approach, combining computational fluid dynamics (CFD) results with the operator's experience and only experimentally testing the designs with the best theoretical performances. Moreover, to accelerate the process, the elements subjected to more modifications, specifically the inlet and distributor, were produced by rapid prototyping techniques.

As a baseline, CFD analysis of the initial sFBB prototype confirmed that the interval of fluid velocities attained in the model included the intended linear flow rates used in the scale-down method. It also confirmed that the system operated at low shear stress levels. within the lower range of physiological shear and thus, suggesting the achieved stress is not harmful for cultured cells [365].

However, the model did not clearly represent the experimentally observed channelling effects suggesting that the definition of the distributor as a porous media did not accurately reflect the real performance of the bioreactor. A reliable CAD model of the distributor could be produced by 3D scanning the feature using, for example, X-ray computed micro-tomography and thus, obtaining more precise data [366]. Moreover, this simulation, and the others which followed, only accounted for the fluid behaviour and did not estimate particle fluidisation, since it was assumed that coherent fluid velocity and dispersion would guarantee minimal fluidisation of the bed. Simulation of complete liquid-solid fluidised bed would require combining CFD with discrete element modelling using Newton's equation to determine the movement of the solids and the liquid-solid, solid-solid and solid-wall interactions [367].

For the optimised prototype, the main body of the bioreactor was conceptualised to be separated in 3 individual parts to create a more practical structure which could tolerate consecutive alterations of the key fluidisation features (inlet and distributor) as well as facilitate maintenance and cleanness, and add flexibility for future needs and purposes.

Although not thoroughly investigated or explored in the literature, the flow inlet point in a fluidised bed bioreactor modulates the fluid behaviour at the start of dispersion. The ideal design diffuses the flow in as many directions as possible as to promote radial movement and a high degree of mixing before it reaches the distributor. Thus, the optimised geometry included 4 openings arranged horizontally in a 90° angle, instead of the initial 2 vertical ones, which corroborated experimentally the performance predicted by the CFD data.

Increasing the number of openings in the inlet to 6 or 2 levels of 4 openings, did not bring any significant advantage to the flow dispersion, presumably due to the range of low flow rates operating in the sFBB setup. This indicated the geometry of the inlet (number and diameter of orifices, length, position) is subjected to the operational flow rates for expansion of the bed. A possible alteration would be to reduce the internal diameter and increase the number of openings per area. Hafiz et al. verified that increasing the number of inlets increased the velocity magnitude and the pressure drop in the calming zone [368]. However, it arose from an increment in the flow rate, as equal flow rates were fed from each inlet point rather than a stream divided into 3 points. Nonetheless, increasing the number of inlets creates a more uniform distribution of the flow and consequently,

reduces the turbulence field in the bioreactor, particularly its propagation throughout the total volume [369].

Another widely referred approach to control the flow entrance in fluidised beds is using tapered fluidised beds which consist of a conical shape vessel where the entering fluid produces an upwards jet of flow forcing the solids to fluidise in the middle and descend on the inclined walls [370]. Often this design generates large portions of static unfluidised regions and erosion of particles [371]. Therefore, a number of devices have adopted this geometry only at the bottom of the column to minimise the dead zones [106]. However, a similar effect was achieved in this system by positioning the inlet at the optimal distance from the distributor and dispersing the flow inside the bioreactor in several directions.

For the distributor, the purpose was to create the simplest design which induced homogeneous fluidisation eliminating the stagnation points near the wall. The perforated plate produced a velocity pattern of jet streams, with potential to originate channelling effects, and did not impact on the stagnant fluid film near the wall. This behaviour has been experimentally demonstrated by magnetic resonance where in the lowest region of the bed jets of fluid induced movement of the surrounding solids but between each pair of jets there were motionless particles sitting on the upper surface of the distributor [372]. Also, this type of distributor is more common in large scales or gas-solid/gas-liquid systems where the turbulent regime prevails [96,373,374]. Given the low velocities achieved in the sFBB, the fluid regime is mostly laminar (with sporadic turbulent points) and thus, the efficacy of the perforated plate could be reduced.

Conversely, the 0.2 mm wide slot distributor produced a homogeneous fluid velocity pattern with the advantage of reducing the stagnant film on the contiguous wall of the distributor. This behaviour was attributed to the significant increase in the open area of the plate. Subsequently, increments in open area are associated with an easier induction of fluidisation since it lowers the minimum fluidisation velocity of the bed due to the higher interstitial fluid velocity, i.e. there is more fluid movement inbetween openings causing the solids in those regions to move which, consequently, promotes a faster fluidisation of the bed [375]. CFD simulation validated this premise when the interstitial space was increased because of the manufacturing limitations and it was visible by the intensification of low fluid velocities on the surface of the solid rings.

Although the modified distributor (0.2 mm wide slots spaced at 0.8 mm) theoretically did not impair fluid dispersion, retaining a similar behaviour and associated velocities to the ideal design, its experimental validation did not corroborate entirely the flow simulation results. Where fluidisation was effectively induced, beads were moving at a fast rate including in the contiguous distributor-wall region, eliminating the stagnant spots. However, expansion was heterogeneous with significant motionless portions of the bed opposite the ones fluidising. This impacted the performance of the bioreactor resulting in diminished cell viability and proliferation, evidencing that the final design did not constitute an optimisation over the initial sFBB prototype.

Preliminary speculation attributed this behaviour to the misassemble of the setup; due to its multiple parts it was more susceptible to leakages and pressure inconsistencies. However, after analysis and careful assessment of the assembly method, the probable cause was the depth of the distributor (1 mm) which does not sustain the fluid sufficiently to align it and thus, any deviation from ideality had a great impact on its performance. In the current setup, inclination of the column, even if not abrupt and only noticeable after attentive observation, appears to be the external force that the thin distributor could not overcome. This was related to the faster motion of beads in the region on the inclination angle.

In deeper distributors, the fluid takes longer to move through, which might imprint more solidly on it the designed orientation and dispersion, as they are also less subjected to influences of external misalignments. For instance, the 4 mm depth and random structure of the sintered glass distributor gave enough robustness to the setup to disregard the effect of any inclination in the fluidisation of the bed. Therefore, the distributor will require further optimisation, primarily increasing its depth and secondly, if the performance is not improved, revisiting the design of the orifices. The effect of the inclination can be preliminarily assessed with CFD by setting the model on an angle. Although, the experimental validation of the design could still be impaired by the manufacturing feasibility and thus, a prototype solution would be to stack several thin distributors to achieve the desired depth; this in itself adds an unwanted level of complexity of alignment.

In terms of orifice design, complex constructions could be explored. Studies have demonstrated that orifices with oblique angles promote an adequate radial distribution

of the flow. Paiva had suggested that the oblique dispersion by the metallic mesh distributor was the likely cause for improvement of the quality of fluidisation compared to a perforated plate with similar pressure drop [376]. More recently, other investigations have supported these findings by demonstrating that inclined holes create a swirling pattern in moving solids where the tangential velocity increases with the radial coordinates, i.e. particles move faster near the wall of the column [98,377]. Regardless of the orifice arrangement, the depth of the distributor plate will most certainly have to be superior to 1 mm.

The distributor pressure drop also plays a crucial role in the bed fluidisation as it needs to be high enough for adequate dispersion of the flow across the bed area [82]. However, at very high or low pressure drops fluid maldistribution occurs particularly at the bottom of the bed, reducing the quality of fluidisation [376,378]. Therefore, there is a fine equilibrium which needs to be attained and is a function of the hydrodynamic conditions as well as the design characteristics of the distributor, namely its open area. Literature rarely includes the thickness of the distributor as a design parameter to consider on the influence of the pressure drop. Qureshi and Creasy have correlated the thickness with the discharge coefficient, which, when associated to the pressure drop, indicated that the distributor pressure drop decreases as the depth of the plate increases [378,379]. Yet, adjustments to the open area and thickness of the distributor did not impact greatly on the pressure levels in the system, and, as alginate beads were not considered in the flow simulations, direct influence on the bed fluidisation could not be assessed.

Moreover, the average velocity in the bioreactor was not substantially altered by the inlet and distributor designs since values were comparable in all simulations. These features appeared to influence the fluid pattern and direction rather than the velocity, leaving it to be governed by the flow rate and H/D ratio. Subsequently, it certifies the use of this ratio (H/D) as a scale down parameter if the purpose is to maintain superficial velocities between scales.

Even though the current prototype did not outperform the initial sFBB, the new concept facilitates optimisation by enabling multiple tests until the best combination of distributor and inlet designs is achieved to promote homogenous fluidisation.

As for rapid prototyping methods, 3D printing proved to be an advantageous technique for creating resistant and biocompatible parts for cell culture since the inlet feature

sustained autoclave sterilisation and 12 continuous days of dynamic culture. This process has been applied to building complete bioreactors with intrinsic features and designs and even on microfluidics, demonstrating its versatility [380,381]. In the context of fluidised beds, it successfully developed complete columns [382] or just features such as distributors both in macro and micro-scale [98,383,384]. However, the use at micro-scale implies a low resolution in all the printing axis for accurate reproduction of the design. In the case of the current distributor, the resolution needed to be lower than 0.2 mm which narrowed down the number of suitable and easily available printers. Also, in small 3D printed pieces surface roughness and other imperfections become more prominent, and even though McDonough et al. verified it did not constitute an impairment in their system [382], it could alter the fluid laminar regime particularly in micro-channels, and deteriorate the alginate beads.

Although the distributor was successfully produced through a laser cutter at a compromised thickness of 1 mm, the difficulty of cutting such fine structures arises from the inherent effect of the laser on the surrounding areas of the incidence point. The energy accumulated in the material creates a molten area around the diameter of the hole to cut, which affects the structure of the material, creating an unstable or rough region around each hole. This effect is a function of the energy and pulse of the laser, which for a better surface resolution and cleaner cut, should use high intensity with shorter pulses [385]. However, the thicker the material, the higher the intensity of the laser needs to be, or longer pulses need to be applied at lower intensities. A strategy to overcome these issues and which may enable producing a piece with smaller interstitial spaces might imply readjusting the laser to cut alternating opposite ends of the design to allow the first to cool down while the other is cut. Yet, this would be a time-consuming process which requires resetting the laser pattern, a task that is not profitable for external providers.

All these features would be possible to manufacture with the desired dimensions but at a higher initial investment, which is characteristic of the prototyping process.

Because fluidised bed bioreactors are developed in the specific context of their application, comparisons between designs are not linear. The UCLBAL is composed of a cylindrical column with a perforated plate distributor coupled with a 200 μm mesh, where the latter further subdivides the fluid that passes through the perforated plate

into smaller channels [130]. Although the UCLBAL served as a model for the current prototype, the aim for the sFBB was also to reduce the number of parts involved and have the distributor design (without a mesh) define the dispersion pattern of the flow. On the other hand, the Suppliver is constituted by four 250 mL FBBs operating in parallel giving additional flexibility to the setup and corroborating the use of several small units, similar to the sFBB prototype, for clinical purposes [386]. However, its design details are not disclosed due to patents in force and cannot be directly compared to the sFBB. Another BAL whose features are not published is the spheroid reservoir bioartificial liver (SRBAL) from Mayo Clinic, although it uses a tapered FBB which has been described, in other contexts, to generate more heterogeneities and erosion of particles compared to cylindrical columns [387]. This becomes particularly relevant since their system does not use hydrogel encapsulation techniques to shield the liver spheroids from hydrodynamic shear stress and preserve their performance.

5.5. Conclusion

To transition the sFBB into a commercial product, optimisation was necessary to produce a consistent and homogenous fluidisation in a standardised design focusing on the inlet and distributor as the main fluidisation modulators, from the theoretical and preliminary CFD data, the optimal geometry for the inlet was a point with 4 openings, horizontally distributed in 90° angle, each with a 4 mm inner diameter; whereas the distributor composed of 0.2 mm wide slots spaced at 0.2 mm induced the most even fluid distribution. Experimental validation of the second sFBB prototype (with a 3-part main body) corroborated the performance of the inlet, but the distributor, whose design had to be compromised for fabrication purposes, produced a heterogenous fluidisation impairing cell viability and proliferation. These results demonstrated the diminished performance of this prototype and the need for improvement of the distributor design.
Nonetheless, rapid cycle testing was an efficient approach in progressing through the several iterations of the design optimisation, assessing quickly the essential parameters and only experimentally implementing the ones with the most promising preliminary

results. Rapid prototyping tools were also advantageous at producing in a timely manner resistant and biocompatible features.

Overall, the current design created a basis for further improvements until the optimal combination of distributor and inlet is achieved to promote homogeneous fluidisation and establish the prototype as a potential commercial product for *in vitro* culture and testing of 3D cell constructs.

The next chapter will address a general discussion of the results and potential future work.

CHAPTER 6

General discussion and future work

Bioreactors are essential devices for the progression of the Tissue Engineering and Regenerative Medicine field since they provide a controlled environment and spatiotemporal distribution of nutrients and external signals (biochemical and biophysical) that impact on cellular viability, proliferation, growth, differentiation and tissue formation, constituting expansion vessels but also improved testing platforms for a range of experimental parameters. This is particularly relevant for three-dimensional (3D) cell constructs as they require an efficient delivery to all constituent cells of the complex structure, minimising the formation of gradients and increasing their performance. Furthermore, bioreactors enable standardisation and reproducibility of the process and scale-up to clinical scale.

Therefore, this project aimed to develop a benchtop fluidised bed bioreactor (sFBB) for long-term culture and test of 3D cell constructs. It involved characterisation of the prototype with the identification and optimisation study of key design features to improve the bioreactor performance. Moreover, the biological validation of the device centred on its application as a cellular expansion vessel for alginate encapsulated cells and simultaneously a testing platform for the impact of the hydrodynamic environment on proliferation, phenotype and metabolic activity. It has also been used as a pilot model for the clinical scale fluidised bed bioreactor (FBB) developed by the Liver Group for the Bioartificial Liver device.

In this chapter, the main achievements of each step are discussed and possible future directions of the project.

6.1. Bioreactor design

In *Chapter 4*, it was hypothesised that the fluidisation technology developed by the Liver Group for the UCLBAL could serve as a model for the sFBB downscaled through

empirical similarity rules. This hypothesis was corroborated when, maintaining between scales the linear flow rate and the ratio of the height of the settled bed to the diameter of the column (H_b/D), produced a bioreactor prototype that successfully fluidised a 30 mL bed of micro alginate beads, yielding a final biomass density comparable to the clinical scale FBB. Moreover, the setup was expandable up to 4 sFBBs operating simultaneously in parallel and demonstrating the reproducibility and robustness of the device.

This first prototype was produced using readily available commercial parts with standard features and dimensions for ease of assembly and manufacture. It created a perfusion environment which promoted homogeneous mixing in the system and faster mass diffusion across the hydrogel compared to conventional static cultures. However, channelling effects were observed in the fluidised bed, particularly immediately above the distributor. These were attributed to the random design of the distributor and the reduced radial dispersion of the flow and highlighted the distributor and inlet point as the critical design features of the bioreactor.

From these results and further biological validation in *Chapter 4*, that certified the application of the sFBB as a versatile device for long-term culture and test of 3D cell constructs, optimisation of the prototype was addressed in *Chapter 5.* It was hypothesised that the rapid-cycle testing approach and rapid prototyping could be used to optimise the bioreactor design. This was proven as evidenced by the CFD results and "operator" experience enabling the fast progression through several iterations of the design optimisation, assessing the essential parameters, and only experimentally testing those which generated the most homogeneous axial and radial dispersion of the flow. Also, rapid prototyping produced features in an efficient timely manner, that were biocompatible and resistant to 12 days of consecutive perfusion. Final iterations of the design demonstrated that 4 openings of 6 mm diameter arranged horizontally at a 90° angle to the inlet point and, a distributor with 0.2 mm gaps interspersed at 0.8 mm promoted the most homogenous flow distribution inside the bioreactor. However, this optimised design underperformed in practice compared to the initial prototype, due to the distributor's depth of 1 mm, making the system more susceptible to external factors (such as inclination) and thus, creating large areas of stagnation. It resulted in diminished cell viability and proliferation because spheroids were not formed homogenously inside each hydrogel bead. Nonetheless, the main body of the bioreactor

was now composed of 3 separate parts which granted flexibility for subsequent improvements on the designs of the distributor and inlet point without compromising the setup, building the basis for an "in progress" prototype. It could also serve as an interchanging device to fit features with different designs adjusted to the required specifications of the system under culture/analysis.

The continuation of this work would focus on finalising the design of the bioreactor which demands further improvements, particularly the distributor component. The most efficient design needs to find a compromise between sufficient open area to facilitate fluidisation by decreasing the minimum fluidisation velocity, with sufficient pressure drop to eliminate channelling effects. However, these parameters could be mutually exclusive as the increase in open area could reduce the pressure drop across the distributor. Increasing the depth of the distributor, which will be essential to mitigate the external influences and provide a more structured dispersion of the fluid, might minimise the alterations in pressure drop. Another design parameter that would be valuable to test and could promote a radial distribution of the flow, is the angle of the holes in the distributor. In terms of the design of the inlet point, although several options have been explored, it would be worth understanding whether decreasing the diameter and increasing the number of openings would benefit the fluid distribution in the system.

Regardless of the design modifications, the CFD simulations should include the movement of solids, i.e. the hydrogel microbeads, to generate a more accurate theoretical prediction of the impact of the flow behaviour in the fluidisation of the bed and its pattern of movement. It could be achieved by considering the fluid phase as a continuum and solving Newton's equations of motion for each particle [367]. Another requirement is to have access to rapid prototyping techniques that are able to manufacture such fine structures in resistant materials, such as 3D printers with narrow nozzles, technologies advances in this area are rapid and will soon be feasible at a reasonable cost.

Further studies on the characterisation of the system will also be needed to establish it as a standard product. The corroboration of the CFD simulations could be achieved through particle tracking systems by incorporating nanoparticles in the beads and dispersed in the medium for experimental measurements of velocity patterns, mixing behaviour, flow regime (laminar or turbulent) and associated shear stress. Moreover,

experimental determination of the pressure variations and, subsequent pressure drop across the bed, are important parameters to define the behaviour of the fluidised bed. Mass diffusion coefficients should be defined for validation of the mass transfer efficacy in the sFBB. Techniques such as Fluorescence Recovery After Photobleaching (FRAP) would provide a direct correlation between the time of recovery and the coefficient [388]. The hydrogel properties impact greatly on mass transfer in the bioreactor and therefore, to understand the sFBB behaviour in different environments, the same study should be conducted with hydrogel beads of varying diameters and compositions. Consequently, a more in-depth characterisation of the hydrogel including porosity, stiffness, surface roughness and stress relaxation through techniques such as mercury porosimetry, atomic force microscopy, compression test or indentation [389–392], would be essential to determine their influence on fluidisation, mass transfer and cellular performance due to the biochemical and biophysical cues that the microenvironment generates [393].

Once the design is established and as a commercial product, the sFBB could become a more compact device, either by further scaling down for a more high throughput setup or by integrating some features such as optical spot sensors (for pH, dissolved oxygen, or carbon dioxide) for tighter control of the environmental parameters, or more innovative approaches like oxygen releasing beads eliminating the external oxygenator to the reservoir [173]. Maintaining the bioreactor design simple will benefit the transition into a commercial biotechnological product by meeting the regulatory demands.

6.2. Biological application of the small-scale fluidised bed bioreactor

6.2.1. Long-term culture of alginate encapsulated HepG2 cells

In *section 4.1*, it was hypothesised that the dynamic environment promoted by the sFBB sustained long-term culture of 3D cell constructs maintaining them viable and leading to a more physiologically relevant phenotype. This hypothesis was proven as alginate encapsulated HepG2 cells cultured for 12 days in the sFBB were highly viable (> 98%) and proliferative, growing into several spheroids and yielding a final cell density 2-fold above conventional static bead culture (tissue culture plates). The phenotype assessed at

the gene expression level demonstrated a general upregulation of hepatic markers including those associated with a more mature state (e.g. CYP3A4, HNF4-α and C/EBPα) in comparison to the control (static culture). The metabolic analysis verified a stable ATP content, low glucose consumption and, at the signalling level, there was significant dephosphorylation of ERK1/2. This could be a consequence of the extensively reported increase in nutrient delivery and homogenous milieu provided by hydrodynamic mixing, which enabled proliferation into a 3D structure and a possible progressive transition into a more physiological relevant hepatic phenotype.

Nonetheless, to draw definite conclusions a detailed investigation of the phenotype and signalling pathways should be conducted. Exploring other hepatic markers associated with the mature phenotype including phase I and II xenobiotic metabolising enzymes (e.g. CYP1A2, CYP2C19, UGT1A1, SULT2A1), transporters (e.g. MRP1, OAT2), as well as enzymes involved in the urea and ammonia cycle and other hepatic nuclear factors (e.g. HNF1-α), would strongly support the alterations in phenotype and cellular performance [175,196,394,395]. Besides molecular analysis, drug metabolism by encapsulated HepG2 cells in the sFBB would produce evidence of their performance and create an *in vitro* model which more closely mimics the *in vivo* milieu. Furthermore, investigation of the glucose metabolism through markers for oxidative pathway and glycolysis would demonstrate the predominant mechanism in these cells, and better correlate the obtained results for glucose consumption and ATP content [202,396].

In terms of the signalling pathways, evaluation of both upstream and downstream proteins (in particular PRAS40, AMPK, PI3K and S6K1, STAT3, SGK, FoxO, respectively) would more accurately indicate the inherent mechanism triggered in response to the hydrodynamic conditions [227]. Other factors to consider would be the expression of membrane transporters (e.g. GLUT1, receptor tyrosine kinases, solute carriers (SLC) for amino acid transport) and ion channels such as TRPV4, implicated in the malignant behaviour of hepatocellular carcinoma and phosphorylation of ERK1/2, to determine the effect of the hydrodynamic environment on these membrane receptors either through delivery of nutrients and solutes, osmotic pressure or mechanical stimuli [229,397].

It would be valuable to prolong the culture time (> 12 days) to understand whether there will be a continuous modification of the phenotype and behaviour, simply governed by the 3D structure and hydrodynamic environment. Moreover, testing other cell lines such

as Caco-2 and MC-7 in the same context would determine if the effect is universally verified and thus, a global mechanism, or if each cell type will have a specific response to the environment.

6.2.2. Long-term culture of alginate encapsulated bone marrow-derived human multipotent stem cells

In *section 4.2*, it was hypothesised that the dynamic environment promoted by the sFBB sustained long-term culture of alginate encapsulated primary bone marrow-derived human multipotent stem cells (MSCs). It was partially proven as a portion of the MSC population were metabolically active after 21 days of culture, although they did not proliferate and even decreased in number probably due to the absence of cell adhesion cues in the hydrogel. However, the performed viability assay did not reflect this loss, not staining positive for the dead cells and attributing that misrepresentation to cells having disintegrated by the time of the assessment.

This process was decelerated under dynamic culture, with Survivin expression at the mRNA level higher than in static culture. Encapsulated MSCs in dynamic culture, once released from the hydrogel bead and seeded to onto a conventional tissue culture plate, preserved their ability to attach and spread, acquiring the characteristic fibroblast-like morphology. They were successfully differentiated into adipogenic and chondrogenic lineages.

The paracrine function of MSCs was evaluated in co-culture with alginate encapsulated HepG2 cells under static conditions, where MSCs reduced HepG2 cell proliferation rate after 14 days, and the latter supported encapsulated MSCs in culture by stabilising their cell number and inducing expression of Survivin.

It is probable that the alginate encapsulation of MSCs had triggered programmed cell death based on anoikis. Nonetheless, this environment (hydrogel encapsulation in a dynamic culture) could mimic the *in vivo* MSC niche inducing a pre-quiescent state of the cells since they did not divide, were metabolically active, responded to stimuli for differentiation and deprivation of cell anchorage indicated an entrance of cells into G_0/G_1 phase (Appendix 1) [398]. The same effect has been identified in another hydrogel system

where the density of encapsulated MSCs also play a role in directing the quiescent state [399]. It is a very speculative hypothesis and detailed experimental work should be conducted to validate it. If the quiescent state is verified, modifying the hydrogel to prevent cell loss and culturing them under dynamic conditions in the sFBB could be a strategy to replicate the native niche and maintain the MSCs in quiescent state in long-term *in vitro* culture without them losing potency or becoming senescent, readily available for scientific experiments or possible cell therapy.

Although modifications to the hydrogel were attempted by introducing collagen I in the alginate matrix resulting in some cells aligning and spreading along the collagen fibres, the crosslinking protocol requires further optimisation since it did not produce a homogenous mix nor spherical beads and cell loss was still observed. The hydrogel could also be manipulated to generate a microenvironment which would drive differentiation and be further potentiated under the dynamic conditions of the bioreactor [400]. Furthermore, using the sFBB as the delivery mechanism of the differentiation cues, i.e. soluble factors, could accelerate the lineage commitment process due to the hydrodynamic environment [401].

Regardless of the phenotype of the encapsulated MSCs (i.e. undifferentiated or differentiated), the release of cells from hydrogels highlights other possible applications since new techniques have been developed to promote temporal controlled hydrogel degradation, for instance, oxidised methacrylate alginate which is more sensitive to hydrolysis [402,403]. Thus, cells encapsulated in these degradable hydrogels and cultured in the sFBB until the desired performance or state is achieved could then be used for scaffold seeding, local tissue repair or as a gene delivery mechanism.

Moreover, due to the influence of MSCs in other cells either through cell-cell contacts or paracrine effects, establishing co-culture systems in the sFBB setup would benefit the cellular performance either for regenerative medicine purposes or as *in vitro* 3D models. For systems that require cell-cell contacts, encapsulation within the same hydrogel, even compartmentalised, will benefit the development of microtissues or organoids in each bead [404]. For paracrine effects, culture in separate sFBBs arranged in parallel will be a closer replication of perfusion *in vivo*.

6.2.3. Cryopreservation recovery and pilot-scale

In *section 4.3*, it was hypothesised that the sFBB could serve as a pilot-scale for the Liver Group clinical scale FBB for process optimisation of biomass recovery after cryopreservation. It was proven when the recovery pattern in the sFBB followed the clinical scale FBB with viability and cell number decreasing post-thawing attaining a minimum 24 h after thawing and recovering to pre-cryopreservation levels on the 5th day. This study also validated the use of multiple sFBB units in parallel, yielding comparable results, and showed that constructs with increased complexity in structure and cell number are more susceptible to cryoinjury and recover at a slower rate.

The data only demonstrated the replication of the recovery behaviour to validate the use of the sFBB for further protocol optimisation. Investigation of cellular performance through protein secretion and influence on phenotype as conducted in *section 5.1* would be valuable to determine the impact of cryoinjury and the complete recovery of cells. Given the hydrodynamic environment and, as mentioned for the previous application, the increased delivery of soluble factors to the cells promoted by the hydrodynamic homogenous milieu could benefit the efficient supply of, for example, antioxidants to minimise the production of reactive oxygen species and recovery time.

To optimise the overall protocol an in-depth examination of the activated signalling pathways would be valuable to understand whether supplementing inhibitors or activators would promote faster recovery such as inhibitors of p53 have been described to improve cell recovery by 20% [344].

6.3. Concluding remarks

The work presented in this thesis established the prototype of a benchtop scale fluidised bed bioreactor (sFBB) for long-term culture of hydrogel encapsulated cells under perfusion conditions. It demonstrated the successful use of scale-down techniques and computational fluid dynamics simulations as a theoretical tool to preliminary test the designs and predict the fluid behaviour inside the bioreactors. Moreover, it highlighted the versatility of the device as a cell expansion vessel, a testing platform for analysing

the impact of external agents and stimuli on cellular behaviour and performance and, a pilot-scale of the clinical scale FBB for process optimisation.

As a potential commercial product, this prototype is a simple, reusable, cost-effective device at a scale that enables "per cell performance" readouts and with potential for increased complexity in terms of scaffold, tissue-like structure and setup through multiple units operating in parallel, enabling simultaneous observations and condition comparison and speeding up the Research & Development process.

References

1. Vacanti, J. P. & Vacanti, C. A. The History and Scope of Tissue Engineering. in *Principles of Tissue Engineering: Fourth Edition* 3–8 (2013). doi:10.1016/B978-0-12-398358-9.00001-X.
2. Shafiee, A. & Atala, A. Tissue Engineering: Toward a New Era of Medicine. *Annu. Rev. Med.* **68**, 29–40 (2017).
3. Antoni, D., Burckel, H., Josset, E. & Noel, G. Three-Dimensional Cell Culture: A Breakthrough in Vivo. *Int. J. Mol. Sci.* **16**, 5517–5527 (2015).
4. Beningo, K. A., Dembo, M. & Wang, Y. L. Responses of fibroblasts to anchorage of dorsal extracellular matrix receptors. *Proc. Natl. Acad. Sci. U. S. A.* **101**, 18024–18029 (2004).
5. Kim, Y. *et al.* Prolongation of liver-specific function for primary hepatocytes maintenance in 3D printed architectures. *Organogenesis* **14**, 1–12 (2018).
6. Li, Z. & Cui, Z. Three-dimensional perfused cell culture. *Biotechnol. Adv.* **32**, 243–254 (2014).
7. Chaudhuri, O. *et al.* Extracellular matrix stiffness and composition jointly regulate the induction of malignant phenotypes in mammary epithelium. *Nat. Mater.* **13**, 970–978 (2014).
8. Hakkinen, K. M., Harunaga, J. S., Doyle, A. D. & Yamada, K. M. Direct comparisons of the morphology, migration, cell adhesions, and actin cytoskeleton of fibroblasts in four different three-dimensional extracellular matrices. *Tissue Eng. - Part A* **17**, 713–724 (2011).
9. Langhans, S. A. Three-Dimensional in Vitro Cell Culture Models in Drug Discovery and Drug Repositioning. *Front. Pharmacol.* **9**, (2018).
10. Dzobo, K. *et al.* Advances in Regenerative Medicine and Tissue Engineering: Innovation and Transformation of Medicine. *Stem Cells Int.* **2018**, 1–24 (2018).
11. Kular, J. K., Basu, S. & Sharma, R. I. The extracellular matrix: Structure, composition, age-related differences, tools for analysis and applications for tissue engineering. *J. Tissue Eng.* **5**, 204173141455711 (2014).
12. Proctor, W. R. *et al.* Utility of spherical human liver microtissues for prediction of clinical drug-induced liver injury. *Arch. Toxicol.* **91**, 2849–2863 (2017).

13. Polonchuk, L. *et al.* Cardiac spheroids as promising in vitro models to study the human heart microenvironment. *Sci. Rep.* **7**, 7005 (2017).
14. DesRochers, T. M., Suter, L., Roth, A. & Kaplan, D. L. Bioengineered 3D Human Kidney Tissue, a Platform for the Determination of Nephrotoxicity. *PLoS One* **8**, e59219 (2013).
15. Edmondson, R., Broglie, J. J., Adcock, A. F. & Yang, L. Three-dimensional cell culture systems and their applications in drug discovery and cell-based biosensors. *Assay and Drug Development Technologies* vol. 12 207–218 (2014).
16. Rodrigues, T. *et al.* Emerging tumor spheroids technologies for 3D in vitro cancer modeling. *Pharmacol. Ther.* **184**, 201–211 (2018).
17. Ingram, M. *et al.* Three-dimensional growth patterns of various human tumor cell lines in simulated microgravity of a NASA bioreactor. *In Vitro Cell. Dev. Biol. Anim.* **33**, 459–66 (1997).
18. Santos, J. M. *et al.* Three-dimensional spheroid cell culture of umbilical cord tissue-derived mesenchymal stromal cells leads to enhanced paracrine induction of wound healing. *Stem Cell Res. Ther.* **6**, 90 (2015).
19. Bartosh, T. J. *et al.* Aggregation of human mesenchymal stromal cells (MSCs) into 3D spheroids enhances their antiinflammatory properties. *Proc. Natl. Acad. Sci. U. S. A.* **107**, 13724–13729 (2010).
20. Del Duca, D., Werbowetski, T. & Del Maestro, R. F. Spheroid preparation from hanging drops: Characterization of a model of brain tumor invasion. *J. Neurooncol.* **67**, 295–303 (2004).
21. Otsuka, H., Sasaki, K., Okimura, S., Nagamura, M. & Nakasone, Y. Micropatterned co-culture of hepatocyte spheroids layered on non-parenchymal cells to understand heterotypic cellular interactions. *Sci. Technol. Adv. Mater.* **14**, (2013).
22. Swaminathan, S., Hamid, Q., Sun, W. & Clyne, A. M. Bioprinting of 3D breast epithelial spheroids for human cancer models. *Biofabrication* **11**, 025003 (2019).
23. Hsiao, A. Y. *et al.* Microfluidic system for formation of PC-3 prostate cancer co-culture spheroids. *Biomaterials* **30**, 3020–3027 (2009).
24. Katt, M. E., Placone, A. L., Wong, A. D., Xu, Z. S. & Searson, P. C. In Vitro Tumor Models: Advantages, Disadvantages, Variables, and Selecting the Right Platform.

Front. Bioeng. Biotechnol. **4**, (2016).

25. Lin, R.-Z. & Chang, H.-Y. Recent advances in three-dimensional multicellular spheroid culture for biomedical research. *Biotechnol. J.* **3**, 1172–1184 (2008).
26. Takebe, T. & Wells, J. M. Organoids by design. *Science (80-.).* **364**, 956–959 (2019).
27. Xinaris, C., Brizi, V. & Remuzzi, G. Organoid Models and Applications in Biomedical Research. *Nephron* **130**, 191–199 (2015).
28. Ghasemi-Mobarakeh, L., Kolahreez, D., Ramakrishna, S. & Williams, D. Key terminology in biomaterials and biocompatibility. *Curr. Opin. Biomed. Eng.* **10**, 45–50 (2019).
29. Bao Ha, T. Le, Minh, T., Nguyen, D. & Minh, D. Naturally Derived Biomaterials: Preparation and Application. in *Regenerative Medicine and Tissue Engineering* (InTech, 2013). doi:10.5772/55668.
30. Cushing, M. C. & Anseth, K. S. MATERIALS SCIENCE: Hydrogel Cell Cultures. *Science (80-.).* **316**, 1133–1134 (2007).
31. Lutolf, M. P. & Hubbell, J. A. Synthetic biomaterials as instructive extracellular microenvironments for morphogenesis in tissue engineering. *Nat. Biotechnol.* **23**, 47–55 (2005).
32. Pina, S. *et al.* Scaffolding Strategies for Tissue Engineering and Regenerative Medicine Applications. *Materials (Basel).* **12**, 1824 (2019).
33. Nam, S., Hu, K. H., Butte, M. J. & Chaudhuri, O. Strain-enhanced stress relaxation impacts nonlinear elasticity in collagen gels. *Proc. Natl. Acad. Sci.* **113**, 5492–5497 (2016).
34. Chaudhuri, O. Viscoelastic hydrogels for 3D cell culture. *Biomater. Sci.* **5**, 1480–1490 (2017).
35. Yung, C. W., Bentley, W. E. & Barbari, T. A. Diffusion of interleukin-2 from cells overlaid with cytocompatible enzyme-crosslinked gelatin hydrogels. *J. Biomed. Mater. Res. - Part A* **95**, 25–32 (2010).
36. Yeo, Y. *et al.* Photocrosslinkable hydrogel for myocyte cell culture and injection. *J. Biomed. Mater. Res. - Part B Appl. Biomater.* **81**, 312–322 (2007).
37. Hiemstra, C., Van Der Aa, L. J., Zhong, Z., Dijkstra, P. J. & Feijen, J. Novel in situ forming, degradable dextran hydrogels by michael addition chemistry: Synthesis, rheology, and degradation. *Macromolecules* **40**, 1165–1173 (2007).

38. Kulig, D., Zimoch-Korzycka, A., Jarmoluk, A. & Marycz, K. Study on Alginate–Chitosan Complex Formed with Different Polymers Ratio. *Polymers (Basel).* **8**, 167 (2016).

39. Liang, H.-F. *et al.* Novel Method Using a Temperature-Sensitive Polymer (Methylcellulose) to Thermally Gel Aqueous Alginate as a pH-Sensitive Hydrogel. *Biomacromolecules* **5**, 1917–1925 (2004).

40. Kuo, C. K. & Ma, P. X. Maintaining dimensions and mechanical properties of ionically crosslinked alginate hydrogel scaffolds in vitro. *J. Biomed. Mater. Res. - Part A* **84**, 899–907 (2008).

41. Wong, R. S. H., Ashton, M. & Dodou, K. Effect of crosslinking agent concentration on the properties of unmedicated hydrogels. *Pharmaceutics* **7**, 305–319 (2015).

42. Lee, J.-H. & Kim, H.-W. Emerging properties of hydrogels in tissue engineering. *J. Tissue Eng.* **9**, 204173141876828 (2018).

43. Kim, H. J., Kim, U. J., Vunjak-Novakovic, G., Min, B. H. & Kaplan, D. L. Influence of macroporous protein scaffolds on bone tissue engineering from bone marrow stem cells. *Biomaterials* **26**, 4442–4452 (2005).

44. Lien, S.-M., Ko, L.-Y. & Huang, T.-J. Effect of pore size on ECM secretion and cell growth in gelatin scaffold for articular cartilage tissue engineering. *Acta Biomater.* **5**, 670–679 (2009).

45. El-Sherbiny, I. M. & Yacoub, M. H. Hydrogel scaffolds for tissue engineering: Progress and challenges. *Glob. Cardiol. Sci. Pract.* **2013**, 38 (2013).

46. Khetan, S. *et al.* Degradation-mediated cellular traction directs stem cell fate in covalently crosslinked three-dimensional hydrogels. *Nat. Mater.* **12**, 458–465 (2013).

47. Koetting, M. C., Peters, J. T., Steichen, S. D. & Peppas, N. A. Stimulus-responsive hydrogels: Theory, modern advances, and applications. *Mater. Sci. Eng. R Reports* **93**, 1–49 (2015).

48. Lee, K. Y. & Mooney, D. J. Alginate: Properties and biomedical applications. *Prog. Polym. Sci.* **37**, 106–126 (2012).

49. Jang, J. *et al.* Effects of alginate hydrogel cross-linking density on mechanical and biological behaviors for tissue engineering. *J. Mech. Behav. Biomed. Mater.* **37**, 69–77 (2014).

50. Donati, I., Holtan, S., Mørch, Y. A., Borgogna, M. & Dentini, M. New Hypothesis on the Role of Alternating Sequences in Calcium−Alginate Gels. *Biomacromolecules* **6**, 1031–1040 (2005).

51. Koo, L. Y., Irvine, D. J., Mayes, A. M., Lauffenburger, D. A. & Griffith, L. G. Co-regulation of cell adhesion by nanoscale RGD organization and mechanical stimulus. *J. Cell Sci.* **115**, 1423–33 (2002).

52. Orive, G. *et al.* Cell encapsulation: technical and clinical advances. *Trends Pharmacol. Sci.* **36**, 537–546 (2015).

53. Andersen, T., Auk-Emblem, P. & Dornish, M. 3D Cell Culture in Alginate Hydrogels. *Microarrays* **4**, 133–161 (2015).

54. Steele, J. A. M., Hallé, J.-P., Poncelet, D. & Neufeld, R. J. Therapeutic cell encapsulation techniques and applications in diabetes. *Adv. Drug Deliv. Rev.* **67–68**, 74–83 (2014).

55. Huang, X., Zhang, X., Wang, X., Wang, C. & Tang, B. Microenvironment of alginate-based microcapsules for cell culture and tissue engineering. *J. Biosci. Bioeng.* **114**, 1–8 (2012).

56. Calafiore, R. & Basta, G. Clinical application of microencapsulated islets: Actual prospectives on progress and challenges. *Adv. Drug Deliv. Rev.* **67–68**, 84–92 (2014).

57. CONSTANTINIDIS, I. *et al.* Non-invasive evaluation of alginate/poly-l-lysine/alginate microcapsules by magnetic resonance microscopy. *Biomaterials* **28**, 2438–2445 (2007).

58. Gattás-Asfura, K. M., Fraker, C. A. & Stabler, C. L. Covalent stabilization of alginate hydrogel beads via Staudinger ligation: Assessment of poly(ethylene glycol) and alginate cross-linkers. *J. Biomed. Mater. Res. Part A* **99A**, 47–57 (2011).

59. Wilson, J. L. & McDevitt, T. C. Stem cell microencapsulation for phenotypic control, bioprocessing, and transplantation. *Biotechnol. Bioeng.* **110**, 667–682 (2013).

60. Paredes Juárez, G. A., Spasojevic, M., Faas, M. M. & de Vos, P. Immunological and Technical Considerations in Application of Alginate-Based Microencapsulation Systems. *Front. Bioeng. Biotechnol.* **2**, (2014).

61. Pazzano, D. *et al.* Comparison of Chondrogensis in Static and Perfused Bioreactor Culture. *Biotechnol. Prog.* **16**, 893–896 (2000).

62. Polacheck, W. J., Charest, J. L. & Kamm, R. D. Interstitial flow influences direction of tumor cell migration through competing mechanisms. *Proc. Natl. Acad. Sci.* **108**, 11115–11120 (2011).

63. Sikavitsas, V. I. *et al.* Flow Perfusion Enhances the Calcified Matrix Deposition of Marrow Stromal Cells in Biodegradable Nonwoven Fiber Mesh Scaffolds. *Ann. Biomed. Eng.* **33**, 63–70 (2005).

64. Yu, F. *et al.* A perfusion incubator liver chip for 3D cell culture with application on chronic hepatotoxicity testing. *Sci. Rep.* **7**, 14528 (2017).

65. Martin, Y. & Vermette, P. Bioreactors for tissue mass culture: Design, characterization, and recent advances. *Biomaterials* **26**, 7481–7503 (2005).

66. Zhao, J. *et al.* Bioreactors for tissue engineering: An update. *Biochem. Eng. J.* **109**, 268–281 (2016).

67. Hansmann, J., Groeber, F., Kahlig, A., Kleinhans, C. & Walles, H. Bioreactors in tissue engineering-principles, applications and commercial constraints. *Biotechnol. J.* **8**, 298–307 (2013).

68. Mandenius, C.-F. *Bioreactors - Design, Operation and Novel Applications*. (Wiley-VCH Verlag GmbH & Co. KGaA, 2016). doi:10.1002/9783527683369.

69. Blose, K. J., Krawiec, J. T., Weinbaum, J. S. & Vorp, D. A. Bioreactors for Tissue Engineering Purposes. in *Regenerative Medicine Applications in Organ Transplantation* 177–185 (Elsevier, 2014). doi:10.1016/B978-0-12-398523-1.00013-6.

70. Selden, C. & Fuller, B. Role of Bioreactor Technology in Tissue Engineering for Clinical Use and Therapeutic Target Design. *Bioengineering* **5**, 32 (2018).

71. Özkaya, B., Kaksonen, A. H., Sahinkaya, E. & Puhakka, J. A. Fluidized bed bioreactor for multiple environmental engineering solutions. *Water Res.* **150**, 452–465 (2019).

72. Burghate, S. P. & Ingole, N. W. Fluidized Bed Biofilm Reactor – A Novel Wastewater Treatment Reactor. *Int. J. Res. Environ. Sci. Technol.* **3**, 145–155 (2013).

73. Kunii, D. & Levenspiel, O. *Fluidization Engineeing*. *Butterworth-Heinemann* (Elsevier, 1991). doi:10.1016/B978-0-7506-9121-5.50001-X.

74. Yang, W.-C. *Handbook of Fluidisation and Fluid-Particle Systems*. *Chemical Engineering* (Taylor & Francis, 2003).

75. Brown, L. F. & Fogler, H. S. Fluidized-Bed Reactors. *University of Michigan*

http://umich.edu/~elements/12chap/html/12prof2a.htm (2008).

76. Farshi, A. EXPERIMENTAL MEASUREMENT OF DIFFERENT FLUIDIZATION. *Pet. Coal* **55**, 311–321 (2013).

77. Sulaymon, A. H., Mohammed, A. A. & Al-musawi, T. J. Predicting the Minimum Fluidization Velocity of Algal Biomass Bed. *Am. J. Eng. Res.* **2**, 39–45 (2013).

78. Shrivastava, P. V, Soni, A. B. & Kumar, H. Hydrodynamic studies of three-phase semi-fluidized beds with irregular particles. *Indian J. Chem. Technol.* **20**, 294–296 (2013).

79. Asif, M. Minimum Fluidization Velocities of Binary-Solid Mixtures: Model Comparison. *Proc. World Acad. Sci. Eng. Technol.* **63**, 175–179 (2010).

80. Formisani, B. Packing and fluidization properties of binary mixtures of spherical particles. *Powder Technol.* **66**, 259–264 (1991).

81. Holdich, R. G. Fluidisation. in *Fundamentals of Particle Technology* 67–76 (Midland Information Technology and Publishing, 2002).

82. Holdich, R. G. *Fundamentals of Particle Technology*. (Midland Information Technology and Publishing, 2002).

83. Escudié, R., Epstein, N., Grace, J. R. & Bi, H. T. Effect of particle shape on liquid-fluidized beds of binary (and ternary) solids mixtures: Segregation vs. mixing. *Chem. Eng. Sci.* **61**, 1528–1539 (2006).

84. Lee, D. H. Transition velocity and bed expansion of two-phase (liquid-solid) fluidization systems. *Korean J. Chem. Eng.* **18**, 347–351 (2001).

85. Hirata, A. & Bulos, F. B. Predicting Bed Voidage in Solid-Liquid Fluidization. *J. Chem. Eng. Japan* **23**, 599–604 (1990).

86. Ngian, K.-F. & Martin, W. R. B. Bed Expansion Characteristics of Liquid Fluidized Particles with Attached Microbial Growth. *Biotechnol. Bioeng.* **XXII**, 1843–1856 (1980).

87. Felice, R. Di & Kehlenbeck, R. Sedimentation velocity of solids in finite size vessels. *Chem. Eng. Technol.* **23**, 1123–1126 (2000).

88. Wu, J. Y., Chen, K. C., Chen, C. T. & Hwang, S. C. J. Hydrodynamic characteristics of immobilized cell beads in a liquid-solid fluidized-bed bioreactor. *Biotechnol. Bioeng.* **83**, 583–594 (2003).

89. Andalib, M., Zhu, J. & Nakhla, G. A new definition of bed expansion index and

voidage for fluidized biofilm-coated particles. *Chem. Eng. J.* **189–190**, 244–249 (2012).

90. Kramer, O. J. I. *et al.* Improvement of the Richardson-Zaki liquid-solid fluidisation model on the basis of hydraulics. *Powder Technol.* **343**, 465–478 (2019).
91. Kmieć, A. Particle distributions and dynamics of particle movement in solid—liquid fluidized beds. *Chem. Eng. J.* **15**, 1–12 (1978).
92. Limtrakul, S., Chen, J., Ramachandran, P. a. & Duduković, M. P. Solids motion and holdup profiles in liquid fluidized beds. *Chem. Eng. Sci.* **60**, 1889–1900 (2005).
93. Mohanty, Y. K., Roy, G. K. & Biswal, K. C. Effect of column diameter on dynamics of gas-solid fluidized bed: A statistical approach. *Indian J. Chem. Technol.* **16**, 17–24 (2009).
94. Ansart, R., Vanni, F., Caussat, B., Ablitzer, C. & Brothier, M. Effects of reducing the reactor diameter on the dense gas–solid fluidization of very heavy particles: 3D numerical simulations. *Chem. Eng. Res. Des.* **117**, 575–583 (2017).
95. Rao, A., Curtis, J. S., Hancock, B. C. & Wassgren, C. The effect of column diameter and bed height on minimum fluidization velocity. *AIChE J.* **56**, 2304–2311 (2010).
96. Wormsbecker, M., Pugsley, T. S. & Tanfara, H. The Influence of Distributor Design on Fluidized Bed Dryer Hydrodynamics. *12th Int. Conf. Fluid.* (2007).
97. Asif, M., Kalogerakis, N. & Behie, L. A. Hydrodynamics of liquid fluidized beds including the distributor region. *Chem. Eng. Sci.* **47**, 4155–4166 (1992).
98. Odeleye, A. O. O. *et al.* On the use of 3D-printed flow distributors to control particle movement in a fluidized bed. *Chem. Eng. Res. Des.* **140**, 194–204 (2018).
99. Cornelissen, J. T., Taghipour, F., Escudié, R., Ellis, N. & Grace, J. R. CFD modelling of a liquid-solid fluidized bed. *Chem. Eng. Sci.* **62**, 6334–6348 (2007).
100. Carlos, C. R. & Richardson, J. F. Solids movement in liquid fluidised beds—I Particle velocity distribution. *Chem. Eng. Sci.* **23**, 813–824 (1968).
101. Garslde, J. & Ai-dibouni, M. I. Velocity-Voidage Relationships for Fluidization and Sedimentation. *Ind. Eng. Chem. Res.* **16**, 206–214 (1977).
102. Patnaik, K. S. K. R. & Sriharsha, K. Fluidization Principles for Three-Phase Fluidized Bed Bio-Reactor. *Int. J. Chem. Eng. Appl.* **1**, 251–255 (2010).
103. Ghatage, S. V. *et al.* Stability analysis in solid–liquid fluidized beds: Experimental and computational. *Chem. Eng. J.* **256**, 169–186 (2014).

104. Kalaga, D. V., Dhar, A., Dalvi, S. V. & Joshi, J. B. Particle-liquid mass transfer in solid-liquid fluidized beds. *Chem. Eng. J.* **245**, 323–341 (2014).

105. Werther, J. Fluidized-Bed Reactors. in *Ullmann's Encyclopedia of Industrial Chemistry* (Wiley-VCH Verlag GmbH & Co. KGaA, 2005). doi:10.1002/14356007.b04_239.

106. Bello, M. M., Abdul Raman, A. A. & Purushothaman, M. Applications of fluidized bed reactors in wastewater treatment – A review of the major design and operational parameters. *J. Clean. Prod.* **141**, 1492–1514 (2017).

107. Jamali, N. S., Md Jahim, J., O-Thong, S. & Jehlee, A. Hydrodynamic characteristics and model of fluidized bed reactor with immobilised cells on activated carbon for biohydrogen production. *Int. J. Hydrogen Energy* **44**, 9256–9271 (2019).

108. Mohd-Sahib, A. A. *et al.* Lipid for biodiesel production from attached growth Chlorella vulgaris biomass cultivating in fluidized bed bioreactor packed with polyurethane foam material. *Bioresour. Technol.* **239**, 127–136 (2017).

109. Ozturk, S. S. & Hu, W.-S. *Cell Culture Technology for Pharmaceutical and Cell-Based Therapies*. (CRC Press, 2006). doi:10.1201/9780849351068.ch1.

110. Kong, D., Cardak, S., Chen, M., Gentz, R. & Zhang, J. High cell density and productivity culture of Chinese hamster ovary cells in a fluidized bed bioreactor. *Cytotechnology* **29**, 215–220 (1999).

111. Wendt, D., Marsano, A., Jakob, M., Heberer, M. & Martin, I. Oscillating perfusion of cell suspensions through three-dimensional scaffolds enhances cell seeding efficiency and uniformity. *Biotechnol. Bioeng.* **84**, 205–214 (2003).

112. van Wenum, M. *et al.* Bioartificial livers in vitro and in vivo : tailoring biocomponents to the expanding variety of applications. *Expert Opin. Biol. Ther.* **14**, 1745–1760 (2014).

113. Carpentier, B., Gautier, a & Legallais, C. Artificial and bioartificial liver devices: present and future. *Gut* **58**, 1690–1702 (2009).

114. Nyberg, S. L., Mao, S. A. & Glorioso, J. M. Bioartificial Liver. in *Pathobiology of Human Disease* vol. 19 1800–1808 (Elsevier, 2014).

115. Gerlach, J. C., Zeilinger, K. & Patzer, J. F. Bioartificial liver systems: why, what, whither? *Regen. Med.* **3**, 575–595 (2008).

116. Allen, J. W. & Bhatia, S. N. Improving the next generation of bioartificial liver

devices. *Semin. Cell Dev. Biol.* **13**, 447–454 (2002).

117. Schrem, H., Kleine, M., Borlak, J. & Klempnauer, J. Physiological incompatibilities of porcine hepatocytes for clinical liver support. *Liver Transplant.* **12**, 1832–1840 (2006).

118. Takebe, T. *et al.* Vascularized and functional human liver from an iPSC-derived organ bud transplant. *Nature* **499**, 481–484 (2013).

119. Doré, E. & Legallais, C. A new concept of bioartificial liver based on a fluidized bed bioreactor. *Ther. Apher.* **3**, 264–267 (1999).

120. Hwang, Y. J. *et al.* Development of bioartificial liver system using a fluidized-bed bioreactor. *Transplant. Proc.* **32**, 2349–2351 (2000).

121. Erro, E. *et al.* Bioengineering the liver: scale-up and cool chain delivery of the liver cell biomass for clinical targeting in a bioartificial liver support system. *Biores. Open Access* **2**, 1–11 (2013).

122. David, B., Doré, E., Jaffrin, M. Y. & Legallais, C. Mass Transfers in a Fluidized Bed Bioreactor using Alginate Beads for a Future Bioartificial Liver. *Int. J. Artif. Organs* **27**, 284–293 (2004).

123. Yu, C.-B. *et al.* Evaluation of a novel choanoid fluidized bed bioreactor for future bioartificial livers. *World J. Gastroenterol.* **20**, 6869 (2014).

124. Gautier, A. *et al.* Impact of alginate type and bead diameter on mass transfers and the metabolic activities of encapsulated c3a cells in bioartificial liver applications. *Eur. Cells Mater.* **21**, 94–106 (2011).

125. Massie, I., Selden, C., Hodgson, H. & Fuller, B. Cryopreservation of encapsulated liver spheroids for a bioartificial liver: reducing latent cryoinjury using an ice nucleating agent. *Tissue Eng. Part C. Methods* **17**, 765–774 (2011).

126. Massie, I. *et al.* GMP Cryopreservation of Large Volumes of Cells for Regenerative Medicine: Active Control of the Freezing Process. *Tissue Eng. Part C. Methods* **20**, 1–46 (2014).

127. Kilbride, P. *et al.* Cryopreservation and re-culture of a 2.3 litre biomass for use in a bioartificial liver device. *PLoS One* **12**, e0183385 (2017).

128. Figaro, S. *et al.* SUPPLIVER: Bioartificial supply for liver failure. *IRBM* **36**, 101–109 (2015).

129. Selden, C. *et al.* Evaluation of Encapsulated Liver Cell Spheroids in a Fluidised-

Bed Bioartificial Liver for Treatment of Ischaemic Acute Liver Failure in Pigs in a Translational Setting. *PLoS One* **8**, e82312 (2013).

130. Selden, C. *et al.* A clinical-scale BioArtificial Liver, developed for GMP, improved clinical parameters of liver function in porcine liver failure. *Sci. Rep.* **7**, 1–19 (2017).
131. Coward, S. M., Selden, C., Mantalaris, A. & Hodgson, H. J. F. F. Proliferation rates of HepG2 cells encapsulated in alginate are increased in a microgravity environment compared with static cultures. *Artif. Organs* **29**, 152–158 (2005).
132. Coward, S. M. *et al.* Alginate-encapsulated HepG2 cells in a fluidized bed bioreactor maintain function in human liver failure plasma. *Artif. Organs* **33**, 1117–1126 (2009).
133. Selden, C., Khalil, M. & Hodgson, H. Three dimensional culture upregulates extracellular matrix protein expression in human liver cell lines - A step towards mimicking the liver in vivo? *Int. J. Artif. Organs* **23**, 774–781 (2000).
134. Kilburn, D. G. & Webb, F. C. The cultivation of animal cells at controlled dissolved oxygen partial pressure. *Biotechnol. Bioeng.* **10**, 801–814 (1968).
135. Cabaret, F., Bonnot, S., Fradette, L. & Tanguy, P. A. Mixing Time Analysis Using Colorimetric Methods and Image Processing. *Ind. Eng. Chem. Res.* **46**, 5032–5042 (2007).
136. Boyd, V., Cholewa, O. M. & Papas, K. K. Limitations in the Use of Fluorescein Diacetate/Propidium Iodide (FDA/PI) and Cell Permeable Nucleic Acid Stains for Viability Measurements of Isolated Islets of Langerhans. *Curr Trends Biotechnol Pharm* **2**, 66–84 (2008).
137. Promega. CellTiter-Glo ® 3D Cell Viability Assay -Technical Manual. *Promega Corporation* (2015).
138. Pozarowski, P. & Darzynkiewicz, Z. Analysis of Cell Cycle by Flow Cytometry. in *Checkpoint Controls and Cancer* (ed. Schönthal, A. H.) vol. 281 301–312 (Humana Press, 2004).
139. Schmittgen, T. D. & Livak, K. J. Analyzing real-time PCR data by the comparative CTmethod. *Nat. Protoc.* **3**, 1101–1108 (2008).
140. Bass, J. J. *et al.* An overview of technical considerations for Western blotting applications to physiological research. *Scand. J. Med. Sci. Sport.* **27**, 4–25 (2017).
141. Mahmood, T. & Yang, P. C. Western blot: Technique, theory, and trouble

shooting. *N. Am. J. Med. Sci.* **4**, 429–434 (2012).

142. Marques, M. P. & Szita, N. Bioprocess microfluidics: applying microfluidic devices for bioprocessing. *Curr. Opin. Chem. Eng.* **18**, 61–68 (2017).

143. Tajsoleiman, T., Mears, L., Krühne, U., Gernaey, K. V. & Cornelissen, S. An Industrial Perspective on Scale-Down Challenges Using Miniaturized Bioreactors. *Trends Biotechnol.* (2019) doi:10.1016/j.tibtech.2019.01.002.

144. Fonsenca, M. M. da & Teixeira, J. A. *Reactores biológicos*. (Lidel, 2007).

145. Li, F. *et al.* A Systematic Approach for Scale-Down Model Development and Characterization of Commercial Cell Culture Process. *Biotechnol. Prog.* **22**, 696–703 (2006).

146. Garcia-Ochoa, F. & Gomez, E. Bioreactor scale-up and oxygen transfer rate in microbial processes: an overview. *Biotechnol. Adv.* **27**, 153–176 (2009).

147. Villiger, T. K. *et al.* Experimental and CFD physical characterization of animal cell bioreactors: From micro- to production scale. *Biochem. Eng. J.* **131**, 84–94 (2018).

148. Tisa, F., Abdul Raman, A. A. & Daud, W. M. A. W. Simulation for supporting scale-up of a fluidized bed reactor for advanced water oxidation. *Sci. World J.* **2014**, (2014).

149. Tahmasebpoor, M., Zarghami, R., Sotudeh-Gharebagh, R., van Ommen, J. R. & Mostoufi, N. Dynamic analysis of the scale-up of fluidized beds. *Adv. Powder Technol.* **28**, 2621–2629 (2017).

150. Choudhury, S. F. An Investigation of Mechanisms Responsible for Modulated Biosynthetic Function in 3-Dimensional Cultures of a Human Hepatocyte Cell Line, for Potential use in a Bioartificial Liver Support System. (University College London, 2004).

151. Tumarkin, E. *et al.* High-throughput combinatorial cell co-culture using microfluidics. *Integr. Biol.* **3**, 653 (2011).

152. Schwager, A.-M., Bliedtner, J., Götze, K. & Bruder, A. Production of glass filters by selective laser sintering. in *3D Printed Optics and Additive Photonic Manufacturing* (eds. von Freymann, G., Herkommer, A. M. & Flury, M.) 22 (SPIE, 2018). doi:10.1117/12.2305695.

153. Kelkar, R. *et al.* Pilot scale studies in a fluidized bed for studying influence of distributor design in bed hydrodynamics. *Indian J. Chem. Technol.* **23**, 362–367

(2016).

154. Agu, C. & Moldestad, B. M. E. Distribution of Solids in a Fluidized Bed Operated without a Gas Distributor. in *Proceedings of The 59th Conference on Simulation and Modelling* 248–254 (2018). doi:10.3384/ecp18153248.

155. Lu, J. *et al.* A New Fluidized Bed Bioreactor Based on Diversion-Type Microcapsule Suspension for Bioartificial Liver Systems. *PLoS One* **11**, e0147376 (2016).

156. Rahimpour, F., Zarghami, R. & Mostoufi, N. Effect of distributor on fluidized bed hydrodynamics. *Can. J. Chem. Eng.* **95**, 2221–2234 (2017).

157. Zheng, Y. & Zhu, J. Radial Distribution of Liquid Velocity in a Liquid-Solids Circulating Fluidized Bed. *Int. J. Chem. React. Eng.* **1**, (2003).

158. Fede, P., Ansart, R., Simonin, O., Lagarde, S. & Ronga, I. Modelling of the dense fluidized bed of very small particles. in *8th International Conference on Multiphase Flow* (2013).

159. Legallais, C., Doré, E. & Paullier, P. Design of a fluidized bed bioartificial liver. *Artif. Organs* **24**, 519–525 (2000).

160. Mendonça da Silva, J. Creation of micro fluidized bed bioreactor for encapsulated 3-dimensional cell culture – towards a first-in-man trial of the bioartificial liver machine. (University College London, 2015).

161. Chen, X., Zhong, W. & Heindel, T. J. Orientation of cylindrical particles in a fluidized bed based on stereo X-ray particle tracking velocimetry (XPTV). *Chem. Eng. Sci.* **203**, 104–112 (2019).

162. Pedersen, J. M. *et al.* Fluid Dynamic Modeling to Support the Development of Flow-Based Hepatocyte Culture Systems for Metabolism Studies. *Front. Bioeng. Biotechnol.* **4**, 72 (2016).

163. Zivkovic, V., Ridge, N. & Biggs, M. J. Experimental study of efficient mixing in a micro-fluidized bed. *Appl. Therm. Eng.* **127**, 1642–1649 (2017).

164. Rodriguez, G., Anderlei, T., Micheletti, M., Yianneskis, M. & Ducci, A. On the measurement and scaling of mixing time in orbitally shaken bioreactors. *Biochem. Eng. J.* **82**, 10–21 (2014).

165. Salehi-Nik, N. *et al.* Engineering parameters in bioreactor's design: A critical aspect in tissue engineering. *BioMed Research International* vol. 2013 (2013).

166. Sun, D. *et al.* Effects of gelling bath on the physical properties of alginate gel beads and the biological characteristics of entrapped HepG2 cells. *Biotechnol. Appl. Biochem.* **65**, 263–273 (2018).

167. Khalil, M. *et al.* Human hepatocyte cell lines proliferating as cohesive spheroid colonies in alginate markedly upregulate both synthetic and detoxificatory liver function. *J. Hepatol.* **34**, 68–77 (2001).

168. Mobed-Miremadi, M., Djomehri, S., Keralapura, M. & McNeil, M. Fickian-Based Empirical Approach for Diffusivity Determination in Hollow Alginate-Based Microfibers Using 2D Fluorescence Microscopy and Comparison with Theoretical Predictions. *Materials (Basel).* **7**, 7670–7688 (2014).

169. Serra, M. *et al.* Microencapsulation technology: A powerful tool for integrating expansion and cryopreservation of human embryonic stem cells. *PLoS One* **6**, 23212 (2011).

170. Vodopivec, M., Lah, L., Narat, M. & Curk, T. Metabolomic profiling of CHO fed-batch growth phases at 10, 100 and 1000 L. *Biotechnol. Bioeng.* (2019) doi:10.1002/bit.27087.

171. Zeilinger, K. *et al.* Scaling down of a clinical three-dimensional perfusion multicompartment hollow fiber liver bioreactor developed for extracorporeal liver support to an analytical scale device useful for hepatic pharmacological in vitro studies. *Tissue Eng. Part C. Methods* **17**, 549–556 (2011).

172. Miller, W. M., Wilke, C. R. & Blanch, H. W. Effects of dissolved oxygen concentration on hybridoma growth and metabolism in continuous culture. *J. Cell. Physiol.* **132**, 524–530 (1987).

173. Lee, C.-S. *et al.* Fabrication of novel oxygen-releasing alginate beads as an efficient oxygen carrier for the enhancement of aerobic bioremediation of 1,4-dioxane contaminated groundwater. *Bioresour. Technol.* **171**, 59–65 (2014).

174. Coronel, M. M., Liang, J.-P., Li, Y. & Stabler, C. L. Oxygen generating biomaterial improves the function and efficacy of beta cells within a macroencapsulation device. *Biomaterials* **210**, 1–11 (2019).

175. Wiśniewski, J. R., Vildhede, A., Norén, A. & Artursson, P. In-depth quantitative analysis and comparison of the human hepatocyte and hepatoma cell line HepG2 proteomes. *J. Proteomics* **136**, 234–247 (2016).

176. Donato, M. T., Tolosa, L. & Gómez-Lechón, M. J. Culture and functional characterization of human hepatoma HepG2 cells. in *Protocols in In Vitro Hepatocyte Research* vol. 1250 77–93 (2015).

177. Westerink, W. M. A. & Schoonen, W. G. E. J. Cytochrome P450 enzyme levels in HepG2 cells and cryopreserved primary human hepatocytes and their induction in HepG2 cells. *Toxicol. Vitr.* **21**, 1581–1591 (2007).

178. Wilkening, S., Stahl, F. & Bader, A. Comparison of primary human hepatocytes and hepatoma cell line HepG2 with regard to their biotransformation properties. *Drug Metab. Dispos.* **31**, 1035–1042 (2003).

179. Williams, J. A. Comparative Metabolic Capabilities of CYP3A4, CYP3A5, and CYP3A7. *Drug Metab. Dispos.* **30**, 883–891 (2002).

180. Schrem, H., Klempnauer, J. & Borlak, J. Liver-Enriched Transcription Factors in Liver Function and Development. Part I: The Hepatocyte Nuclear Factor Network and Liver-Specific Gene Expression. *Pharmacol. Rev.* **54**, 129–158 (2002).

181. Lau, H. H., Ng, N. H. J., Loo, L. S. W., Jasmen, J. B. & Teo, A. K. K. The molecular functions of hepatocyte nuclear factors – In and beyond the liver. *J. Hepatol.* **68**, 1033–1048 (2018).

182. Walesky, C. & Apte, U. Role of Hepatocyte Nuclear Factor 4α (HNF4α) in Cell Proliferation and Cancer. *Gene Expr.* **16**, 101–108 (2015).

183. Jover, R., Bort, R., Gómez-Lechón, M. J. & Castell, J. V. Cytochrome P450 regulation by hepatocyte nuclear factor 4 in human hepatocytes: A study using adenovirus-mediated antisense targeting. *Hepatology* **33**, 668–675 (2001).

184. Love-Gregory, L. & Permutt, M. A. HNF4A genetic variants: Role in diabetes. *Current Opinion in Clinical Nutrition and Metabolic Care* vol. 10 397–402 (2007).

185. Bonzo, J. A., Ferry, C. H., Matsubara, T., Kim, J. H. & Gonzalez, F. J. Suppression of hepatocyte proliferation by hepatocyte nuclear factor 4α in adult mice. *J. Biol. Chem.* **287**, 7345–7356 (2012).

186. Guzman-Lepe, J. *et al.* Liver-enriched transcription factor expression relates to chronic hepatic failure in humans. *Hepatol. Commun.* **2**, 582–594 (2018).

187. Yin, C. *et al.* Differentiation therapy of Hepatocellular carcinoma in mice with recombinant adenovirus carryinghepatocyte nuclear factor-4α gene. *Hepatology* **48**, 1528–1539 (2008).

188. Su, Y. *et al.* Optimizing combination of liver-enriched transcription factors and nuclear receptors simultaneously favors ammonia and drug metabolism in liver cells. *Exp. Cell Res.* **362**, 504–514 (2018).

189. Schrem, H., Klempnauer, J. & Borlak, J. Liver-Enriched Transcription Factors in Liver Function and Development. Part II: the C/EBPs and D Site-Binding Protein in Cell Cycle Control, Carcinogenesis, Circadian Gene Regulation, Liver Regeneration, Apoptosis, and Liver-Specific Gene Regulation. *Pharmacol. Rev.* **56**, 291–330 (2004).

190. Ourlin, J. C., Jounaïdi, Y., Maurel, P. & Vilarem, M.-J. Role of the liver-enriched transcription factors C/EBPα and DBP in the expression of human CYP3A4 and CYP3A7. *J. Hepatol.* **26**, 54–62 (1997).

191. Akai, Y., Oitate, T., Koike, T. & Shiojiri, N. Impaired hepatocyte maturation, abnormal expression of biliary transcription factors and liver fibrosis in C/EBPα(Cebpa)-knockout mice. *Histol. Histopathol.* **29**, 107–25 (2014).

192. Wang, N. D. *et al.* Impaired energy homeostasis in C/EBPα knockout mice. *Science (80-.).* **269**, 1108–1112 (1995).

193. Tan, E. H. *et al.* CCAAT/enhancer binding protein α knock-in mice exhibit early liver glycogen storage and reduced susceptibility to hepatocellular carcinoma. *Cancer Res.* **65**, 10330–10337 (2005).

194. Voutila, J. *et al.* Development and Mechanism of Small Activating RNA Targeting CEBPA, a Novel Therapeutic in Clinical Trials for Liver Cancer. *Mol. Ther.* **25**, 2705–2714 (2017).

195. Xu, L. *et al.* Expression profiling suggested a regulatory role of liver-enriched transcription factors in human hepatocellular carcinoma. *Cancer Res.* **61**, 3176–3181 (2001).

196. Ramaiahgari, S. C. *et al.* A 3D in vitro model of differentiated HepG2 cell spheroids with improved liver-like properties for repeated dose high-throughput toxicity studies. *Arch. Toxicol.* **88**, 1083–1095 (2014).

197. Damelin, L. H. *et al.* Altered mitochondrial function and cholesterol synthesis influences protein synthesis in extended HepG2 spheroid cultures. *Arch. Biochem. Biophys.* **432**, 167–177 (2004).

198. Rahman, T. M., Selden, C., Khalil, M., Diakanov, I. & Hodgson, H. J. F. Alginate-

encapsulated Human Hepatoblastoma Cells in an Extracorporeal Perfusion System Improve Some Systemic Parameters of Liver Failure in a Xenogeneic Model. *Artif. Organs* **28**, 476–482 (2004).

199. Nishida, Y. & Taniguchi, A. A three-dimensional collagen-sponge-based culture system coated with simplified recombinant fibronectin improves the function of a hepatocyte cell line. *Vitr. Cell. Dev. Biol. - Anim.* **52**, 271–277 (2016).
200. Bokhari, M., Carnachan, R. J., Cameron, N. R. & Przyborski, S. a. Culture of HepG2 liver cells on three dimensional polystyrene scaffolds enhances cell structure and function during toxicological challenge. *J. Anat.* **211**, 567–576 (2007).
201. Adeva-Andany, M. M., Perez-Felpete, N., Fernandez-Fernandez, C., Donapetry-Garcia, C. & Pazos-Garcia, C. Liver glucose metabolism in humans. *Biosci. Rep.* **36**, e00416–e00416 (2016).
202. Heiden, M. G. Vander, Cantley, L. C. & Thompson, C. B. Understanding the warburg effect: The metabolic requirements of cell proliferation. *Science (80-.).* **324**, 1029–1033 (2009).
203. Liberti, M. V & Locasale, J. W. The Warburg Effect: How Does it Benefit Cancer Cells? *Trends in Biochemical Sciences* vol. 41 211–218 (2016).
204. Epstein, T., Gatenby, R. A. & Brown, J. S. The Warburg effect as an adaptation of cancer cells to rapid fluctuations in energy demand. *PLoS One* **12**, (2017).
205. Iyer, V. V., Yang, H., Ierapetritou, M. G. & Roth, C. M. Effects of glucose and insulin on HepG2-C3A cell metabolism. *Biotechnol. Bioeng.* **107**, 347–356 (2010).
206. Nagarajan, S. R. *et al.* Lipid and glucose metabolism in hepatocyte cell lines and primary mouse hepatocytes: a comprehensive resource for in vitro studies of hepatic metabolism. *Am. J. Physiol. Metab.* **316**, E578–E589 (2019).
207. Lu, Z. & Xu, S. ERK1/2 MAP kinases in cell survival and apoptosis. *IUBMB Life* **58**, 621–631 (2006).
208. Correa-Meyer, E., Pesce, L., Guerrero, C. & Sznajder, J. I. Cyclic stretch activates ERK1/2 via G proteins and EGFR in alveolar epithelial cells. *Am. J. Physiol. Cell. Mol. Physiol.* **282**, L883–L891 (2002).
209. Meloche, S. & Pouysségur, J. The ERK1/2 mitogen-activated protein kinase pathway as a master regulator of the G1- to S-phase transition. *Oncogene* **26**, 3227–3239 (2007).

210. Buscà, R., Pouysségur, J. & Lenormand, P. ERK1 and ERK2 Map Kinases: Specific Roles or Functional Redundancy? *Front. Cell Dev. Biol.* **4**, (2016).

211. Guégan, J.-P., Frémin, C. & Baffet, G. The MAPK MEK1/2-ERK1/2 Pathway and Its Implication in Hepatocyte Cell Cycle Control. *Int. J. Hepatol.* **2012**, 1–13 (2012).

212. Nelsen, C. J., Rickheim, D. G., Tucker, M. M., Hansen, L. K. & Albrecht, J. H. Evidence That Cyclin D1 Mediates Both Growth and Proliferation Downstream of TOR in Hepatocytes. *J. Biol. Chem.* **278**, 3656–3663 (2003).

213. Diehl, J. A. Cycling to Cancer with Cyclin D1. *Cancer Biol. Ther.* **1**, 226–231 (2002).

214. Vicent, S. *et al.* ERK 1/2 is activated in non-small-cell lung cancer and associated with advanced tumours. *Br. J. Cancer* **90**, 1047–1052 (2004).

215. Ma, J. *et al.* BMP4 promotes oxaliplatin resistance by an induction of epithelial-mesenchymal transition via MEK1/ERK/ELK1 signaling in hepatocellular carcinoma. *Cancer Lett.* **411**, 117–129 (2017).

216. Tsukada, Y.-I., Miyazawa, K. & Kitamura, N. High Intensity ERK Signal Mediates Hepatocyte Growth Factor-induced Proliferation Inhibition of the Human Hepatocellular Carcinoma Cell Line HepG2. *J. Biol. Chem.* **276**, 40968–40976 (2001).

217. Mebratu, Y. & Tesfaigzi, Y. How ERK1/2 activation controls cell proliferation and cell death is subcellular localization the answer? *Cell Cycle* **8**, 1168–1175 (2009).

218. Vetö, B. *et al.* The transcriptional activity of hepatocyte nuclear factor 4 alpha is inhibited via phosphorylation by ERK1/2. *PLoS One* **12**, e0172020 (2017).

219. Templeman, N. M. & Murphy, C. T. Regulation of reproduction and longevity by nutrient-sensing pathways. *Journal of Cell Biology* vol. 217 93–106 (2018).

220. Saxton, R. A. & Sabatini, D. M. mTOR Signaling in Growth, Metabolism, and Disease. *Cell* **168**, 960–976 (2017).

221. Kim, D. *et al.* GβL, a Positive Regulator of the Rapamycin-Sensitive Pathway Required for the Nutrient-Sensitive Interaction between Raptor and mTOR. *Mol. Cell* **11**, 895–904 (2003).

222. Jewell, J. L. & Guan, K. L. Nutrient signaling to mTOR and cell growth. *Trends Biochem. Sci.* **38**, 233–242 (2013).

223. Oh, W. J. & Jacinto, E. mTOR complex 2 signaling and functions. *Cell Cycle* vol. 10 2305–2316 (2011).

224. Kennedy, S. G., Kandel, E. S., Cross, T. K. & Hay, N. Akt/Protein Kinase B Inhibits

Cell Death by Preventing the Release of Cytochrome c from Mitochondria. *Mol. Cell. Biol.* **19**, 5800–5810 (1999).

225. Manning, B. D. & Cantley, L. C. AKT/PKB Signaling: Navigating Downstream. *Cell* **129**, 1261–1274 (2007).
226. Manning, B. D. & Toker, A. AKT/PKB Signaling: Navigating the Network. *Cell* **169**, 381–405 (2017).
227. Pópulo, H., Lopes, J. M. & Soares, P. The mTOR signalling pathway in human cancer. *International Journal of Molecular Sciences* vol. 13 1886–1918 (2012).
228. Joly, M. M. *et al.* Rictor/mTORC2 drives progression and therapeutic resistance of HER2-amplified breast cancers. *Cancer Res.* **76**, 4752–4764 (2016).
229. Mossmann, D., Park, S. & Hall, M. N. mTOR signalling and cellular metabolism are mutual determinants in cancer. *Nature Reviews Cancer* vol. 18 744–757 (2018).
230. Cerino, G. *et al.* Engineering of an angiogenic niche by perfusion culture of adipose-derived stromal vascular fraction cells. *Sci. Rep.* **7**, 14252 (2017).
231. Zheng, H. *et al.* Rotary culture promotes the proliferation of MCF-7 cells encapsulated in three-dimensional collagen-alginate hydrogels via activation of the ERK1/2-MAPK pathway. *Biomed. Mater.* **7**, (2012).
232. Santoro, M., Lamhamedi-Cherradi, S.-E., Menegaz, B. A., Ludwig, J. A. & Mikos, A. G. Flow perfusion effects on three-dimensional culture and drug sensitivity of Ewing sarcoma. *Proc. Natl. Acad. Sci.* **112**, 10304–10309 (2015).
233. Hongo, T. *et al.* Three-dimensional high-density culture of HepG2 cells in a 5-ml radial-flow bioreactor for construction of artificial liver. *J. Biosci. Bioeng.* **99**, 237–244 (2005).
234. Fernekorn, U. *et al.* Microbioreactor design for 3-D cell cultivation to create a pharmacological screening system. *Eng. Life Sci.* **11**, 133–139 (2011).
235. Fernekorn, U. *et al.* Microfluidic 3D HepG2 cell culture: Reproducing hepatic tumor gene and protein expression in in vitro scaffolds. *Eng. Life Sci.* **15**, 340–350 (2015).
236. Nam, S. *et al.* Cell cycle progression in confining microenvironments is regulated by a growth-responsive TRPV4-PI3K/Akt-p27 Kip1 signaling axis. *Sci. Adv.* **5**, (2019).
237. Miki, T., Ring, A. & Gerlach, J. Hepatic Differentiation of Human Embryonic Stem

Cells Is Promoted by Three-Dimensional Dynamic Perfusion Culture Conditions. *Tissue Eng. Part C Methods* **17**, 557–568 (2011).

238. Freyer, N. *et al.* Hepatic Differentiation of Human Induced Pluripotent Stem Cells in a Perfused Three-Dimensional Multicompartment Bioreactor. *Biores. Open Access* **5**, 235–248 (2016).

239. Chen, M. L. *et al.* HNF-4α determines hepatic differentiation of human mesenchymal stem cells from bone marrow. *World J. Gastroenterol.* **16**, 5092–5103 (2010).

240. Kheolamai, P. & Dickson, A. J. Liver-enriched transcription factors are critical for the expression of hepatocyte marker genes in mES-derived hepatocyte-lineage cells. *BMC Mol. Biol.* **10**, 35 (2009).

241. Rodriguez-Antona, C. Transcriptional Regulation of Human CYP3A4 Basal Expression by CCAAT Enhancer-Binding Protein alpha and Hepatocyte Nuclear Factor-3gamma. *Mol. Pharmacol.* **63**, 1180–1189 (2003).

242. Friedman, A. D., Landschulz, W. H. & McKnight, S. L. CCAAT/enhancer binding protein activates the promoter of the serum albumin gene in cultured hepatoma cells. *Genes Dev.* **3**, 1314–1322 (1989).

243. Ning, B. F. *et al.* Hepatocyte nuclear factor 4α suppresses the development of hepatocellular carcinoma. *Cancer Res.* **70**, 7640–7651 (2010).

244. Lazarevich, N. L. *et al.* Deregulation of hepatocyte nuclear factor 4 (HNF4)as a marker of epithelial tumors progression. *Exp. Oncol.* **32**, 167–71 (2010).

245. Wang, Z., Bishop, E. P. & Burke, P. A. Expression profile analysis of the inflammatory response regulated by hepatocyte nuclear factor 4α. *BMC Genomics* **12**, 128 (2011).

246. Hanse, E. A. *et al.* Cyclin D1 inhibits hepatic lipogenesis via repression of carbohydrate response element binding protein and hepatocyte nuclear factor 4α. *Cell Cycle* **11**, 2681–2690 (2012).

247. Reebye, V. *et al.* Gene activation of CEBPA using saRNA: Preclinical studies of the first in human saRNA drug candidate for liver cancer. *Oncogene* **37**, 3216–3228 (2018).

248. Berger, E., Vega, N., Weiss-Gayet, M. & Géloën, A. Gene Network Analysis of Glucose Linked Signaling Pathways and Their Role in Human Hepatocellular

Carcinoma Cell Growth and Survival in HuH7 and HepG2 Cell Lines. *Biomed Res. Int.* **2015**, 1–19 (2015).

249. Zhang, W., Huang, H., Cai, H. & Tan, W. S. Enhanced metabolic activities for ATP production and elevated metabolic flux via pentose phosphate pathway contribute for better CIK cells expansion. *Cell Prolif.* **52**, (2019).
250. Csepregi, R. *et al.* A One-Step Extraction and Luminescence Assay for Quantifying Glucose and ATP Levels in Cultured HepG2 Cells. *Int. J. Mol. Sci.* **19**, 2670 (2018).
251. Jackman, C. P., Carlson, A. L. & Bursac, N. Dynamic culture yields engineered myocardium with near-adult functional output. *Biomaterials* **111**, 66–79 (2016).
252. Liu, P. *et al.* A functional mammalian target of rapamycin complex 1 signaling is indispensable for c-Myc-driven hepatocarcinogenesis. *Hepatology* **66**, 167–181 (2017).
253. Liu, P. *et al.* Central role of mTORC1 downstream of YAP/TAZ in hepatoblastoma development. *Oncotarget* **8**, 73433–73447 (2017).
254. Jiang, G.-L., White, C. R., Stevens, H. Y. & Frangos, J. A. Temporal gradients in shear stimulate osteoblastic proliferation via ERK1/2 and retinoblastoma protein. *Am. J. Physiol. Metab.* **283**, E383–E389 (2002).
255. Chen, T., Buckley, M., Cohen, I., Bonassar, L. & Awad, H. A. Insights into interstitial flow, shear stress, and mass transport effects on ECM heterogeneity in bioreactor-cultivated engineered cartilage hydrogels. *Biomech. Model. Mechanobiol.* **11**, 689–702 (2012).
256. Riedl, A. *et al.* Comparison of cancer cells in 2D vs 3D culture reveals differences in AKT–mTOR–S6K signaling and drug responses. *J. Cell Sci.* **130**, 203–218 (2017).
257. Ullah, I., Subbarao, R. B. & Rho, G. J. Human mesenchymal stem cells - current trends and future prospective. *Biosci. Rep.* **35**, 1–18 (2015).
258. da Silva Meirelles, L., Chagastelles, P. C. & Nardi, N. B. Mesenchymal stem cells reside in virtually all post-natal organs and tissues. *J. Cell Sci.* **119**, 2204–2213 (2006).
259. Dominici, M. *et al.* Minimal criteria for defining multipotent mesenchymal stromal cells. The International Society for Cellular Therapy position statement. *Cytotherapy* **8**, 315–317 (2006).
260. Tsai, C.-C. & Hung, S.-C. Functional roles of pluripotency transcription factors in

mesenchymal stem cells. *Cell Cycle* **11**, 3711–3712 (2012).

261. Shahini, A., Mistriotis, P., Asmani, M., Zhao, R. & Andreadis, S. T. NANOG Restores Contractility of Mesenchymal Stem Cell-Based Senescent Microtissues. *Tissue Eng. - Part A* **23**, 535–545 (2017).

262. Han, J. *et al.* Nanog Reverses the Effects of Organismal Aging on Mesenchymal Stem Cell Proliferation and Myogenic Differentiation Potential. *Stem Cells* **30**, 2746–2759 (2012).

263. Heo, J. S., Choi, Y., Kim, H.-S. & Kim, H. O. Comparison of molecular profiles of human mesenchymal stem cells derived from bone marrow, umbilical cord blood, placenta and adipose tissue. *Int. J. Mol. Med.* **37**, 115–125 (2016).

264. Djouad, F. *et al.* Activin A expression regulates multipotency of mesenchymal progenitor cells. *Stem Cell Res. Ther.* **1**, 11 (2010).

265. Pittenger, M. F. *et al.* Multilineage Potential of Adult Human Mesenchymal Stem Cells. *Science (80-.).* **284**, 143–147 (1999).

266. Mackay, A. M. *et al.* Chondrogenic differentiation of cultured human mesenchymal stem cells from marrow. *Tissue Eng.* **4**, 415–428 (1998).

267. Cortés-Medina, L. V *et al.* Neuronal Transdifferentiation Potential of Human Mesenchymal Stem Cells from Neonatal and Adult Sources by a Small Molecule Cocktail. *Stem Cells Int.* **2019**, 1–13 (2019).

268. Andrzejewska, A., Lukomska, B. & Janowski, M. Concise Review: Mesenchymal Stem Cells: From Roots to Boost. *Stem Cells* **37**, 855–864 (2019).

269. D'souza, N. *et al.* Mesenchymal stem/stromal cells as a delivery platform in cell and gene therapies. *BMC Med.* **13**, 186 (2015).

270. Weiss, A. R. R. & Dahlke, M. H. Immunomodulation by Mesenchymal Stem Cells (MSCs): Mechanisms of Action of Living, Apoptotic, and Dead MSCs. *Front. Immunol.* **10**, 1191 (2019).

271. Yin, K., Wang, S. & Zhao, R. C. Exosomes from mesenchymal stem/stromal cells: a new therapeutic paradigm. *Biomark. Res.* **7**, 8 (2019).

272. Fitzsimmons, R. E. B., Mazurek, M. S., Soos, A. & Simmons, C. A. Mesenchymal Stromal/Stem Cells in Regenerative Medicine and Tissue Engineering. *Stem Cells Int.* **2018**, 1–16 (2018).

273. Munir, H., Ed Rainger, G., Nash, G. B. & McGettrick, H. Analyzing the effects of

stromal cells on the recruitment of leukocytes from flow. *J. Vis. Exp.* e52480 (2015) doi:10.3791/52480.

274. Brown, J. M., Nemeth, K., Kushnir-Sukhov, N. M., Metcalfe, D. D. & Mezey, E. Bone marrow stromal cells inhibit mast cell function via a COX2-dependent mechanism. *Clin. Exp. Allergy* **41**, 526–534 (2011).

275. Chung, E. & Son, Y. Crosstalk between mesenchymal stem cells and macrophages in tissue repair. *Tissue Eng. Regen. Med.* **11**, 431–438 (2014).

276. Chulpanova, D. S. *et al.* Application of Mesenchymal Stem Cells for Therapeutic Agent Delivery in Anti-tumor Treatment. *Front. Pharmacol.* **9**, (2018).

277. Kim, S. M. *et al.* Irradiation enhances the tumor tropism and therapeutic potential of tumor necrosis factor-related apoptosis-inducing ligand-secreting human umbilical cord blood-derived mesenchymal stem cells in glioma therapy. *Stem Cells* **28**, 2217–2228 (2010).

278. Guiho, R. *et al.* TRAIL delivered by mesenchymal stromal/stem cells counteracts tumor development in orthotopic Ewing sarcoma models. *Int. J. Cancer* **139**, 2802–2811 (2016).

279. Gilazieva, Z., Tazetdinova, L., Arkhipova, S., Solovyeva, V. & Rizvanov, A. Effect of Cisplatin on Ultrastructure and Viability of Adipose-Derived Mesenchymal Stem Cells. *Bionanoscience* **6**, 534–539 (2016).

280. Apelgren, P. *et al.* Chondrocytes and stem cells in 3D-bioprinted structures create human cartilage in vivo. *PLoS One* **12**, e0189428 (2017).

281. Yu, J. *et al.* The use of human mesenchymal stem cells encapsulated in RGD modified alginate microspheres in the repair of myocardial infarction in the rat. *Biomaterials* **31**, 7012–7020 (2010).

282. Landázuri, N. *et al.* Alginate microencapsulation of human mesenchymal stem cells as a strategy to enhance paracrine-mediated vascular recovery after hindlimb ischaemia. *J. Tissue Eng. Regen. Med.* **10**, 222–232 (2016).

283. Broughton, G., Janis, J. E. & Attinger, C. E. Wound Healing: An Overview. *Plast. Reconstr. Surg.* **117**, 1e-S-32e-S (2006).

284. Mao, A. S. *et al.* Programmable microencapsulation for enhanced mesenchymal stem cell persistence and immunomodulation. *Proc. Natl. Acad. Sci.* **116**, 15392–15397 (2019).

285. Osiecki, M. J. *et al.* Packed Bed Bioreactor for the Isolation and Expansion of Placental-Derived Mesenchymal Stromal Cells. *PLoS One* **10**, e0144941 (2015).

286. Teixeira, F. G. *et al.* Modulation of the Mesenchymal Stem Cell Secretome Using Computer-Controlled Bioreactors: Impact on Neuronal Cell Proliferation, Survival and Differentiation. *Sci. Rep.* **6**, 27791 (2016).

287. Petry, F., Weidner, T., Czermak, P. & Salzig, D. Three-Dimensional Bioreactor Technologies for the Cocultivation of Human Mesenchymal Stem/Stromal Cells and Beta Cells. *Stem Cells Int.* **2018**, 1–14 (2018).

288. Zhao, F., Chella, R. & Ma, T. Effects of shear stress on 3-D human mesenchymal stem cell construct development in a perfusion bioreactor system: Experiments and hydrodynamic modeling. *Biotechnol. Bioeng.* **96**, 584–595 (2007).

289. Costa, M. H. G., McDevitt, T. C., Cabral, J. M. S., da Silva, C. L. & Ferreira, F. C. Tridimensional configurations of human mesenchymal stem/stromal cells to enhance cell paracrine potential towards wound healing processes. *J. Biotechnol.* **262**, 28–39 (2017).

290. Sailon, A. M. *et al.* A Novel Flow-Perfusion Bioreactor Supports 3D Dynamic Cell Culture. *J. Biomed. Biotechnol.* **2009**, 1–7 (2009).

291. Lee, S., Choi, E., Cha, M.-J. & Hwang, K.-C. Cell Adhesion and Long-Term Survival of Transplanted Mesenchymal Stem Cells: A Prerequisite for Cell Therapy. *Oxid. Med. Cell. Longev.* **2015**, 1–9 (2015).

292. Benoit, D. S. W. *et al.* Integrin-linked kinase production prevents anoikis in human mesenchymal stem cells. *J. Biomed. Mater. Res. Part A* **81A**, 259–268 (2007).

293. Rafiq, Q. A., Brosnan, K. M., Coopman, K., Nienow, A. W. & Hewitt, C. J. Culture of human mesenchymal stem cells on microcarriers in a 5 l stirred-tank bioreactor. *Biotechnol. Lett.* **35**, 1233–1245 (2013).

294. Rodrigues, C. A. V., Fernandes, T. G., Diogo, M. M., da Silva, C. L. & Cabral, J. M. S. Stem cell cultivation in bioreactors. *Biotechnol. Adv.* **29**, 815–829 (2011).

295. Frith, J. E., Thomson, B. & Genever, P. G. Dynamic Three-Dimensional Culture Methods Enhance Mesenchymal Stem Cell Properties and Increase Therapeutic Potential. *Tissue Eng. Part C Methods* **16**, 735–749 (2010).

296. Tang, Y. *et al.* The combination of three-dimensional and rotary cell culture system promotes the proliferation and maintains the differentiation potential of rat

BMSCs. *Sci. Rep.* **7**, 192 (2017).

297. Choe, G. *et al.* Studies on the effects of microencapsulated human mesenchymal stem cells in RGD-modified alginate on cardiomyocytes under oxidative stress conditions using in vitro biomimetic co-culture system. *Int. J. Biol. Macromol.* **123**, 512–520 (2019).

298. Re, F. *et al.* 3D gelatin-chitosan hybrid hydrogels combined with human platelet lysate highly support human mesenchymal stem cell proliferation and osteogenic differentiation. *J. Tissue Eng.* **10**, 204173141984585 (2019).

299. Catelas, I., Sese, N. ;, Helgerson, S. & Tawil, B. FIBRIN GEL: A SCAFFOLD FOR PROLIFERATION AND DIFFERENTIATION OF MESENCHYMAL STEM CELLS. in *50th Annual Meeting of the Orthopaedic Research Society*.

300. Boido, M. *et al.* Chitosan-based hydrogel to support the paracrine activity of mesenchymal stem cells in spinal cord injury treatment. *Sci. Rep.* **9**, 6402 (2019).

301. E. Klontzas, M., Drissi, H. & Mantalaris, A. The Use of Alginate Hydrogels for the Culture of Mesenchymal Stem Cells (MSCs): In Vitro and In Vivo Paradigms. in *Alginates [Working Title]* (IntechOpen, 2019). doi:10.5772/intechopen.88020.

302. Ferreira, S. A. *et al.* Bi-directional cell-pericellular matrix interactions direct stem cell fate. *Nat. Commun.* **9**, 4049 (2018).

303. Lee, H. P., Gu, L., Mooney, D. J., Levenston, M. E. & Chaudhuri, O. Mechanical confinement regulates cartilage matrix formation by chondrocytes. *Nat. Mater.* **16**, 1243–1251 (2017).

304. Goldshmid, R. & Seliktar, D. Hydrogel Modulus Affects Proliferation Rate and Pluripotency of Human Mesenchymal Stem Cells Grown in Three-Dimensional Culture. *ACS Biomater. Sci. Eng.* **3**, 3433–3446 (2017).

305. Rufaihah, A. J. *et al.* The Effect of Scaffold Modulus on the Morphology and Remodeling of Fetal Mesenchymal Stem Cells. *Front. Physiol.* **9**, (2018).

306. Qazi, T. H., Mooney, D. J., Duda, G. N. & Geissler, S. Biomaterials that promote cell-cell interactions enhance the paracrine function of MSCs. *Biomaterials* **140**, 103–114 (2017).

307. Lopez-Mendez, T. B. *et al.* Improved control over MSCs behavior within 3D matrices by using different cell loads in both in vitro and in vivo environments. *Int. J. Pharm.* **533**, 62–72 (2017).

308. Pitrone, M. *et al.* Knockdown of NANOG reduces cell proliferation and induces G0/G1 cell cycle arrest in human adipose stem cells. *Int. J. Mol. Sci.* **20**, 2–13 (2019).

309. Singh, P., Fukuda, S., Liu, L., Chitteti, B. R. & Pelus, L. M. Survivin Is Required for Mouse and Human Bone Marrow Mesenchymal Stromal Cell Function. *Stem Cells* **36**, 123–129 (2018).

310. Ridzuan, N., Al Abbar, A., Yip, W. K., Maqbool, M. & Ramasamy, R. Characterization and Expression of Senescence Marker in Prolonged Passages of Rat Bone Marrow-Derived Mesenchymal Stem Cells. *Stem Cells Int.* **2016**, 1–14 (2016).

311. Deng, B. *et al.* Removal from adherent culture contributes to apoptosis in human bone marrow mesenchymal stem cells. *Mol. Med. Rep.* **15**, 3499–3506 (2017).

312. Lee, J., Abdeen, A. A. & Kilian, K. A. Rewiring mesenchymal stem cell lineage specification by switching the biophysical microenvironment. *Sci. Rep.* **4**, 5188 (2015).

313. Steward, A. J. & Kelly, D. J. Mechanical regulation of mesenchymal stem cell differentiation. *J. Anat.* **227**, 717–731 (2015).

314. Whitehead, A. K., Barnett, H. H., Caldorera-Moore, M. E. & Newman, J. J. Poly (ethylene glycol) hydrogel elasticity influences human mesenchymal stem cell behavior. *Regen. Biomater.* **5**, 167–175 (2018).

315. Duarte Campos, D. F. *et al.* The Stiffness and Structure of Three-Dimensional Printed Hydrogels Direct the Differentiation of Mesenchymal Stromal Cells Toward Adipogenic and Osteogenic Lineages. *Tissue Eng. Part A* **21**, 740–756 (2015).

316. Lee, J., Abdeen, A. A., Tang, X., Saif, T. A. & Kilian, K. A. Matrix directed adipogenesis and neurogenesis of mesenchymal stem cells derived from adipose tissue and bone marrow. *Acta Biomater.* **42**, 46–55 (2016).

317. Chen, D. *et al.* Differential Roles for Bone Morphogenetic Protein (BMP) Receptor Type IB and IA in Differentiation and Specification of Mesenchymal Precursor Cells to Osteoblast and Adipocyte Lineages. *J. Cell Biol.* **142**, 295–305 (1998).

318. Tondreau, T. *et al.* Bone marrow-derived mesenchymal stem cells already express specific neural proteins before any differentiation. *Differentiation* **72**, 319–326 (2004).

319. Li, H. *et al.* Fusion of HepG2 cells with mesenchymal stem cells increases cancer-associated and malignant properties: An in vivo metastasis model. *Oncol. Rep.* **32**, 539–547 (2014).

320. Zhao, D. *et al.* Inhibitory Effect and Mechanism of Mesenchymal Stem Cells Cultured in 3D System on Hepatoma Cells HepG2. *Appl. Biochem. Biotechnol.* **184**, 212–227 (2018).

321. Liau, L. L., Makpol, S., Azurah, A. G. N. & Chua, K. H. Human adipose-derived mesenchymal stem cells promote recovery of injured HepG2 cell line and show sign of early hepatogenic differentiation. *Cytotechnology* **70**, 1221–1233 (2018).

322. Li, T. Z. *et al.* Therapeutic Potential of Bone-Marrow-Derived Mesenchymal Stem Cells Differentiated with Growth-Factor-Free Coculture Method in Liver-Injured Rats. *Tissue Eng. Part A* **16**, 2649–2659 (2010).

323. Kwon, S. Y. *et al.* Hypoxia Enhances Cell Properties of Human Mesenchymal Stem Cells. *Tissue Eng. Regen. Med.* **14**, 595–604 (2017).

324. Elabd, C. *et al.* Comparing atmospheric and hypoxic cultured mesenchymal stem cell transcriptome: Implication for stem cell therapies targeting intervertebral discs. *J. Transl. Med.* **16**, 222 (2018).

325. Pattappa, G., Heywood, H. K., de Bruijn, J. D. & Lee, D. A. The metabolism of human mesenchymal stem cells during proliferation and differentiation. *J. Cell. Physiol.* **226**, 2562–2570 (2011).

326. Fuller, B., Lane, N. & Benson, E. E. *Life in the Frozen State*. (CRC Press, 2004).

327. Fuller, B. *et al.* Applications and optimization of cryopreservation technologies to cellular therapeutics. *Cell Gene Ther. Insights* **3**, 359–378 (2017).

328. Fuller, B. J. Cryoprotectants : the essential antifreezes to protect life in the frozen state . CryoLetters. *Cryoletter* **25**, 375–388 (2004).

329. Best, B. P. Cryoprotectant Toxicity: Facts, Issues, and Questions. *Rejuvenation Res* **18**, 422–436 (2015).

330. Amidi, F., Pazhohan, A., Shabani Nashtaei, M., Khodarahmian, M. & Nekoonam, S. The role of antioxidants in sperm freezing: a review. *Cell and Tissue Banking* vol. 17 745–756 (2016).

331. Minaei, M. B. *et al.* Effect of Trolox addition to cryopreservation media on human sperm motility. *Iran. J. Reprod. Med.* **10**, 99 (2012).

332. Shi, X. *et al.* Protective Effect of Sucrose and Antioxidants on Cryopreservation of Sperm Motility and DNA Integrity in C57BL/6 Mice. *Biopreserv. Biobank.* **16**, 444–450 (2018).

333. Li, Z., Lin, Q., Liu, R., Xiao, W. & Liu, W. Protective effects of ascorbate and catalase on human spermatozoa during cryopreservation. *J. Androl.* **31**, 437–444 (2010).

334. Karlsson, J. O. M. & Toner, M. Long-term storage of tissues by cryopreservation: Critical issues. *Biomaterials* **17**, 243–256 (1996).

335. Bakhach, J. The cryopreservation of composite tissues: Principles and recent advancement on cryopreservation of different type of tissues. *Organogenesis* vol. 5 119–126 (2009).

336. Zhang, C. *et al.* Hydrogel Cryopreservation System: An Effective Method for Cell Storage. *Int. J. Mol. Sci.* **19**, 3330 (2018).

337. Massie, I. R. Development of optimised cryopreservation protocol for encapsulated liver cell spheroids: towards delivery of a bioartificial liver. (University College of London, 2012).

338. Malpique, R. *et al.* Alginate Encapsulation as a Novel Strategy for the Cryopreservation of Neurospheres. *Tissue Eng. Part C Methods* **16**, 965–977 (2010).

339. Pravdyuk, A. I., Petrenko, Y. A., Fuller, B. J. & Petrenko, A. Y. Cryopreservation of alginate encapsulated mesenchymal stromal cells. *Cryobiology* **66**, (2013).

340. Manuchehrabadi, N. *et al.* Improved tissue cryopreservation using inductive heating of magnetic nanoparticles. *Sci. Transl. Med.* **9**, eaah4586 (2017).

341. Briard, J. G. *et al.* Small molecule ice recrystallization inhibitors mitigate red blood cell lysis during freezing, transient warming and thawing. *Sci. Rep.* **6**, 23619 (2016).

342. Karabulut, S., Demiroğlu-Zergeroğlu, A., Yılmaz, E., Sağır, F. & Delikara, N. p53 and mitogen-activated protein kinase pathway protein profiles in fresh and frozen spermatozoa. *Andrologia* **46**, 1113–1117 (2014).

343. Xu, X. *et al.* The roles of apoptotic pathways in the low recovery rate after cryopreservation of dissociated human embryonic stem cells. *Biotechnol. Prog.* **26**, 827–837 (2010).

344. Xu, X. *et al.* Enhancement of cell recovery for dissociated human embryonic stem cells after cryopreservation. *Biotechnol. Prog.* **26**, 781–788 (2009).

345. Roy, R., Hinduja, S. & Teti, R. Recent advances in engineering design optimisation: Challenges and future trends. *CIRP Ann. - Manuf. Technol.* **57**, 697–715 (2008).

346. Arora, J. S. Introduction to Design Optimization. in *Introduction to Optimum Design* 259–275 (Elsevier Inc., 2007).

347. Parkinson, A. R., Balling, R. J. & Hedengren, J. D. *Optimization Methods for Engineering Design*. (Brigham Young University, 2013).

348. Du, X. Introduction to optimization design. 1–22 (1988).

349. Sobieszczanski-Sobieski, J., Morris, A. & van Tooren, M. J. L. *Multidisciplinary Design Optimization Supported by Knowledge Based Engineering*. *Multidisciplinary Design Optimization Supported by Knowledge Based Engineering* (2015). doi:10.1002/9781118897072.

350. Mandenius, C. F. & Brundin, A. Bioprocess optimization using design-of-experiments methodology. *Biotechnology Progress* vol. 24 1191–1203 (2008).

351. Loubière, C. *et al.* Optimization of the impeller design for MSC culture on microcarriers in bioreactors. *Chem. Eng. Technol.* ceat.201900105 (2019) doi:10.1002/ceat.201900105.

352. Patrachari, A. R., Podichetty, J. T. & Madihally, S. V. Application of computational fluid dynamics in tissue engineering. *J. Biosci. Bioeng.* **114**, 123–132 (2012).

353. Rapp, B. E. Finite Difference Method. in *Microfluidics: Modelling, Mechanics and Mathematics* vol. 21 623–631 (Elsevier, 2017).

354. Solving dynamic equations in dye transport. in *Modelling, Simulation and Control of the Dyeing Process* 100–113 (Elsevier, 2014). doi:10.1533/9780857097583.100.

355. Rapp, B. E. Finite Volume Method. in *Microfluidics: Modelling, Mechanics and Mathematics* vol. 16 633–654 (Elsevier, 2017).

356. Moen, R. *Foundation and History of the PDSA Cycle*. https://deming.org/uploads/paper/PDSA_History_Ron_Moen.pdf.

357. Sahno, J. & & Shevtshenko, E. Quality Improvement Methodologies for Improvement of Production Process and Product Quality and their Evolution. in *9th International DAAAM Baltic Conference 'Industrial Engineering'* 181–186 (2014).

358. Berman, B. 3-D printing: The new industrial revolution. *Bus. Horiz.* **55**, 155–162 (2012).

359. Guvendiren, M., Molde, J., Soares, R. M. D. & Kohn, J. Designing Biomaterials for 3D Printing. *ACS Biomater. Sci. Eng.* **2**, 1679–1693 (2016).

360. Gross, B. C., Erkal, J. L., Lockwood, S. Y., Chen, C. & Spence, D. M. Evaluation of 3D printing and its potential impact on biotechnology and the chemical sciences. *Anal. Chem.* **86**, 3240–3253 (2014).

361. Jayanth, N., Senthil, P. & Prakash, C. Effect of chemical treatment on tensile strength and surface roughness of 3D-printed ABS using the FDM process. *Virtual Phys. Prototyp.* **13**, 155–163 (2018).

362. An, J., Teoh, J. E. M., Suntornnond, R. & Chua, C. K. Design and 3D Printing of Scaffolds and Tissues. *Engineering* **1**, 261–268 (2015).

363. Marimuthu, S. *et al.* Characteristics of hole formation during laser drilling of SiC reinforced aluminium metal matrix composites. *J. Mater. Process. Technol.* **271**, 554–567 (2019).

364. Christophe, J. & Planquart, P. Diagnostics for laser cutting efficiency using computational fluid dynamics. *Procedia Manuf.* **29**, 375–382 (2019).

365. Chau, L., Doran, M. & Cooper-White, J. A novel multishear microdevice for studying cell mechanics. *Lab Chip* **9**, 1897–1902 (2009).

366. Pak, T., Archilha, N. L., Mantovani, I. F., Moreira, A. C. & Butler, I. B. An X-ray computed micro-tomography dataset for oil removal from carbonate porous media. *Sci. Data* **6**, 190004 (2019).

367. Huang, Z., Odeleye, A. O. O., Ye, H., Cui, Z. & Yang, A. Fluid dynamic characterization of a fluidized-bed perfusion bioreactor with CFD–DEM simulation. *J. Chem. Technol. Biotechnol.* **93**, 2316–2330 (2018).

368. Hafiz, M. A., Batcha, M. F. M. & Asmuin, N. Effect of plenum chamber depth in a swirling fluidized bed. in *IOP Conference Series: Materials Science and Engineering* vol. 50 (2013).

369. Maurina, G. Z., Rosa, L. M., Beal, L. L. & Torres, A. P. Numerical Study of Different Inlet Configurations on the Fluid Dynamics of an Anaerobic Sequencing Batch Reactor. *Chem. Eng. Trans.* **38**, 127–132 (2014).

370. Zou, Z. *et al.* CFD simulations of tapered bubbling/turbulent fluidized beds with/without gas distributor based on the structure-based drag model. *Chem. Eng. Sci.* **202**, 157–168 (2019).

371. Gernon, T. M. & Gilbertson, M. A. Segregation of particles in a tapered fluidized bed. *Powder Technol.* **231**, 88–101 (2012).

372. Rees, A. C. *et al.* The nature of the flow just above the perforated plate distributor of a gas-fluidised bed, as imaged using magnetic resonance. *Chem. Eng. Sci.* **61**, 6002–6015 (2006).

373. Sobrino, C., Ellis, N. & de Vega, M. Distributor effects near the bottom region of turbulent fluidized beds. *Powder Technol.* **189**, 25–33 (2009).

374. Al-Akaishi, A., Valera-Medina, A., Chong, C. T. & Marsh, R. CFD Analysis of the Fluidised Bed Hydrodynamic Behaviour inside an Isothermal Gasifier with different Perforated Plate Distributors. in *Energy Procedia* vol. 142 835–840 (2017).

375. Hilal, N., Ghannam, M. T. & Anabtawi, M. Z. Effect of bed diameter, distrubutor and inserts on minimum fluidization velocity. *Chem. Eng. Technol.* **24**, 161–165 (2001).

376. Paiva, J. M., Pinho, C. & Figueiredo, R. Influence of the Distributor Plate and Operating Conditions on the Fluidization Quality of a Gas Fluidized Bed. *Chem. Eng. Commun.* **196**, 342–361 (2008).

377. Bakhurji, A., Bi, X. & Grace, J. R. Hydrodynamics and solids mixing in fluidized beds with inclined-hole distributors. *Particuology* **43**, 19–28 (2019).

378. Ghaly, A., Ergudenler, A. & Ramakrishnan, V. Effect of Distributor Plate Configuration on Pressure Drop in a Bubbling Fluidized Bed Reactor. *Adv. Res.* **3**, 251–268 (2014).

379. Qureshi, A. E. & Creasy, D. E. Fluidised Bed Gas Distributors. *Powder Tecirnology* **22**, 113–119 (1979).

380. Raveling, A. R., Theodossiou, S. K. & Schiele, N. R. A 3D printed mechanical bioreactor for investigating mechanobiology and soft tissue mechanics. *MethodsX* **5**, 924–932 (2018).

381. Chen, C. *et al.* 3D-printed microfluidic devices: fabrication, advantages and limitations - a mini review. *Analytical Methods* vol. 8 6005–6012 (2016).

382. McDonough, J. R., Law, R., Reay, D. A. & Zivkovic, V. Fluidization in small-scale gas-solid 3D-printed fluidized beds. *Chem. Eng. Sci.* **200**, 294–309 (2019).

383. Mendonça Lopes, M. G., Santana, H. S., Andolphato, V. F., Silva, J. L. & Taranto, O. P. Flow uniformity data on 3D printed flow distributors. *Data Br.* **23**, 103799

(2019).

384. Park, Y. J., Yu, T., Yim, S. J., You, D. & Kim, D. P. A 3D-printed flow distributor with uniform flow rate control for multi-stacked microfluidic systems. *Lab Chip* **18**, 1250–1258 (2018).

385. Radmanesh, M. & Kiani, A. ND:YAG Laser Pulses Ablation Threshold of Stainless Steel 304. *Mater. Sci. Appl.* **06**, 634–645 (2015).

386. Figaro, S. *et al.* Optimizing the fluidized bed bioreactor as an external bioartificial liver. *Int. J. Artif. Organs* **40**, 196–203 (2017).

387. Li, Y. *et al.* Novel spheroid reservoir bioartificial liver improves survival of nonhuman primates in a toxin-induced model of acute liver failure. *Theranostics* **8**, 5562–5574 (2018).

388. Pincet, F. *et al.* FRAP to characterize molecular diffusion and interaction in various membrane environments. *PLoS One* **11**, (2016).

389. Kim, S. hee & Chu, C. C. Pore structure analysis of swollen dextran-methacrylate hydrogels by SEM and mercury intrusion porosimetry. *J. Biomed. Mater. Res.* **53**, 258–266 (2000).

390. Galluzzi, M. *et al.* Space-resolved quantitative mechanical measurements of soft and supersoft materials by atomic force microscopy. *NPG Asia Mater.* **8**, e327–e327 (2016).

391. Castilho, M. *et al.* Mechanical behavior of a soft hydrogel reinforced with three-dimensional printed microfibre scaffolds. *Sci. Rep.* **8**, (2018).

392. Hu, Y., You, J.-O., Auguste, D. T., Suo, Z. & Vlassak, J. J. Indentation: A simple, nondestructive method for characterizing the mechanical and transport properties of pH-sensitive hydrogels. *J. Mater. Res.* **27**, 152–160 (2012).

393. Kloxin, A. M., Kloxin, C. J., Bowman, C. N. & Anseth, K. S. Mechanical properties of cellularly responsive hydrogels and their experimental determination. *Adv. Mater.* **22**, 3484–3494 (2010).

394. van Wenum, M. *et al.* Selecting cells for bioartificial liver devices and the importance of a 3D culture environment: A functional comparison between the hepaRG and C3A cell lines. *Int. J. Biol. Sci.* **12**, 964–978 (2016).

395. Kamei, K., Yoshioka, M., Terada, S., Tokunaga, Y. & Chen, Y. Three-dimensional cultured liver-on-a-Chip with mature hepatocyte-like cells derived from human

pluripotent stem cells. *Biomed. Microdevices* **21**, 73 (2019).

396. Burns, J. & Manda, G. Metabolic Pathways of the Warburg Effect in Health and Disease: Perspectives of Choice, Chain or Chance. *Int. J. Mol. Sci.* **18**, 2755 (2017).
397. Fang, Y. *et al.* Pharmacological inhibition of TRPV4 channel suppresses malignant biological behavior of hepatocellular carcinoma via modulation of ERK signaling pathway. *Biomed. Pharmacother.* **101**, 910–919 (2018).
398. Rumman, M. *et al.* Induction of quiescence (G0) in bone marrow stromal stem cells enhances their stem cell characteristics. *Stem Cell Res.* **30**, 69–80 (2018).
399. Ferreira, S. A. *et al.* Neighboring cells override 3D hydrogel matrix cues to drive human MSC quiescence. *Biomaterials* **176**, 13–23 (2018).
400. Kim, H. *et al.* Mesenchymal stem cell 3D encapsulation technologies for biomimetic microenvironment in tissue regeneration. *Stem Cell Res. Ther.* **10**, 51 (2019).
401. Pasini, A., Lovecchio, J., Ferretti, G. & Giordano, E. Medium Perfusion Flow Improves Osteogenic Commitment of Human Stromal Cells. *Stem Cells Int.* **2019**, 1–10 (2019).
402. Jeon, O., Alt, D. S., Ahmed, S. M. & Alsberg, E. The effect of oxidation on the degradation of photocrosslinkable alginate hydrogels. *Biomaterials* **33**, 3503–3514 (2012).
403. Kharkar, P. M., Kiick, K. L. & Kloxin, A. M. Designing degradable hydrogels for orthogonal control of cell microenvironments. *Chem. Soc. Rev.* **42**, 7335–7372 (2013).
404. Lu, Y.-C. *et al.* Designing compartmentalized hydrogel microparticles for cell encapsulation and scalable 3D cell culture. *J. Mater. Chem. B* **3**, 353–360 (2015).

Appendix 1

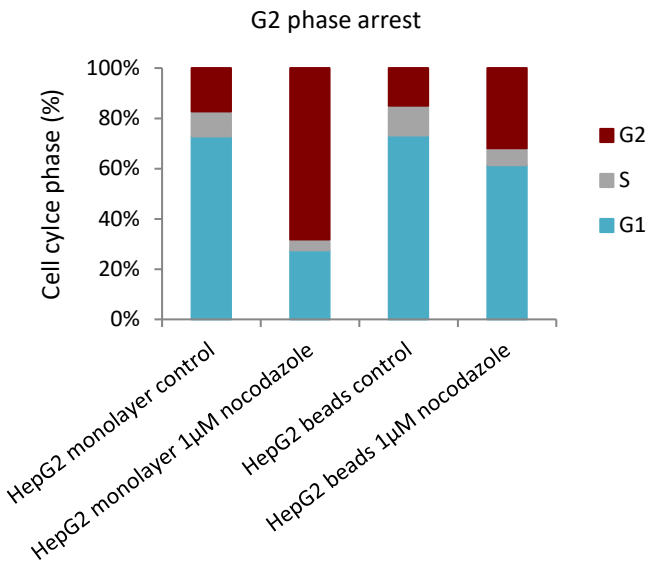

Cell cycle analysis of arrest at G2 phase. HepG2 cells cultured in monolayer and encapsulated in alginate beads were incubated for 24 h with 1 µM nocodazole. Percentage of cells in G_0/G_1, S and G_2 phases determined through quantification of DNA content by PI staining. Data presented corresponds to 10 000 cells analysed by FACS of one experimental replicate (n = 1).

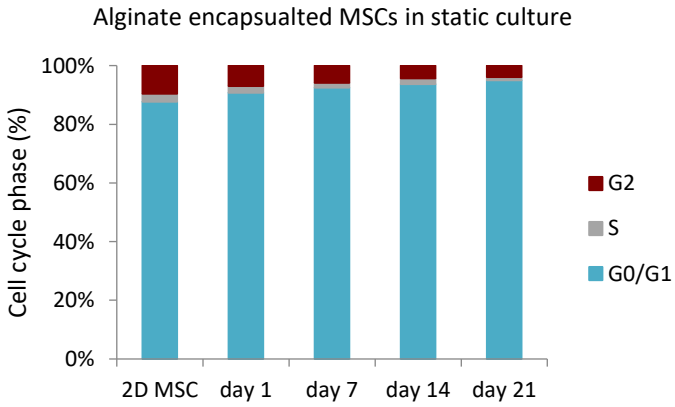

Cell cycle analysis of alginate encapsulated MSCs in static culture. Determining percentage of cells in G_0/G_1, S and G_2 phases on days 0, 1, 4, 8 and 12 through quantification of DNA content by PI staining. Data presented corresponds to 10 000 cells analysed by FACS of one experimental replicate (n = 1).

Appendix 2

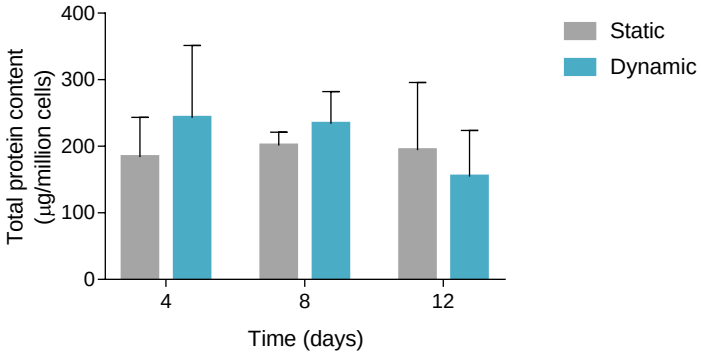

Cellular protein content of alginate encapsulated HepG2 cells cultured over 12 days in static and dynamic conditions. Analysis performed from total protein extracted and concentration measured through Pierce™ BCA protein assay. Data presented as average ± SD (n = 4).

Appendix 3

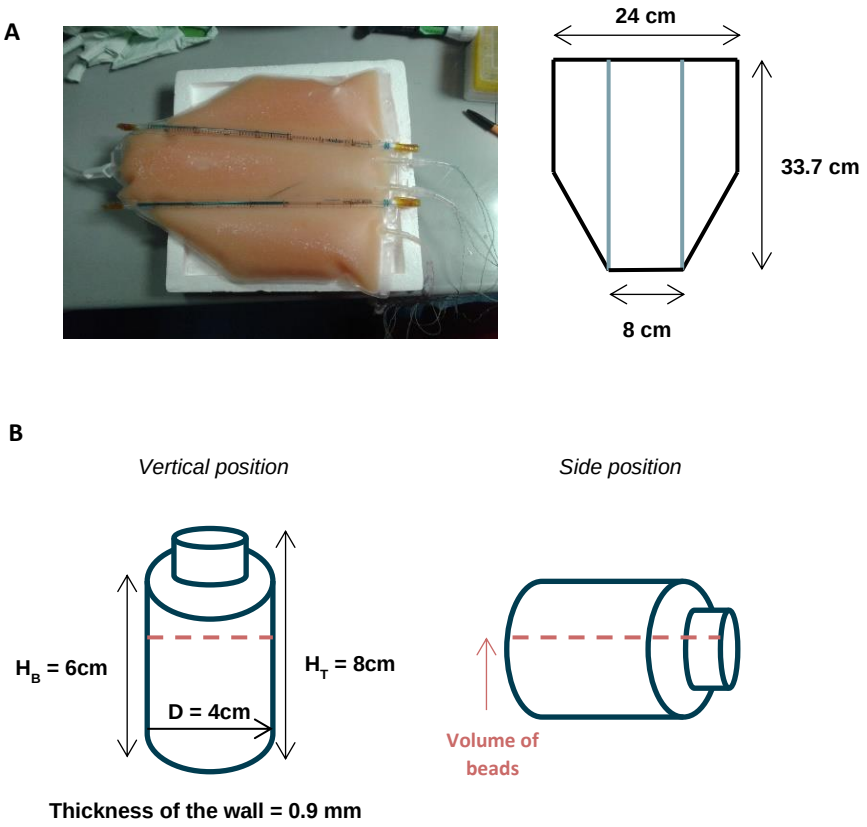

Containers for large and small scale cryopreservation of HepG2 spheroids encapsulated in alginate beads. (A) 2 L volume conical cryobag sectioned in 3 parts to promote homogeneous cryopreservation of encapsulated HepG2 cells and its schematic representation with the respective dimensions. (B) Schematic of small polypropylene bottles for small scale cryopreservation of cell beads. Vertical position indicates bottle dimensions, whereas the side position shows how the bottles were frozen and the height of the volume of cell beads inside.